Experimental and Theoretical Analysis of Pressure Coupled Infusion Gyration for Fibre Production

A dissertation submitted in partial fulfilment of the requirements for transfer to the degree of

Doctor of Philosophy

of

University College London

Xianze Hong

Department of Mechanical Engineering

University College London

September 2019

Declaration

I, Xianze Hong, confirm that the work presented in this thesis is my own. Where information has been derived from other sources, I confirm that this has been indicated in the work.

Signature:

Date:

Dedication

To

My families

And my teachers

Abstract

In this work, we uncover the science of the combined application of external pressure, controlled infusion of polymer solution and gyration in the field of nanofiber preparation. This novel application takes gyration-based method into another new arena through enabling the mass production of exceedingly fine (few nanometres upwards) nanofibres in a single step. Polyethylene oxide (PEO) was used as a model polymer in the experimental study, which shows the use of this novel method to fabricate polymeric nanofibres and nanofibrous mats under different combinations of operating parameters, including working pressure, rotational speed, infusion rate and collection distance. The morphologies of the nanofibres were characterised using scanning electron microscopy, and the anisotropy of alignment of fibre was studied using two dimensional fast Fourier transform analysis. A correlation between the product morphology and the processing parameters is established.

The response surface models of the experimental process were developed using the least squares fitting. A systematic description of the PCIG spinning was developed to help us obtain a clear understanding of the fibre formation process of this novel application. The input data we used are the conventional mean of fibre diameter measurements obtained from our experimental works. In this part, both linear and nonlinear fitting formats were applied, and the successes of the fitted models were mainly evaluated using Adjusted R^2 and Akaike Information Criterion (AIC). The correlations and effects of individual parameters and their interactions were explicitly studied. The modelling results indicated the polymer concentration has the most significant impact on fibre diameters. A self-defined objective function was studied with the best-fitted model to optimise the experimental process for achieving the

desired nanofibre diameters and narrow standard deviations. The experimental parameters were optimised by several algorithms, and the most favoured sets of parameters recommended by the non-linear interior point methods were further validated through a set of additional experiments. The results of validation indicated that pressure coupled infusion gyration offers a facile way for forming nanofibres and nanofibre assemblies, and the developed model has a good prediction power of experimental parameters that are possible to be useful for achieving the desirable PEO nanofibres.

Impact Statement

Many previous studies have already demonstrated and established the important role of nanofibres in an extremely vast scope of applications. Many fabrication methods, such as molecular self-assembly, phase separation, template synthesis and electrospinning, are currently used to fabricate polymeric fibres in the range of nano- to microscale, with electrospinning being the most popular. Although electrospinning may be appropriate for small batches of pharmaceuticals, the product output limitation has severely reduced the commercial viability of the approach for any application whereby large scale manufacture is necessary.

Pressurised gyration (spinning) has drawn increasing attention in the international arena, both academic and industrial, especially in the field of biomaterials processing and development of advanced biomedical engineering applications. There are many large research projects related to gyration methods across the world. Pressurised gyration research on polymers is a UCL invention (W02014155102 A1 of March 2014) in Prof. Mohan Edirisinghe's lab (https://www.edirisinghelab.com/) and is being investigated in depth backed by very recently approved EPSRC funding totally £1.5 million (EP/L023059/1, EP/N034228/1 and now EP/S016872/1). This PhD project takes gyration into another new arena where we combined pressure and flow simultaneously with gyration (namely pressure coupled infusion gyration, PCIG) so that smart, exceedingly fine (few nanometres upwards) nanofibres can be mass-produced in very high yield.

This project integrates experimental investigation and theoretical model developments, which covers rheology, fluid dynamics and computational statistics.

The prototype of the novel gyration method has already been designed and investigated with a model polymer system. Extending the work to different biopolymers and binding peptides (proteins) with biopolymers to produce muti-functional fibres by this new device is on-going. The up-to-date results indicate that the more tailored nanofibres can be produced by PCIG when compared with pressurised gyration or infusion gyration alone.

A deep understanding of the spinning mechanism and modelling of the spinning process was achieved, which is crucial to utilise this novel gyration method to process biomaterials to get products with the desired structure (fibres, and possibly for particles or bubbles in the future). The mathematical modelling of the spinning process of novel gyration provides guidance to more thorough understanding about the effects of different parameters on the product morphology, which will help researchers to make predictions in the quest to find the critical conditions for specific forming applications. It associates with experimental research to promote the iterative optimisation of the novel spinning method, even going as far as to broaden its utilisation in various fields and further promisingly escalate the novel gyration process to the commercial level.

Publications

Hong, X., Edirisinghe, M., & Mahalingam, S. (2016). Beads, beaded-fibres and fibres: Tailoring the morphology of poly (caprolactone) using pressurised gyration. *Materials Science and Engineering: C*, *69*, 1373-1382.

Hong, X., Mahalingam, S., & Edirisinghe, M. (2017). Simultaneous Application of Pressure-Infusion-Gyration to Generate Polymeric Nanofibers. *Macromolecular Materials and Engineering*, *302*(6), 1600564. (award front cover status)

Hong, X., Harker, A., & Edirisinghe, M. (2018). Process modeling for the fiber diameter of polymer, spun by pressure-coupled infusion gyration. *ACS Omega*, *3*(5), 5470-5479.

Hong, X., Harker, A., & Edirisinghe, M. (2019). Empirical modelling and optimization of pressure-coupled infusion gyration parameters for the nanofibre fabrication. *Proceedings of the Royal Society A*, *475*(2225), 20190008. (award front cover status)

Awards

University College London Research Student Scholarship

Best of Macros 2018 (https://www.advancedsciencenews.com/best-of-macros-2018/)

Acknowledgements

I would like to express my sincerest thanks to my primary supervisor Professor Mohan Edirisinghe. Professor Mohan Edirisinghe is a professional scientist and patient mentor. He always encourages me and provides valuable insights into different aspects of biomaterial researches. I am most grateful for his supervisions, supports and tolerances to ensure that I have the best academic and social experience at University College London. His inspiring guidance and timely encouragement helped me to grow into a good researcher. I would also like to express gratitude to my second supervisors Prof. Anthony Harker and Dr. Suntharavathanan Mahalingam, who have offers invaluable guidance and supervisions on my theoretical studies and experiments throughout my PhD. studies. Thanks to my transfer viva examiners Dr. Jie Huang and Prof. Paolo Colombo for their professional advice to improve my thesis. I would also like to Prof. Lingbo Li about his consulting helps in terms of statistics, and the assistance of Dr. Tom Gregory from the Institute of Archaeology of UCL about the SEM imaging in this work. Special thanks to Dr. Simon Banks and UCL Engineering Faculty for the funding support me in the study. Thanks to my colleagues for their encouragement and advice during my research.

The last but not least, I would like to thank my beloved parents for providing me with this precious opportunity to study in UCL and their encouragements that accompanied me all the time. A big thank you goes to my wife Xingyi Li, for her most wonderful way to join in my life. Thank you for your love and support for all early mornings and late nights. Thank you for being my muse, best friend and sounding board. I owe you everything.

Table of Contents

List of Figures

List of Tables

Abbreviation

AIC	Akaike Information Criterion
ANN	Artificial Neural Networks
ANOVA	Analysis of Variance
BP	Back Propagation
DBSCAN	Density-based Spatial Clustering of Applications with Noise
DE	Differential evolution
ECM	Extracellular Matrix
ES	Electrospinning
FE-SEM	Field Emission Scanning Electron Microscopy
FFT	Fast Fourier Transform
GA	Genetic Algorithm
NM	Nelder–Mead
PCIG	Pressure Coupled Infusion Gyration
PCL	Poly(E-Caprolactone)
PEO	Poly(ethylene oxide)
ReLU	Rectified linear unit
RSM	Response Surface Methodology
SA	Simulated Annealing
STEP	Spinneret-based Tunable Engineered Parameter
SVM	Support Vector Machine

1. Introduction

This chapter introduces the motivation of our works, aims, contributions and the overall structure of the thesis.

1.1 Motivation

Due to the unparalleled ability to make complicated and customised geometric shapes directly from various materials, the demand for additive manufacturing technology is increasing (Bhushan & Caspers, 2017; Khani, Nadernezhad, Bartolo, & Koc, 2017; Mota, Puppi, Chiellini, & Chiellini, 2015; Nadernezhad et al., 2016; Ning, Cong, Hu, & Wang, 2017; Ning, Cong, Qiu, Wei, & Wang, 2015). Nanofibres, a one-dimensional nanomaterial with versatile properties and complex structures, can be randomly or directionally arranged in continuous fibre mats or bundles that have ordered internal morphology, such as porous, core sheaths or hollow fibres, and multi-channel microtubes (Z. Li & Wang, 2013; Torres‐Giner, Pérez-Masiá, & Lagaron, 2016; J. Zheng, Zhang, Zhao, & Han, 2012). Ultrafine fibres garnered much attention due to their various outstanding characteristics, such as high surface to volume ratio, high porosity, and excellent mechanical properties (Altun et al., 2018; Brako, Luo, Craig, & Edirisinghe, 2018; Hong, Edirisinghe, & Mahalingam, 2016; Parhizkar, Mahalingam, Homer-Vanniasinkam, & Edirisinghe, 2018; Torres‐Giner et al., 2016; J. Zheng et al., 2012). Despite their versatility, the use of nanofibres is still limited by the lack of proper mass production methods (Hong, Mahalingam, & Edirisinghe, 2017). One of the determinants of successfully applying produced fibres into applications is their diameter have to span in a range from sub-microns to

nanometres (i.e. below 500 nm). However, the rapid and large scale manufacturing of polymer fibres within this range is still challenging.

Prior art techniques for making fine fibres includes template synthesis phase separation and electrospinning, the latter being most promising and versatile during the past few decades. However, the utilisation of electrospinning is limited by its many shortcomings: (1) the process is sensitive to the jet stability and solution conductivity; (2) it is challenging to build products with three-dimensional structures; (3) the uses of high voltage (at kV level) lead to low safety and high cost; (4) the fundamental apparatus of electrospinning produce fibres with low production rate. Although the sister-processes of electrospinning, e.g. multiple needles (Lin, Wang, Wang, & Niu, 2010) or self-organised needle-free (tube electrospinning) (Niu & Lin, 2012) can increase its productivity, the side effects are also introduced, e.g. increase the cost by demanding a bigger size of equipment and the capillary effect between multiple needles.

Many techniques that are primarily derived from the industrial jet spinning have been emerged to overcome the major limitations of electrospinning. These methods use economical centrifugal rotations to consistently yield uniaxially aligned three-dimensional fibre bundles from solution or melt economically and efficiently, and the produced fibres with diameters that span in a range from micron to nanometre. The typical examples of these techniques include centrifugal spinning (X. Zhang & Lu, 2014), force spinning (Hammami, Krifa, & Harzallah, 2014), pressurised gyration (Mahalingam & Edirisinghe, 2013), infusion gyration (Siqi Zhang et al., 2015) and pressure coupled infusion gyration (PCIG) (Hong et al., 2017). Several previous studies have shown that these methods are effective in producing various products

that are not dependent on material properties. Experimental studies on PCIG have shown that it can overcome the discontinuous production of rotary jet spinning and pressurised gyration, and also can produce fibres that are finer than centrifugal spinning and infusion gyration, which can only produce fibres at submicron to micron levels.

Pressure coupled infusion gyration is capable of bringing materials to the nanometre scale and produce uniaxially aligned 3D fibrillary bundles. Hence, the properties of materials are improved, and new advanced features beyond bulk materials are provided. The superior properties of well-arranged fibre structure make it a desirable candidate for many applications compared to nonwoven (randomly aligned) fibres. For example, in tissue engineering, constructing a microenvironment by synthesising scaffolds is important for coaxing cells to work collectively as functional structured tissues. The key measures of these scaffolds include the spatial arrangement of hierarchical fibrous structure, mechanical properties, and biomimetic surface properties. A uniaxial anisotropy has been proved that can equip scaffold with a better tensile limit than random fibrillary structure (Deravi et al., 2017) as well as a good performance when used as a basis for differentiation of peripheral nerves and tendon cells (C. Huang et al., 2015; W. Liu, Thomopoulos, & Xia, 2012).

Determination of optimum levels of operational variables in experiments by conventional methods is often carried out by a one-variable-at-a-time technique. It only monitors the influence of one variable on the experimental responses, fixing others at a constant level. To meet particular requirement of some applications that are sensitive to the surface area, for instance, cellular scaffolds, the fibre preparation should be confined by a given diameter. PCIG is simultaneously affected by different

parameters as well as their interactions, so designing a suitable experimental level is complicated to achieve the desired diameter, and it can be expensive to use a large number of trials to produce fibres with a desirable diameter. The main drawback of the one-variable-at-a-time method is the neglect of the interaction effects between different variables (Baş & Boyacı, 2007; Hong et al., 2017; Montgomery, 2017), as the interaction effect sometimes could be more critical in the process, such as, synergism, antagonist, hybrid welding. Hence, the full impacts of variables on the response cannot be studied (Cho & Zoh, 2007; Ragavendran et al., 2017). Additionally, this method is highly time and cost-consuming, yet does not guarantee the determination of optimal conditions among the variable sets. In order to overcome these disadvantages of the traditional optimisation method, multivariate statistical techniques can be applied to optimise the experimental process and to achieve the description of the (individual or combinational) impact of the parameter in the process. Researchers are trying to find predictive and scientific tools in a variety of manners. Today, many techniques and algorithms in the field of data mining and machine learning that can capably and reliably optimise the experimental process using effective techniques to predict the relationships between data, for instance, response surface methodology (RSM) (Carley, Kamneva, & Reminga, 2004), and artificial neural networks (ANN) (Bishop, 2006).

In this work, a complementary spinning process was invented and studied that is called the pressure coupled infusion gyration (PCIG). It was investigated that PCIG was capable of making nanofibres with diameters that span in a range between 60 and 850 nm in high yield. Poly (ethylene oxide) (PEO) is a well-known basic polymer with good biocompatibility and mechanical properties. PEO was used as the model polymer to demonstrate the characterisation of this new system. Therefore, the

feasibility of producing PEO nanofibres using the lately developed facile process was investigated. In PCIG, the rheological properties of a polymer solution control the size and the homogeneity of the produced nanofibres, especially the chain entanglement has a significant effect on its spinnability. Furthermore, the spinning conditions govern the morphology, dimension and distribution of nanofibres. Hence, infusion flow rate, working gas pressure, rotational speed and orifice-to-collector distance were varied during the experiments and their influences were evaluated along with the polymer concentration. The field emission scanning electron microscopy (FE-SEM) was used to examine the resultant nanofibre morphology and a quantitative measurement of anisotropy of the resulting fibre alignment was achieved by two-dimensional fast Fourier transform analysis as a function of experimental parameters. Different concentrations of spinning dopes were processed on the basis of 144 combinations of key processing parameters in the implementation of the spinning process to study their influences on fibre morphology.

For achieving an insight of the (individual and combinational) effect of the processing parameters and a quantitative basis of the relationships between obtained fibre diameter and experimental parameters, the empirical modelling and optimising of PEO fibres produced by the PCIG process were investigated. In the fitting procedure, a physical frame of rotary jet spinning was considered to have a better understanding of the physical meaning in the spinning process. Using mathematical models to depict the parameters effects allows us to show the influencing factors in a simple and systematic manner and predict the experimental response with different combinations of parameters. Optimisation of the PCIG spinning process was performed to attain combinations of experimental variables that were able to achieve a targeted average fibre diameter with a narrow standard deviation of diameter. The

experimental variables studied in the present work are polymer concentration of solution, applied gas pressure, rotational speed and infusion flow rate. The adequacy of the models was verified by a set of validation experiments.

1.2 Aims and Contributions

The objective of this work is to develop a combined gyration process that takes the advantage of gas blowing to continuously prepare fibres spanned in sub-micron to nanometres level, with the ultimate aim of complementing traditional approaches. And also, assessing the spinning process with the help of mathematics and statistics to analyse the various conditions required for optimal production of desirable fibrous structures. For meeting these objectives, the following procedures were implemented:

1. Designed a prototype of pressure-infusion-gyration spinning system and selected Poly (ethylene oxide) as test polymer.
2. Designed and decided the range of experimental parameters based on our group's results in pressurised gyration and infusion gyration for the comparison reason.
3. Conducted rheological analyses, i.e. measurement of viscosities and surface properties of polymer solutions.
4. Tested the new system under different combinations of concentration of Poly (ethylene oxide) solution system, infusion (flow) rate, applied pressure and rotational speed.

5. The fibre diameters as the response of the system, which were examined using scanning electron microscopy (SEM), and their distributions (in size and orientation) were computed using image analysing software (e.g. image J).
6. Described and investigated the process of this method using Mathematica, and the fibre measurement results were used as input data.
7. Both linear and non-linear approaches were applied and each investigated model was evaluated using consistent fitting/predictive quality metrics (incl. Akaike Information Criterion (AIC) and Adjusted R^2 etc.).
8. Conducted a systematic study to compare and contrast the predictive capabilities of various modelling techniques, and improved the fitted model with rheological/physical studies.
9. Identified the effect and correlation of experimental parameters with fibre produced, and the most significant factor that affects produced fibre diameter was found. And also, verified the predicted combinations of experimental parameters in experiments.

1.3 Thesis Outline

This dissertation focuses on developing a novel fibre generation system, which can achieve mass production of polymeric fibres at sub-microns and nanometres level (~50 – 850 nm) consistently and cost-effectively. It mainly involves introduction and background, literature review, three consecutive works (experiment, process

modelling, optimisation and validation), conclusion and future works. The below chart describes the overall work flow of this thesis:

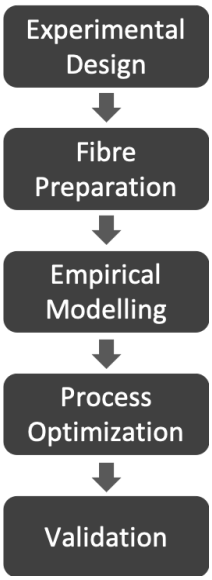

In Chapter 1, the advantages of polymeric nanofibres and its utilisations in a wide range of applications are introduced. The state-of-the-art techniques for producing nanofibres and their challenges for mass production are briefly listed and described. An overview, aims, contributions and objectives of this thesis are also detailed.

In Chapter 2, a literature review of recent studies in the field of fibre generation and various types of fibre production processes are presented. The description of the properties of polymer solutions that used in this thesis is included. The influences of the experimental parameters on the process of pressure coupled infusion gyration are described. The machine learning and statistical techniques for modelling and optimisation of our experimental process are reviewed, categorised and compared. A detailed introduction of the methods applied in our work is given, as well as their applications in the biomaterial processing and modelling field. This part also provides a background to assess the results of this work, some of the challenges that this

work will address and the future applications that may find results from this work are useful.

In Chapter 3, the details of the experimental protocols and procedures of fibre production are introduced. The principles of the characterisation techniques for fibre's morphology analysis used throughout the study are also described. The details of the performance measures, process modelling and optimisation procedures are also introduced.

In Chapter 4, the performance of PCIG for preparing PEO nanofibres are explored. The obtained diameters of produced nanofibres are listed. The anisotropy and diameter distribution of the nanofibres are studied. The influences of processing parameters on the fibre size and morphology that observed in the experiment are explicitly explained and discussed as well.

In Chapter 5, a thorough exploratory analysis of the modelling of the PCIG spinning process is performed based on the experimental results obtained from the previous chapter. This chapter aims to provide a systematic description of the experimental process and the mechanism of the fibre formation process, to identify the parameters that have the most significant impact on the produced fibre size and morphology, as well as to obtain a descriptive model for the further parameter optimisation in the next stage. Different fitting methods and existing physical studies are explored and involved to improve the goodness of the fits empirically and statistically.

In Chapter 6, the theoretical model derived from the previous chapter is extended to conduct optimisation of experimental parameters for achieving desirable nanofibres. An objective function for the optimisation is designed based on the trends and data

features identified in Chapter 5. A systematic study of the optimisation performance of several algorithms is performed and the results of the one with the best result are listed. The prediction performance with a pre-set diameter goal is investigated and the parameters recommended by model are validated using a set of experiments.

In Chapter 7, the entire work is concluded and the primary outcomes are highlighted. The directions for future work are also discussed, including the improvement in the experiments as well as in the theoretical studies.

2. Literature Review

2.1 Introduction

Polymeric nanofibre is a fascinating class of material that has been widely used in a myriad of applications. It had been extensively studied in many biological applications over the past few decades. The literature review aims to highlight and explore the relevant theories and concepts, especially used in nanofibre generation. This review broadly relates to the types and current applications of nanofibres and the various techniques for fibre production. Then, the unique properties of nanofibres and how to define the optimal experimental conditions to obtain desirable fibre morphology are discussed. Applying high pressure and high-speed rotation to generate controllable fibrous structure is a key strategy guiding the course of this work. Therefore, the theories and principles underlying the fibre forming process and the effect of different experimental conditions have been discussed. This study is also seeking to describe the fibre spinning process and define the optimal experimental conditions for preparing fibres with targeted diameter, specifically for

the PCIG process. Hence, the mathematical and statistical methods that are available for assisting this objective have also been deliberated. The review can be organised under three topics. The first topic gave a broad introduction about what is nanofibre and fibrous structure, and what applications do it can be applied to. The second topic reviewed the manufacturing methods of fibre production, and the current limitations are briefly discussed. The last topic deliberated the process modelling for fibre manufacturing, where various methods and algorithms are discussed.

2.2 Introduction to Nanotechnology and Nanofibre

Nano-engineering and Nanoscience can be included in physical, biological, material, environmental and chemical sciences, and nanotechnology is the combined technology of nano-engineering and nanoscience at the nanoscale (Barhoum, Rasouli, Yousefzadeh, Rahier, & Bechelany, 2018; Roco, 2003). It is one of the most important elements of the technological industry revolution in the 21st century. Nanotechnology is likely to profoundly affect human lifestyles and equipment in the foreseeable future and may have a significant impact on the global economy (Bhushan, 2017; Brown & Stevens, 2007; Falkner & Jaspers, 2012; Fang, Niu, Lin, & Wang, 2008; Roco, Mirkin, & Hersam, 2011). The nanomaterials studies incorporate materials science into nanotechnology, using advances in the development of material metrology and synthesis to support micromachining research. The prefix "nano" comes from the Greek word, meaning "dwarf" and was officially recognised as the standard in 1960 (Rosoff, 2001). According to American Society for Testing

and Materials 2012, nanotechnology refers to a variety of techniques for measuring, manipulating or combining materials and/or features, wherein one or more dimension is in the range around 1-100 nm (Barhoum et al., 2018). Nanomaterial can be roughly categorised into natural and artificial synthetic materials. Artificial synthetic materials are materials with specific physicochemical structures and compositions designed or manufactured by humans on a nanometre scale to take advantage of the functions and properties associated with their dimensions. The risk or nature of the nanomaterial is not identified by the manufacturer's intent. The source of materials and processes of manufacturing may not alter their final properties. The properties of manufactured nanofibres can be similar to those naturally existed. The underlying problems of nanomaterials, such as nanofibres and nanoparticles are as listed in the following: (1) the ability to control morphology of the production such as surface and volume; (2) the ability to bring down the scale of materials to nanometres; (3) the development of synthesis and manufacturing process for materials; (4) the ability to control the crystal structure and chemical composition of materials; (5) a deep understanding of the impact of the fibre morphology, dimension and influence of interface that can help achieve the desired physical, chemical and mechanical properties of materials; (6) the human health (toxicological) and environmental risk of using materials (Barhoum et al., 2018; Borm et al., 2006; Colvin, 2003; Farré, Gajda-Schrantz, Kantiani, & Barceló, 2009).

With the development of nanoscience and nanotechnology, a wide variety of component materials, for example, nanofibres, nanorods, nanoparticles, and nanosheets have been created and studied for different applications in a variety of applications during the past two decades. Gleiter raised the first idea of nanomaterials' classifications in 1995, he classified the nanomaterials based on the

chemical compositions and the crystalline forms of nanomaterials (Gleiter, 2000; Tiwari, Tiwari, & Kim, 2012). But, the Gleiter's solution was not complete, as he did not consider the dimensions of the nanomaterials. The nanostructures themselves and the dimensions of their components are used to determine and classify various nanostructured materials. A new classification scheme for nanomaterials was reported by Pokropivny and Skorokhod (Pokropivny & Skorokhod, 2007). In their studies, the nanomaterials were generally classified into 0- to 3-dimensional materials. The 0-dimensional nanomaterial is referred to as particles and clusters, 1-dimensional nanofibres and nanotubes, 2-dimensional nanoplate and nanolayers, and the 3-dimensional matrix. The more detailed classifications of the nanostructure can be seen in Figure 2.1. Thus far, many types of nanofibre materials have been reported, and various other nanofibre and nanofibre materials are expected to emerge in the future.

Nanofibre and nanofibre materials are typically classified based on their morphology (such as core-shell, hollow, non-porous, biological components, multi-component), dimension (diameter and length) and composition (such as polymer, carbon, metal, metal oxide, ceramic and mixture) (Barhoum et al., 2018; Buzea, Pacheco, & Robbie, 2007). According to the above scheme and applications of fibrous structure, nanofibre and nanofibrous structure can be roughly classified into four types: polymer nanofibres, carbon-based nanofibres, inorganic nanofibres and composite nanofibres.

2.2.1 Polymer Nanofibres

Polymer fibres are ubiquitous and extensively used in many areas of human life, including clothing, filters (such as for air conditioning and cigarettes), surgical

materials (like vascular valves and grafts) and so on. These applications use nano- to micro-sized fibres from various polymers. Up-to-date, about over 50 different kinds of polymers have been successfully manufactured into ultrafine fibres with diameters that spanned in a range from <3 nm to over 1 μm (Barhoum et al., 2018) by using various methods. For the polymer fibre manufacturing, spinning-based method and electro-hydrodynamic based techniques are relatively more popular recently. For meeting certain specific characteristics of different polymers and their applications, a number of derived/modified processes have been developed. For instance, Koombhongse et al. reported the preparation of polymer fibres with various morphologies (flat, ribbon, split and branched) using electrospinning technique (Koombhongse, Liu, & Reneker, 2001). Most polymers are needed to be dissolved in some solvents (either inorganic or organic solvent) for fibre preparation, and some of them are melted in high temperature (Haggenmueller, Gommans, Rinzler, Fischer, & Winey, 2000; Larrondo & St. John Manley, 1981; Xu et al., 2016).

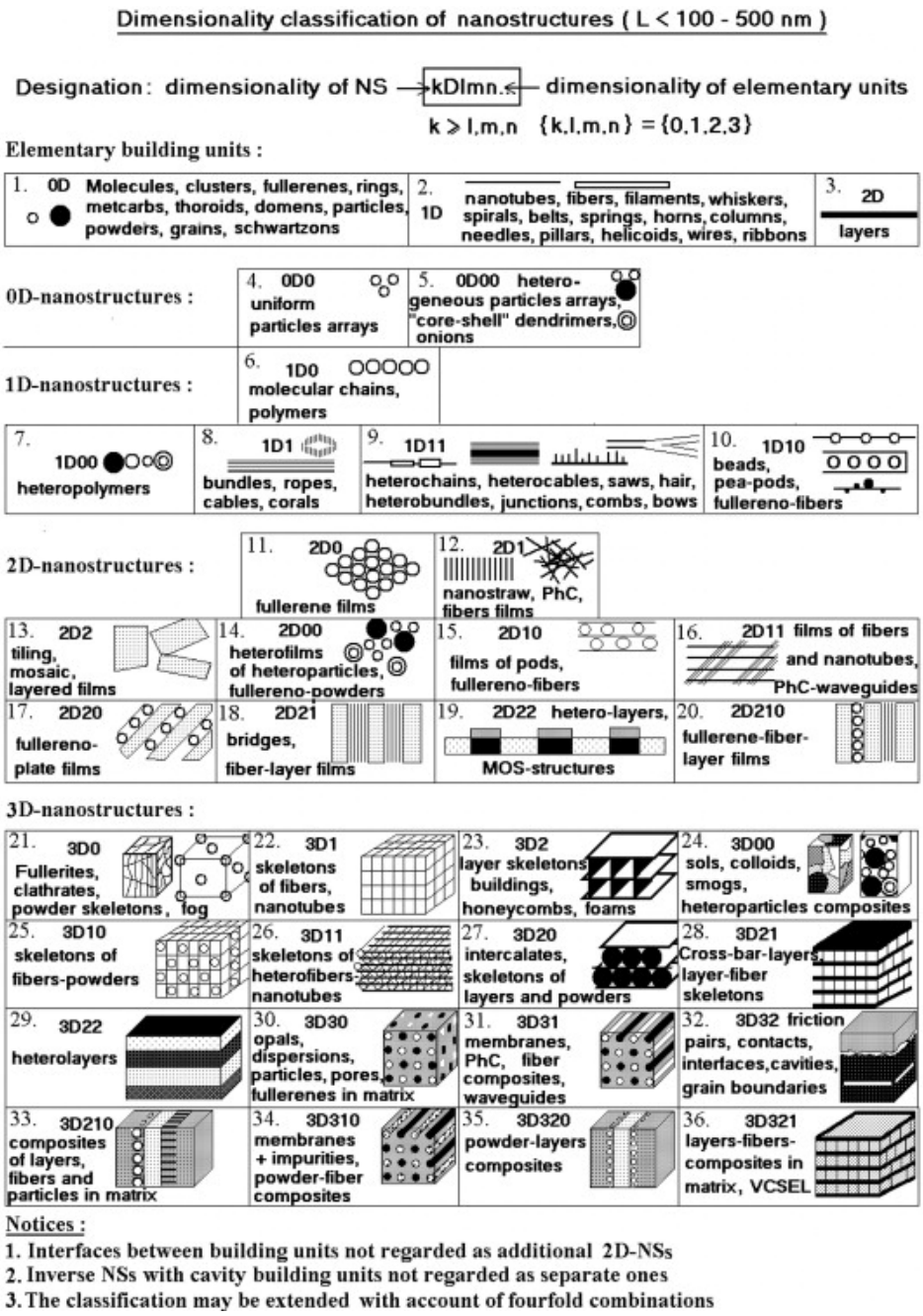

Figure 2.1 Dimensionality classification of nanostructures (Pokropivny & Skorokhod, 2007).

2.2.2 Carbon Nanofibres

Carbon is considered an extraordinary chemical element. The carbon's unique electron structure enable it can form covalent bonds with other elements in different structures such as long chain or ring. Carbon-based nanofibre is regarded as 1-dimensional nanomaterials that are primarily consisting of carbon. Due to its outstanding mechanical and physicochemical properties, carbon nanofibre has recently attracted interests and been innovated in many applications, such as electrochemical catalysis (Hsin, Hwang, & Yeh, 2007; W. Li et al., 2003), reinforcement material (Coleman, Khan, & Gun'ko, 2006; Gojny, Wichmann, Köpke, Fiedler, & Schulte, 2004; Hammel et al., 2004), selective adsorption(Kabiri, Tran, Altalhi, & Losic, 2014) and hydrogen storage (Darkrim, Malbrunot, & Tartaglia, 2002; C. Liu et al., 1999). The arrangement of carbon layer in nanofibres can influence the overall mechanical properties. Recent studies disclose that the graphite planar layers of the majority of carbon nanofibres are usually not in line with the fibre axis. According to the angle of the graphene layers that make up the filament, carbon nanofibres can be categorised into three different types: (a) platelet or stacked: the graphene layer is stacked perpendicular to the fibre growth axis, (b) tubular or ribbon: the graphene layer is parallel to the fibre growth axis, (c) fishbone or herringbone: the graphene layers are accumulated at an angle between vertical and fibre growth axis. The different arrangements of graphene layer rely on the catalyst geometry (e.g. for metal nanoparticles) and the gaseous carbon feedstock (hydrocarbon or CO gas) introduced during the synthesis processing. It has been reported that different arrangements of graphene layer play different roles in the physicochemical behaviour of carbon nanofibres. For example, it was suggested that the type of basal plane of carbon nanofibre has the ability to enhance the adsorption

of ethylbenzene, and the edge plane modified with the oxygen-containing fragment is the active site of the oxidative dehydrogenation reaction (Barhoum et al., 2018).

The carbon nanotubes are the graphene layers of carbon nanofibres wrapped in a perfect cylinder shape. One of the earliest records of technology contributing to synthetic nanofibres was the Hughes and Chambers' patent in 1889 (Hughes & Chambers, 1889). The mechanism of forming carbon nanofibre and nanotube mainly involves atoms mass diffusion through the catalyst and carbon formation from hydrocarbons on mono- or bi-metallic catalysts such as Fe, Co, Ni, and some other transition-metal are active. Nevertheless, the differences between carbon nanofibres and nanotubes in growth mechanism are that the nanofibres refers to the formation of graphene structures, which are apparently arranged as stacked cones, and the nanotubes growth refers to the formation of perfectly cylindrical structure with one or more graphene walls (Lobo, 2017). Alternatively, carbon nanofibres can be prepared by the combination of spinning fibres from precursor polymers and carbonisation of the obtained nanofibres that are carried out in an inert atmosphere (Weihan Li, Li, Adair, Sun, & Yu, 2017; X. Wu et al., 2016). Carbon nanofibre does not only inherit the fascinating properties of conventional carbon fibres including inherently inert and hydrophobic. It also has the characteristics such as large surface area effect, small size effect and quantum size effect.

For the purpose of achieving multifunctional carbon nanofibres, it is necessary to change their surface properties before use. For adjusting the specific surface area and surface porosity, the most active carbon atoms should be removed from the surface of fibre. The formation of porous structure of activated carbon is highly dependent on the nature of the precursor and the reaction conditions of synthesis

process. There are typically three techniques commonly used for carbon nanostructures and change their dimensions: chemical vapour deposition, laser ablation, and arc discharge (Lai, Guo, Wu, Reneker, & Hou, 2008). High surface area is one of the most critical factors for realising better thermal, electrical and sensing performance. Therefore, nanopores are introduced on the surface for controlling the fibre's surface area. The template strategies are often used with many kinds of inorganic materials, for instance, metals oxides or metal to produce porous carbon nanofibres having a high-volume percentage of mesopores and large surface area. High thermal conductivity is a priority feature of carbon nanofibres. It can be used to improve contact thermal conductivity in electronic packaging applications (Pop, Mann, Wang, Goodson, & Dai, 2006). Another important feature of carbon nanofibre is electrical conductivity. Carbon nanofibres are often used in the manufacture for sensors, batteries or supercapacitors electrodes, and electronic devices (Lichao Feng, Xie, & Zhong, 2014; G. Zheng, Yang, Cha, Hong, & Cui, 2011).

2.2.3 Inorganic Nanofibres

Many kinds of inorganic nanofibres can be prepared by spinning their precursor and following by the calcination step. Typical inorganic nanofibres include compound nanofibres (such as Ag/ZnO nanofibres and LiCl/TiO_2 nanofibres), metal nanofibres (e.g. Ag nanofibres and Cu nanofibres) and oxides and sulphide nanofibres (such as ZnO nanofibres, CuO nanofibres and ZnS nanofibres). Inorganic nanofibres are extensively used in a variety of forms in our lives. The products made from metal oxide, ceramic and metal nanofibres provide better performance than the traditional bulk materials (Nakane & Ogata, 2010). Also, inorganic nanofibres can grant the

production with fascinating electronic and optical properties, and have various applications, including nanocomposite filters with high electric, magnetic, photocatalystic and mechanical properties, and electrodes for sensors and batteries (Moon, Park, Lee, Zyung, & Kim, 2010; H. Shi et al., 2018; Song, Kim, Ihn, Jo, & Kim, 2004; Yamamoto, Otsuka, Takahara, & Wada, 2002). In cosmetic applications, the unique properties of nanofibres eliminate the possible negative effects on consumer health and retain the whitening effect of nanoparticles. TiO_2 nanofibres have the same whitening properties as the previously used nanoparticles. While the risk of toxicity of nanoparticles that may infiltrate into body cells, nanofibres remain on the surface (Barhoum et al., 2018; Zanin, Cerize, & de Oliveira, 2011). In contrast to polymeric nanofibres, the inorganic nanofibres have better performance in separation, as they are endowed with relative higher heat resistance, solvent stability and mechanical properties(H. Y. Zhu, Riches, & Barry, 2002). The inorganic nanofibres typically can be first spinning from their precursor solutions using many approaches such as electrospinning and gyration-based methods (H.-Y. Liu et al., 2013; Mondal & Sharma, 2016; X. Shi et al., 2015), and then following by the thermal treatments e.g. sintering to obtain the resultant nanofibres. The parameters of thermal treatment including heating rate and temperature also have a significant effect on the produced fibre morphology. The transient fibres usually undergo two stages during the thermal treatment. In the first stage, the residual solvents and the water vapour in the fibres are removed. The second stage is where actual fibre shrinkage occurs during the removal of organic materials, polymerisation, condensation and structural relaxation (Shendokar, Kelkar, Mohan, Bolick, & Chandekar, 2008). Depending on material property and temperature, another stage is the glass transition of material, and most of the thermal treatment ends in the

second stage, in order to obtain nanofibres. In addition, the precursor solution may also interact with the ambient environment in the spinning and the subsequent calcination, and finally changes the physical properties of produced fibres.

Ceramic nanocrystalline nanofibre has recently been recognised as ideal candidates for building three-dimensional elastic component block. The gyration-based spinning and solution blowing methods have the natural advantage of assembling nanofibres into large-scale 3D networks easily and effectively than the electrospinning. Wang et al. used an efficient solution blowing technique to prepare large-scale 3D sponges from various ceramic nanofibres (L. Wang et al., 2011). The produced ceramic sponge exhibited several desirable properties, for example, effective energy absorption during cyclic loading, ultra-low density, photocatalytic activity and elastic-dependent electrical resistance (H. Wang et al., 2017).

2.2.4 Composite Nanofibres

Composite nanofibres typically comprise at least two phases of different chemical constituents or structures, and at a minimum one of which is of nanometre dimensions (Sahay et al., 2012). Due to the improved physico-chemical properties, the composite nanofibres have a wide range of applications, such as photocatalysis (Guo et al., 2013), batteries (Goyal, Reddy, & Ajayan, 2011; Jeong et al., 2014), fuel cells (C. Lee et al., 2013), light weight sensors (Y. Li, Gong, He, & Deng, 2011; Mohamad et al., 2017), tissue scaffold (Rijal et al., 2018) and drug delivery(Cui et al., 2018). Many spinning techniques can be used to fabricate composite nanofibres, for instance, self-assembly, electrospinning, pressurised gyration and polymer template methods. Composite nanofibres can be prepared by any of the following procedures: (1) no less than two precursors are used in the spinning process and obtaining the

multicomponent fibres at one step; (2) posttreatment of precursor fibres such as carbon composite fibres; (3) dispersing other insoluble components in the spinning dope to achieve loaded fibres, for example, silver nanoparticle loaded nanofibre.

2.3 Application of Nanofibres

Researchers are increasingly interested in the unique properties of nanomaterials. Notable applications of nanofibres and mats includes drug delivery, tissue engineering, healthcare, enzyme immobilisation, biosensors, filtration, energy storage, small diameter vascular graft implants and so forth (Ramakrishna et al., 2006; Reneker, Yarin, Fong, & Koombhongse, 2000; Smith & Ma, 2004). The nano- to submicron range of fibres have the advantages of large specific surface area, adjustable nanofibre composition and the ability of tuning structure porosity to achieve desired performance and function. In recent years, many fabrication methods have been investigated, and more than 200 polymers have been spun for a variety of utilisations, and the number is still increasing. With these perspectives, our goal is to present an overview of potential applications of nanofibres in this part.

2.3.1 Drug Carrier

Controlling drug release rate and clear delivery time is possible to be achieved with polymers biodegradable and biocompatible polymer matrices. Hence, they are mainly applied as the systems for therapeutic agent delivery, due to these polymers can be easily performed as the carrier and designed for use in a controlled manner programmed transmission (Kenawy et al., 2002; Kost & Langer, 2012). The delivery system is highly dependent on the principle that the granule drug's dissolution rate,

which increases with the surface area of the drug and the corresponding carrier. The nanofibre mats with high functional characteristics have been used as drug carrier in the delivery system. The large surface area associated with nanofabric allows for rapid and efficient solvent evaporation, which provides limited time for recrystallisation of the combined drug, facilitating the formation of amorphous dispersions or solid solutions. Depending on the polymer properties, the dose release can be designed to be immediate, rapid, delayed or modified dissolution (Verreck, Chun, Peeters, Rosenblatt, & Brewster, 2003). There are many research works that have successfully encapsulated drugs in spin fibres by mixing the drug in a solution using various fabrication techniques (Brako, Thorogate, et al., 2018; Kenawy et al., 2002; Luu, Kim, Hsiao, Chu, & Hadjiargyrou, 2003; Jing Zeng et al., 2003)

Various solutions loaded with low molecular weight drugs that have been prepared, including lipophilic therapeutics such as progesterone (Brako, Thorogate, et al., 2018), paclitaxel (Jing Zeng et al., 2003), cefazolin (Katti, Robinson, Ko, & Laurencin, 2004) and ibuprofen (H. Jiang, D. Fang, B. Hsiao, B. Chu, & W. Chen, 2004a), as well as hydrophilic drugs like mefoxin (K. Kim et al., 2004; Zong et al., 2002) and so on. Proteins also can be encapsulated in the polymer fibres. Siqi Zhang et al. demonstrated the integration of engineered protein, gold-binding peptide tag genetically conjugated to red fluorescence protein, to tack the successful loading of gold nanoparticles along the polyethylene oxide fibres using an infusion gyration method (Siqi Zhang et al., 2015). Y. Zhang et al. studied the encapsulation of engineered proteins, bovine serum albumin conjugated with fluorescein isothiocyanate, and polyethylene glycol in polycaprolactone fibres using a coaxial configuration. They found a relatively stable drug release from electrospun nanofibre

mats for a period of five days (Y. Zhang, Venugopal, Huang, Lim, & Ramakrishna, 2006).

2.3.2 Filter Systems

Filtration is another very typical application of nanofibres, especially using (composite) polymeric nanofibres for the air filtration applications, in which the structural elements and channels must match with the dimension of the particles or droplets to be captured. It has been recognised that the filters consist of very-small-diameter fibres are easy to catch the small particles with the order of less than 0.5mm due to their high surface area to volume ratio and high surface adhesion, thus improving the filtration efficiency. Electrospun nonwoven fabric has been successfully developed into high performance air filters. Nanofibre membranes demonstrate a very efficient removal i.e. reject almost 100% of airborne particles that have the diameters in a range from 1 to 5 μm through electrokinetic capture and physical entrapment mechanisms of air filters (Ramakrishna et al., 2006). Polymer nanofibres can also be charged by static electricity, improving the electrostatic attraction of the particles without increasing the pressure drop, further enhancing the filtration efficiency by combining nanofibres charging and spinning in one step (Tsai, Schreuder-Gibson, & Gibson, 2002). The fineness of produced fibres is closely related to the efficiency of filtration, and it is a critical factor affecting filtration performance. Usually, the filtration efficiency has an inversed-linear correlation with the applied pressure and the thickness of the membrane. The filtration efficiency was observed that enhanced at the same pressure drop, which is may be related to the fibres with diameters less than 500 nm (Subbiah, Bhat, Tock, Parameswaran, & Ramkumar, 2005). Ahn et al. evaluated the filtration efficiency of nylon 6 membrane

that constituted by nanofibres of 80 – 200 nm in diameter and pressure drop across the membrane and found that 99.993% high-quality nylon 6 filters were more efficient than the commercial high-efficiency particulate air filters (HEPA) that uses 300 nm test particles at a speed of 5 cm/sec (Ahn et al., 2006). Other studies such as antibacterial applications (against Staphylococcus aureus and E. coli) (Burger, Hsiao, & Chu, 2006; Son, Youk, & Park, 2006) and adsorption membrane for purification of large biomolecules were also widely studied in the past decades (L. Zhang, Menkhaus, & Fong, 2008).

2.3.3 Tissue Engineering

Using biomaterials, cells and/or growth factors to repair and regenerate human tissues and organs is a huge challenge for tissue engineers and surgeons. Tissue engineering is a multidisciplinary field that involves life science and engineering principles for the development of biological alternatives and the restoration, maintenance or improvement of organisational functions. Biomaterial is an emerging domain that is increasingly important in tissue engineering through its role as a substrate for cell growth, proliferation, and three-dimensional tissue formation (Mikos et al., 1993; Bhardwaj & Kundu, 2010)

Since the early 1980s, polymer nanofibres were spun to form scaffold using various techniques and have already been frequently explored and proposed for engineering living tissues, for example, vascular and breast prostheses applications. The orientation and fineness of nanofibres play a crucial role in the micro- and macroscopic properties of scaffolds. Biodegradable scaffolds are often considered essential elements for the engineering living tissues because they are used as temporary templates for cell seeding, invasion, proliferation, and differentiation

before the natural extracellular matrix (ECM) regeneration. These scaffolds are reported to actively promote inter-cell and cell matrix interactions with normal phenotypic shapes and gene expression (Shuguang Zhang, 2003). The diameter of the spun nanofibre is similar to that of the fibril in the extracellular matrix that mimics the natural tissue environment and has been shown to be effective as a substrate for cell growth (Friess, 1998; Shuguang Zhang, 2003), e.g. Figure 2.2. Natural polymers are commonly used to prepare nanofibre scaffolds because of their biofunctional motifs and enhanced biocompatibility, for instance, collagen, starch, chitosan, alginate etc. Also, because the mixture of natural and synthetic polymers can improve overall cellular compatibility (Almany & Seliktar, 2005; Cunha, Panseri, & Antonini, 2011; Geng, Kwon, & Jang, 2005; C. Zhang, Yuan, Wu, Han, & Sheng, 2005). C. Li et al. studied the use of silk fibroin scaffolds containing bone morphogenetic factor 2 and/or hydroxyapatite nanoparticles for in vitro bone formation of human bone marrow mesenchymal stem cells. Their study suggested that the fibroin scaffold as an ideal candidate for bone tissue engineering (C. Li, Vepari, Jin, Kim, & Kaplan, 2006). Electrospun PLGA fibre mat is considered an ideal choice for tissue-engineered scaffolds as they have a porosity greater than 90%, the high surface area allows higher cell adhesion, and multiple adhesion points on individual fibres with nanoscale diameters. The spun mat assists the cell growth and proliferation, for instance, mouse fibroblasts adhere to the fibre orientation and spread well on PLGA nanofibres (W. J. Li, Laurencin, Caterson, Tuan, & Ko, 2002).

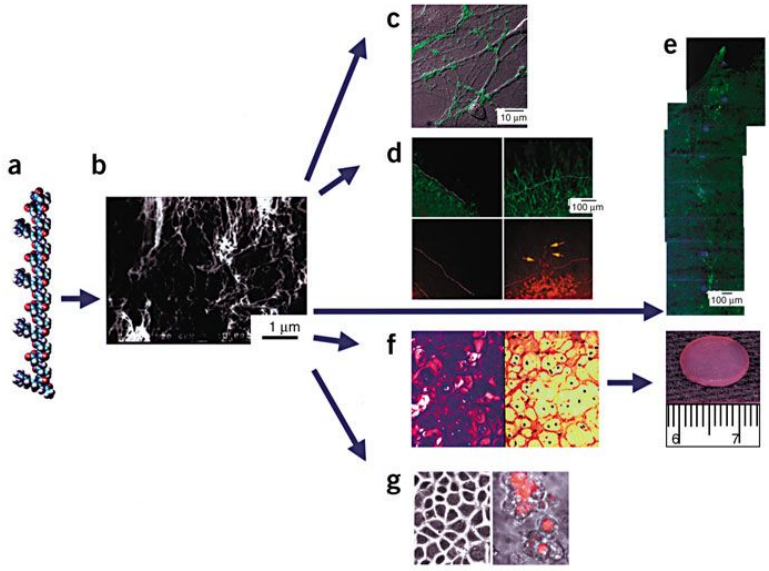

Figure 2.2 Self-assembling peptides form a three-dimensional scaffold woven from nanofibres ~10 nm in diameter (Shuguang Zhang, 2003).

2.4 Fibre Generation Methods

2.4.1 Template Synthesis

Template synthesis is a straightforward method for preparing heterogeneous nanostructures, for example, generic nanofibres, hollow nanofibres and coaxial nanofibres. It simply uses a porous membrane as a template, and wets its pore walls by the solution indicated for the decomposition of materials, then giving nanofiborous products after removing the template. This process also can synthesise nanostructures chemically and electrochemically with the aids of either a “soft” or “hard” template. Examples of “hard” templates are saline minerals channels (e.g. zeolite channels (C.-G. Wu & Bein, 1994)), processed metallic oxides (like anodised alumina (C. Wang, Wang, Li, & Li, 2001)) and polymer films (such as track-etched

polycarbonate (Martin, 1996)) etc. For the “soft” templates, the examples include micelles (Z. Wei, Zhang, & Wan, 2002), polyacids (J.-M. Liu & Yang, 1991) and surfactants (J.-M. Liu & Yang, 1991).

The main feature of template synthesis method is that widely choices of materials can be spun (deposited), for example, ceramics, polymers, metals, carbon nanotubes and fibrils. The schematic process of template synthesis is shown in Figure 2.3. The synthesis duration of this method is consistently too long, so its production efficiency is low. However, the advantage of this method is the uniformity and morphology e.g. diameter and length of fibre can be well-controlled by the properties of template membrane (such as pore size and depth). Therefore, the morphology distribution of products is pretty uniform (Lin Feng et al., 2002). Feng et al developed and used a novel template synthesis method, which simply uses pressure to extrude the solution of polyacrylonitrile precursor into another solidifying solution to prepare a super hydrophobic surface that constitutes with nanofibres. The obtained aligned fibres were around 104.6 nm, and it was presented that the large air fraction on the surface of nanostructure that consist of these fibres was promoted.

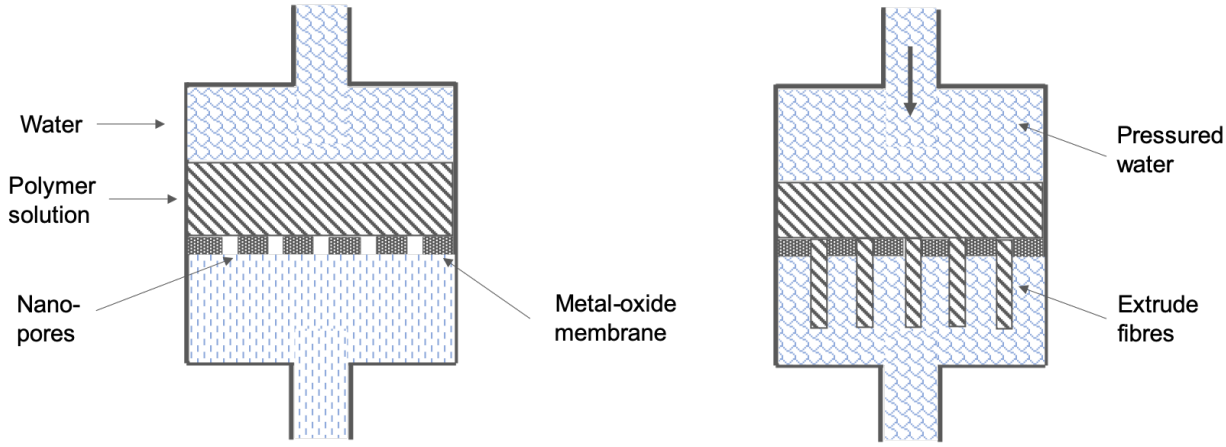

Figure 2.3 Using template synthesis methods to fabricate nanofibres.

2.4.2 Molecular Self-assembly

Molecular self-assembly is spontaneously reorganising the arrangement of molecules through non-covalent interactions under near thermodynamic equilibrium conditions (Shuguang Zhang, 2003). It is a powerful phenomenon that scientists draw from nature and apply it in chemical synthesis of supramolecular structures (Subramani & Ahmed, 2012). Molecular self-assembly is a kind of bottom-up approach by which molecules are placed in a defined arrangement without the direction from outside. Therefore, the pre-defined structure can be well self-guided and programmed in the shape and functional groups of the molecule (Dahman, Y. 2017).

The self-assembly method mainly has two types: dynamic assembly and static assembly. The dynamic assembly is undergoing autonomously without human intervention, the component units, for example, cells, molecules, molecular groups and macroscopic objects aggregate together and spontaneously build well-ordered assemblies by non-covalent or weak covalent bonds (electrostatic, van der Waals etc.) (Whitesides & Grzybowski, 2002). Despite these forces are individually insignificant and weak, the collective interactions between molecules can produce stable structures chemically and structurally (Shuguang Zhang, 2003). The formation of well-ordered blocks in static assembly usually needs external energies, like stirring and external electromagnetic fields. But generally, the structure built by this approach (static self-assembly) is stable once it is built. Once a self-assembly process begins, an expected end will be reached automatically, and component units will be allocated in a well-ordered pattern spontaneously. This method requires its component units to be mobile and able to adjust their position to one another once in

an aggregation. The advantages of self-assembly method include the less manipulate errors in the process as less human interventions, and the interactions between units can be selected and controlled by proper design of unit functions. Its disadvantage is similar to phase separation i.e. low efficiency because of complex process.

The method of self-assembly has been proved and investigated well to produce stable nanofibre structures (also known as amyloid fibres) from a broad range of peptides and proteins (Fändrich, Fletcher, & Dobson, 2001; Perutz, Finch, Berriman, & Lesk, 2002). These nanofibres are very well-ordered and have a significant regularity and, in some cases, a good helical periodicity (Shuguang Zhang, 2003). Hartgerink et al synthesised a peptide amphiphile based self-assembling system and incorporated phosphoserin residue to enhance hydroxyapatite mineralisation. They observed the obtained nanofibre diameter from 5 to 8 nm, and the length of fibres at sub-micron level. They also observed the hydroxyapatite crystals were formed to the radial orientation that along the nanofibres. It was indicated that this structure are similar as the orientation of collagen fibres of bone and hydroxyapatite crystals in mineralised extracellular matrix of bone tissue (Hartgerink, Beniash, & Stupp, 2001).

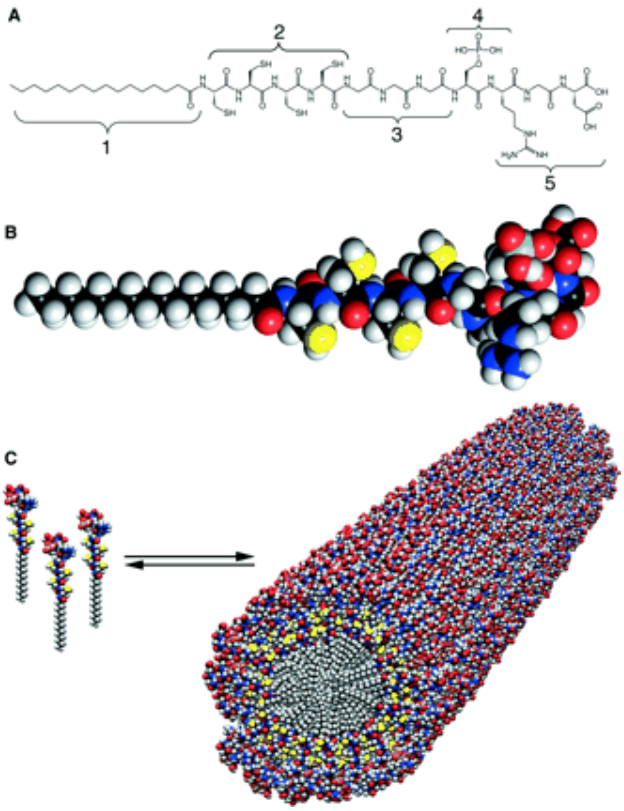

Figure 2.4 Molecular Self-assembly for producing peptide amphiphile nanofibres: (a) Chemical structure of the peptide amphiphile; (b) Molecular model of the peptide amphiphile; (c) Schematic of a cylindrical fibril formed by self-assembly of peptide amphiphile (Hartgerink, Beniash, & Stupp, 2001).

2.4.3 Phase Separation

Phase separation is a method that frequently used in the preparation of 3-D scaffold for tissue engineering. Generally, this method creates a polymer-rich domain and a solvent-rich domain from polymer solution, in which the morphology can be fixed by quenching under low temperature (Z. Ma, Kotaki, Inai, & Ramakrishna, 2005). The phase separation method separate a homogenous solution into muti-phases by chemical-physical changes (e.g. thermodynamics). This method asks the fibre forming solutions to be kept in the environment that's above its phase separation temperature, in order to encourage the macromolecular chains of dissolved polymer

to be fully outspread. Then, through the way of decreasing temperature (thermal induced phase separation) or adding non-solvent in spinning solution (non-solvent induced phase separation), the dissolved polymer initiates to crystallise as the process of phase separation, as a result of forming nanofibres (also known as polymer gelation, which is the most critical step to control the porosity of the product). Finally, a new equilibration of thermodynamics and kinetics will be reached in the system of solution. The salient advantages of this system are: the formation of three-dimensional interconnected fibrous foam can be achieved directly; the porous morphology of foam can be controlled via changing temperatures in gelation step. For example, a high temperature (or low cooling rate) may result in the nucleation and growth of crystals, hence lead to platelet-like formation. A low temperature (or fast cooling rate) will generate fibrous networks at nanometre level. The principle challenges in this method include the restricted selections in materials that are applicable to be used in this system, and the gelation process of dissolved polymer that is time consuming. Ma and Zhang studied a thermal-induced liquid to liquid phase separation system to produce nanofibrous scaffold with 98.5% porosity. They found that polymer concentration had a significant impact on the properties of obtained fibrous foam, for example, the decreases of the porosity and the increases of mechanical properties (tensile strength and modulus) followed with the increase of concentration (P. X. Ma & Zhang, 1999; R. Zhang & Ma, 2000).

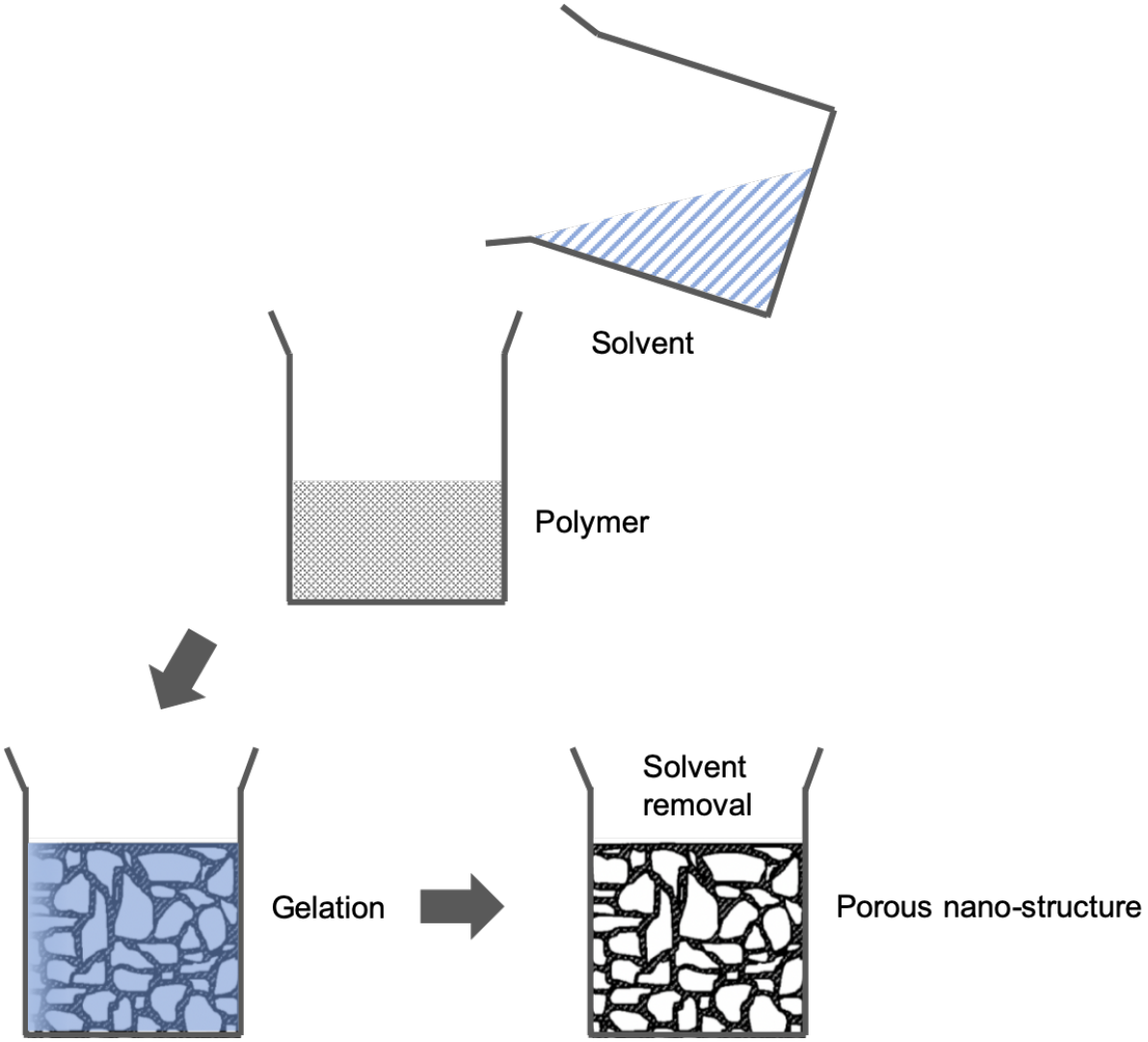

Figure 2.5 Schematic of phase separation for obtaining nanofibrous structure.

2.4.4 Solution Spinning

Solution spinning is the process of extruding a jet of solution to produce fibres. Solvent will be removed during spinning due to evaporation (with the aids of thermodynamics in dry spinning) or simply by solidification (in wet spinning) (V. Gupta & Kothari, 2012). Well-known examples of solution spinning such as wet spinning and dry spinning as display in Figure 2.6 and Figure 2.7.

2.4.4.1 Wet Spinning

Wet spinning is one kind of precipitation based, facile fluid assembly approach to produce fibrous structures. It requires polymers dissolved in a solvent to be spun and filaments directly extrudes into a liquid bath to draw out solvent, leaving only the polymer while stretching. So, one of the crucial parameters of wet spinning is the rolling rate, as there might be some micro-voids that were left during the stretching and forming defective fibres. Wet spinning has been used to produce biopolymer fibres since the middle of 20 centuries. For example, Rupprecht used wet spinning to prepare oriented DNA films that are suitable for polarised infrared studies (Rupprecht, 1966).

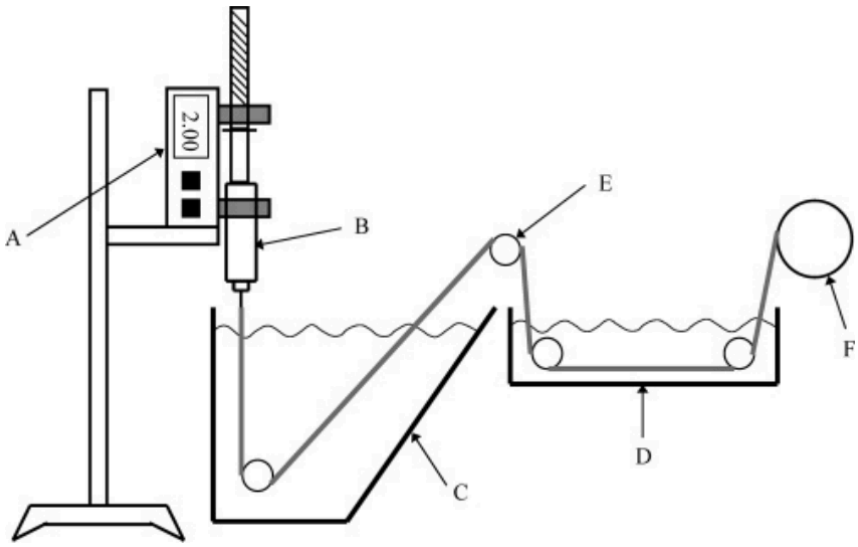

Figure 2.6 Schematic of a benchtop device for wet spinning of fibres A: mechanical pump; B: raw materials (e.g. polymer solutions); C: coagulation bath; D: wash bath; E: transmission rolls; F: rolling collector (Ha, Tonelli, & Hudson, 2005).

2.4.4.2 Dry Spinning

In dry spinning, the fibre-forming polymer used in this method must be dissolved in a volatile solvent, and the polymer solution will be extruded from the spinneret to form a thread under extrusion provided by the introduced pressure. The extruded solution thread will then enter the rotating shaft for heat exchange with the forthcoming hot air stream and the solvent will be removed by the rapidly evaporating hot air stream. At the same time, the liquid thread is solidified as the solvent evaporation and elongation under the thinning effect of the winding layer. There is only heat and mass transfer that exists between the polymer solution (spinning dope) and the surrounding gaseous medium without any chemical change. The spinning speed depends on the solvent evaporation rate of the solution. Generally, a wider distribution of the spun fibre diameter will be given when using solutions with low solid concentrations. And, the concentration of polymer solution should be as close as possible to the upper limit under a certain range of polymer solubility and solution viscosity. The solvent should be chosen to have a relatively low boiling point and a smaller latent heat of evaporation. Therefore, in the conversion process from solution to fibres, the amount of evaporated solvent would be reduced during the conversion from polymer solution to fibres, so as to shrink energy consumption and further improve the production rate. Dry spinning is mainly used for manufacturing the long filaments, and only those selective materials that with enough viscoelasticity and capable of withstanding large enough elongation could be stretched into fibres. This method can incorporate with a rolling substrate in the process, so aligned fibres can be collected (as shown in Figure 2.7).

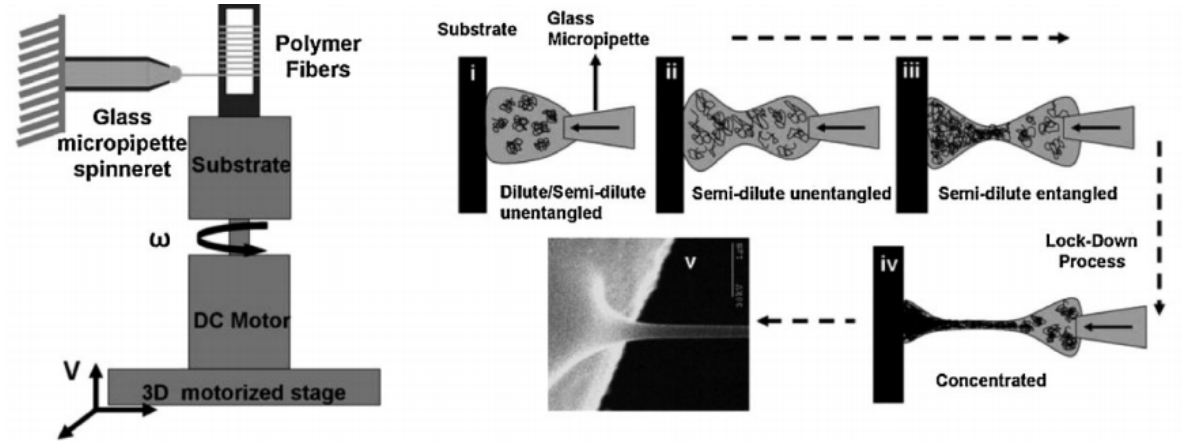

(a) (b)

Figure 2.7 (a) Schematic of dry spinning with rolling substrate, (b) fibre formation process of dry spinning (Nain, Sitti, Jacobson, Kowalewski, & Amon, 2009).

2.4.5 Electro-hydrodynamic Process

Bose recorded the world first study on electro-hydrodynamic processing (also known as EHD processing) in 1745 (Bailey, 1988; Hayati, Bailey, & Tadros, 1987), and later, in 1879, Rayleigh explained the instability of the EHD process and the analysis of jetting and dripping effects. According to Rayleigh, the formation of droplets during EHD is the effect of two forces: the outward electrical stress and the offset surface tension. Electrical stress acts to tear the droplets while surface tension attempts to hold the droplets together, and once equilibrium is reached, droplets are formed (Lord, 1878; Rayleigh, 1882). The stability of the droplet depends on the balance of the force between the outward electrical stress and the counter surface tension. The electrical force tends to break the droplet, while the counteracting surface tension acts to hold the droplet together (Rayleigh, 1882).

2.4.5.1 Electrospinning

The method of electrospinning has been developed and investigated for over one centuries. Morton (Morton, 1902) and Cooley (Cooley, 1902) discovered the electrospinning process in 1902, and Formhals (Anton, 1939) subsequently investigated the method about a decade and got nine US patents on different aspects of electrospinning. Although their works and patents investigated several potential solutions to optimise the preparation of “fine fibres”, they were not aware of the manufacturing of nanofibres and their potential applications (Sarkar et al., 2010). The electrospinning was re-introduced by Reneker and Doshi and as popularised since 1995 (Doshi & Reneker, 1995). From then on, the scanning electron microscope (SEM) was commonly available for the perspectives of nanofibre morphology analysis. In their paper, they identified varous applications of the electrospun fibres in diverse fields, including structuring, textile, membrane and medical applications. They also coined the new term “electrospinning” from the historical “electrical spinning” (Sarkar et al., 2010).

The electrospinning is one of the most widely used (Figure 2.8), non-mechanical techniques for manufacturing fibres with high electric field. During electrospinning, an external electric field provided by high voltage is applied between collector and the end of spinneret to charge the polymer solutions or melts. The solution flow was induced and deformed under electrostatic forces (Doshi & Reneker, 1995; Z.-M. Huang, Zhang, Kotaki, & Ramakrishna, 2003; D. Li & Xia, 2004; Ramakrishna, 2005; Reneker & Chun, 1996). Electric field force (in some application also with gravity) exceed the surface tension of polymer drops and reach an equilibration to form a suspended conic (known as Taylor cone) and the charged polymer jets will be

ejected out from the tip of spinneret. The jetted polymer jets will then undergo a further elongation-and-whipping process, and finally solidified gradually to form fibres with the solvent evaporation. The duration of spinning controls the thickness of fibres that accumulated on the ground collector. The fibre morphology can be tailored by controlling a number of parameters, including, the intrinsic solution properties (polymer concentration, surface tension and electric properties of solution e.g. conductivity and dielectric constant), and the processing conditions such as voltage, infusion (flow) rate and collection distance (D. Li & Xia, 2004; Teo & Ramakrishna, 2006). The fibre diameter produced by this method is generally at nanometre level, and it has been widely used in manufacturing of tissue scaffold or cell growth scaffold material. The choice of solvent also can influence the morphology, mechanical properties and critical minimum concentration of electrospun fibres via solvent-polymer interactions. C. J. Luo et al. studied the effects of 49 common solvents in the electrospinning of PCL (polycaprolactone) fibres, and the scale range of obtained fibres is 57.4 – 5600 nm (Luo, Stride, & Edirisinghe, 2012). Bhardwaj and Kundu gave a comprehensive summary of the effects of various parameters of electrospinning on fibre morphology (Bhardwaj & Kundu, 2010), as listed in Table 2.1.

Table 2.1 Effects of electrospinning parameters on the spun fibre morphology

Parameters	Effect on fibre morphology	References
Processing parameters		
Flow rate	Fibre diameter is decreasing with the decreases of flow rate; generation of beads with too high flow rate.	(Sill & von Recum, 2008; C. Zhang et al., 2005; Zuo et al., 2005)
Applied voltage	Fibre diameter is decreasing with the increases of voltage.	(Demir, Yilgor, Yilgor, & Erman, 2002; B. Kim, Park, Lee, & Sigmund, 2005; Zeng, Haoqing, Schaper, Wendorff, & Greiner, 2003)
Collection distance	A minimum distance is a prerequisite for fibre formation; a too small or too large distance will lead to bead formation.	(Buchko, Chen, Shen, & Martin, 1999; C. Zhang et al., 2005)
Environmental parameter		
Temperature	Fibre diameter is decreasing with the increases of temperature.	(Mit-uppatham, Nithitanakul, & Supaphol, 2004; Reneker & Chun, 1996)
Humidity	High humidity causes circular pores on the fibre.	(D. Li & Xia, 2004; Mit-uppatham et al., 2004)
Rheological properties		
Polymer concentration	Fibre diameter is decreasing with the decreases of concentration.	(B. Kim et al., 2005; Son, Youk, Lee, & Park, 2004)
Viscosity	Bead formation and narrower fibre diameter are promoted by the decreases of viscosity.	(H. Jiang, D. Fang, B. S. Hsiao, B. Chu, & W. Chen, 2004b; C. Zhang et al., 2005; Zhao et al., 2005)

Polymer molecular weight	Formations of beads and droplets are restrained by increasing molecular weight.	(Chen & Ma, 2004; Demir et al., 2002; P. Gupta, Elkins, Long, & Wilkes, 2005)
Surface tension	High surface tension increases the instability of jets; No conclusive connection with fibre morphology.	(Hohman, Shin, Rutledge, & Brenner, 2001; Mit-uppatham et al., 2004; C. Zhang et al., 2005)
Conductivity	Fibre diameter is decreasing with the increases of conductivity.	(Jiang et al., 2004b; Koski, Yim, & Shivkumar, 2004)

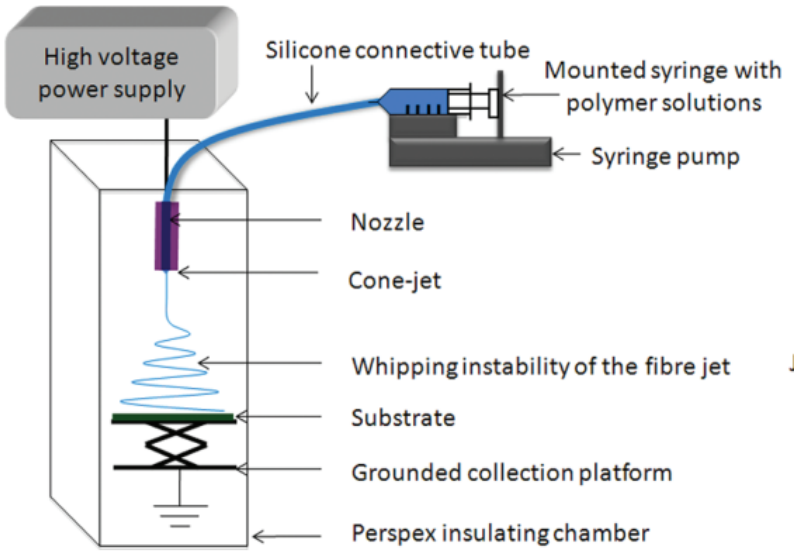

Figure 2.8 Schematic diagram of conventional electrospinning device (Luo et al., 2012).

Despite the versatility of this method, there are several major challenges that still limit the utilisations of electrospinning: (i) restricted selections of materials because of requiring minimum critical electrical properties. Huang et al summarised a list of 44 materials that can be used to produce fibres by electrospinning method in solution system, and the scale range of produced fibres is < 3 nm to over 1000 nm (Z.-M.

Huang et al., 2003); (ii) random orientations of collected fibres due to the whipping process in the spinning; (iii) a high voltage at kV level is required, which raises the safety and cost concerns; (iv) only single nozzle is generally carried out during the process, hence low production rate. To meet the requirement of mass production, people developed some alternative electrospinning process, with the multiple needle electrospinning and needless electrospinning being most popular.

2.4.5.2 Multi-needle Electrospinning

Increase the number of spinnerets (needles) is the most direct way to improve production rate (Figure 2.9). The configurations of multiple needle array mainly have two styles – linear distributed and two dimensionally distributed, for instance, square and circular etc. (F. L. Zhou, Gong, & Porat, 2009). This method shares same mechanism with conventional single-nozzle electrospinning, but with more complex parameters, including, needle number and inter-needle distance. Because the distorted electric field that caused by the existing expulsion and attraction between the polymer jets with same or inversed charges. Hence, a minimum inter-needle space should be pre-defined at the initial stage of the processing. Additionally, this minimum space is also depending on the properties of different materials, e.g. the minimum space of 3.5 mm was found in the spinning of poly(vinylalcohol) and poly acrylonitrile fibres. The generic linear array of multi-needle spinning was found to give a relative poor quality of production by unevenly spinning and bond between adjacent jets. Therefore, most of studies on muti-needle electrospinning have been focused on two dimensional arrays (F. L. Zhou et al., 2009). Theron et al. studied a 3×3 matrix array of 9 needle electrospinning and found this design can improve the

stability of spinning as well as for production efficiency (Theron, Yarin, Zussman, & Kroll, 2005).

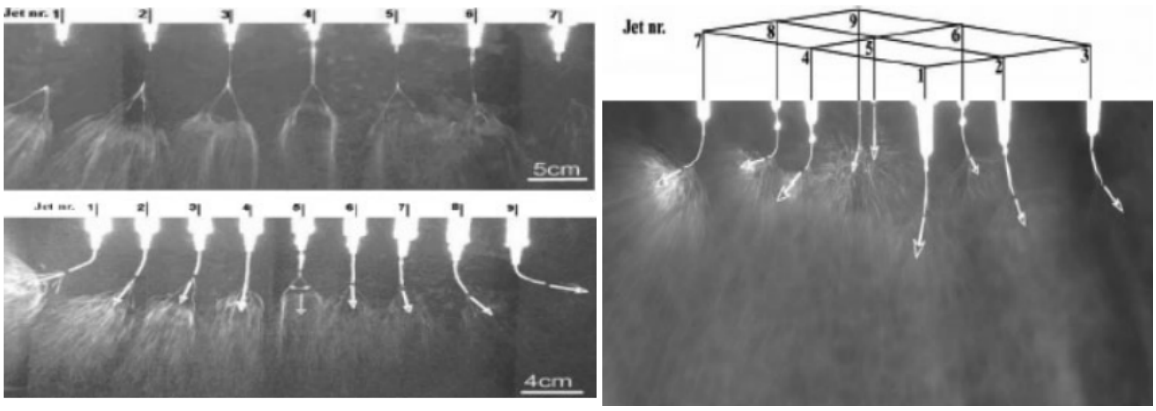

Figure 2.9 (a) linear array of 7 needles and 9 needles electrospinning (b) 3×3 matrix array of 9 needles electrospinning (F. L. Zhou et al., 2009).

2.4.5.3 Needless Electrospinning

Compare with multi-needle spinning, the needless electrospinning has more sister-processes. According to the shape of spinnerets, it could be divided into: ball, beaded chain, disc, spiral coil, cylinder spinnerets. According to the motion of spinnerets, it could be divided into rotating type (Figure 2.10) and stationary type (Figure 2.11). The solutions that used as raw materials in spinning can be provided by continuously ejecting on the surface of spinnerets or immersing spinnerets in a pool of solution.

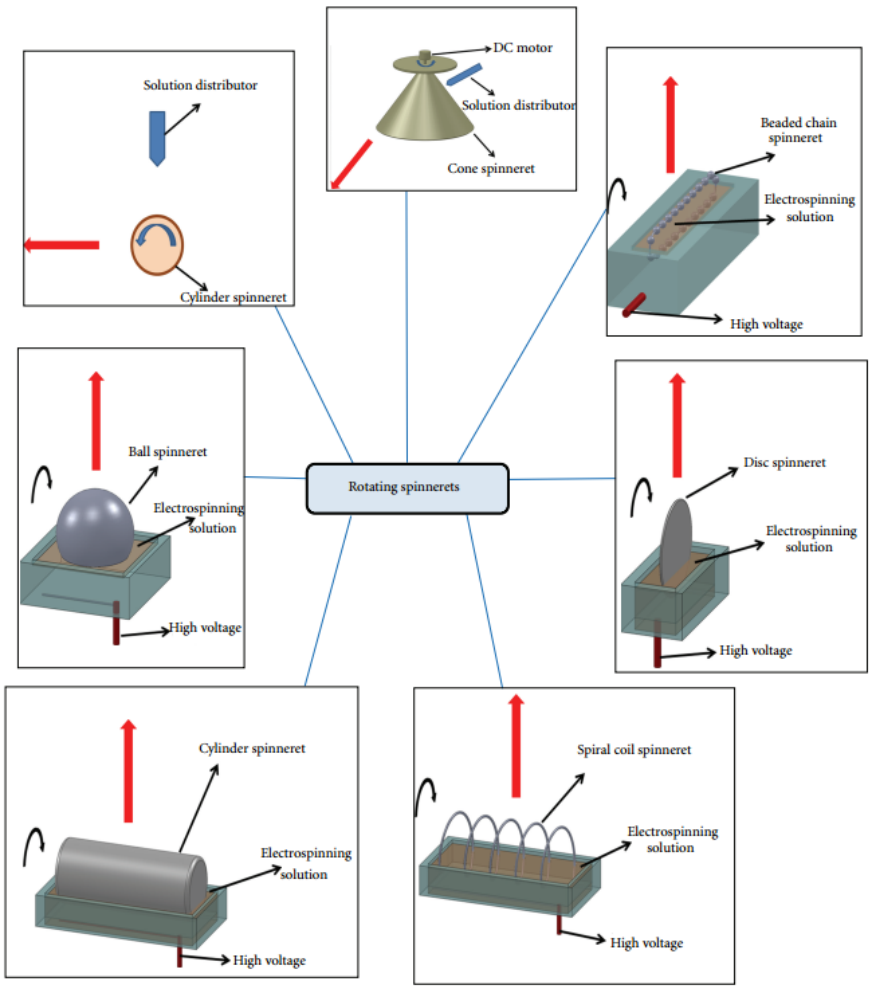

Figure 2.10 Schematic summary of needless electrospinning with rotating spinnerets (the red arrows point at the fibre collection direction) (Niu & Lin, 2012).

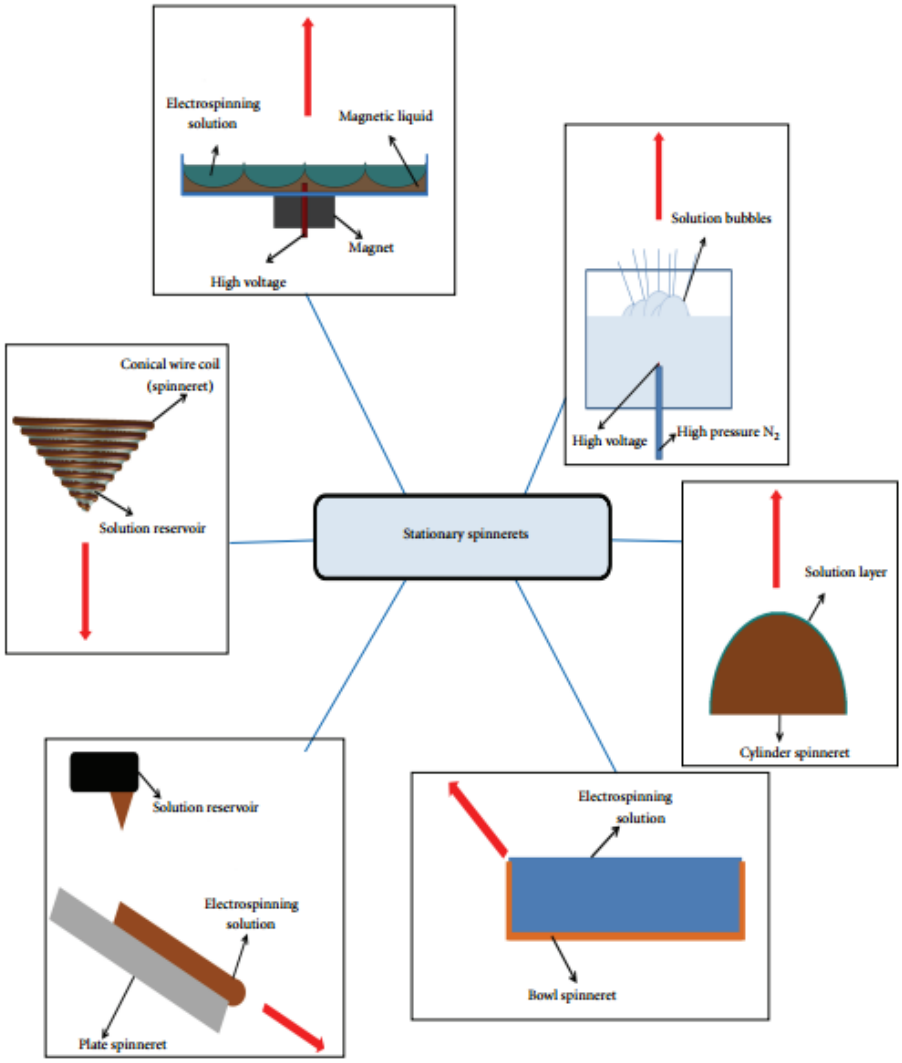

Figure 2.11 Schematic summary of needless electrospinning with stationary spinnerets (the red arrows point at the fibre collection direction) (Niu & Lin, 2012).

The major feature of this method is the polymer jets initiate naturally at the position, of where meet the processing conditions. The spinning process can be mainly described as: due to the surface injection, immersion or rotation within a pool of solution or melts, a layer of solution/melts is formed on the surface of spinnerets; the perturbation of the layer existing on the surface of spinnerets will promote a formation of jet-initiate spikes, which will concentrate electric force to form Taylor

cones; The polymer jets will be initiated and further stretched out and finally form fibres (Niu & Lin, 2012).

Niu .H et al. compared the influences of several different spinnerets in the electrospinning process, they indicated that the production rate and the quality of produced fibres have significant differences between different spinnerets' geometries. They found the disc spinneret can produce better morphology of nanofibre (257 ± 77 nm) with narrower distribution when compared with a cylinder type (357 ± 127 nm) and ball type (344 ± 105 nm). This attribute to the intense electric field that concentrates and narrowly distributed at the top area of the disc, which enhances stretching of polymer jets. Lin et al. developed a spiral coil spinneret and proved that this design could lead to more intense and uniform distribution of the electric field. Hence, better morphologies of produced fibres and higher production rate can be achieved. However, the applied voltages in needless electrospinning methods are commonly much higher, for example, in T. Lin's study the used voltage from 45 – 60 kV (Lin et al., 2010). Additionally, some of the other types of needless method with shapeless 'spinnerets' e.g. ferromagnetic fluid method developed by Yarin and Zussman (Niu & Lin, 2012; Yarin & Zussman, 2004), which requires an extra magnetic field to trigger the ferromagnetic fluid to form spikes for jets initiation. These will further increase the cost and safety concerns by requiring a bigger size of equipment, and hampering its commercial viability.

2.4.6 Gyration-based Spinning Process

The gyration-based spinning mainly takes use of centrifugation to prepare fibres, and the fabrication of fibres is independent of solution conductivity. The general processing parameters for gyration methods are the physical properties of the

polymer solution and rotational speed. Most of the method in this branch only capable of producing fibres in a scale of sub-micron or micrometres, but some of them are able to decrease the diameter to nanometres level when incorporated with other factors, for instance, infused gas flow.

2.4.6.1 Centrifugal/Force/Rotary-jet Spinning

Centrifugal spinning, force spinning and rotary-jet spinning are the techniques mainly rely on centrifugal rotation to fabricate fibrous structure through extruding polymer jets. The main difference between these methods is the design of the apparatus of the rotatable solution container. Centrifugal spinning is not new to the industry, it has been widely used in the manufacturing of micrometres fibreglass in the industry for over half a century, but its utilisation of preparing polymeric fibres can be traced back around the 1990s (X. Zhang & Lu, 2014). In this process (Figure 2.12), the polymer solution is pre-loaded in a vessel (or spinning head) that driven by an electrical motor. When the process started, centrifugal force will extrude polymer solution out from the several holes or nozzles that on the surface of the vessel to form polymer jets at high rotational speed, and jetted polymer jets then solidifies as solvent evaporation to form fibres. This formation process relies upon the competition between centrifugal force and physical properties of the solution, particularly surface tension. The major obstacles of centrifugal spinning are (i) discontinuous production, which asks the raw material must be preloaded at the initial stage of each experiment; (ii) during the acceleration of rotation at the beginning of process, the formation of droplets is generated, because lack of enough centrifugal force to overcome the surface tension of solution to form jets. The force spinning (Figure 2.13) is similar as centrifugal spinning but with a different spinneret, which consists of two symmetrical needles

that connected with a reservoir that holds the polymer solution/melts (Hammami et al., 2014). The major obstacle of force spinning is same as centrifugal spinning, i.e. the discontinuous production.

M. R. Badrossamay et al. and P. Mellado et al. developed an alternative process (rotary jet spinning) as shown in Figure 2.14 (Badrossamay, McIlwee, Goss, & Parker, 2010; Mellado et al., 2011), which shares the same mechanism with centrifugal spinning, but the device only with one orifice rather than multiple, and the polymer solution in this method is continuously fed into the vessel. P. Mellado et al. also studied the physical process and gave a physical model of rotary jet spinning, which was used as one of the references to improve the mathematic model of our work. They also identified that the produced fibre diameter is a function of solution viscosity, angular speed of rotation, nozzle-to-collector distance, and initial jet radius.

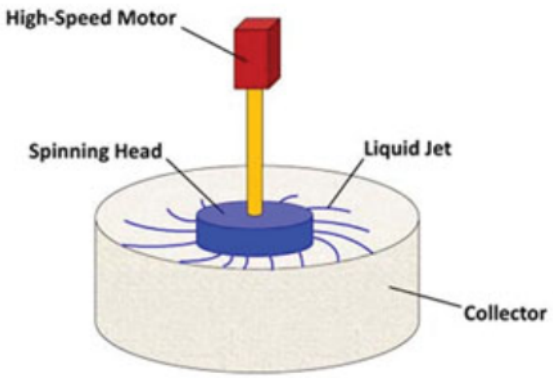

Figure 2.12 Schematic of centrifugal spinning process (X. Zhang & Lu, 2014).

Figure 2.13 Apparatus of force spinning device (Hammami et al., 2014).

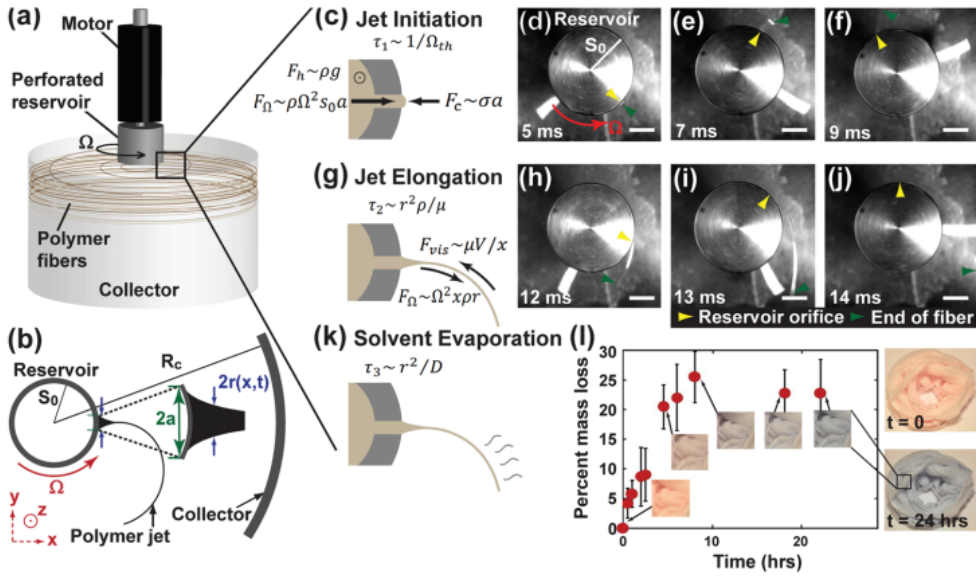

Figure 2.14 (a) Schematic diagram of rotary jet spinning. (b) Top view diagram of fibre formation process (c)-(f) Jet initiation. (d)-(f) Photographic images capture initiation of the jet from the reservoir. Green arrows denote the end of the jet and yellow arrows mark orifice position. (g)-(j) Jet elongation. In (d)-(f) and (h)- (j), s0 = 0.85 cm and scale bars are 0.42 cm. (k) Solvent evaporation. (l) Fibre colour is an indication of the presence of solvent in the collected fibres, as solvent evaporates, fibre colour changes from red to blue. Colour evolution is in good agreement with the measured mass change of the collected fibres (Mellado et al., 2011).

2.4.6.2 Pull Spinning

The pull spinning is one of the recent method, which was built by the same group who developed the rotary jet spinning (Deravi et al., 2017). They separated the solution feeding system and rotary system by feeding the solution from the bottom of a static tube stand and replaced the reservoir using a horizontal bristle at the edge of a rotational plate (**Figure 2.15**). In the experiment, one polymer droplet emerges at the top of tube stand, and the rotating bristle attaches and pulls the droplet to form jet and then solidifies as fibres. The fibre diameter obtained in this system depends on solution viscosity, rotational speed and collection distance.

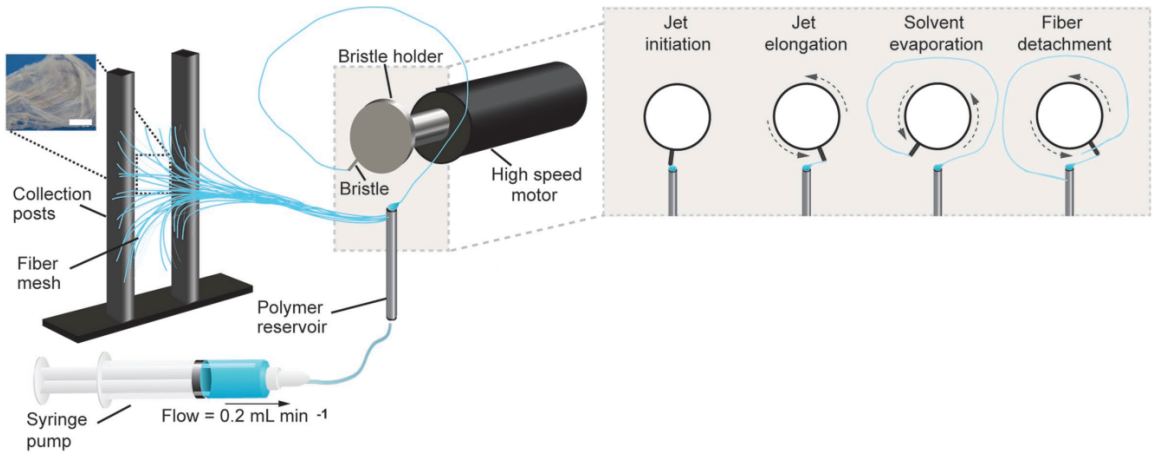

Figure 2.15 Schematic of pull spinning process (Deravi et al., 2017).

2.4.6.3 Pressurised Gyration

The schematic process and basic setup of pressurised gyration are shown in Figure 2.16 (Mahalingam & Edirisinghe, 2013). It simply uses centrifugal force by a rotating vessel at a fast-rotational speed against the surface tension of the solution. The solution was extruded from the orifices under the driven of gas blowing and centrifugal force during the spinning, and the formed polymer jets will then be stretched into homogenous fibres. Due to the additional applied pressure provided

by the introduced gas steam in the process, the solvent evaporation will be affected as well as the fibre morphology. There are 20 orifices with identical geometry (0.5 mm in diameter) and equidistantly located on the wall of the rotational vessel. Therefore, several polymer jets simultaneously emerge from fibre jetting orifices during the spinning, and a polymeric web will be generated in one simple step. Attribute to the applied pressure, the produced fibres are thinner than the centrifugal spinning and more efficient and cost saving compared with other conventional methods. S. Mahalingam et al. compared the production rate between this method and several other conventional spinning processes (Table 2.2), which shows the pressurised gyration is more suitable for mass production of fibres. The parameters of this method include rotational speed, polymer solution/melt properties, and applied pressure. Discontinuous production is the major challenge of pressurised gyration, i.e. asking raw materials pre-loaded in the rotational vessel before the spinning.

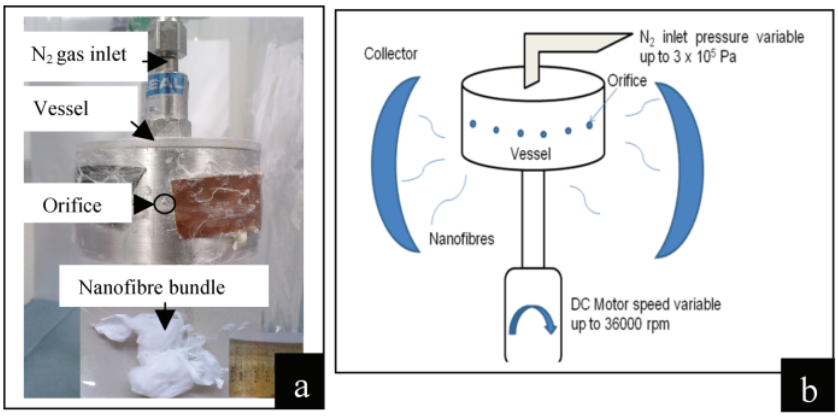

Figure 2.16 (a) Pressurised gyration apparatus and prepared products (b) Schematic of pressurised gyration process (Mahalingam & Edirisinghe, 2013).

Table 2.2 Comparison of fibre diameter and production rate between different methods.

Method	Yield ($kg\ h^{-1}$)	Fibre diameter (nm)
Centrifugal spinning	0.06	45 – 400
Solution blowing	7 – 8	1000
Electrospinning	0.17	50
Pressurised gyration	6	60 - 1000

S. Mahalingam and M. Edirisinghe invented and studied using this method to fabricate functional fibres for many applications in a different field, for example, shape memory fibres and carbon fibre (X. Wu et al., 2016) and ceramic fibres (Mahalingam, Pierin, Colombo, & Edirisinghe, 2015) and so on. Zhang et al. developed an alternative application based on S. Mahalingam's work, which replaces the gas inlet of pressurised gyration using an in-flow of solution. The method is called infusion gyration. S. Zhang et al. utilised this process to continuously prepare gold nanoparticle-peptides loaded functional fibres, which can be prepared for a promising application for imaging and sensing (Siqi Zhang et al., 2015). L.F. Deravi et al. compared the advantages, limitations, fibre formation mechanisms and produced fibres geometries for several common spinning methods and their sister-processes e.g. pressurised melt gyration, centrifugal melt spinning and melt electrospinning and so forth, as listed in Table 2.3.

Table 2.3 Comparison of fibre formation mechanism, advantage and limitation between several spinning methods (Deravi et al., 2017).

Process	Mechanism	Production specifications	Yield (gh^{-1})	Process advantages	Process limitations
Pull spinning	Axial, rotational stretching	45 000 rpm	0.15	• Portable • Point-of-use fabrication • Amenable to wide range of polymers • High throughput • Control of fibre orientation • Easy-of-use	• Lower throughput than previous force spinning method
ES	Electric field	<30kV	0.01-0.1	• Amenable to wide range of polymers	• Lower throughput than previous force spinning method • Require high V power supply • Alignment is not inherent to process; additional tools required
Near field ES	Electric field	0.2-1.8 kV	NA	• Amenable to wide range of polymers • Precise control of fibre alignment and deposition •	• Low throughput • Require high V power supply • Short distance to collector impedes fibre solidification
Rotary jet (force) spinning	Centrifugal force	Up to 75 000 rpm	60	• Hight throughput • Amenable to wide range of polymers • Easy-of-use •	• Bench-top system, not easy potable • Fibres formed circumferentially • Requires postprocessing for use as scaffolds
STEP	Capillary force	550 rpm	NA	• Performs in air • Formation of high aspect ratio fibres • Precise control over fibre spacing •	• Low throughput, based on production rates • Not easily scalable
Touch spinning	Axial stretching	500-2500 rpm	NA	• Amenable to wide range of polymers • Performs in air • Control of fibre orientation • Easy-of-use	• Low throughput, based on production rates
Brush spinning	Axial stretching	3000 rpm	NA	• Performs in air • Control of fibre orientation • Easy-of-use	• Removing sheets from brush may damage loose fibres • Requires postprocessing for use as scaffolds

Pressurised gyration	Centrifugal force, solution blowing	Up to 36 000 rpm	6000	• High production rate	• Gas pressure contributes to fibre elongation • Requires volatile solvents
Pressurised melt gyration	Centrifugal force, high temperature	Up to 36 000 rpm	NA	• Eliminates dependence on volatile solvents • Crystalline polymers formed using gyration temperature	• Requires high T • Unsuitable for biopolymers • Limited to microfibre production
ES rapid prototyping	Electric field	3.2 kV	NA	• Amenable to wide range of polymers • Precise control of fibre alignment and deposition	• Require high V power supply • Vibration of collector a affects fibre morphology • Incomplete fibre solidification between layer decomposition distorts fibre morphology
Centrifugal melt spinning	Centrifugal force, high temperature	11 000-13 630 rpm	NA	• Amenable to wide range of polymers • Eliminates dependence on volatile solvents	• Unsuitable for biopolymers
Gas jet nanofibers	Axial stretching, gas blowing	NA	0.09-8.6	• Scalable process is amendable to multiple fibre morphologies	• Low production rates • Requires volatile solvents for nanofiber formation
Melt ES	Electric field, high temperature	5-100 kV	12.5	• Highly uniform and reproducible fibre diameters	• Low production rates • Only applicable for nonconductive polymers
Direct write melt ES	Electric field, high temperature	Up to 12 kV	NA	• Control of fibre deposition and orientation • Produces complex multi-layered structures	• Requires high V power supply • Lag between jet and collector speed yields errors over time • Unsuitable for biopolymers • Limited to microfibre production

2.5 Process Modelling Methods

Multivariate statistical techniques allow for a significant reduction in the number of experiments and a description of the effects of (individual or combined) processing parameters (Amini & Younesi, 2009). These powerful data modelling tools are able

to capture the complex non-linear pattern and relationships between the independent features and responses of the system (Witek-Krowiak, Chojnacka, Podstawczyk, Dawiec, & Pokomeda, 2014). Hence, this helps the investigation and optimisation of the operating system.

2.5.1 Response Surface Methodology

There are several widely-used methods for formulating surrogate models, for example, Radical Basic Function (Buhmann, 2003), Gaussian process regression (Kriging) (Stein, 2012) and Response Surface Method (Myers, Montgomery, & Anderson-Cook, 2016) and so on.

Response Surface Method was developed by Box and Wilson in 1950s (Bruns, Scarminio, & de Barros Neto, 2006; Gilmour, 2006). This name stems from a graphical perspective generated after mathematical fitness and its utilisation has been widely adopted in texts. RSM is a collection of mathematical and statistical techniques for empirical model development and optimising based on the experimental data. To achieve this goal, a linear (usually with first order) or non-linear polynomial function (higher order) is used to describe the system under study, and thus to explore the experimental conditions until their optimisation (Teófilo & Ferreira, 2006). RSM mainly constituted by experimental strategies for independent variables or space of process, empirical modelling to establish appropriate approximations between experimental outputs and process variables, and optimisation methods for finding proper values of process variables to produce desirable response.

RSM has important application in determining the behaviour of data sets for statistical forecasting. It can define the influence of independent variables individually or in combination on a response or a set of responses of a process, and simultaneously optimise the levels of experimental variables to attain the optimal performance of the system. Some examples of the RSM applications of optimisation of chemical or biomedical process are enzymatic processing (Ashrafi, Nasseri, Alimohammadi, Mahvi, & Faramarzi, 2016; Nongonierma, Maux, Esteveny, & FitzGerald, 2017), heat transfer with nano-fluid (Iranmanesh et al., 2016; Shirvan, Mamourian, Mirzakhanlari, & Ellahi, 2017), micro-extraction for pre-concentration (Dil et al., 2016; Rahmani, Ghasemi, & Sasani, 2017; Reubsaet, Norli, Hemmersbach, & Rasmussen, 1998), ultrasonicated adsorption and extraction process (Saad, Tahir, Khan, Hameed, & Saud, 2017), cooling strategy for batteries (Wei Li, Xiao, Peng, Garg, & Gao, 2019; Ling et al., 2018) and fibre manufacturing (Davoudpour et al., 2015; Dayan et al., 2018; Gu, Ren, & Vancso, 2005; Khanlou et al., 2015).

RSM is used to approximate the functional relationship between the independent variables and the process response based on experimental data, and it is valuable in obtaining insight of variable contributions through the coefficients in the developed model. The developed model can be saved and used as a prediction tool for the optimal combinations of experimental variables that can achieve the optimum response. Moreover, RSM is scalable to design and predict a model equation with a higher degree than the second order, but it should be noted that the selection of the order should be conducted after carefully analysing the input data. A lower order model may not be able to capture the variance of the data and result in a highly biased model (also known as underfitting), and a higher order may lead the fitting

curve pass through most of the data points and result in a less generalised mode (also known as overfitting).

In RSM, usually, if the problem with N inputs variables (up to second order), there are (N+2)(N+1)/2 coefficients that need to be determined, so the overall computational complexity is $O(N^2/2)$. The general stages of RSM as an optimisation technique are as follows: (1) according to the research purpose and the experience of the researcher, select independent variables that have a significant impact on the system through screening studies and demarcation of experimental range; (2) selecting an experimental design and conducting experiments according to the selected experimental matrix; (3) mathematical statistical processing of experimental data by fitting polynomial functions; (4) evaluating models; (5) verifying the necessity and possibility of displacement in the direction of the optimal experimental conditions (to determine, through hypothesis testing, significance of the coefficients of the variables); (6) predicting the optimum experimental conditions that result in desirable outputs (either maximum or minimum in objectives) over a certain region of interest (Bezerra, Santelli, Oliveira, Villar, & Escaleira, 2008).

RSM should not be extrapolated beyond the scope of the original observations, and the model developed may not explicitly express the physical meaning of the whole system under investigation.

2.5.1.1 Selecting Variables

In experiments, there are probably many variables that affect the outcome directly or indirectly. It is impossible to identify and precisely control each small contribution. Hence, practically, it is necessary to pick the variables that have significant impact

on the response of the whole system. A design of variable screening should be performed to determine which of several experimental variables and their interactions have more effects. For the purpose of improving efficiency and economy, sometimes full or fractional two-level designs for factors may be applied (Lundstedt et al., 1998).

2.5.1.2 Selecting Experimental Design

The objective of RSM is to figure out a proper approximating functional model between the experimental response (denoted as y) and independent variables (denoted as x_k which is also called coded variables, where k denotes the k-th variable). Usually, the relationship is

$$y = f(x_1, x_2, \ldots, x_k) + \varepsilon \tag{2.1}$$

where f is called as response function and its true form is unknown (can be low- or high-ordered). ε represents other sources of variability that not accounted for in the response function f. In general, the ε consists of the background noise, effect of other or unknown variables and error of measurements. In the computations, ε is generally treat as statistical error, it is also called as residual, and assuming its values obey a normal distribution with mean zero and variance σ^2. Then, for the all experimental data, can have

$$E(y) = E[f(x_1, x_2, \ldots, x_k)] + E(\varepsilon) \tag{2.2}$$

As the true form of response function is unknown, it is necessary to approximate it, and the successful use of RSM depends to a large extent on the ability of the researcher to develop a proper approximation of response function. Conventionally,

the first-order model (linear function) is applied at the preliminary stage of a response surface investigation (for example, Eq. 2.3), and in many cases, either a low-order (first or second) or higher-order (over third) model is used according to the non-linearity of the research problem. A low-order model such as a first-degree function may be proper if the researcher tends to approximate the true response surface in a relatively small range of independent variables in a position with small curvatures in the response function f. For instance,

$$y = \beta_0 + \sum_{i=1}^{k} \beta_i x_i + \varepsilon \tag{2.3}$$

which is also called a main effects model, as in the Eq. 2.3, only the individual effects of independent variables were considered (Carley et al., 2004). Here, x_i is the i-th variable, β_i is the corresponding coefficient, k represents the number of independent variables, β_0 is a constant term (also known as intersection). The response from Eq. 2.3 should not present any curvature, as it only consists of the main effects of the independent variables. In order to evaluate curvature, a second or high order model should be applied. Fractional two-level designs are used to estimate first-order effects, but they fail when other effects (e.g. second-order effects) are significant. Therefore, a central point in two-level factorial designs and additional terms, which represent the interactions between the different independent variables should be added according to the Eq. 2.4 presented below:

$$y = \beta_0 + \sum_{i=1}^{k} \beta_i x_i + \sum_{i<}\sum_{j=2}^{k} \beta_{ij} x_i x_j + \varepsilon \tag{2.4}$$

In general, the first-order model (even with interactive terms) is not sufficient to capture the strong curvature in the true response surface. So, it is necessary to include quadratic terms in the model to determine the critical (maximum, minimum or saddle) points, as shown in Eq. 2.5.

$$y = \beta_0 + \sum_{i=1}^{k} \beta_i x_i + \sum_{i<}\sum_{j=2}^{k} \beta_{ij} x_i x_j + \sum_{i=1}^{k} \beta_{ii} x_i^2 + \varepsilon \quad (2.5)$$

The second or higher-ordered model is used extensively in RSM for a number of reasons:

1. Flexible form, A minimum second-order model assumes a diverse range of functional forms and is therefore usually a good approximation to the true response surface

2. Easy to estimate, as least square method can be used, so it is easy to estimate the parameters (β in the model) of the model.

3. There are numerous experiences show that the second or higher-ordered models solve the practical response surface problems well.

The general motivation of approximation for the true response function *f* is based on the Taylor series expansion around the point $x_{10,}x_{20,\dots,}x_{k0}$ (Carley et al., 2004). For the purpose of parameter estimations, often the design of experiment must ensure that the study variables are performed at least at three levels. Then, researchers can use the symmetrical response surface designs, for instance, central composite design, Doehlert design, Box-Behnken design and three-level factorial design etc

(Lundstedt et al., 1998). The main differences of these symmetrical designs with each other include their selection of experimental points, the number of levels of variables, and the number of runs and blocks (Bezerra et al., 2008).

2.5.1.3 Mathematical Statistical Processing of Data

According to the experimental data, it is necessary to fit a mathematical function to describe the behaviour of the response of the system. Thus, it is essential to estimate the coefficients (β in the model) in models. Writing Eq. 2.3 – 2.5 in matrix notation as:

$$\boldsymbol{y} = \boldsymbol{X\beta} + \boldsymbol{\varepsilon} \tag{2.6}$$

where $\boldsymbol{X}$ is the matrix of the experimental design, $\boldsymbol{y}$ is the response vector, $\boldsymbol{\beta}$ is the matrix of the parameters of the model, and $\boldsymbol{\varepsilon}$ is the residual vector.

Least square method is normally performed to solve the Eq. 2.6 and estimate the parameters of the model (Baş & Boyacı, 2007), and the Eq. 2.6 can be written as below (Eq. 2.7) to construct a response surface that describes the behaviour of the response in the experimental domain.

$$\widehat{\boldsymbol{\beta}} = (\boldsymbol{X^T X})^{-1}(\boldsymbol{X^T y}) \tag{2.7}$$

$\widehat{\boldsymbol{\beta}}$ represents the estimated coefficient matrix. Least square is a multiple regression technique used to fit a mathematical model to a set of experimental data with lowest possible residual. It is assumed that the residuals obey a normal distribution with a zero mean, a common variance (unknown), and a variance-covariance matrix given

by $\sigma^2 \boldsymbol{I}_n$. In this way, the estimation of variance for each element of the $\widehat{\boldsymbol{\beta}}$ can be typically obtained by authentic repetitions of the central point, as shown in Eq. 2.8 (André I Khuri & Mukhopadhyay, 2010).

$$\boldsymbol{Var}\left(\widehat{\boldsymbol{\beta}}\right) = (\boldsymbol{X^T X})^{-1}\boldsymbol{X^T}(\sigma^2 \boldsymbol{I}_n)\boldsymbol{X}(\boldsymbol{X^T X})^{-1} = \sigma^2(\boldsymbol{X^T X})^{-1} \tag{2.8}$$

Therefore, the standard errors of the coefficients ($\widehat{\boldsymbol{\beta}}$) constituting the response surface equation is obtained by extracting the square root of each element of $\boldsymbol{Var}\left(\widehat{\boldsymbol{\beta}}\right)$, thereby allowing evaluation of its significance. After getting the $\widehat{\boldsymbol{\beta}}$, the prediction of response is $\widehat{\boldsymbol{y}}(\boldsymbol{x})$ and

$$\widehat{\boldsymbol{y}}(\boldsymbol{x}) = f(\boldsymbol{x})'\,\widehat{\boldsymbol{\beta}}, \qquad \boldsymbol{x} \in \boldsymbol{R} \tag{2.9}$$

where $\boldsymbol{R}$ denotes the experimental region for any point of x. As the $\widehat{\boldsymbol{\beta}}$ is an unbiased estimator of $\boldsymbol{\beta}$, so the variance of the $\widehat{\boldsymbol{y}}(\boldsymbol{x})$ is

$$\boldsymbol{Var}\left(\widehat{\boldsymbol{y}}(\boldsymbol{x})\right) = \sigma^2\, f(\boldsymbol{x})'\,(\boldsymbol{X^T X})^{-1}\, f(\boldsymbol{x}) \tag{2.10}$$

It is crucial that the prediction variance in Eq. 2.10 must be as small as possible.

2.5.1.4 Evaluating Fitted Model

At this stage, it is necessary to fit all the models (regression equations) involving different combinations of variables (also called regressors). These regression models will be evaluated on the basis of some appropriate criterions, and the model with the best performance will be selected. If k regressors are assumed involve in the equation, then there are 2^k total equations to be estimated and examined. Clearly,

evaluating all possible functional models can be computationally cumbersome, a variety of methods have been studied to evaluate only a subsets of regression equations by adding or deleting one regressor at a time. These methods can be divided into three categories generally: forward selection, backward elimination and stepwise regression, the latter one is a popular combination of the previous two (Carley et al., 2004).

Forward selection starts from the hypothesis that no regression variable in the model apart from the intercept (i.e. β_0), and try to find the best subset of variable combinations by inserting one regressor into the model each time. The first regression variable selected for adding to the model is the variable with the largest simple correlation (either positive or negative) with the response of the system y. At each step, each selected and entered regressor must has the current largest value of the *F*-statistic (or t-statistic) that exceeds a preselected *F*-value for testing significance of regression. These correlations are called as partial correlations. The process terminates when the partial *F*-statistic for a particular step does not exceed the preselected *F*-value or the last candidate variable is added to the model.

Backward elimination tries to attain a suitable model by working in the opposite direction as the forward selection. It starts from a model that contains all the candidate variables, and then calculates the partial *F*-statistic for each variable as if it were the last variable entering the model. The variable whose partial *F*-statistic value smaller than the preselected *F*-value will be removed from the model. The process of backward elimination will terminate until the smallest partial *F*-value is greater or equal to the preselected *F*-value.

The above two procedures proposed many possible combinations. The most popular of these is the stepwise regression method. In this method, all regressions previously added into the model are re-evaluated by their partial *F*-statistics in each step. Because of the relationship between the early added and current regressors, the regressor that entered in the earlier step may now be redundant. As similar in the backward elimination method, if a variable's *F*- statistic is less than the preselected *F*-value (cut-off value), the variable will be dropped from the model. The principle difference between the stepwise method and the above two is the stepwise method needs two cut-off values for adding and dropping regressors. Generally, the adding cut-off value was set larger than the dropping cut-off value, to make it relatively difficult to add a variable than to delete one, although this is not necessary.

It is necessary to verify none of the assumptions of least square regression are violet and the fitted model has an adequate approximation to the true response of the system. One of the reliable and commonly used way to evaluate the fitting quality is analysis of variance (ANOVA). The core idea is to compare the variation in the combination of variable levels with the variation due to random errors inherent in the measurement of the resulting response (André I Khuri & Mukhopadhyay, 2010). Thus, considering the source of the experimental variance, the significance of the regression used to predict the response can be evaluated. In ANOVA, the variation of data is evaluated by studying its dispersion, given in the Eq. 2.11.

$$Deviation_i{}^2 = \left(y_{ij} - \widehat{y_{iJ}}\right)^2 \tag{2.11}$$

Here, y_{ij} is the j-th repletion of the observation y_i, and $\widehat{y_{ij}}$ is the model's prediction that related with y_{ij}.The sum of the square due to residuals is called the sum of squares of the residuals (SSE):

$$SSE = \sum_{i=1}^{n} \left(y_{ij} - \widehat{y_{ij}}\right)^2 = \quad \boldsymbol{e^T e} \tag{2.12}$$

As $\boldsymbol{X^T X\widehat{\beta}} = \boldsymbol{X^T y}$, hence the Eq. 2.12 can be derived as

$$SSE = \boldsymbol{y^T y} - \boldsymbol{\widehat{\beta}^T X^T y} \tag{2.13}$$

An unbiased estimator of $\sigma^2$is

$$\sigma^2 = \frac{SSE}{n - p} \tag{2.14}$$

where n is the total number of experimental observations, p is the number of regression coefficients. The total sum of squares (SST) denotes the sum of the square of total observation deviations, as presented in Eq. 2.15.

$$SST = y'y - \frac{(\sum_{i=1}^{n} y_i)^2}{n} = \sum_{i=1}^{n} {y_i}^2 - \frac{\left(\sum_{i=1}^{n} y_i\right)^2}{n} \tag{2.15}$$

the total sum of squares can be dissembled in the sum of the square due to regression (due to model) (SSR) and in the sum of squares of the residuals, i.e.

$$SST = SSE + SSR \tag{2.16}$$

The sum of squares of the residuals consists of two parts: the sum of squares of pure error (SSP) and the sum of the square due to the lack of fit (SSL). When the division of the sum of squares of each variation source (total, residuals, regression, pure error and lack of fit) is made by its respective degrees of freedom, the “media of the square” (MS) are obtained (Bezerra et al., 2008) and Table 2.4 shows the equations that associated with the source of variations for calculating the sum of squares (Bruns et al., 2006; Teófilo & Ferreira, 2006).

Table 2.4 Analysis of variance for fitted model to an experimental data set using multiple regression (Bezerra et al., 2008).

Variation source	Sum of the square	Degree of freedom	Media of the square
Regression	$SS_{reg} = \sum_i^m \sum_j^{n_1} (\hat{y}_i - \bar{y})^2$	$p-1$	$MS_{reg} = \frac{SS_{reg}}{p-1}$
Residuals	$SS_{res} = \sum_i^m \sum_j^{n_1} (y_{ij} - \hat{y}_i)^2$	$n-p$	$MS_{reg} = \frac{SS_{res}}{n-p}$
Lack of fit	$SS_{lof} = \sum_i^m \sum_j^{n_1} (\hat{y}_i - \bar{y}_i)^2$	$m-p$	$MS_{lof} = \frac{SQ_{lof}}{m-p}$
Pure error	$SS_{pe} = \sum_i^m \sum_j^{n_i} (y_{ij} - \bar{y}_i)^2$	$n-m$	$MS_{pe} = \frac{SS_{pe}}{n-m}$
Total	$SS_{tot} = \sum_i^m \sum_j^{n_i} (y_{ij} - \bar{y})^2$	$n-1$	

n_i, number of observations; m, total number of levels in the design; p, number of parameter of model; $\hat{y}_i$, estimated value by the model for the level i; $\bar{y}$, overall media; y_{ij}, replicates performed in each individual levels; $\bar{y}_i$, media of replicates performed in the same set of experimental conditions.

From Table 2.4, the ratio of the media of the square of regression to the media of the square of residual can be used to evaluate the significance of regression. Comparing these sources of variation by using the Fisher distribution and consider their respective degrees of freedom associated with residual (v_{res}) and regression (v_{reg}) variances:

$$\frac{MS_{reg}}{MS_{res}} \approx F_{v_{res},v_{reg}} \tag{2.17}$$

The mathematical model is well fitted to the experimental data if the value of the ration in Eq. 2.17 is higher than the tabulated value for F.

The coefficient of determination (i.e. R^2) is a measure of the reduction in the variability of response y obtained by using the regression variables in the model. The coefficient of multiple determination R^2 is defined as:

$$R^2 = 1 - \frac{SSE}{SST} \tag{2.18}$$

As the value of R^2 always increases as the added variables to the model (regardless of the additional variable is statistically significant or not), hence a large value of R^2 does not necessarily implies that the current model has a good fitting quality. The adjusted R^2 is one alternative approach that can avoid the above drawback of the R^2. The adjusted R^2 is defined as:

$$R^2_{adj} = 1 - \frac{\frac{SSE}{n-p}}{\frac{SST}{n-1}} = 1 - \frac{n-1}{n-p}(1 - R^2) \tag{2.19}$$

As the adjusted R^2 considering the number of the coefficients used in the model, so its value will not always increase as the number of additional terms. If unnecessary variables are added, the value of adjusted R^2 will often decrease. Adding variables to a regression model always results in an increase in the sum of squares of the regressions, and a decrease in the sum of squared errors. It is necessary to determine if the increase in the sum of squares of the regressions is adequate to ensure that additional variables are used in the model. The mean square error will be increased, and the usefulness will be decreased if adding unnecessary variables to the model. If a model exhibits significant regression and a non-significant lack of fit, then the model will fit the experimental data well. In other words, the regression model must be able to describe the main part of variation observation, and the rest of

the variation must be due to the residuals (Andre I Khuri & Cornell, 2018; Pimentel & Neto, 1996).

Visually inspecting the residual graph is also a popular approach to inspect the information about the model suitability. For example, if the model yields large residuals, hence it is insufficient to provide proper inferences/approximations about the behaviour of experimental data. The residual graph (distribution) should give a behaviour that suggests a normal distribution, if a well-fitted model is obtained. Furthermore, if there are other terms that required for the model, it also will be able to be inspected the behaviours from the residual graph that indicates the kind of term that needed to be entered to the model (Bruns et al., 2006).

2.5.1.5 Predicting the Optimum Experimental Conditions

The surface generate by our model can be used to indicate the direction in which the original design must be shifted for finding the region of optimal conditions. For example, in fibre manufacturing, the region of optimal conditions can be defined as the sets of experimental variables that can achieve a desirable fibre morphology (in diameter, standard deviation or quantity). However, the optimal operating conditions must be visually inspected within the experimental conditions of the study, if the experimental region cannot be shifted because of realistic reasons (for example, the instrument cannot reach enough measurement precision or unrealistic experimental conditions). The critical point of a model can be characterised as minimum, maximum or saddle point. The coordinates of the critical point can be calculated using derivative information of the mathematical model, for example the gradients and Hessians. The visualisation of the regression model can be applied using the response surface plot. The dimension of graphical response is often n, and

represents as a surface in the (n + 1)-D space. The dimension of a representation lower and equals to 3 can be directly plotted. The drawing visualisation is only possible when one or more regressors are set to constant values, if more than 3 regressors in the model.

The input combination that minimises or maximises the output of the objective function can also be explored using RSM, and then be used to optimise the output of the real system. When validating or optimising a stochastic simulation model, one attempts to approximate the model parameters of a particular stochastic output that optimises the simulation model (Carley et al., 2004). RSM is often used for optimisation of stochastic simulation models (Kleijnen, 1998). RSM approximates the objective functions by polynomial functions over a small sub-region of the domain. Through applying the ordinary least squares to the objective functions' observations, the coefficients of the objective function are estimated. Therefore, the objective function is evaluated in an arrangement called a point of experimental design (Kleijnen, 1998). According to the fitted model, a local optimal point is derived which is used as an optimal current estimate and as the centre point of the new experimental region that can generate preselected output.

Based on the objective function, the optimal region of experimental conditions can be determined using constrained or unconstrained optimisation algorithms. In contrast to the constrained optimisation, the unconstrained optimisation considers the problem of minimising or maximising the objective function that depends on the actual variable but does not limit its range of values. However, the experimental variables always have a realistically operational range of values. For example, in the fibre manufacturing problems, the polymer concentration sometimes been picked as

one of the variables in the fitted model and its value should be limited in the experimental region. Constrained optimisation can be generally divided into direct search methods and gradient-based methods. The direct search methods do not use derivatives, such as simulated annealing (SA), genetic algorithm (GA), Nelder–Mead method (NM) and so on. The gradient-based methods take a use of first-order derivative information (gradients) or second-order derivative information (Hessians matrices) to find the set of variables that optimise objective functions. The common gradient-based methods including (non-linear) interior point methods, augmented Lagrangian, and sequential quadratic programming etc. In contrast with direct search methods, the gradient-based methods generally tend to converge more quickly, but can be less tolerant to the presence of noise in the function and constraints.

The optimisation problem can typically be solved “locally” or “globally”. The local optimisation method is a heuristic method that only build up local model of the problems. To ensure convergence of the iterative process, a number of local optimisation methods only adhere to a certain decrease of the objective function. If converge, these algorithms will only find local optimum and referred to as local optimisation algorithms. On the other hand, global optimisation algorithms attempt to find the global through allowing both decrease and increase of the objective function, but the conducting of these algorithms arte often more computationally expensive. Furthermore, finding global optimums can be arbitrarily difficult even without constraints, so the methods used may fail. It may often be useful to optimise the function multiple times and pick the best results (global optimum or fine local optimum) (Forsgren, Gill, & Wright, 2002).

In this work, several optimisation algorithms (either in direct search methods or gradient-based methods) were attempted to find the global optimum for our objective function to find the optimal (experimental) conditions that can generate desirable fibre diameter and narrow standard deviations, such as simulated annealing, Nelder–Mead, Differential Evolution (DE) and non-linear interior method.

Simulated annealing is a metaheuristic (analogous) method used to approximate global optimisation in large search spaces. It is a simple stochastic function minimiser that driven from the annealing process of metallurgy, in which a metal is heated to a high temperature and slowly cooled down. The annealing process in metallurgy makes the metal tougher by settling its atomic structure to a lower energy state. In optimisation problems, the random motion of points that resemble high temperatures, and the low temperature represents little randomness of points. Annealing in optimisations enables the structure to escape from local minima (minimum) and continue to explore and finally converge at better, hopefully, global optimum (minimum) values. The "slow cooling" in the simulated annealing can be rendered as the probability of accepting a more inferior is decreased slowly as the solution space is discovered. Accepting a more inferior solution is a basic attribute of metaheuristics, as it enables a broader search for global optimal solutions (Granville, Krivánek, & Rasson, 1994; Kirkpatrick, Gelatt, & Vecchi, 1983; Vetterling, Teukolsky, Press, & Flannery, 1992).

Simulated annealing begins from a random search at high temperature and ultimately becomes a pure greedy descent because it moves towards to temperature of zero. Randomness should tend to jump out of local minima and find areas with low heuristics; greedy descent will result in the convergence on local minima.

Deterioration steps are more likely to occur at high temperatures than at lower temperatures (Poole & Mackworth, 2010). Simulated annealing maintains the assignment of the current values to the variables. It randomly selects a variable and then randomly selects a value in each step. If there is an improvement after assigning this value to the variable, then accepting this assignment as the new current assignment. If not, it accepts the assignment with a certain probability, which is depend upon how bad it is compared with the current assignment and the temperature. The current assignment will be remained If it does not accept the change (Poole & Mackworth, 2010). Simulated annealing uses multiple starting points and starts to look for optimum from each of the points. An initial variable subset is randomly selected from the full set of variables, then the algorithm selects a random subset near the current state, measure its performance on the basis of any of the simulated annealing rules and decides whether to maintain the current one or move to it: (1) if higher value of the criterion of the alternative subset; or (2) with the probability p defined by Eq. 2.20 if the criterion value of the alternative subset is lower than the value of the current solution, where the temperature (T) is decreased in the iterations of the algorithm (Carley et al., 2004). The stopping criterion of the algorithm is either the algorithm converges to a point, or the method remains consecutively at the same point until the maximum number of iterations is reached.

$$p = exp\,[(E(A) - E(A'))/T] \tag{2.20}$$

where the A represents the current assignment of the value of each variable, and the $E(A)$ is the evaluation of the current assignment A that to be minimised. Simulated annealing randomly selects a neighbour, and gives a new assignment of A'. If $E(A')$

$\leq E(A)$, it accepts that the A' becomes the new assignment. Otherwise, the assignment is only randomly accepted with the probability p. The probability p decreases exponentially with the "badness" of the movement - assessing the amount of deterioration $(E(A) - E(A'))$ (Carley et al., 2004). For the temperature parameter T, it is more likely to allow a "bad" movement at higher value of T. When T approaches to zero, they become less and less likely before the algorithm behaves more or less like a local search (Russell & Norvig, 2016). Simulated annealing usually used when the search space is discrete. Simulated annealing may be more appropriate to other alternative methods such as gradient descent for finding that the global optimal approximation is more important than finding a precise local optimum in a fixed amount of time.

Nelder-mead method was originally proposed by John Nelder and Roger Mead in 1960s (Nelder & Mead, 1965). It is a well-known direct search method that is useful for the multidimensional unconstrained optimisations without using derivatives. It is usually used to solve non-linear optimisation problems, which derivatives may not be known. Nevertheless, the Nelder-Mead is a heuristic search method so that it is able to converge to non-stationary points on problems that can be solved by alternative methods (Kolda, Lewis, & Torczon, 2003; Powell, 1998; Wright, 1996). Usually, Nelder-Mead method includes the following steps:

- For a function with n variables, Nelder-Mead generate other n points $\{x_2, x_3, \ldots\ x_{n+1}\}$ according to the initial point (x_i is n-dimensional vector), which form the vertices of a polyhedron in a n-dimensional and maintains a set with n+1 points space. In each iteration of the algorithm, the n+1 points $\{x_1, x_2, x_3, \ldots\ x_{n+1}\}$ form a

polyhedron, and the order of these points is such that $f(x_1) \leq f(x_2) \leq f(x_3) \leq \ldots \leq f(x_{n+1})$.

- Make m be the centroid (average position of the first n points) of the polyhedron contains the best n points, $m = \frac{1}{n}\sum_{i=1}^{n} x_i$.

- Calculate the reflection point of x_{n+1} with respect to the centroid point, $r = m + \alpha(m - x_{n+1})$, where α is a scaling parameter and larger than zero.

- If $f(x_1) \leq f(r) < f(x_n)$, i.e. the reflection point is not better than the worst point but better than the second worst, then replacing the worst point using the reflection point $x_{n+1} = r$, and go back step 1 and enter the next loop.

- If the reflection point r is the best point so far, $f(r) < f(x_1)$, then compute the expanded point, $s = m + \beta(r - m))$ with $\beta > 1$. If the expanded point is better than the reflection point, $f(s) < f(r)$, replacing the worst point using the expended point i.e. let $x_{n+1} = s$. Otherwise, replacing the worst point using the reflection point i.e. let $x_{n+1} = r$, and go back step 1 and enter the next loop.

- If the reflection point r is worse than the second worst point x_n i.e. $f(x_{n+1}) \leq f(r)$, the polyhedron is assumed to be too large and needs to be contracted. Then a new contracted point is defined as $x_c = \begin{cases} m + \gamma(x_{n+1} - m), if\ f(r) \geq f(x_{n+1}) \\ m + \gamma(r - m), if\ f(r) < f(x_{n+1}) \end{cases}$ with $0 < \gamma < 1$. If the contracted point is better than the reflection point and the worst point, $f(x_c) < \min(f(r), f(x_{n+1}))$, then the contraction is successful and replacing the x_{n+1} using x_c. Otherwise, it will conduct a further contraction.

From the above steps, it can be seen that when the position of the local minimum is outside the pattern (polytope) consisted by n+1 points, the pattern tends to become

larger and accelerate to move to the minimum value. When the position of the minimum is inside the graph, the graph tends to shrink. As the number of loops increases, these n+1 points will eventually gather toward the local minimum.

The Differential Evolution algorithm is a branch of evolutionary computation raised by Rainer Storn and Kenneth Price for the optimisation problems in the continuous domain (Storn & Price, 1997). It is one of the genetic type algorithms and capable of handling non-linear, non-differentiable and multimodal objective functions. It is also a metaheuristic method as it can search for very large spaces in the candidate solution and makes little or no assumptions about the problem being optimised. Differential Evolution is a stochastic parallel direct search evolution strategy optimisation method that is quite fast and fairly robust, and has been frequently used in the fields of constrained optimisation, multiobjective optimisation and parallel computing (Chakraborty, 2008; Onwubolu & Babu, 2013; Kenneth Price, Storn, & Lampinen, 2006). It is also utilised to train neural networks with real and constrained integer weights (Ilonen, Kamarainen, & Lampinen, 2003; Plagianakos & Vrahatis, 2002). The search mechanism of Differential Evolution referred to as mutation, to guide the search to the prospective regions in the feasible region. Usually, genetic type algorithm generates a series of populations using selection mechanisms, and uses mutation and crossover as search mechanisms. The major difference between Differential Evolution and genetic algorithms is that genetic algorithms rely on crossover, which is a probabilistic and useful information exchange mechanism between solutions, which can find better solutions, while evolutionary strategies (such as Differential Evolution) use mutations as the primary search mechanism.

Differential Evolution is a population-based search technique that uses NP (number of parent) variables as a population of D-dimensional parameter vectors for each generation. It maintains a population with m points, $\{\boldsymbol{x_1}, \boldsymbol{x_2}, \ldots\ \boldsymbol{x_m}\}$, where m >> n, n is the number of variables. The initial point is randomly picked from the population if there is no additional information available about the problem. The basic idea behind this method is a new scheme for generating test parameter vectors. The working flow of Differential Evolution is presented in Figure 2.18. Differential Evolution yields new parameter vectors by adding a weighted difference vector between two members to the third member. If the resultant vector generates a better result of objective function than the predetermined member, then the newly generated vector replaces the vector it compared with. Moreover, to track progress made in the optimisation process, the best parameter vectors are evaluated for each generation (Kenneth Price et al., 2006). In every iteration (generation), a new population with m points is generated. Generating a new vector (mutant) by selecting three random vector $\boldsymbol{x_a}$, $\boldsymbol{x_b}$ and $\boldsymbol{x_c}$, and forming $\boldsymbol{x_s} = \boldsymbol{x_c} + F(\boldsymbol{x_a} - \boldsymbol{x_b}))$, where F is a real-valued weighting or scaling factor and supplied by users (to control the evolve rate) in the optimal range from 0.5 to 1 (K Price & Storn, 2001). In every generation, the primary array vector $\boldsymbol{x_j}$ is targeted for crossover with a vector $\boldsymbol{x_s}$. Additionally, to ensure the test vector (after crossover) does not duplicate $\boldsymbol{x_j}$, constructing test vector $\boldsymbol{x_{new}}$ by taking the coordinate of a random index i ($1 \leq i \leq n$) from $\boldsymbol{x_s}$ with a crossover probability, otherwise getting from $\boldsymbol{x_j}$. If the test vector can deliver a lower value of the objective function, then using $\boldsymbol{x_{new}}$ replaces the $\boldsymbol{x_j}$ in the population. The value of crossover probability is user defined and falls in a range from zero to one, it indicates the probability that the child inherits the values of the parameter from the random vector. If the probability equals to zero, all parameters except one test vector

parameter are from the target vector. On the other side, if the probability equals to one, all the test vector parameters must come from x_s (Das & Suganthan, 2011).

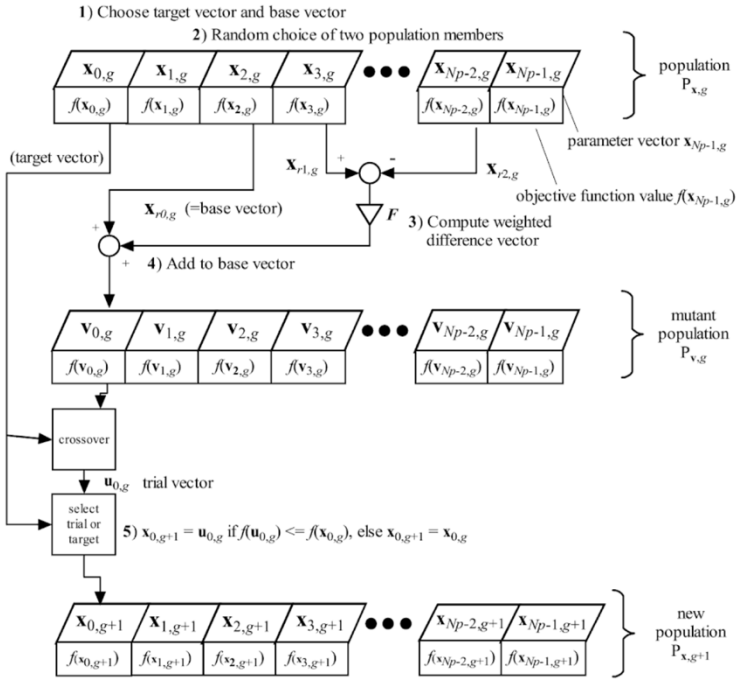

Figure 2.17 A flow chart of the generate and test loop of basic Differential Evolution (Kenneth Price et al., 2006).

In the constrained optimisation problems, the inequality constraints are the difficult parts of optimisation as their “duality”. If the optimal solution strictly satisfied the inequality, the inequality constraints do not affect the results and can be removed from the model, as the optimum is in the interior of the constraints. Otherwise, the original inequality constraints must exist and can be considered as equality from the beginning. The boundaries that defined by the inequality constraints can be avoided by the iterations generated by interior point method. As the optimisation continues to advance, the iterator can gradually approach to the boundary and finally converge to the optimum that may be on the boundary. From a practical perspective, the interior point method usually only takes dozens of iterations. Each of them involves solving

massive amount of equations and considering all the variables and constraints in each iteration.

The interior point method is a linear or non-linear programming method that optimises by traversing the middle of the entity of the problem rather than around its surface. It has several advantages, such as the ability to exploit second-order derivatives and is effective on loosely constrained and unconstrained problems. The interior point method was firstly introduced by John von Neumann for finding a feasible solution for a linear program with a convex constraint (Dantzig & Thapa, 2006). The revolution in the interior point method led to a shift in thinking about continuous optimisation fundamentally. The beginning of the interior point method revolution was the Karmarkar's study of a linear programming method that announced in 1984, which ran in provably polynomial time and was 50 times faster than the simplex method (Forsgren et al., 2002). The interior method is characterised by the continuous parameterised families of approximate solutions that are asymptotically converging to the exact solution. These convergence paths track smooth trajectories with geometric and algebraic attributes (for example, a precisely defined "centred") that can be utilised and analysed by algorithms. A number of interior methods are described as "path tracking" to indicate that they depend on the paths attributes that provide the basis for all complexity analysis of interior point algorithms for programming (such as convex, linear and quadratic).

2.5.2 Machine Learning Techniques

Machine learning techniques are the general name of the collection of computational algorithms that are able to capture rules from a certain amount of input data (the process also known as training or learning) and apply these on testing data

(prediction) without being explicitly programmed (Bishop, 2006; Cesa-Bianchi & Lugosi, 2006; Hastie, Tibshirani, & Friedman, 2009). Among other uses, they can automate manual tasks to help human experts analyse large, complex data sets. This chapter reviews the categories of machine learning techniques. The categories of different type of machine learning techniques are concisely discussed in the appendix. A brief introduction about the techniques applied in this work are given below.

2.5.2.1 Artificial Neural Networks

The origin of the term "neural network" is the attempt to find a mathematical representation of the processing of information in biological systems (Rumelhart, Hinton, & Williams, 1985). Although artificial neural networks (also known as "perceptrons") have existed since the 1940s (McCulloch & Pitts, 1943), they have only become a major part of artificial intelligence in the past few decades. The simplest learnable artificial neural model is called the perceptron, which consists of input units ($\boldsymbol{x}$), connection weights ($\boldsymbol{\omega}$) and a bias ($\boldsymbol{\omega_0}$), as well as an output unit (**y**). Given a datum of $x \in \mathbb{R}^D$), the output value y is obtained from an activation function, which takes the weighted sum of the input, as presented below:

$$y_k(\boldsymbol{x}; \boldsymbol{\Theta}) = f\left(\sum_{i=1}^{D} x_i\, \omega_{ki} + \omega_{k0}\right) = f\left(\boldsymbol{\omega}_k{}^{\boldsymbol{T}}\boldsymbol{x} + \omega_{k_0}\right) \tag{2.21}$$

Where $\boldsymbol{\Theta}$ denotes a parameter set, $\boldsymbol{\omega}$ is a weight factor that equals to $[\omega]_{i=1}^{D} \in \mathbb{R}^D$, k is the index number of output. The $f(\cdot)$ is called activation function, which takes the weighted sum (denoted as z) of all the input from the previous layer. The most common activation function is logistic sigmoid function i.e., $\sigma(z) = \frac{1}{1+e^{-z}}$, which is

usually used for a binary classification problem when $k = 1$. For the case of multiple output, for example, multiple output regression/multiple class problems, a softmax function $s(z)_k = \frac{e^{z_k}}{\sum_{i=1}^{K} e^{z_i}}$ is used as the activation function and its outputs can be regarded as probability.

Although the use of non-linear activation functions, one of the major limitations of one layer neural networks comes from the linear separation of classification tasks. This limitation is evaded by introducing hidden layers between the input and output layers, as seen in Figure 2.19. Notably, multiple cells can exist in each layer, and the cells of adjacent layers are fully connected, but not in the same layer. For a neural network with one or more hidden layers (the input layer usually regarded as layer zero), which is also known as a multi-layer perceptron, as presented in Eq. 2.22 and the bias term is omitted for simplicity.

$$y_k = f^{(L)}\left(\sum_l \omega_{kl}^{(L)} f^{(L-1)}\left(\sum_m \omega_{lm}^{(L-1)} f^{(L-2)}\left(\dots f^{(1)}\left(\sum_i \omega_{ji}^{(1)} x_i\right)\right)\right)\right) \tag{2.22}$$

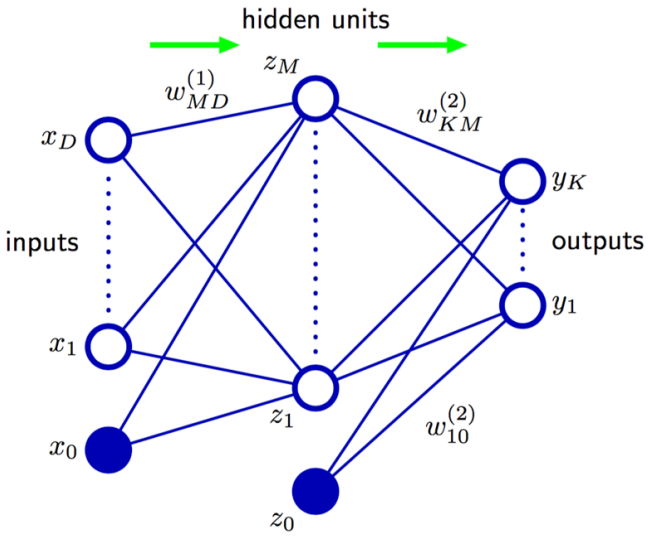

Figure 2.18 Schematic of a two-layer neural network with bias (x_0, z_0). The connections between the nodes are the weight parameters and the green arrows indicate the direction in which the information flows through the network during forward propagation (Bishop, 2006).

where the superscript denotes the layer index, and (l, m, i) denote the cell index. It should be note that the activation should be non-linear and the same type of activation function is generally applied to the hidden layers in the literature. There are various choices of activation functions, such as sigmoid, hyperbolic tangent, rectified linear unit (ReLU) and non-linear cube functions. The different activation function squashes the real values to different ranges, for instance, the range of the output value of sigmoid function and ReLU is [0,1] but for the hyperbolic tangent and non-linear cube function is [-1,1] (S. K. Zhou, Greenspan, & Shen, 2017).

In the aspect of network training, two basic problems: network architecture training and parameter training. Generally, the network learning is referred to as network parameter learning, as the architecture training is still an open question (Rumelhart et al., 1985). The problem of learning feedforward neural network parameters can be

expressed as error (cost) function minimisation. For a classification problem with total K classes, the most common used cost function is cross entropy function (S. K. Zhou et al., 2017), as presented in Eq. 2.23.

$$J(\Theta) = -\left(\sum_{n=1}^{N}\sum_{k=1}^{K} t_{nt}\ln(y_{nk})\right) \tag{2.23}$$

where the n is the index of the input data and denoted by $\boldsymbol{x}_n \in \mathbb{R}^D$. Each target (ground truth output) is a class indicator vector with a one-hot encoding of K and denoted by $\boldsymbol{t}_n \in \{0,1\}^{\boldsymbol{K}}$. The t_{nt} represents the k-th element of the target output $\boldsymbol{t}_n$ and y_{nk} is the k-th element of the hypothesis (predicted) output vector $\boldsymbol{y}_n$ with the input of $\boldsymbol{x}_n$. Other common cost function including Kullback–Leibler divergence, Hellinger distance, exponential cost and Itakura–Saito distance. Due to the Eq. 2.23 is a non-convex and non-linear function, so there is no analytical solution of parameter set Θ to minimise the Eq. 2.23 and gradient descent algorithm can be used to iteratively updating parameter. Backpropagation is the most popular technique to evaluate the updates of gradients in the neural networks. The principle idea behind of backpropagation algorithm is to propagate errors (difference between ground truth and prediction) from the output layer back to the input layer through chain rules and adjust/estimate parameters. For example, for a neural network with total L layers, the parameters of the layer l can be adjust/estimate as (S. K. Zhou et al., 2017):

$$\frac{\partial J}{\partial \boldsymbol{\omega}^{(l)}} = \frac{\partial J}{\partial \boldsymbol{a}^{(L)}}\frac{\partial \boldsymbol{a}^{(L)}}{\partial \boldsymbol{a}^{(L-1)}} \cdots \frac{\partial \boldsymbol{a}^{(l)}}{\partial \boldsymbol{z}^{(l)}}\frac{\partial \boldsymbol{z}^{(l)}}{\partial \boldsymbol{\omega}^{(l)}} \tag{2.24}$$

where $\boldsymbol{z}^{(l)}$ represents the weighted sum of the input of the layer l (before passed to activation function) and $\boldsymbol{a}^{(l)}$ represents the activation vector of the layer l. Figure 2.22 shows the graphical representation of using gradient descent backpropagation to estimate the parameters of a network.

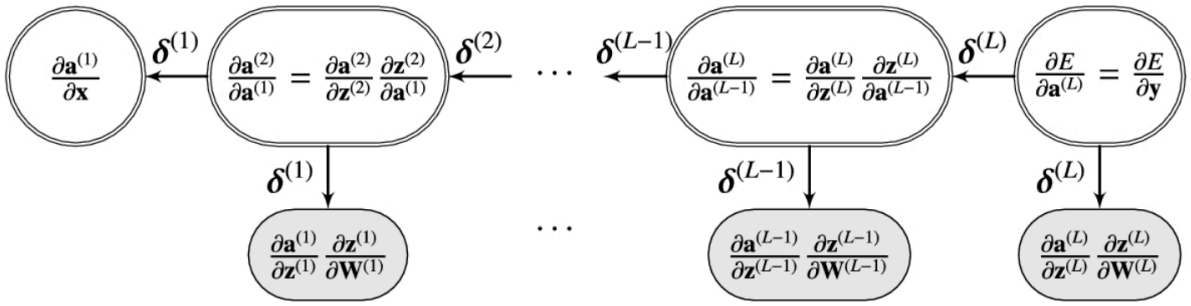

Figure 2.19 Graphical representation of gradient descent backpropagation (S. K. Zhou, Greenspan, & Shen, 2017).

For many applications, the well-trained neural network can be significantly more compact compared with other techniques, e.g. support vector machine and therefore achieve faster evaluation (Bishop, 2006; S. K. Zhou et al., 2017). The cost of this compactness is that the probability function that forms the basis of network training is no longer a convex function of model parameters. In practice, however, it is often worth investing in significant computing resources in the training phase in order to obtain a compact model for quickly processing new data (Bishop, 2006).

Artificial neural networks (ANN) and response surface methodology (RSM) are two widely used models of mathematical modelling and computer simulation for computational processes (Ketabchi, Naghibzadeh, Adabi, Esnaashari, & Faridi-Majidi, 2017; Nasouri, Shoushtari, & Khamforoush, 2013). In ANN, there are different populations of interconnected processing units (neurons) within layers, and these

units are interconnected with each other to investigate their inter-relationships and predict the specific outputs that relate to different input data and specific functions used. ANN, more precisely, the two-layer back propagation (BP) ANN has been used as a tool of modelling the electrospinning processes, as well as for predicting the geometry and mechanical properties of spun fibres. The units in the hidden layer can be manipulated as required. Hence any continuous functions can be represented at any precision. In addition, BP-ANN is able to solve multivariate regression problems (linear/non-linear) by training models through computing functions' gradient, then adjusting the weights and thresholds between neurons in each layer along the negative gradient direction, to optimise the functions (also known as gradient descent algorithm) (Basheer & Hajmeer, 2000; Reisi-Dehkordi & Eslami-Farsani, 2015).

However, despite the aforementioned strengths of ANN, there are also several known limitations of ANN, including: the slow convergence when the estimated value is close to the target; sensitivity to the noise of the training sample, i.e. relative poor training effect if there are intense changes in the sample; more notably, a tricky issue is that there is currently no general formula for the determination of the number of units (neurons) in the hidden layer, when the network structure was designed. As the number of the units directly determines the ability of the network to dig linear/non-linear information from data, insufficient quantity of selected units may lead information to be expressed inadequately; an excessive quantity of units will increase the computational overhead exponentially, also resulting in a decline in network generalisation (Ketabchi et al., 2017).

2.5.2.2 Ridge Regression

Ridge regression is one of the members of regularised least square methods, and also known as Tikhonov regularisation. Ridge regression is a biased estimation method dedicated to collinear data analysis. In essence, it is an improved least square estimation method. By giving up the unbiasedness of the least square method, a regression method that is more practical and more reliable can be obtained at the cost of losing part of the information and reducing precision. Due to the regression parameters of ridge regression have prior distribution (compared with least square has no restriction on the parameters), and limiting the prior distribution of the parameters will make the values of the obtained regression parameters not very ill-posed. Therefore, ridge regression always has a better performance in fitting compared with ordinary least square for the ill-posed problems. Mathematically, a non-negative factor is artificially added to the main diagonal elements of the information matrix of independent variables. The parameter optimisation problem as changed in Eq. 2.25, where $\hat{\beta}$ denotes the optimised parameter, denotes the y_i i-th ground truth output and λ denotes the coefficient of regularisation term.

$$\widehat{\beta}^{ridge} = argmin\left\{\sum_{i=1}^{N}\left(y_i - \beta_0 - \sum_{j=1}^{p}\beta_j x_{ij}\right)^2 + \lambda\sum_{j=1}^{p}\beta_j{}^2\right\} \tag{2.25}$$

2.5.2.3 DBSCAN

The task of clustering methods is to group a set of objects so that the objects in the same group (called a cluster) are relatively more close (similar) to each other than objects in other groups. To identify the clusters of the predicted parameter sets after optimisations, clustering algorithms were applied in this work. Clustering methods are quite frequently used in the field of information retrieval, data compression, bioinformatics and image analysis etc. The clustering methods can be categorised according to their clustering model: centroid-based (e.g. K-Means), distribution-based (such as Gaussian mixture), connectivity-based (e.g. agglomerative clustering) and density-based clustering (DBSCAN).

In density-based clustering, a cluster is defined as a region that is denser than the rest of the data. The points in the sparse regions are generally considered to be boundary and noise points that are necessary to separate clusters. The most popular density-based clustering method is density-based spatial clustering of applications with noise (DBSCAN) (Ester, Kriegel, Sander, & Xu, 1996; Kriegel, Kröger, Sander, & Zimek, 2011). DBSCAN assumes cluster-intensive areas and does not require that each point be assigned to a cluster. Hence, instead of partitioning the data, it extracts "dense" clusters and classifies sparse backgrounds as "noise." Based on the density of data, DBSCAN firstly transforms the space, and therefore, the points in the dense area are kept separately, while the points in the sparse area are moved further. Then DBSCAN applies a single link cluster to the transformation space to get a tree diagram, which was cut based on pre-defined distance parameters (the minimum distance between two points) to get the cluster.

In contrast with other methods, DBSCAN clusters consist of all densely connected points (which can form clusters of any shape rather than the unalterable globular cluster of K-Means) and all objects within the scope of these points. Therefore, the result of this method is not as dependent upon initialisation as other methods, and the noise and core points are deterministic for each operation. DBSCAN also requires researcher has little knowledge about the dataset, build algorithms based on local area queries and use various techniques, such as kdtree to get good scale and performance according to the size of the data set. Another attractive property of DBSCAN is its low computational complexity (Ester et al., 1996; Schubert, Sander, Ester, Kriegel, & Xu, 2017). The main drawback of DBSCAN is that the selection of algorithm parameters may be difficult if the dataset has variable density clusters. As it relies on the detection of the cluster boundaries by some sort of density drop, for example, for a dataset with overlapping Gaussian distributions, the cluster boundaries generated by DBSCAN usually appear arbitrary. For solving the issue of varying density clusters in DBSCAN, a recent algorithm i.e. Hierarchical DBSCAN (HDBSCAN) was developed (Campello, Moulavi, Zimek, & Sander, 2015). In the part of optimisation in this project, DBSCAN was applied to identify the groups of parameters that can offer desirable geometry and morphology of nanofibrics. It should note that the objective "correct" clustering algorithm is not existed. For a particular problem, it is often necessary to conduct experiments to select the most appropriate clustering algorithm, only if there are mathematical reasons are available for choosing one model instead of another (Estivill-Castro, 2002).

3. Experimental Details

In this part, the materials and equipment used throughout the whole work are described. Starting with a description of the materials used and details of suppliers are given. Detailed information about the equipment, manufacturer or supplier, as well as an overview of their operations and instrument settings are introduced in the relevant sections. This section also highlights the experimental conditions and outcomes that analysed by these equipments and their relevance to the objectives of the project.

3.1 Materials

Poly(ethylene oxide) (PEO) is one of the few non-toxic, biocompatible and biodegradable synthetic polymers that are soluble in water and organic solvents and has been widely used in pharmaceutical, cosmetics, food products. It has been demonstrated in animal studies and exhibited rapid and complete elimination after ingestion, and remarkable swelling capacity (Fouda, El-Aassar, & Al-Deyab, 2013). PEO is a free-flowing powder with a white to off-white colour and a slight ammonia odour (Fouda et al., 2013). It is a non-ionic homo-polymer of ethylene oxide units, and its chemical structure as shown in Figure 3.1 (Rowe, Sheskey, & Quinn, 2009). Due to its molecular structure, PEO has been recognised as a valuable spinning agent that can assist and associate with other materials such as alginates, polysaccharides and cellulose-based materials into fibres (Desai, Kit, Li, & Zivanovic, 2008; K. Y. Lee, Jeong, Kang, Lee, & Park, 2009).

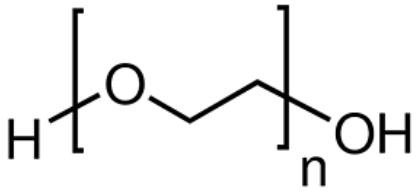

Figure 3.1 Molecular structure of PEO (Rowe et al., 2009).

Poly (ethylene oxide) (PEO) with molecular weight (Mv) of 200,000 g/mol that was purchased from Sigma-Aldrich (Poole, UK). It was used as-received and dissolved in deionised water. Five different weight percentages (3, 5, 10, 15, and 21 wt%) of PEO were selected and prepared in solutions. To obtain homogeneous spinning dopes before processing, these solutions were magnetically stirred for 24 hours at the ambient temperature (25°C). The concentrations of PEO solutions chosen in this work are similar to the previous works of our group (Mahalingam & Edirisinghe, 2013; Siqi Zhang et al., 2015) on the pressurised gyration and infusion gyration, for achieving the comparative studies of the performance of PCIG

3.2 Gyration Set-up for Nanofibre Preparation

The novel method that invented and used in this project is called pressure coupled infusion gyration, which inherits the benefit from pressurised gyration and infusion gyration and able to bring materials to the nano-scale. Not only to improve their properties and afford them new advanced features beyond bulk materials but also to produce well-aligned 3D fibrous bundles consistently and cost-effectively. The schematic diagram of this method as shown in Figure 3.2. The cylindrical rotational

vessel of PCIG apparatus in this work is 60 in diameter and 40 mm in height. There are 20 orifices distributed on the wall of vessel symmetrically and equidistantly, each of them is around 0.5 mm in diameter. The cross section and geometry of produced fibres can be customised by the feature of orifices and vessel (size and geometry).

With the continuous injection of solution streams and high rotational speeds, PCIG can efficiently use materials and generate fibres rapidly, and can significantly increase fibre production at increased flow rates. A DC motor was used to provide power for rotation and was controlled up to 36 000 rpm. using a control panel. During the spinning process, the steam of polymer solution was fed simultaneously using a syringe pump (Harvard Apparatus Ltd., Edenbridge, UK). A circular copper mesh collector was centrally placed that surrounds the rotational vessel, was used to collect fibres ejected from the orifices of the vessel. After collection, the fibres were covered, dried, and stored.

During rotational spinning, PCIG feeds the polymer solutions into the vessel continuously during rotation and utilises gas blowing and high-speed rotation to extrude several parallel polymer jets from orifices that are equally spaced on the surface of the vessel. Fibres with controlled morphology can be prepared by selectively adjusting processing parameters. The key processing parameters of PCIG include polymer concentration, the infusion flow rate of polymer solution into the vessel, applied gas pressure, rotational speed and the distance at which the nanofibres are collected. In contrast with other gyration methods, the fibre produced using the PCIG method is much thinner. This is because the mass transfer of dynamic fluid flow can be regulated by the infusion rate of the solution when flowing across the orifice during spinning. Therefore, the input material can be effectively

used to obtain the desired product morphology by balancing different combinations of processing parameters with solvent evaporation.

For studying the comparative performance with previous gyration methods and investigating how these parameters of PCIG affect the obtained fibre morphology, all spinning dopes were processed at the ambient conditions of 25 °C and 38.5% relative humidity. The spinning processes of PCIG were recorded by a Photron Version SA1.1 high-speed camera, with the help of a powerful LED floodlight. Both high and low magnifications were applied. A 54000 fps of recording frame rate was used. The screenshots of these monochrome videos (12bit) are included in the appendix, for the analysis of the fibre jetting process.

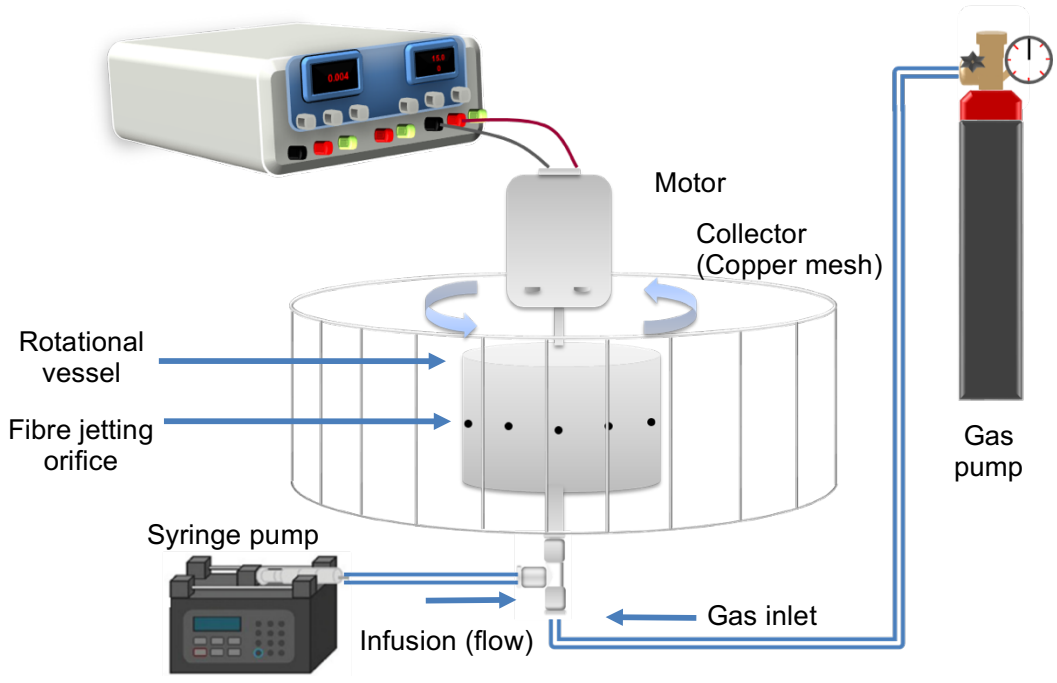

(a)

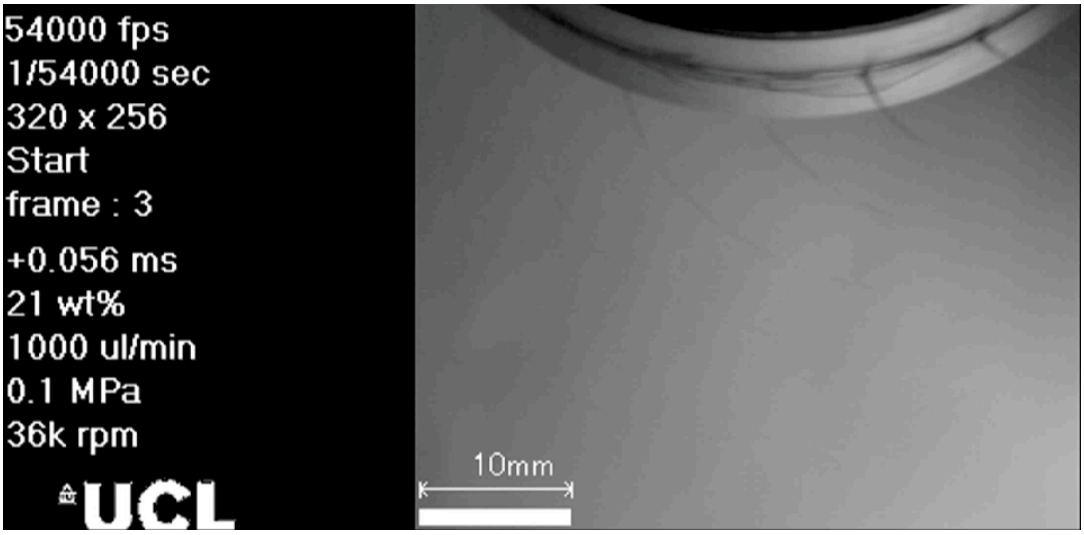

(b)

Figure 3.2 (a) Pressure coupled infusion gyration set-up and (b) fibre formation process captured using a high-speed camera (Hong, Harker, & Edirisinghe, 2019).

3.3 Controlling Parameters of Fibre Generation

3.3.1 Polymer Concentration

The concentration of the polymer solution is one of the most critical parameters for determining the morphology and dimension of the fabricated fibre. According to much of the previous work, there is a lower as well as upper limits for the spinning dope, the specific value depends on the nature of the polymer. As stated above, five different concentrations (3, 5, 10, 15, and 21 wt%) of PEO-water system was selected in this project for comparing the results of the previous works of our group about the pressurised gyration and infusion gyration.

The viscoelasticity of polymer solution has a greatly impact on its spinnability, in particular, the chain entanglement of the solution. To achieve this, the polymer solution must contain a critical minimum concentration with a certain degree of molecular chain entanglement.

3.3.2 Infusion Flow Rate

In a pressure coupled infusion revolution, there is a hydrostatic pressure at the orifice that is constant for a fixed flow rate, a fixed working pressure and rotational speed. As the infusion rate increases, the hydrostatic pressure will increase. Nevertheless, the effect of hydrostatic force is insignificant than the dominated centrifugal force. Therefore, the nanofibre formation process can be simply interpreted as the balance between the external forces (centrifugal force and gravitational force) and the surface tension of the polymer solution. During the rotating action, a syringe pump is first used to continuously inject a steady and continuous flow of polymer solution from the bottom of the rotating vessel. (Figure 2.17). Then, the Marangoni effect occurs due to the surface tension gradient of the liquid-vapor interface of the polymer drops emerging from the orifice. This result in a mass transfer of solution to the tip of the drop, forming a polymer jet. Owing to the pressure difference at the orifice and the centrifugal force, the jet is further elongated. Finally, the ejected polymer jet is thinned and solidified to form nanofibres as the solvent evaporation takes place. In this work, six different levels of injection rate were implemented (500, 1000, 2000, 3000, 4000, 5000 μL min^{-1}) to investigate different scenarios.

3.3.3 Working Pressure

The primary dominant forces in the PCIG spinning process include centrifugal force and dynamic fluid flow. The combination of these two forces resists the surface tension of the solution to form fibres (Badrossamay et al., 2010). Through applying gas pressure, solvent evaporation can be enhanced due to the gas stream introduced during the spinning process, which promotes the relative gas flow speed at the liquid-air interface on the polymer drops. Three levels of applied pressure (1, 2, 3 × 10^5 Pa) were set to study their effects on the fibre size and morphology that produced by PCIG process.

3.3.4 Rotational Speed

Like other rotation-based techniques, the centrifugal force is the fundamental force for the fibre generation. The combination of centrifugation and solution blowing resist surface tension results in deformation of the polymer drops, thereby enabling the formation of fibres. Typically, the increases in centrifugal force by the higher rotational speed will enhance this deformation. In contrast to the shear stress existing in a non-Newtonian fluid, there is normal stress acts in the same direction as the deformation plane (Mahalingam & Edirisinghe, 2013). Hence, the centrifugal force will accelerate the jet stretching, which will be further enhanced by gas blowing.

Numerous studies shown that the final diameter of fibre is determined by the changes of rotational speed. During the solvent evaporation, there is a temperature gradient that occurs along the ejected jet. Consequently, the viscosity of the solution can vary during spinning.

The work of Mahalingam and Edirisinghe pointed out that the time constant of shearing forces applied on jets will be decreased as the rotational speed increases

(Mahalingam & Edirisinghe, 2013). In addition, the response of polymer chains is determined by the time constant of shearing forces. The higher time constant, the longer the viscous response of the polymer solution as the increases of the time constant and vice versa. Thus, sufficient viscous solution response should be guaranteed by a minimum rotational speed, which enables nanofibres production from a diluted polymer solution. In this project, three different levels of rotational speed (10 000, 24 000 and 36 000 rpm) were used to investigate their effects on the produced fibres.

3.3.5 Collection Distance

The importance of collecting distance has been well investigated in the field of electrospinning (Bhardwaj & Kundu, 2010; Doshi & Reneker, 1995; Ramakrishna, 2005). In PCIG, the appropriate distance of fibre collection is determined on the basis of the duration of solvent evaporation and the diameter required for the helical trajectory of the polymer jet. The travel time of the polymer jet is entirely dependent on the distance of the orifice from the collector. For any type of spinning dope, the selection of the minimum critical collection distance is subject to the critical time of the solvent evaporation or cooling. The ejected fibre does not elongate sufficiently until it reaches the collector if the distance between the hole and the collector is relatively short. This will lead to coarser or thicker fibres. On the other hand, if the collection distance exceeds the critical value, the effect of the collection distance on the fibre morphology is negligible. To decide the critical collection distance for the PCIG, the orifice-to-collector distance was horizontally adjustment based on five levels ranging from 4 to 15 cm.

3.4 Characterisations

3.4.1 Characterisations of Solution

A Brookfield DV-III ultra-programmable rheometer (Harlow, Essex UK) was used to measure the viscosity of the five PEO-water solutions with the precision: RPM (0.01), shear rate (0.01/second) in room temperature (23.5°C to 24.2°C, humidity 38.5%) and viscosity (0.1 mPa s) at specific shear rates. Brookfield DV-III is a rotational rheometer that uses the torque of a rotating shaft immersed in the fluid being analysed to measure the absolute viscosity of the fluid to calculate flow resistance. In short, the viscosity measured by the device is a function of the resistance encountered when the spindle is rotating through the liquid being analysed under particular shear stress. In measurement, sample solution (around 5 mL) followed by a mandrel (No. 18) was placed in a cylindrical tube, and let the mandrel fully immersed in the sample to be analysed. The meter readings associated with various shear rates were recorded every 5 minutes to obtain an accurate number when the spindle stably rotated.

3.4.2 Characterisations of Fibres

3.4.2.1 Scanning Electron Microscopy

The characterisation of the morphology of the resulting nanofibres using field emission scanning electron microscopy (FE-SEM) (JEOL JSM6310F). Some key parameters of characterisation are listed as follows: 6–7 μA extract current for acquiring high resolution image; 5 kV extract voltage; 1 mm working distance for positioning the area where the photomicrograph is taken. To avoid fuzzy

micrographs caused by the floating nanofibres in the photomicrographing, all the samples (produced nanofibres) were sputtered with gold-palladium by sputter machine (Quorum Q 150R ES) for 120 seconds before inspection. Low- and high-magnification images were taken at randomly selected positions (~10) within each sample. The average fibre diameter was determined based on the average of over 100 measurements analysed from different locations of each sample by using IMAGE J software. In some cases, the produced fibres are not completely uniform along the length, but because of the high number of measurements, this does have a dramatic impact on the results. Gaussian distribution was drawn and fitted based on the measurement results of each sample.

3.4.2.2 Two-dimensional Fast Fourier Transform analysis

Anisotropic alignment of nanofibres characterised by scanning electron microscope (SEM) was evaluated using two-dimensional fast Fourier transform (2D FFT) analysis. Prior to the analysis, the uncompressed SEM images were used at the most appropriate magnification in the quest to preserve the quality. The images were cropped in a uniform size of 512 x 512 pixel and de-speckled where necessary. 2D FFT analysis converts spatial domain information into a mathematically defined frequency distribution that maps the rate of changes of pixel intensity on the original data image (Brunet-Imbault, Lemineur, Chappard, Harba, & Benhamou, 2005; Nivison‐Smith & Weiss, 2012). The resulting image also includes quantitative information about the degree of fibre orientation in the data image (grey pixels in a pattern distribution). Subsequently, the Oval Profile Plot Plug-in (William O'Connell) of Image J software was used to measure the pixel intensity over 360° by applying radial summation based on the obtained grayscale pixel distribution (Persano et al.,

2013; Shang et al., 2010). The image selected from the original radial summation data set is normalised. The line graph based on the sum of pixel intensities for each relevant acquisition angle is obtained under the normalised FFT alignment with the acquisition degree. The line graph shows the relative distribution of the regions of interest along the acquisition angle. The degrees of alignment in these graphs are reported by the shape and height of the peaks.

3.5 Process Modelling Details

3.5.1 Response Surface Methodology Implementation

In order to capture the influences of all processing variables, 120 experiments were performed at different combinations of parameters set at various levels with a fixed collection distance of 100 mm. For achieving a high degree of fit, the input data should be accurately measured and sensitive to the experimental parameters. For each experiment, more than 100 diameters were obtained from random fibres of each sample. The averaged value for each sample was accepted as one input data to fit the model. However, there were 19 combinations only delivered defective products (beaded fibres or droplets), so the results from the remaining 101 experiments were employed.

After measuring the fibre diameter associated with each parameters combination, in order to describe the behaviour of the response, it is necessary to fit the mathematical function according to the level of the study. To acquire significant regression, the main part of the experimental data variations must be fitted

(interpreted) by regression equations, and the rest will certainly be induced by the residuals. The major variation of the fitting residuals is caused by errors, in which case it is related to the random fluctuations during the measurement and the spread of the measured diameter. The spread of diameters is expected as the dominant source of the variations. To process the experimental results, the least square algorithm was performed using Mathematica. Least squares algorithm is a multiple regression analysis for exploring a mathematical model to a set of experimental data with the lowest residual. Consequently, linear and non-linear models were employed because either linear or non-linear mapping was assumed between the parameters and the fibre diameter. The goodness of the models was compared using adjusted R^2 and the Akaike information criterion (AIC) test. The adjusted R^2 depicts the total variability level that can be expected from the resultant model, adjusted from R^2 to handle more fitting variables. AIC, a model selection criterion based on information entropy, which can penalise overly complex models (with redundant variables) by increasing their AIC values. AIC is a metric in terms of model comparison, i.e. a single AIC value may not be able to give good indications of a fitted model but the difference between two does. Generally, a lower AIC value (compared to the baseline model e.g. a primary linear model) is preferred because there is a small residual between the ground truth (experimental data) and the fitted curve. Analysis of variance (ANOVA) was applied to assess the quality of the fit, since the mathematical models found after fitting the function to the data sometimes failed to describe the experimental domains in the linear model study satisfactorily. The core idea of ANOVA is to compare the variations caused by alterations in the level of the parameters with the variations in the random errors inherent in the resulting response measurements. Accordingly, the assessment of the significance

of the regression used to predict the responses and the source of the experimental variance can be achieved.

3.5.2 Exploratory Data Analysis

In this project, various techniques was used to evaluate the quality of our modelling process for example, response surface plot, residual plots, and box plots and so forth. Our goal is to assist in the experimental design, development of hypotheses and to provide an intuitive and qualitative understanding of the experimental results.

A box plot, also called box-whisker chart is way to depict digital data sets through descriptive statistical graphs. The chart uses three main components to display the interior and outliers of the data i.e. boxes, whiskers, and circles. As shown in Figure 3.2, the top, internal band and bottom of the box indicate the third (upper), second(median) and the first (lower) quartiles of the data respectively. From observing the spacing between the different parts of the box, the degree of dispersion and skewness in the data can be assessed. The top and the bottom whiskers indicate the maximum and the minimum values of inliers.

In Figure 3.3, the outer circle represents the data point whose value is greater than 1.5 times the range of the quartile. Box plot is a non-parametric technique and It displays the sample variation and does not make any assumptions about the underlying statistical distribution in the population. Box charts may look more primitive than histogram graph, but they take up less space so are useful for comparing distributions between different data groups particularly.

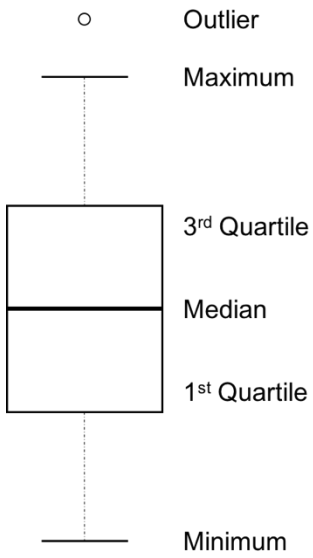

Figure 3.3 Anatomy of box-whisker chart.

3.5.3 Process Optimisations and Validations

Several optimisation algorithms were applied and compared according to their performances, including Nelder-Mead, differential evolution, simulated annealing and non-linear interior method. In this part, the selection of the range of the parameters was confined with reasonable precision. The experimental parameter sets obtained by the optimisation algorithm were evaluated through DBSCAN clustering method and further validated through a set of experiments. Their results were compared with the pre-defined diameter.

4. Generate Poly(ethylene oxide) Fibres Using Pressure Coupled Infusion Gyration

4.1 Introduction

The production of nanofibres has recently attracted much attention because of their unique characteristics, which presents them fascinating in potential applications in tissue engineering scaffolds, delivery vehicles and catalyst carriers. As compared to non-woven (randomly aligned) fibres, the superior properties of a well-aligned fibrous structure renders it in the utilisations include, the substrate for distinguishing peripheral nerves and tendon cells, composite reinforcing material and other candidate materials for the applications requiring specific orientation (Buet-Gautier & Boisse, 2001; Kumbar, James, Nukavarapu, & Laurencin, 2008; W. Liu et al., 2012; H. Y. Zhu et al., 2002). Despite the surge in interest in nanofibres, the main challenges still limit their implementation due to the lack of high yields.

In this work, a complementary spinning process was investigated called the pressure coupled infusion gyration (PCIG). Nanofibrous mats were produced at different combinations of parameters, including the infusion flow rate (500, 1000, 2000, 3000, 4000, 5000 μL min^{-1}), working gas pressure (1×10^5, 2×10^5, 3×10^5 Pa), rotational speed (10 000, 24 000, 36 000 rpm) and collection distance (4, 5, 7, 10, 15 cm). The result of the study in this chapter shows that the diameters obtained range from 60 to 850 nm with high yields.

4.2 Fibre Generation and Morphology Analysis

4.2.1 Effects of Rheological Proprieties of Solution

The effect of polymer concentration on the formation and morphology of the fabricated fibres by tuning rheological features of the solution, for example, degree of chain entanglement and viscosity, is of crucial importance for uniform fibre formation (Bassi, Gough, Zakikhani, & Downes, 2011; Shang et al., 2010). Numerous previous studies indicate that the minimum critical polymer concentration associated with the entanglement of the minimum critical chain entanglement is a prerequisite for the successful formation of uniform fibres (Bassi et al., 2011; Casper, Stephens, Tassi, Chase, & Rabolt, 2004; Humphrey, Duggan, Saha, Smith, & Käs, 2002; Luo et al., 2012). The increase in solution viscosity increases the physical chain interlock of the polymer. This interlocking of the polymer chains acts in a manner similar to chemical cross-linking and plays a dominant role in stabilising the polymer jet, which together with solvent evaporation controls the process of fibre formation. The difference may be due to the relative sliding between the polymer chains, which affects the viscoelasticity of the solution (Humphrey et al., 2002). The jet formation is largely suppressed by the polymer chain entanglement (Casper et al., 2004; Humphrey et al., 2002). Within a certain range of viscosities, as the viscosity of the polymer solution increases to a critical value, the fibre diameter also increases, and the relaxation time required for polymer jet elongation increases due to the increased amount of physical entanglement between the polymer chains. As the solution viscosity approaches to the minimum critical value, the polymer jet can still retain a shape after stretching and eventually form a beadless fibre (Badrossamay et al.,

2010; P. Gupta et al., 2005), but if the viscosity falls below a critical value, fibres having bead-on-string structure will be formed.

The intrinsic viscosity can be used to estimate the critical chain entanglement of the spinning dope. This estimation was performed using Barnes & Price's method (Barnes & Price, 1961) and is approximately 0.7 wt% of the polymer concentration of PEO. In the process of fibre generating, the extension of polymer jet can be hindered and stabilised by a higher concentration. As the combined effects (of gas blowing and centrifugal force), it has greater resistance to the stretching of the solution, thus thicker fibres were promoted. As can be seen in Appendix, Figure 1S, the average fibre diameter exhibits a steeper slope with changes in concentration and pressure levels, implying that the response is more sensitive to concentration and pressure than flow rate and speed. The formation and morphology of the resulting fibres are affected by the rheology of the fluid, such as the viscosity of the solution, which can typically be selectively adjusted by manipulating polymer concentration, temperature, and molecular properties (structure and weight). The observed shearing thinning effects in the viscosity measurements for spinning dopes are clearly shown in the Figure 4.1. The zero-shear viscosity of solutions increased from 500 to 89 500 mPa s as the polymer concentration increased from 3 to 21 wt%. The fitted power law of ($\eta = K\dot{\gamma}^{n-1}$) to the viscosity–shear rate data are listed in the Table 4.1, where η is the measured apparent viscosity, $\dot{\gamma}$ is shear rate, and K and n are constants. The associated coefficient ($R^2 \approx 1$) of multiple linear regressions indicates high multilinear correlations between the measured viscosities and shear rates, and the dimensionless flow behaviour index n indicates significant shear-thinning for more viscous solutions.

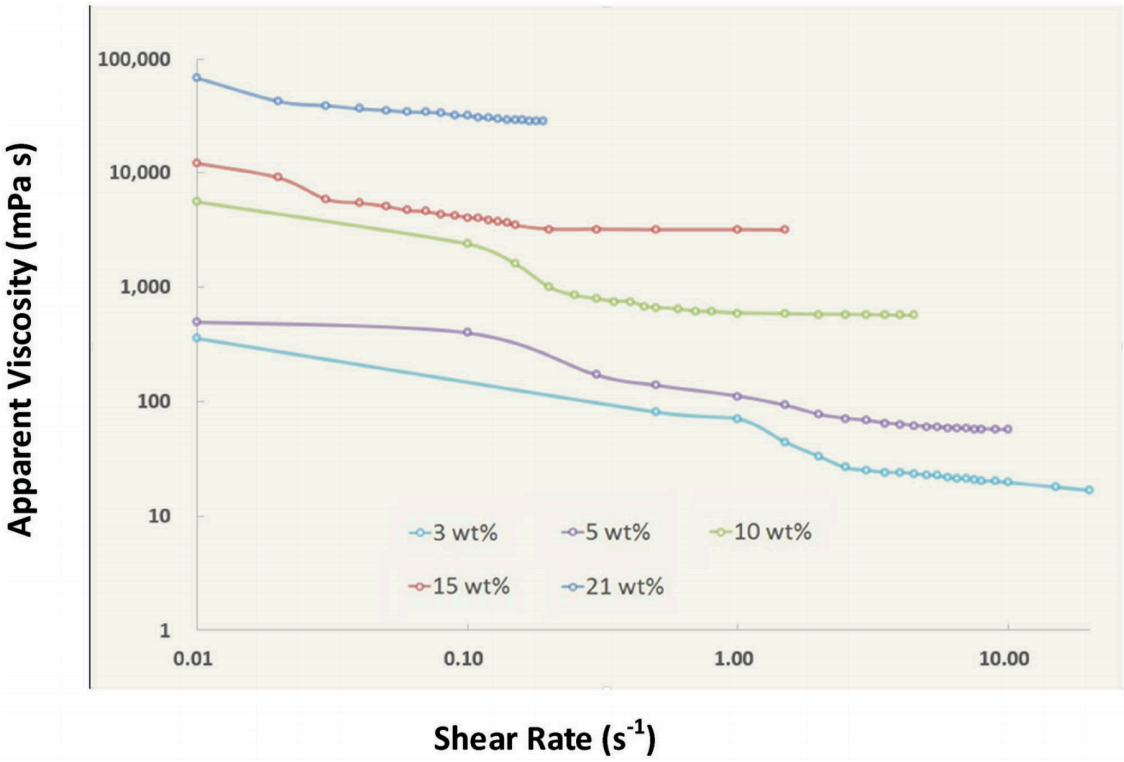

Figure 4.1 Correlation between apparent viscosity and shear rate for PEO spinning dopes.

Table 4.1 Fitted power law for apparent viscosities in Figure 4.1.

Polymer concentration (wt%)	Trend line equation	R^2	n
3	$y = 49.351x^{-0.44}$	0.9	0.56
5	$y = 111.61x^{-0.40}$	0.8	0.60
10	$y = 676.68x^{-0.34}$	0.8	0.66
15	$y = 2498.5x^{-0.26}$	0.9	0.74
21	$y = 18109x^{-0.24}$	0.9	0.76

4.2.2 Effects of Infusion Flow Rate

The combined influences of experimental parameters on fibre diameters are correlated, as shown in Figure 4.2. It was observed by experimentation that there were almost no fibrous products, but droplets were obtained by spinning 3 wt% solution. Therefore, critical chain entanglement and polymer concentration are of crucial importance (Casper et al., 2004; Mahalingam et al., 2015). The intrinsic viscosity of polymer solution can be used to estimate the critical solution concentration of chain entanglement (P. Gupta et al., 2005) and the estimation using the method of Barnes et al. (Barnes & Price, 1961), and is ≈ 0.7 wt%. Although the approximation is <3%, it is closest to the critical polymer concentration value, which may be the reason why the fibre cannot be obtained. For the rest of the solutions, fibre mats were obtained and the averaged fibre diameter increases with increasing polymer concentration and other parameters remain fixed.

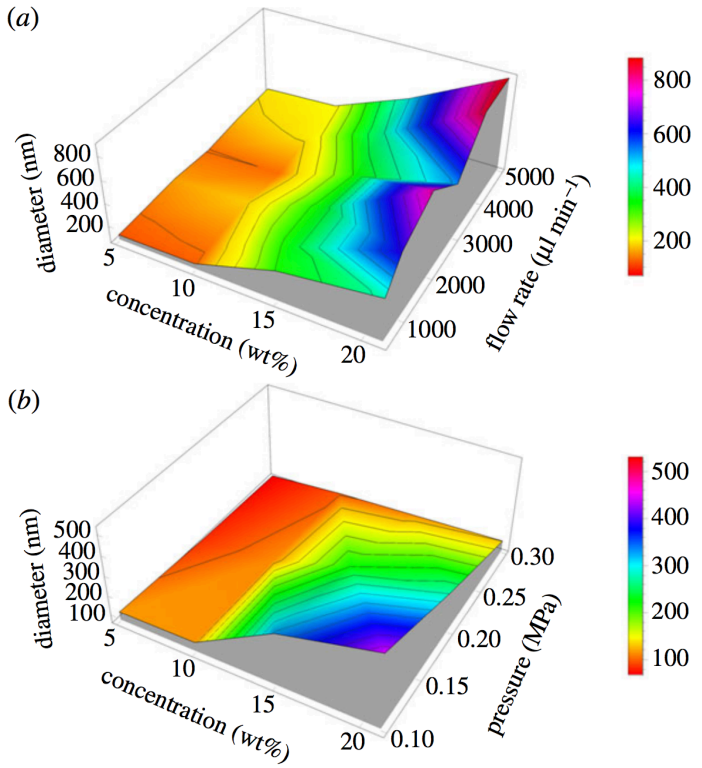

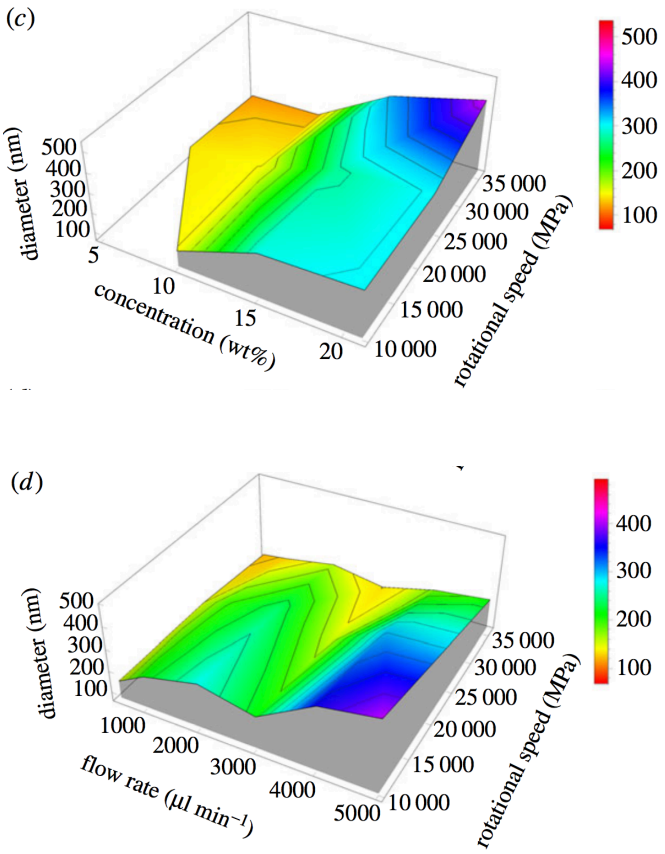

Figure 4.2 Response surface graphs exhibits effect on fibre diameters as a function of: (a) flow rate and concentration, (b) concentration and pressure, (c) concentration and rotational speed and (d) flow rate and rotational speed.

Figure 4.3 a–l shows the SEM images and the corresponding size distributions of spun fibres subjected to a fixed 36000 rpm rotational speed and 1 x 10^5 Pa pressure using 5 and 21 wt% solutions. It can be seen that, generally, wider size distribution is obtained at lower infusion rate. The obtained values of polydispersity of the 5 wt% solution were 42%, 33%, 31%, 48%, 32% and 30% at flow rate of 500–5000 μL min^{-1}. For the 21 wt% solution, the values of polydispersity were 53%, 45%, 42%, 50%, 45%, and 24% for 500–5000 μL min^{-1} flow rate. The averaged fibre diameters are listed in Table 4.2. At fixed 1 × 10^5 Pa and 36 000 rpm, increasing the infusion

rate showed a tendency to increase the average fibre size. This is attributed to the mass and volume of the solution transferred through the orifice, which is controlled by the infusion rate, thus forming a thicker polymer jet at a higher infusion rate (5000 μL min^{-1}). Moreover, a higher polymer concentration hinders evaporation of the solution, resulting in a greater transfer rate of the solution on the orifice of the container. Therefore, a higher flow rate results in a lower evaporation/relaxation time during the stretching of the polymer jet prior to collection. This results in the formation of coarser fibres. Surprisingly, it was observed that the averaged diameter first increased and then decreased at the infusion rate of 3000 μL min^{-1}, and subsequently increased as the infusion rate was further increased. The same phenomenon also occurred in some electrospinning studies (Adabi, Saber, Faridi-Majidi, & Faridbod, 2015; De Schoenmaker, Van der Schueren, Ceylan, & De Clerck, 2012; Faridi‐Majidi, Ziyadi, Naderi, & Amani, 2012). It suggests that the reduction in averaged diameter is due to a balance of the solution transfer volume through the orifice, which competes with other experimental variables, including infusion rate and pressure. Furthermore, the generation of multiple secondary jets from the initial jet may also contribute to this phenomenon because the solidified polymer solution at the orifice forces the jet to be ejected from the surrounding unsolidified surface, which results in a smaller secondary jet formation compared to the initial jet and forms thinner fibre (as seen the highlights in Figure 4S in appendix).

Table 4.2 Average fibre diameter (nm) obtained under different infusion rates, 0.1 MPa pressure and 36,000 rpm rotational speed.

Flow rate (µL min^{-1}) \ Polymer Concentration (wt%)	5	10	15	21
500	108	112	326	438
1000	118	130	357	637
2000	142	164	360	795
3000	114	116	331	538
4000	158	178	422	859
5000	177	206	473	885

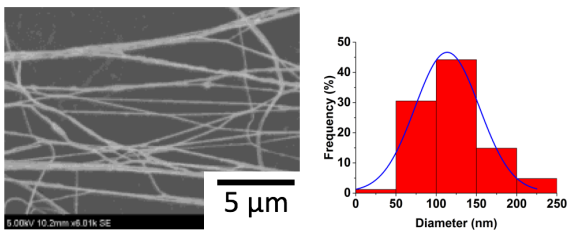

(a)

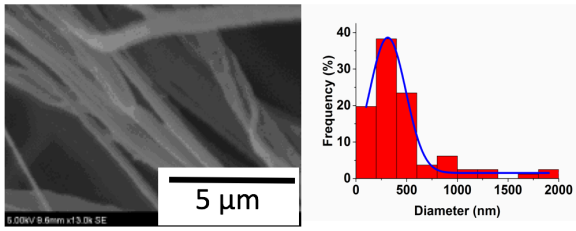

(g)

Flow rate: 500 µl/min

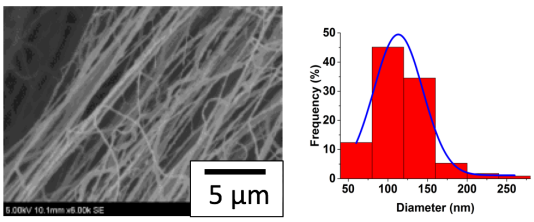

(b)

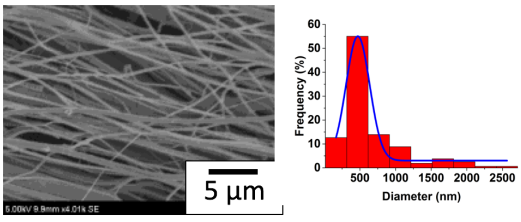

(h)

Flow rate: 1000 µl/min

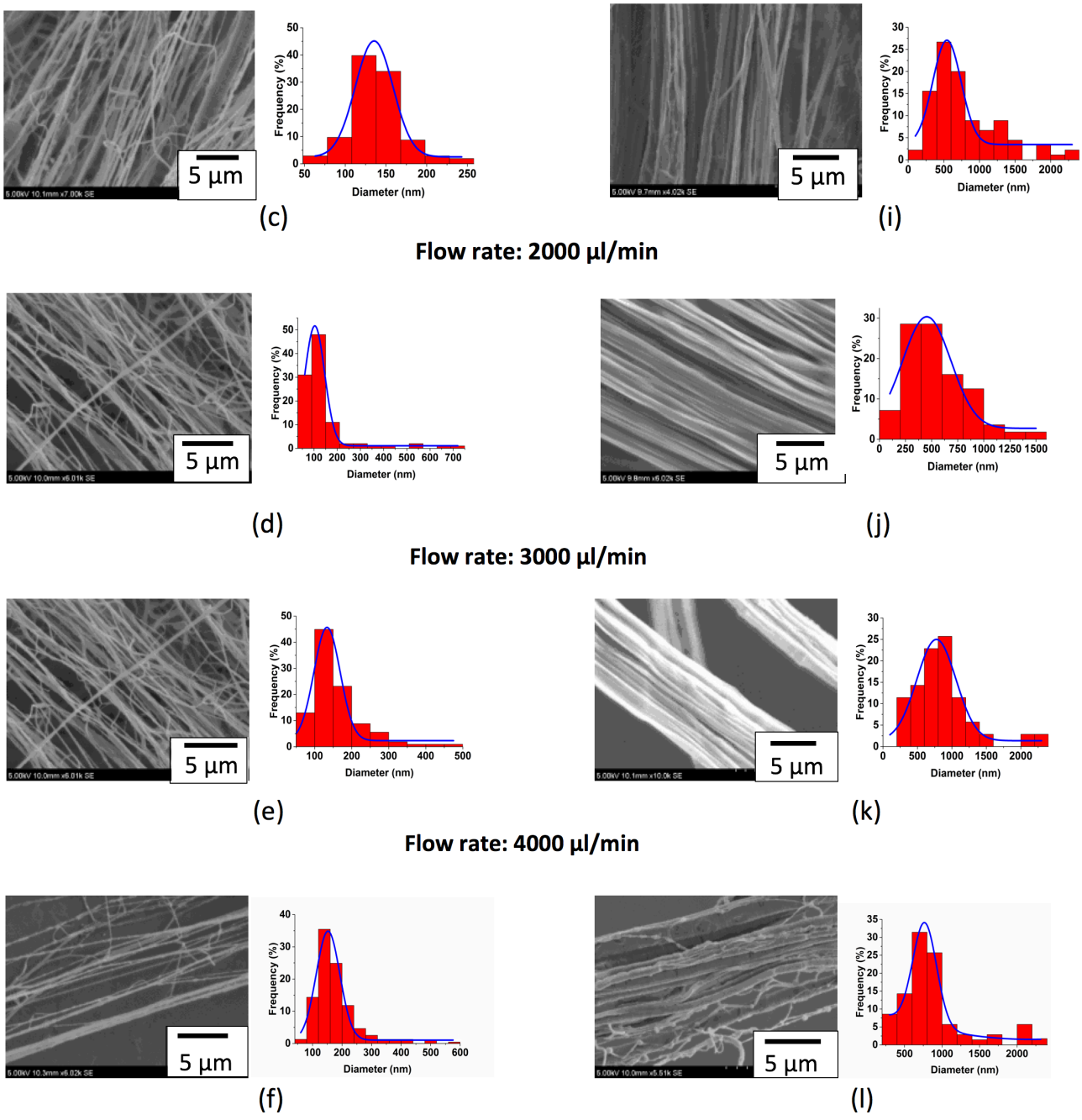

Figure 4.3 Scanning electron micrographs for the (a-f) 5 wt% and (g-l) 21 wt% of PEO fibres obtained under 500 – 5000 µl min^{-1}, 36000 rpm and 1×10^5 Pa.

4.2.3 Effects of Applied Gas Pressure

The effects of the gas pressure applied during the experimental process on the different fibre morphology were investigated by fixing the rotation speed at 36 000

rpm and performing a 5-21 wt% solution at 1 x 10^5, 2 x 10^5 and 3 x 10^5 Pa (Table 4.3). It is evident that a narrower fibre diameter distribution is usually achieved at higher applied gas pressures. The fibre diameter distributions in Figures 4.4 a-f gave 31%, 29% and 43% polydispersity values to the 10 wt% solution at 1000, 2000 and 3000 µL min^{-1} and 1 x 10^5 Pa. It also shows the values of polydispersity of 36%, 34%, and 40% for the same range of infusion rate at 3 × 10^5 Pa pressure. Table 4.3 shows the geometry of the products for four different solutions at different infusion rates and pressures. The shaded cells in Table 4.3–4.5 show that the beaded structures (grey) and droplets (black) were formed during experiments. For all spinning dopes used in this work, the tendency of the fibre diameters to decrease was observed by increasing the gas pressure. This is because the introduced gas flow enhances the composite shear force (composed of gas blowing and centrifugal force) against the surface tension in the stretched flow of the polymer jets. Thus, reducing the diameters of the ejected jets at the orifices, which enhances the formation of thinner fibres (as seen in Figure 5S of appendix). The evaporation of the solvent can be facilitated by the gas blowing that affects the relative velocity of the gas stream at the liquid-air interface in the polymer drops and solvent diffusion across polymer drops to the surface, thereby promoting fibre formation.

Table 4.3 Average fibre diameter (nm) under various pressures, infusion rates, and fixed rotational speed (36 000 rpm).

Flow rate (µL min^{-1}) \ Polymer concentration (wt%)	5	10	15	21	Working pressure (MPa)
500	108	112	326	438	0.1
	81	108	209	268	0.2
	68	92	105	121	0.3
1000	118	130	357	637	0.1
	87	114	222	291	0.2
	73	97	117	236	0.3
2000	142	164	360	795	0.1
	97	129	227	324	0.2
	90	114	127	276	0.3
3000	114	116	331	538	0.1
	83	109	203	275	0.2
	71	87	111	124	0.3
4000	158	178	422	859	0.1
		159	242	336	0.2
		130	139	294	0.3
5000	177	206	473	885	0.1
			250	347	0.2
				332	0.3

At a pressure of 2 x 10^5 Pa, uniform fibres were produced at 500–3000 µL min^{-1} for 5 wt% solution. When the flow rate increased to 4000 and 5000 µL min^{-1}, the bead fibre was obtained (as seen in Figure 4.5 a,b). The size of the beads ranged from 58–201 and 157–350 nm in width and 64–202 and 173–370 nm in length, respectively.

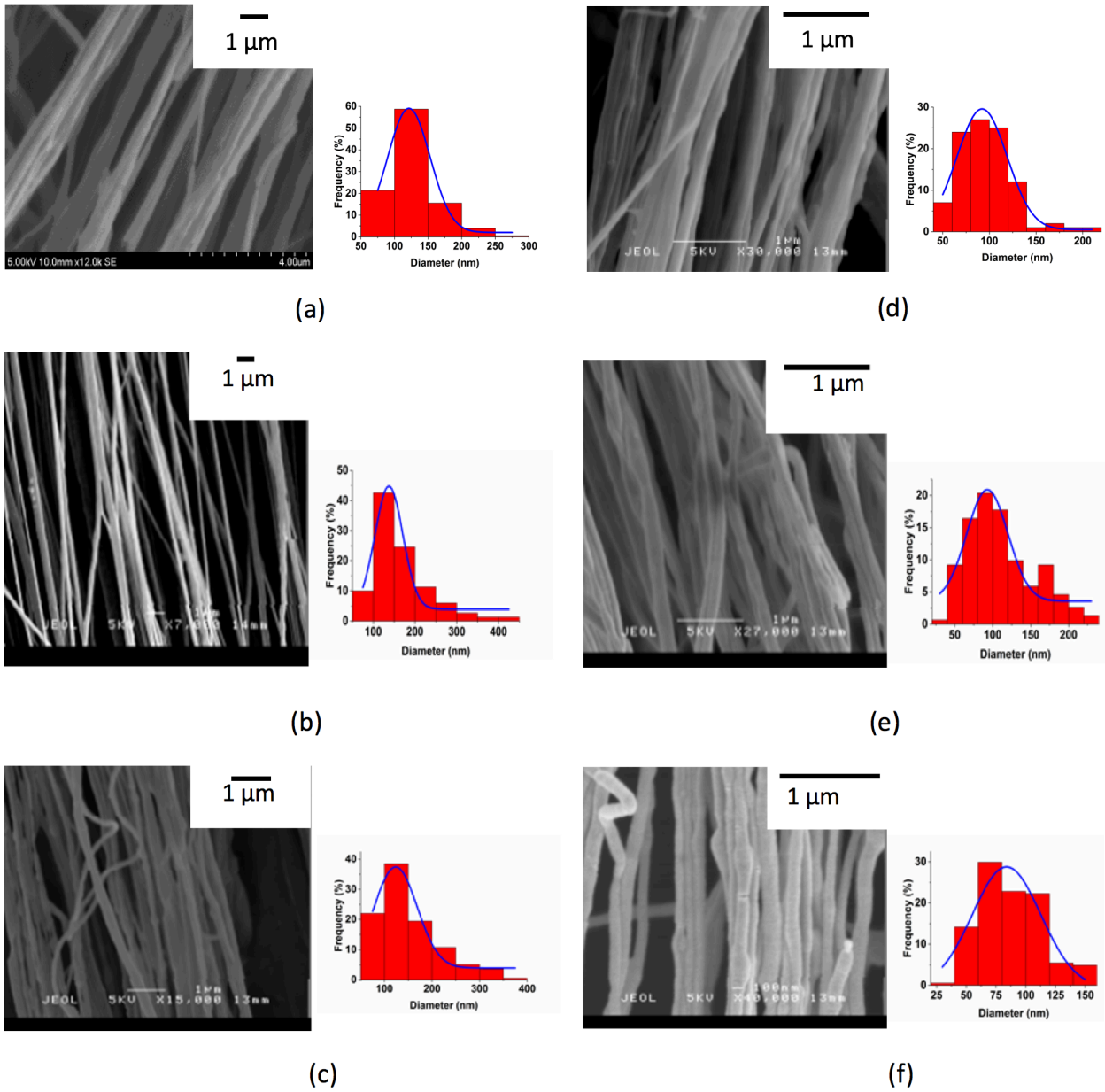

Figure 4.4 Scanning electron micrographs and the corresponding distributions of the fibre diameters for 10 wt% solution at a–c) 1 × 10^5 and d–f) 3 × 10^5 Pa, 1000, 2000, and 3000 µL min^{-1}, 36 000 rpm.

When the gas pressure was further increased to 3 × 10^5 Pa, the formation of beads was promoted at an infusion rate of 4000 µL min^{-1} and larger beads and a wider size range were obtained. There were only droplets can be collected at 5000 µL min^{-1}. The same trend was also captured for the 10 wt% solution. Figure 4.5 d shows the

formation of coarser fibres at a flow rate of 3000 μL min^{-1} and 2 x 10^5 Pa. Figure 4.5 e,g show the fibres obtained at 4000 μL min^{-1} and the pressure of 2 × 10^5 to 3 × 10^5 Pa, respectively. The beaded fibres were formed at 5000 μL min^{-1} and pressures of 2 x 10^5 and 3 x 10^5 Pa instead of droplets. The range of the length of beads is 201–400, 217–471, and 167–371, 192–373 nm in width at the gas pressure of 2 × 10^5 and 3 × 10^5 Pa, respectively.

The introduced gas intensifies the instability of the polymer jetting, which foster the formation of beads. It also enhances the solvent evaporation, which occurs in the radial direction of the jet. The experimental outcomes also show that the polymer concentration has a notable influence on the morphology of the as-spun fibre, that is, the more viscous solution stabilises the polymer jet against the centrifugal force and dynamic solution blowing, thereby promoting thicker fibre diameter and larger bead size. The form of the beads of the 15 wt% solution at 5000 μL min^{-1}, 3 × 10^5 Pa showed a spindle-like shape compared to the spherical beads produced under 5 and 10 wt% solution. The beads size was also increased, with the width of 152-368 nm and the length of 226-565 nm. When increased the polymer concentration continuously, the formation of beads eventually disappeared with 21 wt% solution. This can be attributed to the solvent evaporation was hindered by the higher polymer concentration, thus resulting in a relatively long relaxation time/evaporation time during stretching. Furthermore, there were considerable differences in the size between some of the adjacent beads as formed in several SEM images, e.g., Figure 4.5 h. It takes place due to the stretching phenomenon caused by the instability and elastic recoil occurs at the neck region formed between fibre and bead. It is probably a balance between inertia, capillarity, and viscoelasticity of the polymer solution (Chang, Demekhin, & Kalaidin, 1999; Fong, Chun, & Reneker, 1999; Oliveira, Yeh, &

McKinley, 2006; L. Wang, Shi, Liu, Secret, & Chen, 2011). The fibre produced using PCIG was much thinner than typical pressurised gyration (Mahalingam & Edirisinghe, 2013) (Table 4.4). This is because the injection rate of the solution can regulate the dynamic fluid flow as it flows through the orifice during spinning. Consequently, the spinning dopes can be used effectively, and the desired product morphology can be achieved by balancing different combinations of experimental variables and solvent evaporation. Although less obvious, the Figure 4.2 also indicates an enhanced thinning effect due to the higher shear force provided by gas blowing compared to infusion gyration. Table 4.5 lists all the details of the comparison of the produced fibre sizes. The infusion also has the benefit of avoiding loss of pre-fill material during initial acceleration before achieving the desired rotational speed.

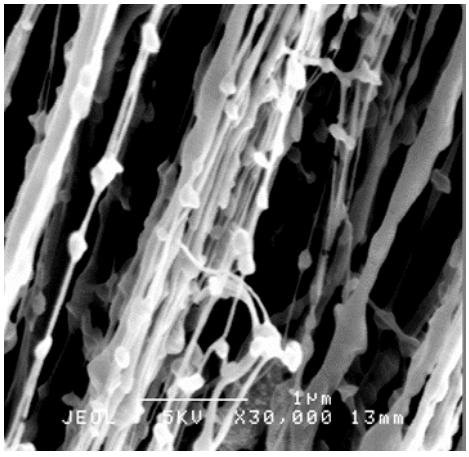

(a)

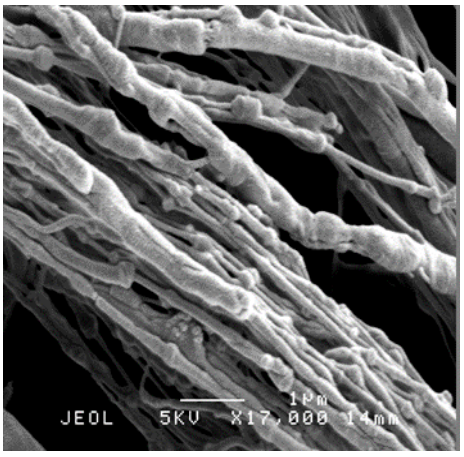

(f)

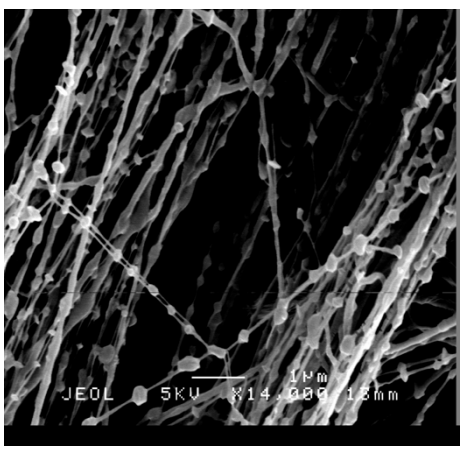

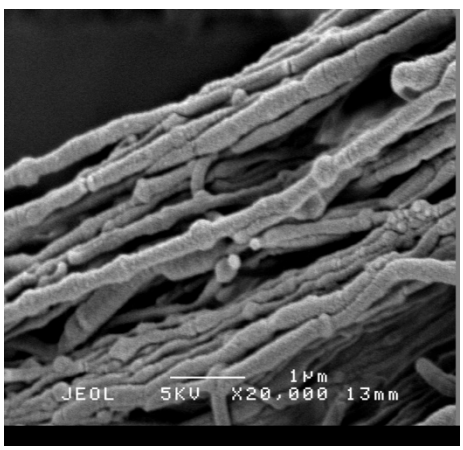

(b) (g)

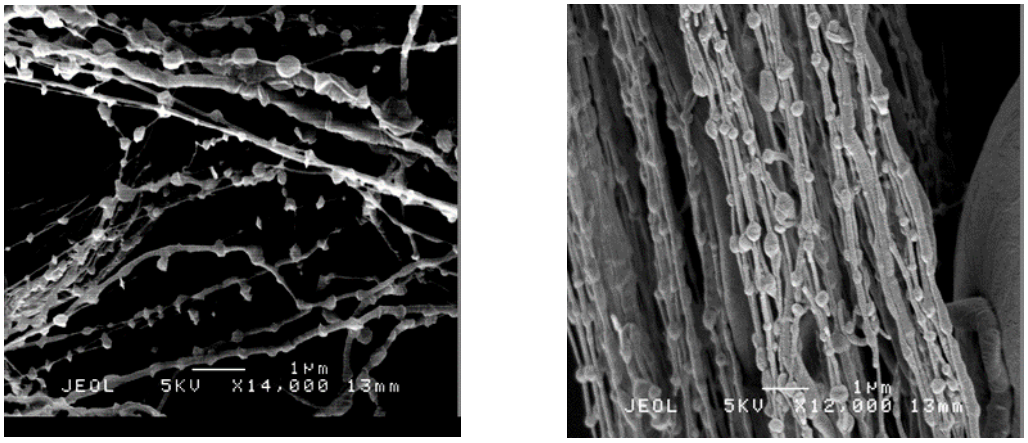

(c) (h)

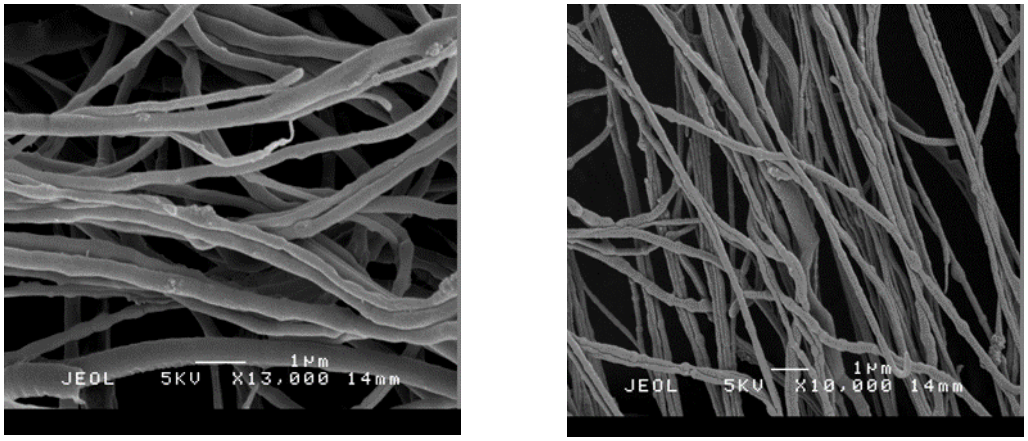

(d) (i)

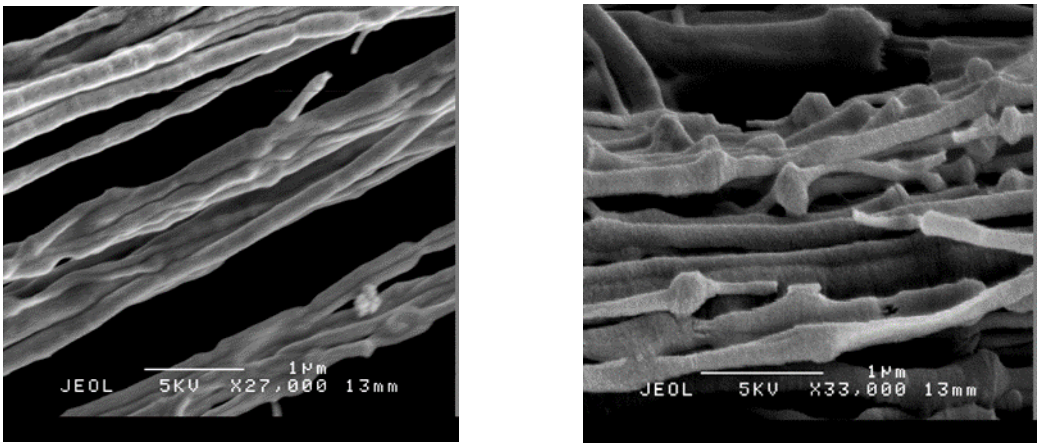

(e) (j)

Figure 4.5 Scanning electron micrographs of different morphologies produced at 36 000 rpm speed: a,b) beaded fibres of 5 wt% solution under 2 × 10^5 Pa pressure, 4000–5000 µL min^{-1} flow rate; c) beaded fibres of 5 wt% solution

under 3 × 10^5 Pa pressure, 4000 µL min^{-1} flow rate; d,e) coarser fibres of 10 wt% solution under 2 × 10^5 Pa pressure, 3000–4000 µL min^{-1} flow rate; f,h) beaded fibres of 10 wt% solution under 2 × 10^5 and 3 × 10^5 pressure, 5000 µL min^{-1} flow rate; g) coarser fibres of 10 wt% solution under 3 × 10^5 Pa pressure, 4000 µL min^{-1} flow rate; i) uniform fibres of 15 wt% solution under 3 × 10^5 Pa pressure, 4000 µL min^{-1} flow rate; j) beaded fibres of 15 wt% solution at 3 × 10^5 Pa pressure, 5000 µL min^{-1} flow rate.

Table 4.4 Comparison of the results of PCIG and typical pressurised gyration, the black cells indicates the formation of droplets.

Polymer concentration (wt%) / Flow rate (µL min^{-1})	5	5 (PG)[a]	15	15 (PG)	21	21 (PG)	WP[b] (MPa)	RS[c] (rpm)
500	108	210	326	518	438	970	0.1	36000
	81	175	209	250	268	400	0.2	36000
	68	106	105	135	121	141	0.3	36000
	131		260	560	302	600	0.2	24000
			276		303	692	0.2	10000
1000	118		357		637		0.1	36000
	87		222		291		0.2	36000
	73		117		236		0.3	36000
	164		286		303		0.2	24000
			314		327		0.2	10000
2000	142		360		795		0.1	36000
	97		227		324		0.2	36000
	90		127		276		0.3	36000
	223		291		309		0.2	24000
			315		333		0.2	10000
3000	114		331		538		0.1	36000
	83		203		275		0.2	36000
	71		111		124		0.3	36000
			160		297		0.2	24000
			213		314		0.2	10000

a) PG = pressurised gyration; b) WP = working pressure; c) RS = rotational speed

4.2.4 Effects of Rotational Speed

Similar to pressurised gyration, the fundamental governing forces in PCIG include dynamic fluid flow and centrifugal force. The combination of solution blowing and centrifugal force against the surface tension results in deformation of polymer droplets, thereby enabling the formation of fibres from the container orifice. Compared to the shear stress in non-Newtonian fluid, there is normal stress, and the stress acts in the same direction as the deformation plane. Thus, a high speed of rotation will enhance the deformation of the solution by increasing the centrifugal effect. Enhanced gas blowing induced by high pressure would reinforce the thinning effect and also promotes solvent evaporation that takes place along the radial direction of spinning. The change in rotational speed during rotation affect the final fibre size. The viscosity of the solution can vary during spinning due to the temperature gradient that occurs as the solvent evaporates through the polymer jet. Mahalingam and Edirisinghe pointed out that the time constant of the shear forces applied on the polymer jets during the rotation will decrease as the speed increases (Mahalingam & Edirisinghe, 2013). Additionally, the time constant of shearing forces governs the responses of polymer chains, that is, lower the time constant the shorter the viscous response of polymer solution, and vice versa. Thus, a minimum rotational speed that can result in a sufficient viscous response enables the production of nanofibres at lower polymer concentrations.

To determine the correlation between rotational speed and fibre morphology, all polymer solutions were spun at a fixed of 2 x 10^5 Pa pressure, and the infusion rate and rotational speed were varied. Table 4.5 shows the determined relationship between polymer concentration, infusion rate, rotational speed and the obtained

diameter. For comparison, the results obtained at 36,000 rpm and 2 x 10^5 Pa are also listed here. Overall, increasing the speed of rotation accelerates the stretching of the polymer jet, which reduces the diameter of the polymer jet at the orifice of the vessel and allows for thinner fibres (Figure 4.6 a–f). The 15 wt% solution gave 276 and 260 nm of mean diameter at 10 000 and 24 000 rpm at the same infusion rate of 500 µL min^{-1}, and 399 and 376 nm of mean diameter at 10 000 and 24 000 rpm at a same infusion rate of 5000 µL min^{-1}. It can be clearly seen that, in general, narrower size distribution is obtained at higher rotational speed. For the 15 wt% solution, with a fixed 2 × 10^5 Pa pressure in spinning, the obtained polydispersity was 40%, 37% and 47% for lower rotational speed (10 000 rpm) and infusion rates of 1000, 2000 and 3000 µL min^{-1}, respectively. At higher rotational speed (36 000 rpm) with the same range of infusion rates, the polydispersity was 36%, 34% and 45%. It is noteworthy that, with a typical pressurised gyration method, the 5 wt% solution cannot be spun at 2 × 10^5 Pa pressure and ≤24 000 rpm rotational speed. However, PCIG is capable of spinning these and this is also true for the 15 wt% solution spun at 2 × 10^5 Pa and 10 000 rpm. This is due to the mass transfer of the polymer solution through the orifice by controlling the infusion.

Table 4.5 Average fibre diameters (nm) under various rotational speeds and infusion rates, in all cases pressure was fixed at 2 × 10^5 Pa.

Polymer Concentration (wt %) / Flow rate (µL min^{-1})	5	10	10 (IG[a] at 0 pressure)	15	21	RS[b] (rpm)
500	[redacted]	147		276	303	**10000**
	131	140		260	302	**24000**
	81	108	117	209	268	**36000**
1000	[redacted]	212		314	327	**10000**

	164	192		286	303	**24000**
	87	114	161	222	291	**36000**
2000		266		315	333	**10000**
	223	231		291	309	**24000**
	97	129	170	227	324	**36000**
3000		213		278	314	**10000**
		160		269	297	**24000**
	83	109	132	203	275	**36000**
4000				365	370	**10000**
		292		344	358	**24000**
		159	190	242	336	**36000**
5000				399	466	**10000**
				376	448	**24000**
			216	250	347	**36000**

a) IG = infusion gyration; b) RS = rotational speed

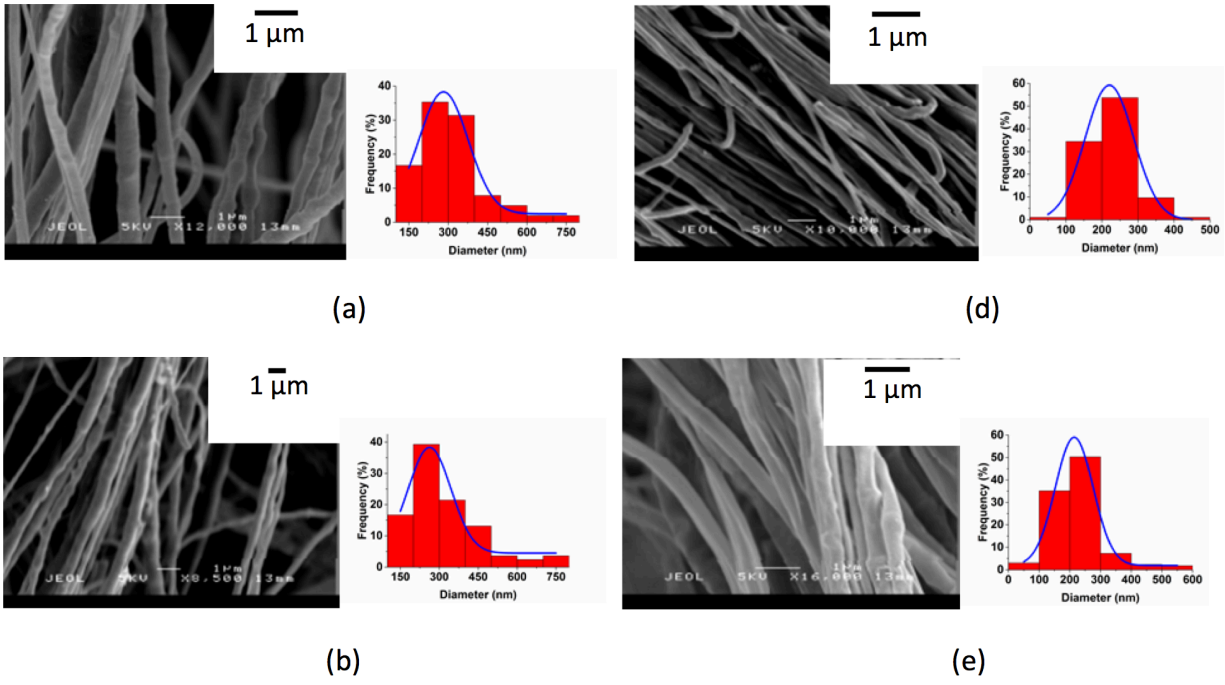

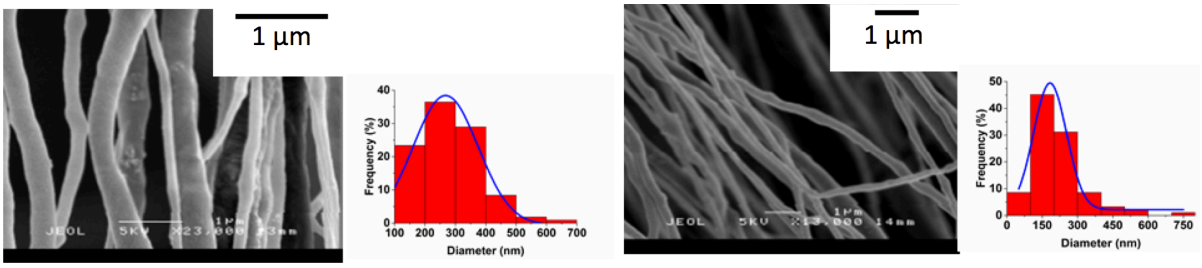

(c) (f)

Figure 4.6 Scanning electron micrographs and the corresponding distributions of the fibre diameters for 15 solution under 2 × 10^5 Pa, 1000, 2000, and 3000 µL min^{-1}, and different rotational speed: a–c) 10 000 and d–f) 36 000 rpm.

4.2.5 Effects of Collection Distance

In PCIG, the appropriate distance for fibre collection is determined based on the diameter required for the spiral trajectory of the polymer jet, the type of collector and the duration of solvent evaporation. The travel time of the polymer jet is completely dependent on the distance of the orifice from the collector. The selective minimum critical distance between the orifice and the collector is related to the critical time for solvent evaporation. If the collection distance is relatively short, the fibre does not elongate sufficiently before it reaches the collector. This will promote thicker fibres. On the other hand, as previously mentioned, if the critical value is exceeded, the effect of the collection distance on the fibre morphology is negligible.

Figure 4.7 a–e shows the SEM images and the corresponding sizes distribution of nanofibres produced under different collection distances: 4, 5, 7, 10 and 15 cm, with an infusion rate of 5000 µL min^{-1}, 1 ×10^5 Pa pressure and 36 000 rpm rotational speed. The results here show that a narrower fibre diameter distributions were obtained at longer collection distances. For instance, the polydispersity index was 29%, 25%, and 29% for 7–15 cm collection distance, respectively. The polydispersity

index for 4–5 cm was 33% and 31%, respectively. In Figure 4.7 a, it is obviously seen that the fibres of 21 wt% solution (1118 nm of mean diameter) collected at a 4 cm orifices-to-collector distance were severely aggregated and formed joint blocks. This is due to the fact that the PCIG process produces polymer webs in a very short time and the insufficient solvent evaporation of polymer jets before they reach the collector, causing the accumulation of fibres in the vicinity. These aggregations were slightly improved at 5 cm, and the density of "joint fibres" was lowered, and the average fibre diameter was 1088 nm.

When the collection distance was increased to 7 and 10 cm, the morphologies of produced fibres were improved, and finer fibres without joint blocks were obtained (Figure 4.7 c,d). The fibre diameters produced at 7 and 10 cm were measured and found to have insignificant differences, i.e. 898 and 900 nm, respectively. When the collection distance was continuously increased to 15 cm, the average fibre diameter showed a negligible change (888 nm). It elucidates the need to have a minimum collection distance in PCIG to allow sufficient evaporation of the solvent in the polymer jet. The results indicate that the solvent has evaporated sufficiently at a distance of 7 cm and further evaporation of the solvent of the jet is due to the collector distance extending to 10 and 15 cm. Compared with other experimental parameters, the influence of the collection distances more than 7 cm has little effect on the morphology of the product. In the case of the 21 wt% PEO solution, an attempt was made to reduce the distance to 3 cm, but there was no fibrous product collected except for the polymer droplets.

With an appropriate collection distance, the yield of produced fibres depends on the interaction of the three process control parameters—infusion rate, gas pressure, and

rotational speed. The previous works on infusion rotation and pressurised gyration have shown how the yield of fibres will change when the infusion flow rate and gas pressure change independently at a rotational speed (Mahalingam & Edirisinghe, 2013; Siqi Zhang et al., 2015). In particular, for the infusion gyration with varying flow rates, significant improvement in yield was not seen until a flow rate of 5000 μL min^{-1}. Many phenomena occur in the vessel prior to the fibres were ejected from the orifices. Previous studies on pressurised gyration (Mahalingam & Edirisinghe, 2013) and ongoing studies on PCIG have suggested that fibres are produced by the rupture of a blob of the polymer jet at the orifice. Moreover, the rotation can include the formation of a vortex in the vessel and evaporation of the solvent resulting in a more concentrated solution from which the fibres evolve. Thus, the flow may not be continuous relative to the initial polymer solution fed to the vessel. The above scenarios are currently being investigated in our laboratory.

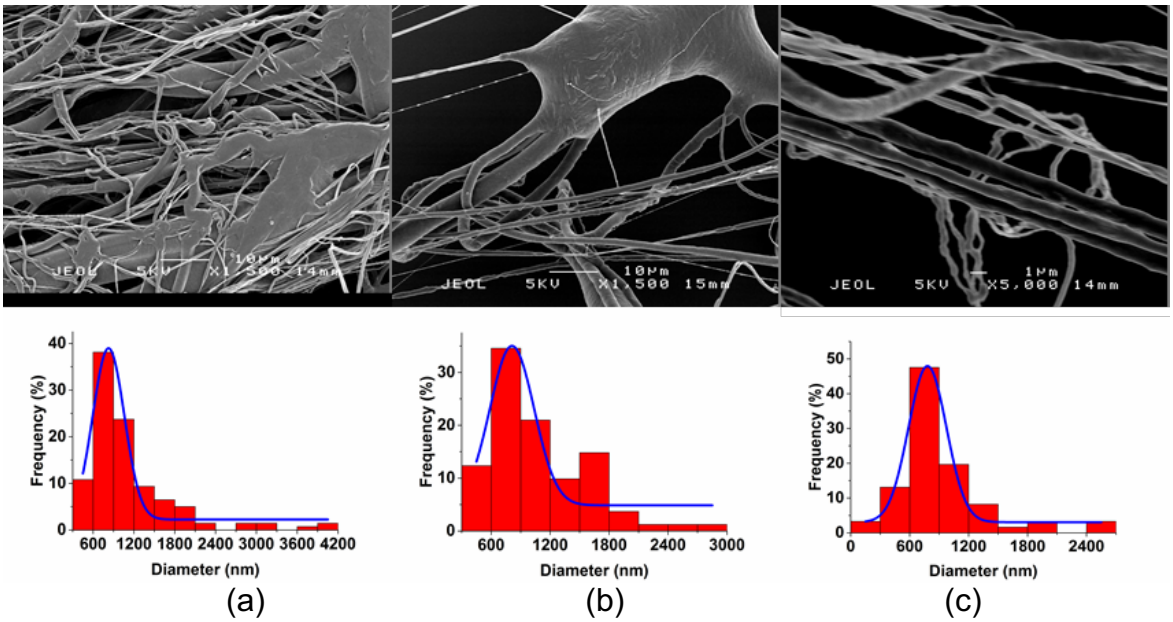

(a) (b) (c)

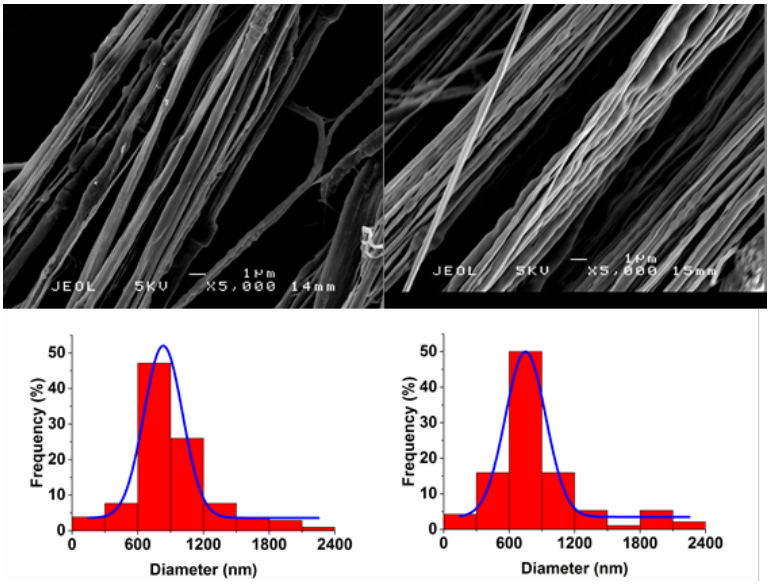

Figure 4.7 Scanning electron micrographs and the corresponding diameter distributions of the fibres obtained under 21 wt% concentration, 5000 µL min^{-1} flow rate, 1 × 10^5 Pa pressure, 36 000 rpm speed and various collection distances of a) 4, b) 5, c) 7, d) 10, and e) 15 cm.

4.2.6 Analysis of Fibre Anisotropy

Fast Fourier transform (FFT) analysis of SEM images was used to characterise the degrees of fibre alignment and anisotropy of scaffold. The influence of various processing parameters on product morphology can be evaluated by FFT to assign a relative alignment number to the produced matrix. FFT is a fast way to evaluate fibre alignment in tissue engineering materials (Ayres et al., 2006; Brunet-Imbault et al., 2005). In this analysis, the degree of fibre alignment in a line graph is depicted by the height and shape of the peak compiled statistics from FFT plot (Figure 4.8). More uniform orientation of fibres will give more spindle-like shape in the frequency map, which is related to the overall orientation of the fibres in the original SEM image.

The more spiked peaks, that is, the intensities of the pixel detected in the frequency map, such as Figure 4.8 c, are almost unidirectional. The more randomly oriented fibres will provide a circular shape at the centre of the plotted frequency map and provide broader peaks at relatively lower amplitudes (Ayres et al., 2006). The broader peaks with low amplitude were generally caused by background noise, and in most cases, the distinct sharp spikes at single specific values were due to edge effects, which can be manually removed. The PCIG product spun from a starting concentration of 10 wt% exhibit clear evidence of alignment at any infusion flow rate, gas pressure and rotational speed, hence give rise to bead-on-string structures or fibres.

The Statistical analysis in section of **4.2.3** and **4.2.4** shows that fibres produced from 10 and 15 wt% solutions at a fixed 36 000 rpm speed have uniform fibre alignment and smooth surface roughness (Figures 4.4 and 4.6). The peak height and width of the curve both indicate the relative degree of the alignment, and the position of the peak indicates the principal axis of the fibre orientation in the associated SEM image. Higher magnitudes of peaks were obtained at higher infusion rates, as indicated in Figures 4.8 a-h. When the infusion rate was increased from 2000 to 5000 μL min^{-1} at a fixed rotational speed and a pressure of 1 x 10^5 Pa, the 10 wt% solution gave alignment of 0.17–2.20 units and the 15 wt% solution gave alignment of 1.60–3.02 units. In addition, for both solutions, relative loose alignment were obtained at 3000 μL min^{-1} (Figure 4.8 b,f,j). This is due to the fibre mat consisting of thicker fibres is more stable so it retains the structure during transport and before arriving at the collector. As seen in Figure 4.8 j, broad and shoulder-like peaks with nearly the same amplitude can be induced and show a portion of fibres deviated from the overall orientation of the produced mat. Comparing the sub-peaks due to noise and

background information in other plots, the relatively wide sub-peaks in Figure 4.8 i can be ascribed to the random elements. For example, the beads produced by 15 wt% solution in the image are indicated at a frequency of pixel intensity, which can be specified to any angle within 360°(Gaharwar, Nikkhah, Sant, & Khademhosseini, 2014).

The widths of peaks of the fibres produced by 10 and 15 wt% solutions decreased sequentially as a function of infusion rate and rotation speed but increased as the gas pressure increased. The relative higher pressure such as 3 x 10^5 Pa gave lower values of alignment (1.35–2.07) and broader peaks (Figure 4.8 i–l).

Moreover, the produced fibres of 15 wt% solution were relatively well-aligned in contrast to the fibres of 10 wt% solution. This is ascribed to the more viscous solution, which is easier to spin in comparison with diluted solutions such as 10 wt%.

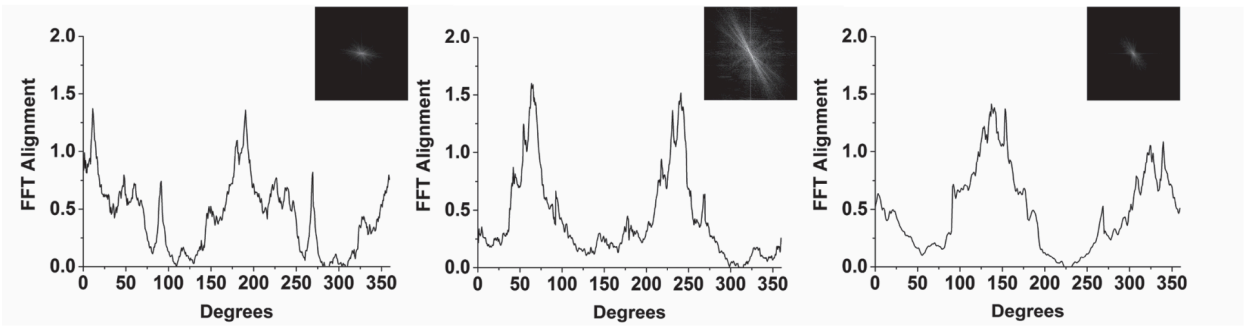

(a) (e) (i)

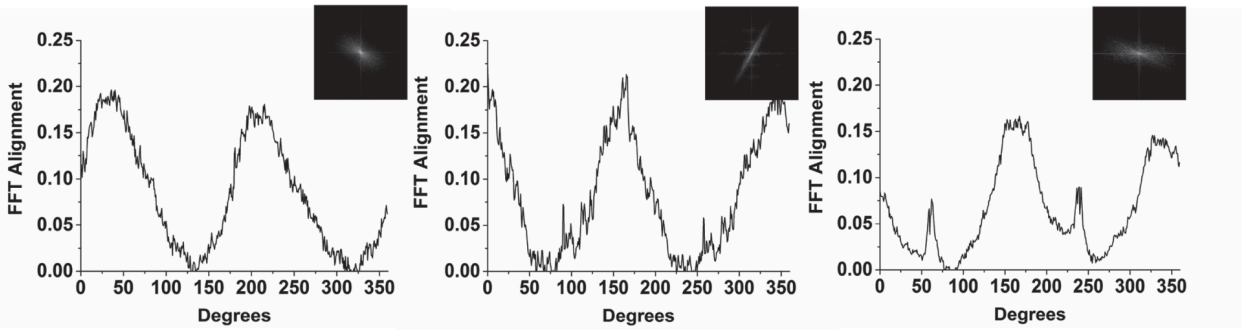

(b) (f) (j)

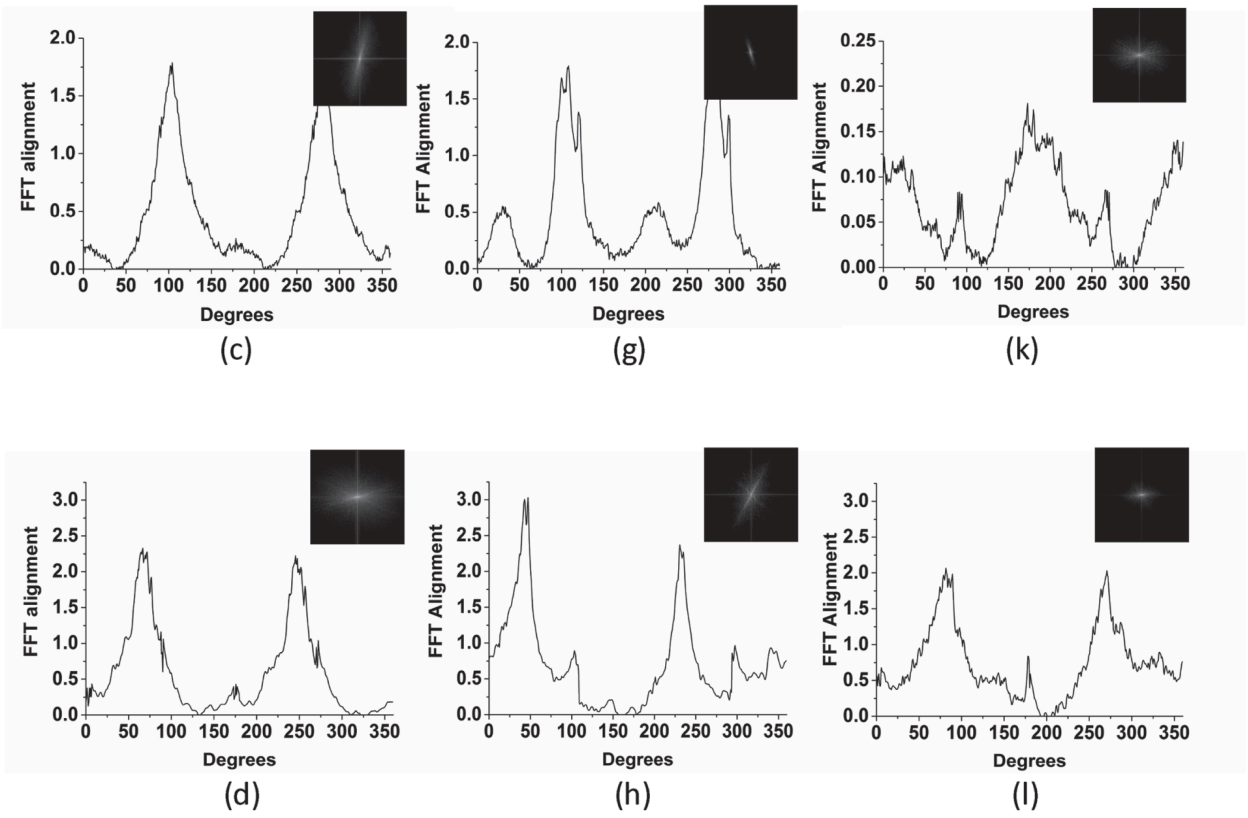

Figure 4.8 Two-dimensional fast Fourier transform alignment analysis of fibres obtained under: a–d) 10 wt% solution, e–h) 15 wt% solution with 2000, 3000, 4000, and 5000 μL min^{-1} infusion rate, 1 × 10^5 Pa pressure and 36 000 rpm rotational speed; i–l) 15 wt% solution at 3 × 10^5 Pa, the same range of infusion rate and the rotational speed as in (e)–(h).

4.3 Summary

In this part of work, an efficient gyration-based system for fabricating polymeric fibrous structures has been introduced. Poly(ethylene oxide) was used as the model material, and this study indicates the use of this new method to prepare polymer nanofibres and nanofibre mats at different experimental parameters, including, infusion flow rate, gas pressure, rotational speed and collection distance. The

anisotropy and morphology of the produced fibres were characterised using two-dimensional fast Fourier transform analysis and scanning electron microscope. A correlation between experimental variables and the product morphology was also established. The polymeric nanofibre mats were obtained at a 10 cm collection distance, and the diameters of fibres spanned in 50-850 nm. A minimum collection distance i.e. 7 cm is identified for obtain uniform fibre morphology using PCIG spinning with PEO-water system. The results of anisotropy analysis indicated that a relative higher concentration (such as 15 wt%) or infusion flow rate (such as 5000 μL min^{-1}) plays a role of stabilising the solution jetting process, and resulted in well-aligned fibrous structure. However, the increases of applied pressure acted in a reversed direction, the loosely aligned fibres were produced at a higher pressure (e.g. 3×10^5 Pa). To obtain a comprehensive understanding about the spinning process and optimise the experimental region of PCIG, empirical models were developed to disclose the internal relationships between the experimental parameters and produced fibres, and discussed in the next chapter.

5. Empirical Modelling of Pressure Coupled Infusion Gyration process

5.1 Introduction

In Chapter 4, the performance of pressure coupled infusion gyration process under different combinations of experimental parameters was investigated, with PEO-water as the model solution. To meet particular requirement of some applications that are sensitive to the surface area (as determined by fibre diameter), the fibre preparation should be confined by a given diameter. However, PCIG is simultaneously affected by the parameters respectively and interactively. Thus, designing a suitable experimental procedure is complicated to obtain the desired diameter, and using a large number of tests to produce fibres having the desired diameter would be time-consuming and expensive. Researchers have attempted to find scientific and predictive tools in a variety of processes.

The Response Surface Method (RSM) is a convenient method that requires less experimentation than other methods to build an effective model. It gives good performances if the data have good statistical distribution in the experimental design (Carley et al., 2004). Based on the training data, RSM uses statistical methods, taking into account the combined influences of several parameters in the fitting procedures. It fits an empirical model (linear/non-linear) to estimate the functional relevance and the response of the modelling process. The resulting model can then be evaluated and further used as a tool for predicting and optimising the independent

variable settings to reduce residuals (Bezerra et al., 2008). In some past research works, RSM has been used to optimise material properties and processing in different fields, such as, thermoplastic elastomers (Acherjee, Misra, Bose, & Venkadeshwaran, 2009), diamond-like carbon films (Wächter & Cordery, 1999) and poly(vinyl alcohol) hydrogel (Y. Zheng, Liu, & Wang, 2011).

In this work, RSM was used to achieve an insight of the (individual and combinational) effect of the processing parameters and a quantitative basis of the relationships between obtained fibre diameter and experimental parameters. Using mathematical models to describe the effects of experimental parameters allows us to systematically and straightforwardly represent the impact parameters and predict the response of the experiments with different combinations of parameters. Besides, due to the benefits of RSM, the number of experiments used to test the effects of all possible combinations of parameters on obtained fibre diameter can be reduced. In this part of the work, the PCIG experimental process was modelled in linear and non-linear fit formats to allow for optimisation of processing parameters in the next phase. The adjusted R^2 and Akaike Information Standards (AIC) were used as the evaluation metrics to assess the success of the fitted model.

5.2 Design of Experiments

In this study, different fibre diameter was obtained by adjusting four experimental variables: PEO solution concentration, infusion (flow) rate, gas pressure and rotational speed. Their relations to the fibre diameter were studied using RSM. All

other conditions, such as humidity (38.5%) and ambient temperature (25 °C) were fixed during the experiments.

Based on the work in the Chapter 4, The appropriate collection distance was found to be determined by the diameter of the spiral trajectory required for the polymer jet and the duration of the solvent evaporation. Insufficient collection distance will result in the formation of coarser fibres or polymer joint that did not have sufficient elongation before arriving the collector. On the other side, if the selected collection distance exceeded the critical value required for solvent evaporation, the influence of a further increase in distance was observed as negligible. In this part, only the fibre groups obtained at the collection distance of 100 mm was used.

The concentration of spinning dope is one of the important determinants in the fibre generation process (denoted as c). It selectively influences the formation and morphology of spun fibres by adjusting the fluid properties of the spinning dope, such as viscosity, surface tension and chain entanglement, which is essentials for the fibre formation. A relative higher polymer concentration can help stabilise the polymer jets during processing, which is critical for the formation of thicker fibres. The results of 5, 10, 15, and 21 wt % were used in this part of work, due to the 3 wt% solution cannot give us enough observable fibre samples in PCIG system.

The infusion rate (denoted as f) influences the hydrostatic pressure at the orifices and also controls the mass and volume of the spinning dope passing through the orifice. Higher infusion rates will shorten the polymer jets stretching/solvent evaporation time, thereby promoting thicker and multiple jets formed during spinning, as discussed in detail in Chapter 4. In the modelling works, six levels (500, 1000, 2000, 3000, 4000, and 5000 μL/min) of infusion rate were selected.

The effects of applied gas pressure were investigated by conducting experiments at three pressure levels (1 x 10^5, 2 x 10^5, 3 x 10^5 Pa). At any fixed polymer concentration, high pressure would result in a decrease in fibre diameter. This is ascribed to the gas blowing enhanced thinning effect so that evaporation of the solvent occurring in the radial direction of the polymer jets can also be promoted by higher applied pressure. Furthermore, enhanced gas blowing would intensify the jets instability at the orifice, which would encourage the formation of beaded or "defective" fibres.

The combination of solution blowing and centrifugal force acts on the surface tension of the solution and give rise to the deformation of the polymer droplet, thus enabling fibres to be formed from the container orifice. This deformation will be facilitated by an increased centrifugal force due to a higher rotational speed. The presence of non-Newtonian fluid shear stress acts against normal stress and causes the deformation and tension in the same direction as the planar effect (Mahalingam & Edirisinghe, 2013). Therefore, the stretching in the polymer jet is further encouraged by the centrifugal force. Three levels (10 000, 24 000, and 36 000 rpm) of rotational speed were selected in this study.

5.3 Model Fitting of Fibre Spinning Process

The goal of this part of work is to find an optimal model to describe the relationship between fibre diameter ($\boldsymbol{y}$) and selective experimental parameters, i.e. $\boldsymbol{y} = \boldsymbol{f_d}(\boldsymbol{c}, \boldsymbol{p}, \boldsymbol{f}, \boldsymbol{g})$, including {polymer concentration (c), infusion rate (f), pressure (p) and speed (g)}; The introduction of physical frameworks in the model building stage may

help us gain more insight into the mechanism of the fibre formation process and improve the goodness of the fittings. For example, Merado et al. studied a basic theoretical rotary spinning frame to characterise the production regimes of poly(lactic acid) nanofibres (Mellado et al., 2011), and the model can be denoted as

$$r^{1.09\pm0.05} \sim \frac{aU^{\frac{1}{2}}v^{\frac{1}{2}}}{R_c^{\frac{3}{2}}\Omega} \tag{5.1}$$

where *r* is the radius of the spun fibre; *a* is the initial jet radius; *U* is the mass velocity; *v* is the kinematic viscosity (calculated by extensional viscosity/density of solution); R_c is the collection distance (90–180 mm in their work); *Ω* is the rotational speed (ranging from 4000 to 37 000 rpm).

The experimental parameters of PCIG influence the average fibre diameters to different extents. The corresponding effects of each parameter on the fibre diameter are given in Figure 1S of the Appendix, which indicates that infusion rate (mass velocity) and polymer concentration (viscosity) have positive correlations with fibre diameter. Equation 5.1 also gives us some guidance, and the minimum critical rotational speed (Ω_c) of fibre formation is expressed by Eq. 5.2.

$$\Omega_c \sim \frac{\rho {R_c}^2 \sigma^2}{a^2}\mu^{-3} \tag{5.2}$$

where *ρ*, *σ, μ* is the density, surface tension and extensional viscosity of the spinning dope, respectively. The Eq. 5.2 implies that the speed can be considered to have a power-law relationship with other parameters. Nevertheless, the framework of Mellado et al. did not incorporate additional injected flow and gas pressure. Therefore, it is suggested to use some mathematical expressions, taking into

account the trend of diameter changes shown in Figure 2S, including a quartic relationship between the infusion rate and diameter, linear dependences are suggested with respect to concentration and pressure, and include a power. The fitted model is presented as Eq. 5.3, which adjusted R^2 is 95.1%m, and the AIC value is 1142.35. The relevant coefficients of the model are shown in Table 5.1. A typical example of the residual plot and the distribution of the fitted residuals (as seen in Figure 5.1) show that the residuals of the data points associated with the current model vary widely (the distribution details and all other residual plots are given in Table 2S and Figure 2S). Therefore, this fitted model is not sufficient to make precise inferences of the data behaviour within the experimental scope of the work. It is worth noting that the pressure term in the Eq. 5.3 has an extremely large power but is multiplied by a very small constant ($\beta_7 \ll \beta_8$; as seen in Table 5.1). The pressure term can be rewritten in this limit in the form of the exponential function for the future improvements of fittings, i.e., $e^{\beta p}$.

$$\boldsymbol{y = \beta_0\,(1 + \beta_1\, f + \beta_2\, f^2 + \beta_3\, f^3 + \beta_4\, f^4)\,(1 + \beta_5 c)^{\beta_6}(1 + \beta_7\, p)^{\beta_8}\, g^{\beta_9}} \qquad (5.3)$$

Table 5.1 Estimated coefficients for non-linear model derived from the work of Mellado et al.: Eq. 5.3.

Estimated coefficient($\boldsymbol{\beta_n}$)	
β_0	-1.89×10^{-11}
β_1	-4.11×10^{-10}
β_2	2.74×10^{-7}
β_3	-7003.52
β_4	0.59
β_5	0.09

β_6	2.08
β_7	-2.58×10^{-5}
β_8	213588
β_9	-0.11

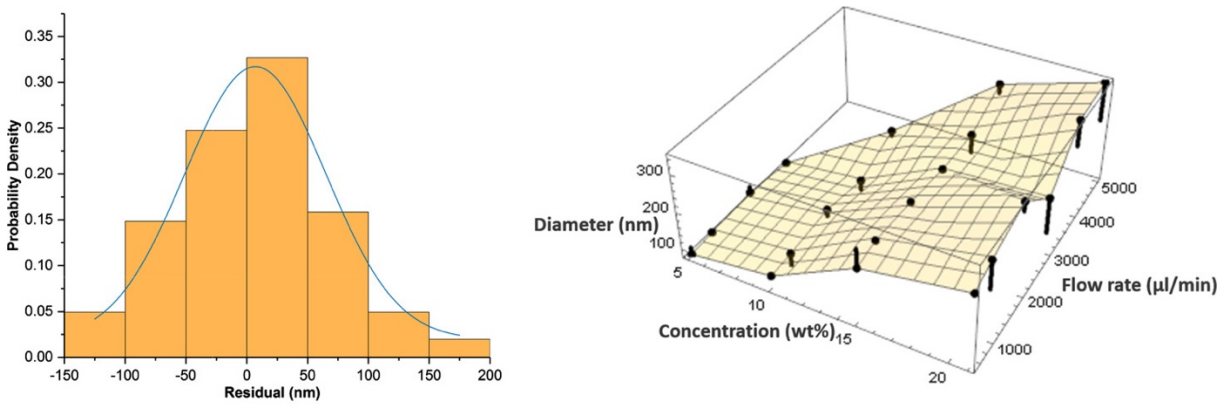

Figure 5.1 Residual distribution (a) and typical residual plot (b) of the Eq. 5.3 (varying the polymer concentration and infusion flow rate, at a fixed 2 × 10^5 Pa pressure and 36 000 rpm rotational speed).

PCIG is a more complex process than the given frame of basic rotary spinning, and it is not clear how the interactions between different parameters, such as how the concentration influences viscosity through evaporation and how the pressure influences solution flow. Hence, it is necessary to develop empirical models based on the experimental data to establish quantitative relationships between combined parameters and fibre diameter.

5.3.1 Linear Model Fitting

The general equations for response *y* (average diameter) are developed by exploring fitting to multivariate experimental data using all possible polynomial functions of the variables up to a given order. The fitted polynomial functions also can readily be

extended to higher orders. Initially, For the comparison reason, the polynomial functions were confined to linear combinations with independent variables (experimental parameters) up to second-order forms, which provide a certain degree of complexity to the models, but did not take into account the trend of the experimental results that shown in Figure 1S. This results could be used as another baseline to compare with the results of the following updates, apart from the results of Mellado et al.'s work as given in Eq. 5.3. A default 95% confidence interval was used for all fitting trials in this work. In the first fitting test, the functions that include all possible combinations of variables up to quadratic form were checked, which involves examining 16 384 non-repeating combinations in 1 048 576. Additionally, effects of pressure and rotational speed act within an inverse relationship to the fibre diameter, as shown in Figure 1S c,d. Therefore, it suggests that the polynomials in the inverse pressure term and rotational speed term may be better (using 1/*g* and 1/*p* rather than *g* and *p* in the model fit), which is consistent with the work of Mellado et al. in Eq. 5.1. Eq. 5.4 shows the best-fitted quadratic equation for the average fibre diameter. The most complex quadratic model is presented as Eq. 5.5, which provided a slightly worse adjusted R^2 of 85.9% and a higher value of AIC 1125.10. The results of analysis of variance for Eq. 5.5 are listed in Table 1S.

$$\boldsymbol{y = \beta_0 - \beta_1 c + \beta_2 c^2 + \beta_3 cf - \beta_4 c/g - \beta_5 / (g)^2 - \beta_6/p + \beta_7 c/p + \beta_8 f/p + \beta_9/(gp)} \quad (5.4)$$

$$\boldsymbol{y = \beta_0 - \beta_1 c + \beta_2 c^2 - \beta_3 f + \beta_4 cf + \beta_5 f^2 + \beta_6 /g - \beta_7 c/g + \beta_8 f/g - \beta_9 /(g)^2 - \beta_{10} /p + \beta_{11} c/p + \beta_{12} f/p + \beta_{13} /(gp) + \beta_{14} /(p)^2} \quad (5.5)$$

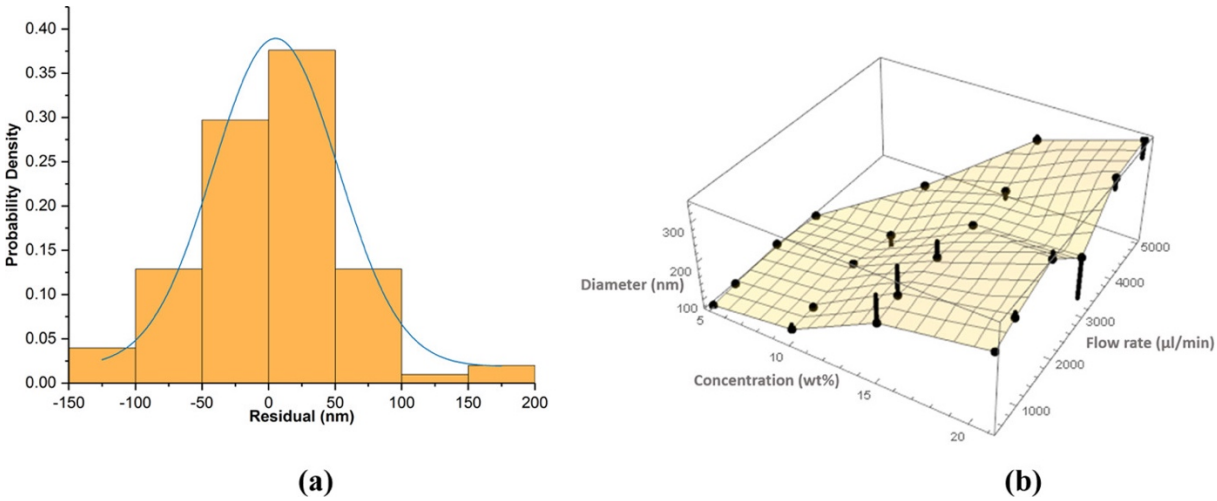

Figure 5.2 Residual distribution (a) and typical residual plot (b) of the linear model: Eq. 5.4 (varying the polymer concentration and infusion flow rate, under a fixed pressure of 2 × 10^5 Pa and a rotational speed of 36 000 rpm).

Table 5.2 ANOVA table of the first linear model：Eq. 5.4.

	Estimated coefficient (β_n)	SS	F-Statistic	P-Value
1	290.32			
c	-25.42	1.04×10^{6}	307.35	6.32×10^{-31}
c^2	0.68	8020.60	2.37	0.13
cf	9.63×10^{-4}	1.43×10^{5}	42.19	4.31×10^{-9}
c/g	-1.09×10^{5}	2880.85	0.85	0.36
$1/g^2$	-6.84×10^{10}	3.49×10^{4}	10.30	1.83×10^{-3}
1/p	-95.09	4.60×10^{5}	136.04	9.19×10^{-20}
c/p	4.37	3.78×10^{5}	111.57	1.71×10^{-17}
f/p	1.81×10^{-3}	7031.03	2.08	0.15
1/gp	2.32×10^{6}	7.70×10^{4}	22.74	7.00×10^{-6}

It is noteworthy that an overly complex expression may not perform as well as optimal expression; This is due to both adjusted R^2 and AIC penalise the use of too many free parameters that do not actually help to improve (interpret) the original

variance. Figure 5.2 a presents the distribution of data point fit residuals, and Figure 5.2 b is a typical diagram showing how well the function fits each data point. The ANOVA analysis of Eq. 5.4 as indicates in Table 5.2, where SS stands for the sum of the squared observation deviations, which can be dismembered in the sum of the squares of regressions and the sum of the squares due to the model residual. P-values represent the level of impact significances of the coefficients on the fibre diameter. As a 95% confidence interval is used, if the p-value is greater than 0.05, the related variable has little influence on the average fibre diameter on the basis of the related fitting model, and it also discloses the quality of the current model. Table 5.2 shows that the regression coefficients of c^2, *c/g, f/p* are pretty random, and the obtained adjusted R^2 and AIC were 86.2% and 1118.93, which indicates that the quality of the current fit is not very good, as to find the major explanatory variables, the adjusted R^2 should be $\geqslant$95%.

To improve the model, visual inspection of the experimental data and the residual map details helps to generate valuable guidance on the suitability of the model by indicating a response that indicates the kind of terms that need to be added to the model for improvement. Figure 1S b suggests that the flow parameter has a bimodal dependence on the infusion rate (f), so entering the fourth power entering of f would help improve our model.

$$\boldsymbol{y = \beta_0 - \beta_1 c + \beta_2 c^2 + \beta_3 f - \beta_4 f^2 + \beta_5 cf^2 + \beta_6 f^3 - \beta_7 f^4 - \beta_8 c/g - \beta_9 /(g)^2 - \beta_{10} /p + \beta_{11} c/p + \beta_{12} f/p + \beta_{13} /(gp)^2} \quad (5.6)$$

Equation 5.6 shows the linear model with the best AIC out of 524 287 non-repeating combinations of experimental variables required to test after the infusion rate was

pushed to the fourth position. It gave a slightly better result of adjusted R^2 of 88.1% and an AIC of 1107.22. The ANOVA table, as shown in Table 5.3, clearly shows that the given coefficient estimation of the correlation model was more precise than the previous linear model, and the estimations of the coefficients were more significant than the first two at 95% confidence intervals. Besides, the terms of polymer concentration, the pressure^{-1} (inverse pressure), the infusion rate and the interaction term between the concentration and the pressure^{-1} have been shown to have significant effects on the average diameter of the obtained fibres. The addition of the fourth power term in *f* has certainly helped to improve the fitting performance. As seen in the Figure 5.3, the fitting performance was certainly improved by the added fourth power term in *f* and the residuals were effectively reduced.

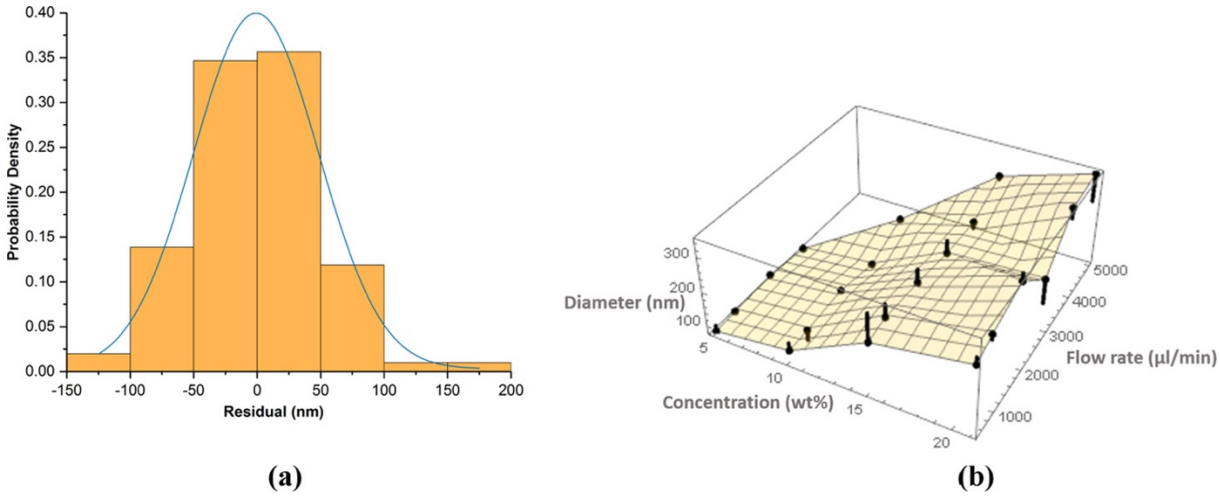

Figure 5.3 Residual distribution (a) and typical residual plot (b) of the fourth power incorporated linear model: Eq. 5.6 (varying the polymer concentration and infusion flow rate, at a fixed pressure of 2×10^5 Pa and a rotational speed of 36 000 rpm).

Table 5.3 ANOVA table of the linear model with QUARTIC form of flow rate, inversed pressure and rotational speed parameters: Eq. 5.6.

	Estimated coefficient (β_n)	SS	F-Statistic	P-Value
1	137.99			
c	23.45	1.04×10^{6}	357.17	1.51×10^{-32}
c^2	0.63	8020.60	2.75	0.10
f	0.40	1.21×10^{5}	41.66	5.94×10^{-9}
f^2	2.86×10^{-4}	1.95×10^{4}	6.70	0.01
cf^2	2.92×10^{-7}	1.81×10^{4}	6.23	0.01
f^3	7.17×10^{-8}	3.16×10^{4}	10.85	1.00×10^{-3}
f^4	6.03×10^{-12}	1.76×10^{4}	6.04	0.02
c/g	1.06×10^{5}	2550.71	0.88	0.35
g^2	6.95×10^{-10}	3.35×10^{4}	11.51	1.00×10^{-3}
1/p	97.10	4.59×10^{5}	157.71	3.07×10^{-21}
c/p	4.30	3.67×10^{5}	125.86	1.38×10^{-18}
f/p	2.80×10^{-3}	1.04×10^{4}	3.56	0.06
g/p	2.34×10^{-6}	7.67×10^{4}	26.33	1.73×10^{-6}

The goodness of fit of the applied linear test did not give an adequate adjusted of R^2 (up to 88.1%), and it is well known that more parameters used in the function will help improve the precision of fitting. However, the number of fitting parameters in the Eq. 5.6 has already reached 14, but the observed measurements of fibre diameters gave only 101 data. Continuously increasing the complexity of the fit function may result in overfitting because its excessive parameters will make the equation less generalised. It was edging above the rule of thumb of no more than 1 fitting parameter per 10 measurements. Therefore, it suggests that non-linear models can be used to update the model, as fewer parameters can be used to achieve more complex functions. In addition, the estimate of the error variance (also known as the estimation variance) is the basis for showing the variance of the fitted parameters. It

is based on the sum of the squared errors and takes into account the number of parameters used in the fit, which can be used to measure the quality of the fit.

5.3.2 Non-linear Model Fitting

In contrast with the linear-quadratic model, which has a general type of function that consists of simple multiplication and summation between parameters up to the second-order, the forms of the non-linear model are almost infinite, such as the incorporation of exponential functions and trigonometric functions. Testing all possible combinations of non-linear components is computationally expensive. Therefore, each of the sub-graphs in Figure 1S was inspected based on our experience and all the empirical components were combined together to perform a non-linear fit. As can be seen from Figure 1S a, a similar quadratic form applies to the dependence on *f* under all conditions. The dependency on *f* from the last best-fit linear function was picked up here because it produces a noticeable improvement after changing the parameter of *f* to a fourth power, while the others remain linear. The non-linear response function that was fitted by the non-linear method based on the Levenberg–Marquardt algorithm is as determined with the best AIC in equation Eq. 5.7 (see Table 5.4 for the estimated coefficients).

$$\boldsymbol{y = \beta_0 \left(1 + \beta_1 f + \beta_2 f^2 + \beta_3 f^3 + \beta_4 f^4\right)\left(1 + \beta_5 c\right)\left(1 + \beta_6 / p\right)\left(1 + \beta_7 / g\right)} \qquad (5.7)$$

Table 5.4 Estimated coefficients of first non-linear model: Eq. 5.7.

Estimated coefficient($\boldsymbol{\beta_n}$)	
$\boldsymbol{\beta_0}$	2.59×10^{-10}
$\boldsymbol{\beta_1}$	0.028
$\boldsymbol{\beta_2}$	-1.85×10^{-5}

β_3	4.75×10^{-9}
β_4	-4.04×10^{-13}
β_5	5.88×10^{8}
β_6	1.09
β_7	3648.73

The residual distribution and a typical residual plot are shown in Figure 5.4. The adjusted R^2 obtained was 94.9%, and the lowest achievable AIC was 1145.23. This is much better in terms of adjusted R^2, and the obtained estimate of variance is 4470.67. However, a higher AIC was given in this trial. This is because the adjusted R^2 would be increased only if the new fitting parameter improves the model over the expected, and only eight coefficients was used in the current trial, which is less than the coefficients in any previous model in the linear fitting work. Hence, this AIC value is perhaps acceptable. It is crucial to find suitable terms that accurately describe the trends of training data, as well as the optimal compromise between the low AIC values and possible high adjustment R^2 that need to be achieved.

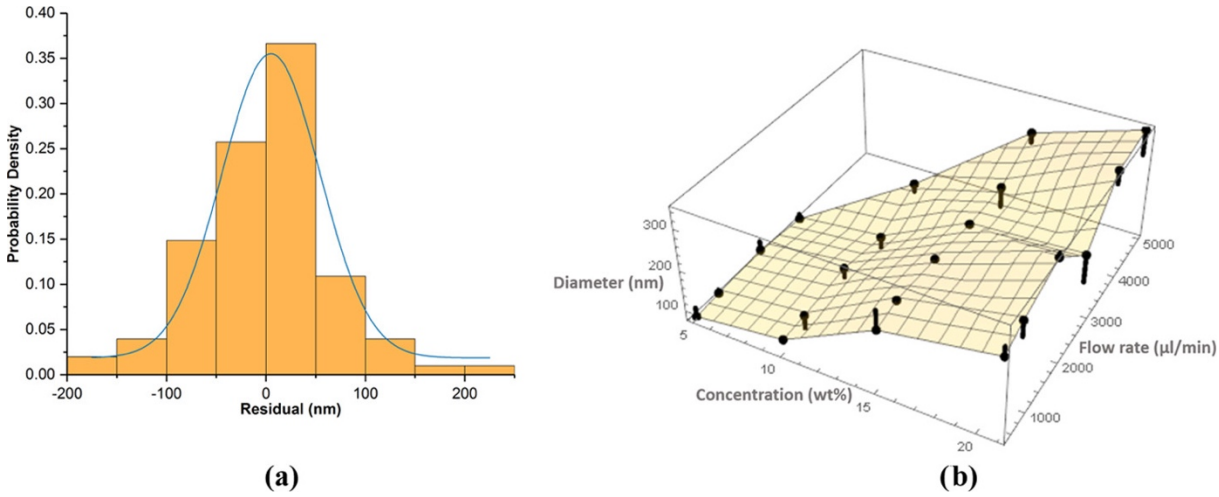

Figure 5.4 Residual distribution (a) and typical residual plot (b) of the first non-linear model: Eq. 5.7 (varying the polymer concentration and infusion rate, under a fixed pressure of 2×10^5 Pa and a rotational speed of 36 000 rpm).

As reported by the fitting result of the linear model of Equation 5.6 (which AIC is 1107.22), the more suitable quadratic parameters for polymer concentration and rotational speed are suggested, but linearly dependent on the terms of pressure. Hence, the order of *c* and *g* were increased up to second and the optimised function as given in Eq. 5.8 (the estimations of coefficients are given in Table 5.5)

$$y = \beta_0(1 + \beta_1 f + \beta_2 f^2 + \beta_3 f^3 + \beta_4 f^4)(1 + \beta_5 c + \beta_6 c^2)(1 + \beta_7 /p)(1 + \beta_8 /g + \beta_9 /(g)^2) \quad (5.8)$$

Table 5.5 Estimated coefficients of the non-linear model with quadratic concentration and rotational speed terms, but linear pressure terms: Eq. 5.8.

Estimated coefficient(β_n)	
β_0	0.04
β_1	0.02
β_2	-1.29×10^{-5}
β_3	3.28×10^{-9}
β_4	-2.74×10^{-13}
β_5	0.12
β_6	9.17×10^{-3}
β_7	2.96
β_8	223977
β_9	-1.59×10^{9}

The obtained the adjusted R^2 from this trial was 95.5%, and the value of AIC was decreased to 1132.72. It can be concluded from Figure 5.5 that by providing a lower residual, the quadratic sub-function depends on the terms of polymer concentration and the rotational speed and the linear pressure term can help improve the fitting performance (with an estimated variance of 3880.16)

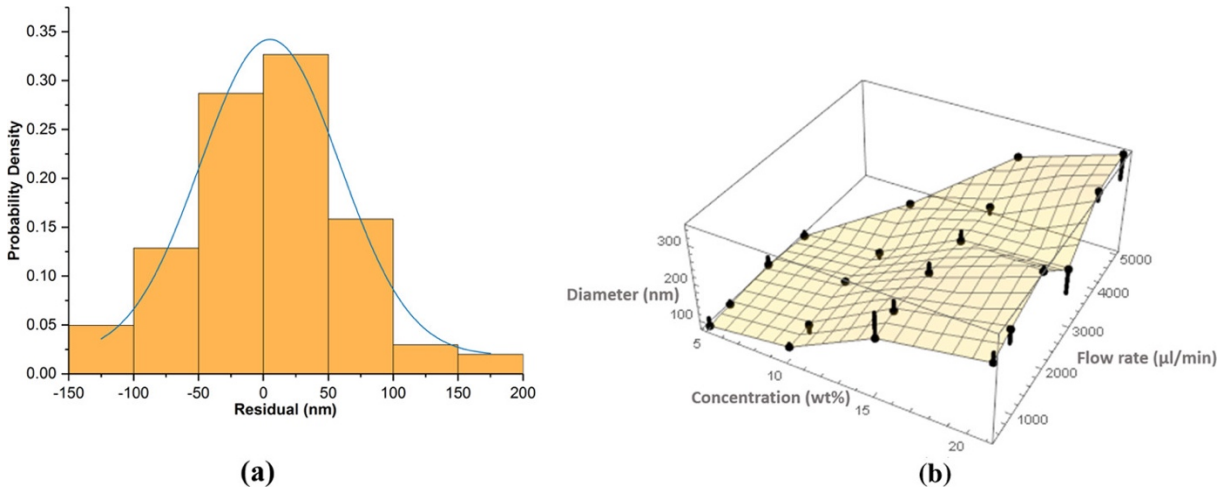

Figure 5.5 Residual distribution (a) and typical residual plot (b) of the non-linear model with quadratic terms of concentration and rotational speed but linear terms of pressure: Eq. 5.8 (varying the polymer concentration and infusion rate, at a fixed pressure of 2×10^5 Pa and a rotational speed of 36 000 rpm).

To further improve the model, it is necessary to find out which part of the function space gives the most significant deviation as well as residuals. In Figure 5.6, the Box-Whisker charts shows the effects of fluctuations in the experimental parameters by using the fractional residual as part of the average diameter. They represent the median, 25% and 75% quartiles, and the upper and lower limits as a function of polymer concentration, infusion rate, pressure and speed. It should be noted that pressure and speed are in their inverse forms here.

Figure 5.6 also shows that the deviations of the residuals are random, and some are very large. Higher polymer concentrations and lower rotational speed produce relatively lower deviations. It suggests that there may be systematic relationships that exist in the deviations of pressure and rotational speed. The random deviation is probably because the robust process of PCIG is a quantitative adjustment method

for fabricating nanofibres, but with a compromise of the precise control of the parameters affecting the average fibre diameter.

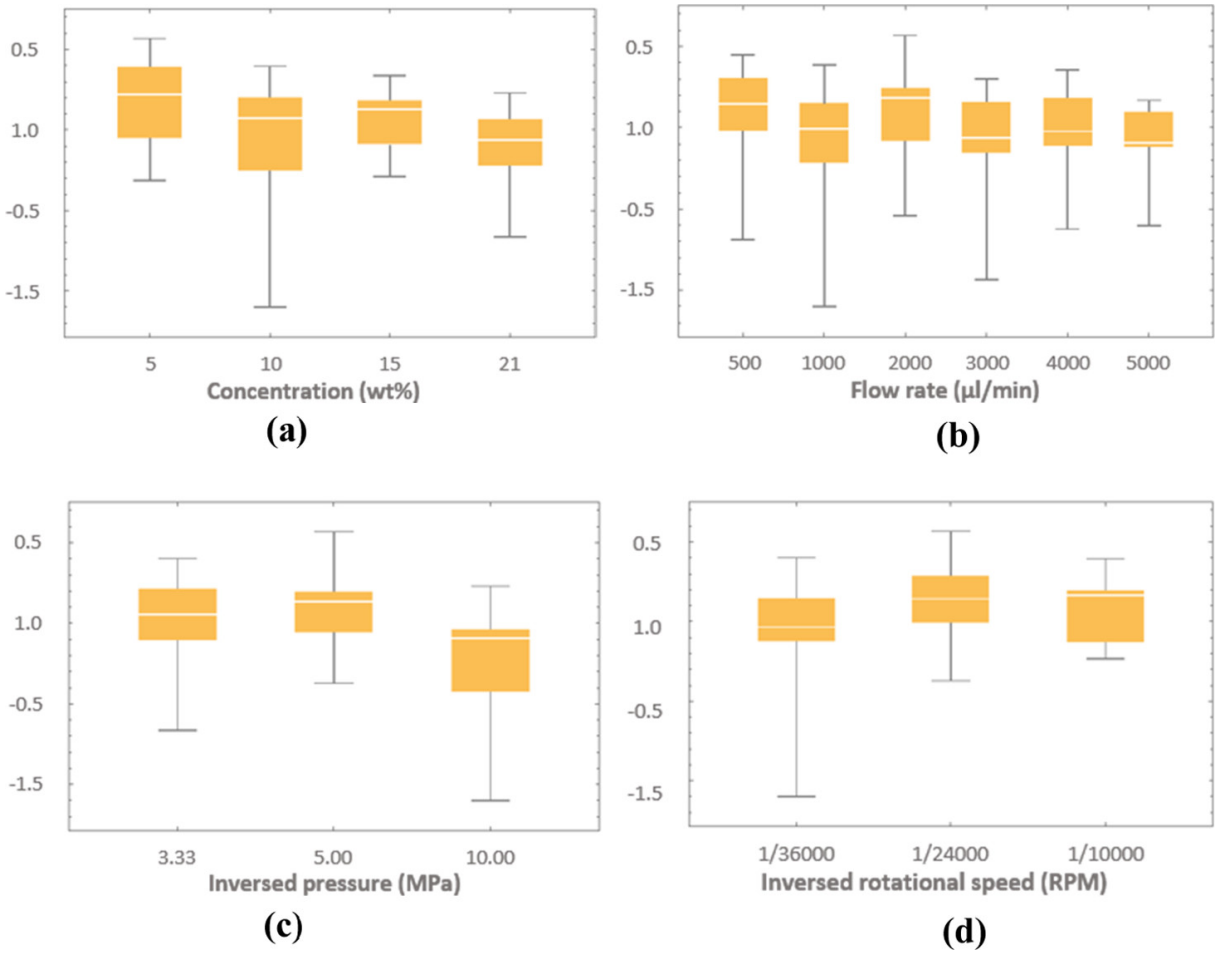

Figure 5.6 Box–Whisker charts for the fractional residuals (unit free) vs. the experimental parameters: (a) polymer concentration, (b) infusion rate, (c) inverse pressure, and (d) inverse rotational speed.

The means of the experimental parameters selected in this work as seen in Table 5.6, which shows that the constant term for infusion rate (f) and rotational speed (g) in the model are possibly negligible in the future updates due to the small coefficients with a very low multiplying power at the beginning of the function. Displaying this change on plots shows that the curves are forced to pass the origin. This is also sensible from the physical point of view of the process of PCIG, as it can be

explained that if the infusion rate is reduced to infinity, the resulting fibre will have an infinitesimal diameter. Taking into account all the optimisations that have proposed so far, the updated model can be expressed as

$$\boldsymbol{y} = (\boldsymbol{\beta_0}\, \boldsymbol{f} + \boldsymbol{\beta_1}\, \boldsymbol{f^2} + \boldsymbol{\beta_2}\, \boldsymbol{f^3} + \boldsymbol{\beta_3}\, \boldsymbol{f^4})(\mathbf{1} + \boldsymbol{\beta_4}\, \boldsymbol{c} + \boldsymbol{\beta_5}\, \boldsymbol{c^2})\, \boldsymbol{e^{\beta_6 / p}}\, (\mathbf{1}/\boldsymbol{g} + \boldsymbol{\beta_7}\, /(\boldsymbol{g})^2) \qquad (5.9)$$

Table 5.6 Mean of the Experimental Parameter Used in the PCIG Process.

Processing	Mean
Concentration (wt%)	13.86
Flow rate (μL/min)	2311.88
Pressure (MPa)	0.20
Rotational speed	29505.00
Diameter (nm)	251.91

Figure 5.7 indicates that the residuals have been reduced in the model of Eq. 5.9 (with an estimated error variance of 3800.86). The residuals for each combination of experimental parameters as presented in Table 3S and all other residual plots are shown in Figure 3S. The obtained adjusted R^2 for this test was 95.7% and the value of AIC was 1128.83. The interval between 5% and 95% cumulative probabilities as listed in Table 5.7. The related confidence intervals for the estimated coefficients of polymer concentration, gas pressure and rotational speed were fairly standard,

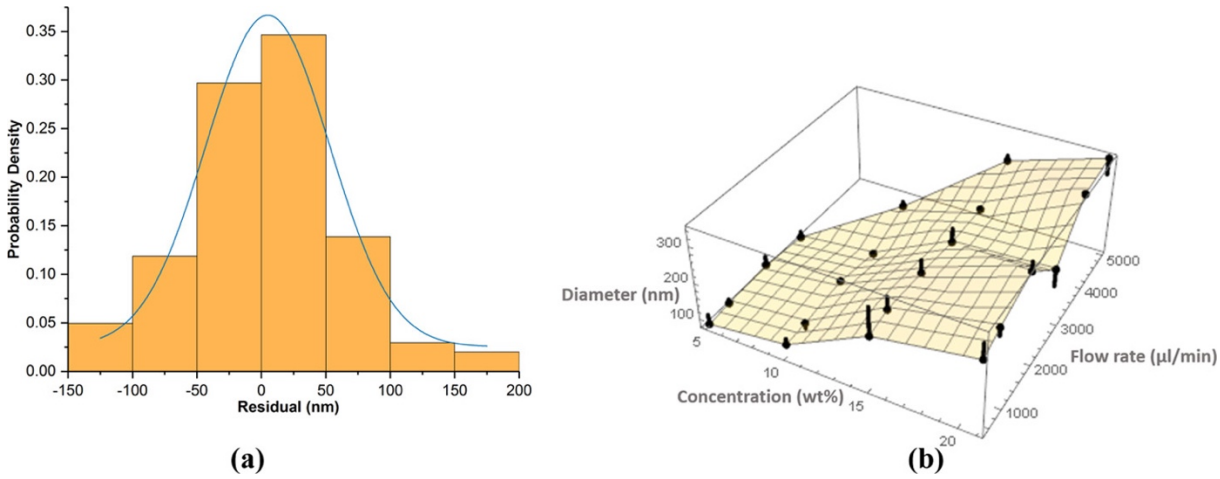

Figure 5.7 (a) Residual distribution and (b) typical residual plot of the optimised non-linear model: Eq. 5.9 (varying the polymer concentration and infusion rate, under a fixed pressure of 2 × 10^5 Pa and a rotational speed of 36 000 rpm).

Table 5.7 Confidence Interval of the Fitting Parameters in the Best-Fitted Non-linear Model: Eq. 5.9

	Estimated coefficient (β_n)	Confidence Interval
β_0	1818.47	(-477.27 , 4114.22)
β_1	-1.20	(-2.73 , 0.33)
β_2	3.04×10^{-4}	(-8.64×10^{-5} , 6.95×10^{-4})
β_3	-2.56×10^{-8}	(-5.88×10^{-8} , 7.60×10^{-9})
β_4	0.12	(-0.23 , 0.47)
β_5	9.26×10^{-3}	(3.38×10^{-3} , 1.51×10^{-2})
β_6	0.14	(0.13 , 0.16)
β_7	-7046.28	(-7455.68 , -6636.89)

5.4 Summary

In this part, RSM was applied to investigate the novel PCIG process for nanofibre formation. ANOVA (variance) was performed at a 5% significance level to examine the effect of input parameters on the average fibre diameter, such as the polymer concentration, infusion rate, gas pressure and rotational speed. In order to use this method in experimental optimisation, it is crucial to select a suitable experimental design to fit a mathematical formula to evaluate the quality and accuracy of the fitted model based on the experimental data obtained. It can be concluded that the best-fitted linear model provided a determination of coefficient (adjusted R^2) of 88.1% with an AIC value of 1107.22. The results also indicated that the PEO polymer concentration and pressure have more significant effects than other parameters, such as rotational speed on produced fibre diameter. For the best non-linear model, the obtained coefficient of determination was 95.7% and the AIC was 1128.83. In the Chapter 6, this model will be used for predicting and optimising the process of fabrication nanofibres, using the PCIG method.

6. Optimisation and Validation of pressure-coupled infusion gyration parameters for the nanofibre fabrication

6.1 Introduction

One of the main goals of the RSM is to determine the optimal settings for the control parameters that result in the minimum (or maximum) response to a particular control region of interest. A well-fitted model is the prerequisite that provides a sufficient representation of the average response of the studied system, as such a model will be used to determine the optimal response value. The optimisation technique used in RSM depends on the nature of the fitted model (André I Khuri & Mukhopadhyay, 2010). For the first-level model, the most viable technique is the method based on steepest decent (or ascent) for moving sequentially to the optimal response. This method is described in detail in many previous studies (Box & Draper, 2007; Myers & Montgomery, 1995). As the first-level model is usually used in the initial stage of the response surface survey, only the optimisation techniques applicable to the second- or higher degree models were mentioned in this part. Such models are used after a series of experiments in sequence until it is considered to contain the region of the optimal response position.

In Chapter 4 and 5, the polyethylene oxide was used as the model material and the empirical modelling of the spinning process was conducted based on the results of

produced fibre by PCIG. In order to better understand the physical meaning of the spinning process, a physical framework of rotary jet spinning was considered in the fitting process. In this part of work, to make the built model (obtained in the last chapter) can help to obtain the combinations of experimental variables capable of achieving the predetermined/desired fibre morphology, the optimisation of the PCIG spinning process was performed. In here, the “desirable fibre” was defined as the produced fibre with targeted average fibre diameter and narrow standard deviation of diameter. A numerical model of the interaction effects of experimental parameters was developed and optimized, which can be used as a framework for selecting the optimal conditions for obtaining PEO fibres having the desired morphology. The experimental variables studied in the present work are the same as in the Chapter 4 and 5: polymer concentration (c), infusion rate (f), gas pressure (p), and rotational speed (g). In the final step, in order to verify the applicability and reproducibility of the developed model, a set of experiments was performed under the optimal conditions of prediction and their results were compared with our target values.

6.2 Regression Analysis

In the last chapter, the non-linear method based on the Levenberg–Marquardt algorithm was utilised to fit the experimental fabrications with the response of fibre diameters. The determined equation is shown in Equation 6.1. The adjusted R^2 obtained was 95.7%, and the AIC value was reached at 1128. Since the adjusted R^2 represents the level of the total variability that can be expected from the fitted model, the results of Eq. 6.1 indicate that the non-linear model is sufficient to explain the

relationship between the variables, and it probably is useful for predicting the desired diameter.

$$f_d(c,p,f,g) = \left(1818.47\,f - 1.20\,f^2 + (3.04\times10^{-4})\,f^3 - (2.56\times10^{-8})\,f^4\right)\left(1 + 0.12\,c + (9.26\times10^{-3})\,c^2\right)\,e^{0.14/p}\,\left(1/g - 7046.28/(g)^2\right) \quad (6.1)$$

In order to explore the statistical characteristics of the standard deviation of the obtained mean diameter, regression analysis was also conducted on the standard deviation. It was found that a strong linear correlation between fibre diameter and standard deviation existed in the experimental results. To optimise the narrow standard deviation, the standard deviation was predicted based on the average fibre diameter used as input, and the difference between the predicted value and the experimental value of the standard deviation was calculated. Eq. 6.2 is the best-fitted linear-quadratic model for the difference of standard deviation of average diameter. $f_s(c, p, f, g)$ is the response of the model, i.e. the standard deviation difference of fibre diameter. An adjusted R^2 of 80% and AIC of 924 were given by Eq. 6.2, and Table 6.1 shows its ANOVA results. The significance of each factor was determined by considering a 5% significance level of p-value. Table 6.1 lists the estimations of coefficients of the fitted linear model, where the SS is the sum of squared observation deviations. Table 6.1 indicated that the fitted model was hierarchically well formulated, in other words, it had involved the significant effects presented in the high order terms. For example, the pressure term (1/p) observed the highest relative impact on the differences of standard deviation; The subdominant factors included the terms of polymer concentration and infusion rate. There was insufficient statistical evidence to justify the interaction term *f/p* (infusion rate and gas pressure). Even if this term is not significant, their individual values still have significant impacts

on the diameters. Therefore, the interaction term should also be incorporated into the model, as well as the quadratic term of polymer concentration.

$$f_s(c, p, f, g) = \alpha_0 - \alpha_1 c + \alpha_2 c^2 + \alpha_3 f - \alpha_4 cf - \alpha_5 c/g + \alpha_6/g^2 - \alpha_7/p + \alpha_8 c/p - \alpha_9 f/p + \alpha_{10}/p^2 \quad (6.2)$$

Table 6.1 ANOVA table of the fitted model of standard deviation reference to Eq. 6.2.

	Estimated coefficient (α_n)	SS	F-statistics	P-Value
1	94.53			
c	7.26	2813.95	5.75	0.02
c^2	0.14	115.27	0.24	0.63
f	0.02	2293.26	4.69	0.03
cf	9.58×10^{-4}	4134.27	8.45	4.59×10^{-3}
c/g	52951.70	2.00×10^{4}	40.90	7.00×10^{-9}
$/g^2$	5.31×10^{9}	4988.81	10.20	1.93×10^{-3}
/p	34.99	4.81×10^{4}	98.40	4.20×10^{-16}
c/p	1.55	4.23×10^{4}	86.48	8.20×10^{-15}
f/p	1.12×10^{-3}	1368.65	2.80	0.10
$/p^2$	1.91	4294.58	8.78	3.89×10^{-3}

6.3 Process Variables Optimisation

One of the aims of optimisation is to discover the most appropriate experimental conditions for making nanofibres with the desired diameter, and in this part of the work, 300 nm was used as a target example. The effects of the relationship between experimental variables on diameters are depicted using three-dimensional graphs. Data were generated by first setting the target diameter in advance and maintaining

three variables in the corresponding intermediate range at a time and changing the fourth to achieve the target fibre diameter. Figure 6.1 indicate the distributions of allowable experimental variables, which were predicted would result in targeted diameter. The colour of each data point in the graphs represents the level of the variable variation, so the colour from violet to red corresponds to increasing the value of the variable from low to high. It can be seen from Figure. 6.1 a, b that there is a clear linear boundary between concentration and pressure. The correlation matrix of the operational variables (Figure 6.2) indicates a strong positive correlation between the gas pressure and polymer concentration, and there is a weak positive correlation between infusion rate and rotational speed. Physically, this means that if the concentration of the polymer solution increases, it becomes more viscous, so higher pressure is required to drain the solution through the orifice of the vessel. Also, the flow rate should be adapted to allow more time for stretching the jetting fibres and increase the speed of rotation to enhance the centrifugal effect.

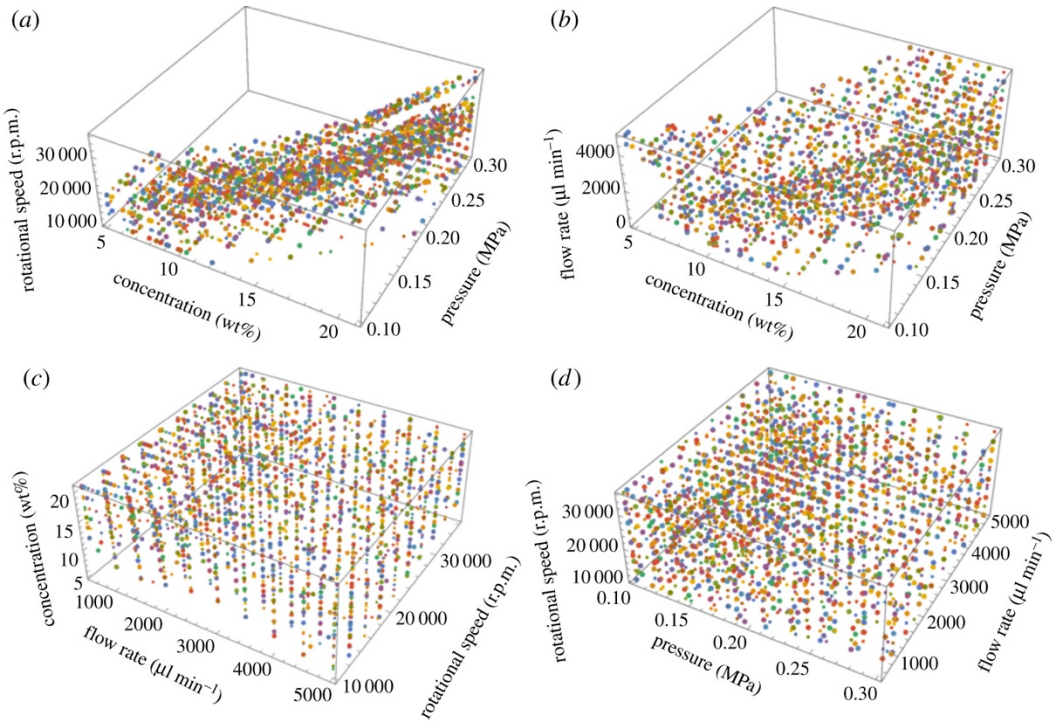

Figure 6.1 3D plots of experimental variables modelled with non-linear model (Eq.1) for pre-defined (targeted) 300 nm average diameter.

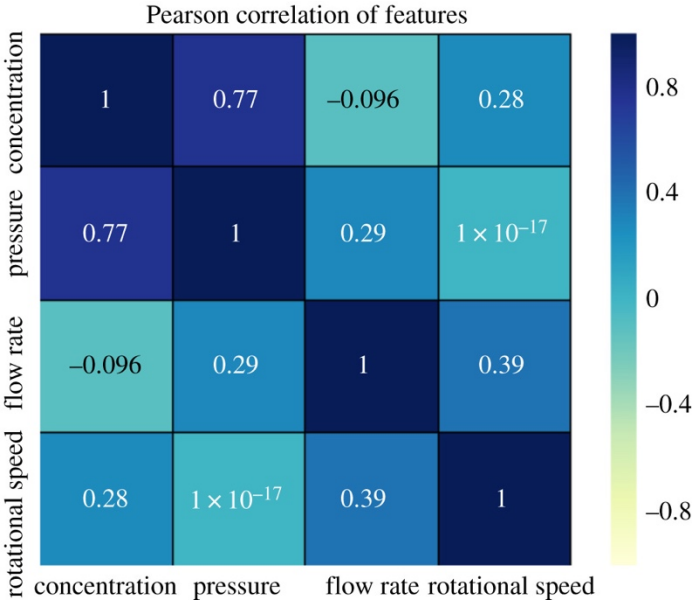

Figure 6.2 Correlation matrix of experimental variables.

From the optimisation perspective, the term “desirability” was defined as two responses related to numerical optimisation in this study; the final response should explore the main points of maximising the “desirability” function (Bezerra et al., 2008). Numerical optimisation used the model developed in Section 6.2 to search the design space to obtain sets of variables that generate the defined target nanofibres on the basis of minimising the value of cost function (maximising desirability).

The initial idea was to seek a set of combinations of experimental parameters (*c, p, f, g*) to minimise both the difference of the mean diameter $\mu\big((c,p,f,g)\big)$ from the desired diameter $\hat{\mu}$ and the spread of diameters $\sigma\big((c,p,f,g)\big)$, by minimising the cost function

$$\boldsymbol{J\big((c,p,f,g)\big) = w_1(\mu\big((c,p,f,g)\big) - \hat{\mu})^2 + w_2\sigma\big((c,p,f,g)\big)^2} \quad (6.3)$$

where w_1 and w_2 are dimensionless weighting parameters expressing the relative importance of having the correct mean diameter and of having narrow distributed diameters. The square of the standard deviation (i.e. $\sigma\big((c,p,f,g)\big)^2$) is used so that the dimensions of the two terms are the same.

However, there is a strong correlation between the average diameter and the standard deviation, so that using the Eq. 6.3 will have the effect of pushing the optimisation towards an incorrect value of the average diameter. This can be seen, as follows. The correlation between average diameter and the spread of the diameter can be represented in Eq. 6.4.

$$\boldsymbol{\sigma\big((c,p,f,g)\big) = \alpha\mu\big((c,p,f,g)\big) + \delta\big((c,p,f,g)\big)} \quad (6.4)$$

As the standard deviation can affect the diameter on both two directions, so the absolute value of the deviation, i.e. $|\delta((c,p,f,g))|$ is to be expected as small as possible when compared with $\alpha\mu((c,p,f,g))$. Take Eq. 6.4 into the Eq. 6.3

$$\boldsymbol{J((c,p,f,g))} = (\boldsymbol{w_1} + \boldsymbol{\alpha^2 w_2})\left(\boldsymbol{\mu((c,p,f,g))} - \frac{\boldsymbol{w_1\hat{\mu} - \alpha\, w_2\, \delta((c,p,f,g))}}{\boldsymbol{w_1 + \alpha^2 w_2}}\right)^2 + \frac{\boldsymbol{w_1 w_2}\left(\boldsymbol{\alpha\hat{\mu} + \delta((c,p,f,g))}\right)^2}{\boldsymbol{w_1 + \alpha^2 w_2}} \quad (6.5)$$

In the ideal case, it is expected that the objective function can be minimised at a diameter equal to $\hat{\mu}$ (except in the case when w_2 = 0 i.e. no weight is placed on the minimisation of the spread of diameters). However, according to the Eq. 6.5, even a perfect correlation is assumed between diameter and standard deviation (i.e. $\delta((c,p,f,g)) = 0$), the function will be minimised at a diameter equal to $\frac{w_1\hat{\mu}}{w_1 + \alpha^2 w_2}$ rather than $\hat{\mu}$. To solve this problem, several data analysis approaches were tested, including ridge regression, linear regression and a three-layers artificial neural networks to explore the relationship between the standard deviation and the mean diameter, as presented in Eq. 6.6.

$$\boldsymbol{\sigma_0}\left(\boldsymbol{\mu((c,p,f,g))}\right) = \boldsymbol{\alpha\mu((c,p,f,g))} + \boldsymbol{\beta} \quad (6.6)$$

where $\alpha = 0.58$ and $\beta = -31.26$. Then, due to the trend that was observed in Figure 5.6 as well as the linear correlations between the standard deviation and mean diameter, an expression for the residual standard deviation in terms of the parameters was defined and as presented below.

$$\boldsymbol{\delta((c,p,f,g))} = \boldsymbol{\sigma((c,p,f,g))} - \boldsymbol{\sigma_0}\left(\boldsymbol{\mu((c,p,f,g))}\right) \quad (6.7)$$

Where σ_0 regarded as the unavoidable contributions to the spread of diameters, and $\delta\big((c,p,f,g)\big)$ regarded as a contribution, which might be positive or negative, which fitted with Eq. 6.2 and can be used to optimise the spread. Thus, a new suitable cost function for achieving the 'desirable' diameter with narrow spread was defined and given by the below equation (Eq. 6.8), where the form of the second item is chosen such that the terms are of the same size but retain the sign of δ.

$$\boldsymbol{f_e\big(d_0, w_1, w_2, c,\ p,\ f,\ g\big) = w_1\big(d_0 - f_d(c,p,f,g)\big)^2 + w_2\ (\ f_s(c,p,f,g)\ |f_s(c,p,f,g)|\ )} \tag{6.8}$$

In Eq. 6.8, d_0 is the targeted diameter (in nm), w_1 and w_2 were both initialised to one at the beginning of the optimisation process. Since PCIG is a robust process for large-scale production of nanofibres, and the rotational speed shows a weaker effect in regression analysis, it was not necessary to tune it to very high precision. Hence, in the process of optimisation, the ranges of the experimental variables were selectively confined to those which were reasonable ranges for the real experiments, such as, polymer concentrations (5–20 wt%), pressure (1×10^5–3×10^5 Pa), infusion rate (500–5000 μL min^{-1}), rotational speed (12 000–36 000 rpm). the results of several optimisation algorithms (direct search method and gradient-based method) were compared, and non-linear interior point algorithm offered better results. Finding global optimum can be arbitrarily tricky even without constraints, so the methods used may fail. It may often be useful to optimise the function multiple times and pick the best results (global optimum or fine local optimum) (Forsgren et al., 2002).

As shown in Table 6.2, there were six sets of experimental variables were suggested by the optimisation. Interestingly, for all optimal (including comparative local and

global optimal) conditions, there are recommendations for high polymer concentrations, and most of them were ≥ 15 wt%. This result is also consistent with other studies that have concluded that the optimal experimental conditions for spinning fibre are highly dependent on polymer concentration (P. Gupta et al., 2005; Macossay, Marruffo, Rincon, Eubanks, & Kuang, 2007). It is suggested that a dilute polymer solution, for example, 5 wt % may result in a broader spread of fibre diameter. The average diameter produced in our experimental studies ranged from about 50 to 850 nm, so this model is best suited for predicting the groups of parameters that can make the fibre diameter within this range. In addition, the only variable characteristic of fluid properties is the polymer concentration in the model.

6.4 Validation

Up to this stage of our study, the PCIG experimental parameters including polymer concentration, gas pressure, infusion rate and rotational speed were computationally optimised to obtain nanofibres with a targeted average diameter and narrow spread. For the purpose of checking the reliability and reproducibility of the RSM model, a group of experiments was performed under the predicted optimal conditions, and the results are as follows.

Table 6.2 Validation results of the predicted optimal conditions.

Conditions No.	Concentration (wt%)	Rotational speed (rpm)	Pressure (MPa)	Flowrate ($\mu Lmin^{-1}$)	Predicted diameter (nm)	Validated diameter (nm)	Standard deviation (nm)
1	11	12000	0.1	566	316.58	348	91
2	15	12000	0.2	1021	298.59	271	95
3	15	24000	0.2	3323	299.83	297	84
4	20	24000	0.2	685	299.88	291	84
5	20	36000	0.2	1553	298.56	297	90
6	20	36000	0.3	4983	289.59	295	88

The spun fibres were collected at a collection distance of 100 mm, and the corresponding images of PEO nanofibres under optimal conditions were captured by SEM (Figure 6.3). The results of validation experiments derived from the observations in Figure 6.3 are shown in Table 6.2, which depicts the measured fibre diameters are in good agreement with the values that were predicted using the optimised model. This suggests that the proposed model is capable of predicting the operating conditions of the fibre diameter with high accuracy.

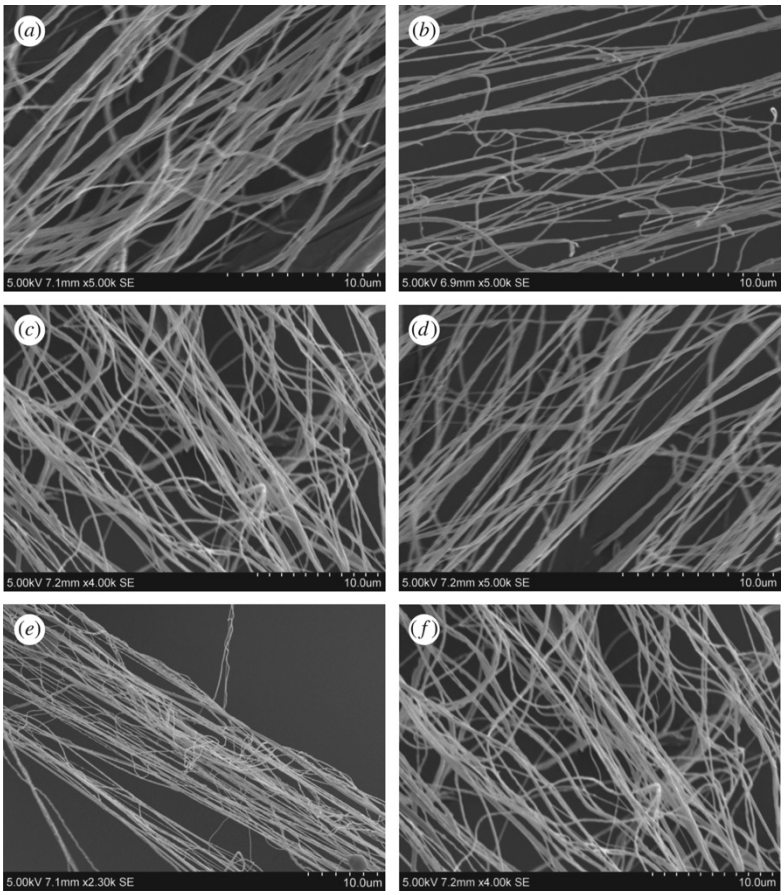

Figure 6.3 Scanning Electron micrographs of PEO fibres generated for validation experiments set in Table 6.2 at conditions: (a):1, (b):2, (c):3, (d):4, (e):5, (f):6.

6.5 Summary

The study in this chapter focuses on understanding how the PCIG experimental variables, i.e. polymer concentration of solution, infusion rate, applied gas pressure and rotational speed, affected the morphological characteristics of the spun polyethylene oxide nanofibres. A numerical model for the interactional effects of experimental variables was developed and optimised using a non-linear interior point method. It can be used as a framework for selecting the optimal conditions to obtain

polyethylene oxide fibres with the desired morphology features (targeted average diameter and narrow standard deviation). The adequacy (accuracy) of the model was verified by a group of validation experiments. The results prove that the optimal conditions for prediction were close to the targeted average diameter that matches the pre-set expectation, with a difference of less than 10%.

7. Conclusions and Further Works

7.1 Conclusions

Several new spinning methods have been developed recently to mass produce polymeric fibres. The fibre diameter plays a pivotal role for the mechanical, electrical, and optical properties of the produced fibre mats. The design approach reported in this thesis, namely pressure coupled infusion gyration, which is simple and efficient system that combines the benefits of several existing gyration-based methods to produce the well-aligned 3D fibrous bundles in one step. Due to the increasing utilisations of nanofibres in many fields of research, comprehensive knowledge of the spinning process as the most popular fibre production is necessary. We are keen to investigate its spinning performance as well as to understand the impact of the experimental parameters through modelling and optimising the fibre formation process. This study draws the following conclusions:

7.1.1 Generating Nanofibres Using Pressure Coupled Infusion Gyration

Using the PEO-water system, PCIG has been demonstrated that can help to achieve mass production of fibres. Compared with other existing spinning methods, PCIG is easy to be deployed, inexpensive and has relatively low requirements for spinning dopes. It inherits the advantages of typical gyration-based methods (such as pressurised rotary and infusion rotations), so that it is also applicable for large-scale production of highly aligned fibres along the radial direction of the spinning vessel, providing fibres with better geometry and extending the spinnable range for the dilute

solution. For example, using a selective combination of parameters for 5 wt%. The effects of experimental parameters (infusion flow rate (500–5000 μL min^{-1}), applied (working) pressure (1×10^5 to 3×10^5 Pa), rotational speed (10 000–36 000 rpm) and collection distance (4–15 cm)) and solution concentration (3–21 wt%) on product morphology were investigated in detail.

7.1.2 Influences of Experimental Parameters on Fibre Morphology

When increasing working pressure, increasing infusion rate, and fixed rotational speed, droplets and beaded fibres appeared in the products of 5–15 wt% solutions, and this demonstrated that the enhanced pressure and infusion rate will affect the balance of polymer transfer across the vessel orifices in spinning to promote droplets and bead formation. At fixed pressure, fixed infusion rate, and changing rotational speed, the obtained fibre diameter shows a trend of increase as rotational speed decrease, and this is due to the centrifugal force being proportional to rotational speed. The orifice-to-collector distance directly affects the produced fibre morphology, as well as a minimum critical collection distance (7 cm in the present work with PEO-water system) existed that favoured obtaining desirable morphology and this value tends to be less influential once this critical value is exceeded. The method allows the product morphology to be substantially controlled by different combinations of the above-mentioned processing parameters. It is anticipated that the simplicity and versatility of this method could make it another potential way to produce nanofibres in high volume and cost effectively.

7.1.3 Modelling Fibre Formation Process of Pressure Coupled Infusion Gyration

Prior to more expensive experimental techniques, modelling techniques are a valuable tool for managing the contributing factors in the fibre generation process. In this part, the experimental process is modelled using response surface methodology, both in linear and non-linear fitting formats, to allow optimisation of processing parameters.

The results of fibre diameters that produced at 100 mm of collection distance were used as input data during the modelling. The processing parameters, including polymer concentration, infusion (flow) rate, working pressure, and rotational speed were regarded as the variables to control fibre diameters in the fitted models. The fitted models were improved empirically based on the trends of the experimental results, and also introduced a physical framework derived from others' study to improve the fitting performance. The successes of the fitted models are evaluated using adjusted R^2 and Akaike information criterion (AIC). A systematic description of the experimental process could be obtained according to the model in this study. The non-linear model was founded that had a better fitting performance that is an adjusted R^2 of 95.7% with an AIC of 1128.83 and was applied as the response function of fibre diameter in the following optimisation and prediction stages. From the analysis of variance, it is concluded that the polymer concentration of the solution and the working pressure affected the fibre diameters more strongly than other parameters.

7.1.4 Optimising and Validating the Pressure Coupled Infusion Gyration

The last part of study focuses on understanding how the PCIG experimental variables, namely solution's concentration, pressure, flow rate and rotational speed, affected the morphological features of spun PEO nanofibres. RSM was used to optimise the experimental variables for fabricating PEO fibres with a desired diameter and narrow standard deviation. A non-linear model that was fitted with a quartic equation and another linear model that was fitted with a quadratic equation was developed for the prediction and optimisation of average fibre diameter and standard deviation of diameter, respectively. These two models were optimised by omitting the non-significant variables. The resulting adjusted R2 and AIC values indicated that there was no evidence of lack of fit. The results of ANOVA demonstrated that the standard deviation differences of diameter had experienced the highest impact from the pressure and the average diameter was strongly affected by the concentration, and besides, the flow rate and rotational speed played subdominant roles for controlling the spun fibre morphology. The optimal conditions of experiments were found by developing a cost function that uses the fitted models and optimising it with non-linear interior point methods.

Interestingly, for obtaining the desired diameter with a narrow standard deviation, a condition with higher concentration and moderate pressure was suggested. Validation experiments verified the adequacy (accuracy) of our models. PEO nanofibres (close to averagely 300 nm diameter in this study) were obtained at the optimal conditions given in Table 6.2. The difference between predicted and validated results (experimentally observed) was less than 10%. It can be concluded

that the proposed models are in good agreement with the validation results; the models were applicable and replicable in determining the optimal experimental variables for getting the desired PEO nanofibres with the intended diameter.

7.2 Future Works

7.2.1 Improvement of the Pressure Coupled Infusion Gyration Setup

In this project, it has been demonstrated that the pressure coupled infusion gyration can fabricate the polymeric fibre with controlled size and morphology effectively and continuously from PEO-water system. Its sister process, i.e. pressurised gyration has been proved to producing various structures (nanoparticles, microbubbles and fibres) from a wide range of materials, and has the potential to be an alternative to electrospinning in some fields. Therefore, the method should be tested with different material system to further explore the future adequacy of manufacturing.

Compared with pressurised gyration, this approach is more efficient by reducing the waste of materials at the beginning of each spinning, and it is relatively new and as expected, but its setup is still fundamental. A further improvement work of redesigning the setup, including parameter control device such as dial and stop button, tubes and connections with suitable materials, in order to handle varies solvents, for instance, the caustic solvents like chloroform.

The rotational vessel used in this project has the same dimensions as the pressurised gyration and infusion gyration works in our group. However, neither of them are able to manufacture productions with complex structure, e.g. core-shell fibres and multi-layered particles. For the future improvements, different designs of vessel, for example, varying the size of vessel, number and geometry of spinning orifices should be conducted, which may have an influence on the morphology and yield of production of fibres.

The solvent selection is important for any spinning methods. As the water has a relative higher boiling point than other organic solvents, the potential of PCIG with more volatile solvents has not been fully explored. The fibre spinning performance of PCIG under Poly(E-Caprolactone) (PCL)/acetone system was compared with our previous study in pressurised gyration (Hong et al., 2016). The early indications are that it is able to produce fibrous structure rather than beaded fibres with 10 wt% PCL/acetone solution. However, due to the high pressure was introduced to enhance the solvent evaporation during the spinning, the PCIG approach also has a similar risk of blockage at the orifices as other spinning techniques. Moreover, the operation of PCIG approach would be further simplified, providing better control of experimental parameters.

According to the observational results during the experiments, the humidity and temperature of the ambient environment has a significant impact on the yield and morphology of the produced fibres. The PCIG is a robust process, which will increase the humidity around the rotating vessel quickly when the process starts. The increased humidity will further hinder the solvent evaporation and leads to coarser fibres and a reduction of yield. Therefore, an enclosed spinning environment

with strongly controllable ventilations should be designed and implemented, in order to guarantee the better usability and productivity.

7.2.2 Managing Information Generated by Experiment

Currently, the length and yield of has not been fully investigated, which definitely should be studied in the future and may be able to incorporate with the empirical model in the future.

Assessment of the produced fibres could be further extended through more performance testing, for example, mechanical tests, to justify the new method as suitable for the fibrous production.

The pressure coupled infusion gyration has five processing parameters, including polymer concentration, rotational speed, applied pressure, infusion flow rate and collection distance. Although a full experimental design will generate a large amount of data, it would contribute to the computational and statistical analyses and have an insight into variable effects. The utilisations of PCIG can be encouraged between different studies for preparing various structures from different materials. The resultant data could be used as the input to the model, thereby stimulating the improvements from various sources to contributing its theoretical studies and as one of the mainstream production methods.

7.2.3 Improvement of the Theoretical Study of Pressure Coupled Infusion Gyration

An empirical model was explored to describe the spinning process of producing PEO fibres using PCIG. However, it should be noted that the model developed in this

project using response surface methodology should not be inferred outside the range of the original experimental observations, i.e. the prediction results are more reliable under the ranges of parameters as stated in section 3.3. Hence, more experimental data should be acquired so that more advanced techniques could be applied to study the spinning process.

Moreover, an existing framework of rotary-jet spinning was referred, and the model was improved with more physical sense at the current stage. Nevertheless, the collection distance was not added in the model building stage, due to the appropriate collection distance is also determined by the duration of the solvent evaporation. If it warrants to be used for different polymer and solvent combinations, the model should be revised to include physical properties of spinning dopes, such as viscosity and surface tension that have substantial differences based on the different type of polymers and solvents would have to be developed. This would bring a certain workload and unknown effects of variables if also extend its usage for modelling the process of producing functional nanofibres (e.g. drug-loaded and composite fibres). Additionally, other modelling approaches can also be tested in the improvement process, this could be addressed in the subsequent work.

References

Acherjee, B., Misra, D., Bose, D., & Venkadeshwaran, K. (2009). Prediction of weld strength and seam width for laser transmission welding of thermoplastic using response surface methodology. *Optics & Laser Technology, 41*(8), 956-967.

Adabi, M., Saber, R., Faridi-Majidi, R., & Faridbod, F. (2015). Performance of electrodes synthesized with polyacrylonitrile-based carbon nanofibers for application in electrochemical sensors and biosensors. *Materials Science and Engineering: C, 48*, 673-678.

Ahn, Y., Park, S., Kim, G., Hwang, Y., Lee, C., Shin, H., & Lee, J. (2006). Development of high efficiency nanofilters made of nanofibers. *Current Applied Physics, 6*(6), 1030-1035.

Almany, L., & Seliktar, D. (2005). Biosynthetic hydrogel scaffolds made from fibrinogen and polyethylene glycol for 3D cell cultures. *Biomaterials, 26*(15), 2467-2477.

Altun, E., Aydogdu, M. O., Koc, F., Crabbe‐Mann, M., Brako, F., Kaur‐Matharu, R., Ozen, G., Kuruca, S.E., Edirisinghe, U., Gunduz, O. & Edirisinghe, M. (2018). Novel Making of Bacterial Cellulose Blended Polymeric Fiber Bandages. *Macromolecular Materials and Engineering, 303*(3), 1700607.

Amini, M., & Younesi, H. (2009). Biosorption of Cd (II), Ni (II) and Pb (II) from aqueous solution by dried biomass of Aspergillus niger: Application of response surface methodology to the optimization of process parameters. *CLEAN–Soil, Air, Water, 37*(10), 776-786.

Anton, F. (1939). Method and apparatus for the production of artificial fibers: Google Patents.

Ashrafi, S., Nasseri, S., Alimohammadi, M., Mahvi, A., & Faramarzi, M. (2016). Optimization of the enzymatic elimination of flumequine by laccase-mediated system using response surface methodology. *Desalination and Water Treatment, 57*(31), 14478-14487.

Ayres, C., Bowlin, G. L., Henderson, S. C., Taylor, L., Shultz, J., Alexander, J., Telemeco, T.A. & Simpson, D. G. (2006). Modulation of anisotropy in electrospun tissue-engineering scaffolds: Analysis of fiber alignment by the fast Fourier transform. *Biomaterials, 27*(32), 5524-5534.

Badrossamay, M. R., McIlwee, H. A., Goss, J. A., & Parker, K. K. (2010). Nanofiber assembly by rotary jet-spinning. *Nano letters, 10*(6), 2257-2261.

Bailey, A. G. (1988). *Electrostatic spraying of liquids*: Wiley New York: Wiley.

Barhoum, A., Rasouli, R., Yousefzadeh, M., Rahier, H., & Bechelany, M. (2018). Nanofiber Technology: History and Developments. *Handbook of Nanofibers*, 1-42.

Barnes, W. J., & Price, F. P. (1961). Intrinsic and bulk viscosities of some polyethylene oxide polymers. *Journal of Polymer Science, 50*(153), S25-S26.

Baş, D., & Boyacı, I. H. (2007). Modeling and optimization I: Usability of response surface methodology. *Journal of food engineering, 78*(3), 836-845.

Basheer, I. A., & Hajmeer, M. (2000). Artificial neural networks: fundamentals, computing, design, and application. *Journal of microbiological methods, 43*(1), 3-31.

Bassi, A., Gough, J., Zakikhani, M., & Downes, S. (2011). The chemical and physical properties of poly (ε-caprolactone) scaffolds functionalised with poly (vinyl phosphonic acid-co-acrylic acid). *Journal of tissue engineering, 2011*.

Bezerra, M. A., Santelli, R. E., Oliveira, E. P., Villar, L. S., & Escaleira, L. A. (2008). Response surface methodology (RSM) as a tool for optimization in analytical chemistry. *Talanta, 76*(5), 965-977.

Bhardwaj, N., & Kundu, S. C. (2010). Electrospinning: a fascinating fiber fabrication technique. *Biotechnology advances, 28*(3), 325-347.

Bhushan, B. (2017). *Springer handbook of nanotechnology*: Springer.

Bhushan, B., & Caspers, M. (2017). An overview of additive manufacturing (3D printing) for microfabrication. *Microsystem Technologies, 23*(4), 1117-1124.

Bishop, C. M. (2006). *Pattern recognition and machine learning*: springer.

Borm, P. J., Robbins, D., Haubold, S., Kuhlbusch, T., Fissan, H., Donaldson, K., Schins, R., Stone, V., Kreyling, W., Lademann, J. & Krutmann, J (2006). The potential risks of nanomaterials: a review carried out for ECETOC. *Particle and fibre toxicology, 3*(1), 11.

Box, G. E., & Draper, N. R. (2007). *Response surfaces, mixtures, and ridge analyses* (Vol. 649): John Wiley & Sons.

Brako, F., Luo, C., Craig, D. Q., & Edirisinghe, M. (2018). An Inexpensive, Portable Device for Point‐of‐Need Generation of Silver‐Nanoparticle Doped Cellulose Acetate Nanofibers for Advanced Wound Dressing. *Macromolecular Materials and Engineering, 303*(5), 1700586.

Brako, F., Thorogate, R., Mahalingam, S., Raimi-Abraham, B., Craig, D. Q., & Edirisinghe, M. (2018). Mucoadhesion of Progesterone-Loaded Drug Delivery Nanofiber Constructs. *ACS applied materials & interfaces, 10*(16), 13381-13389.

Brown, P., & Stevens, K. (2007). *Nanofibers and nanotechnology in textiles*: Elsevier.

Brunet-Imbault, B., Lemineur, G., Chappard, C., Harba, R., & Benhamou, C.-L. (2005). A new anisotropy index on trabecular bone radiographic images using the fast Fourier transform. *BMC medical imaging, 5*(1), 4.

Bruns, R. E., Scarminio, I. S., & de Barros Neto, B. (2006). *Statistical design-chemometrics* (Vol. 25): Elsevier.

Buchko, C. J., Chen, L. C., Shen, Y., & Martin, D. C. (1999). Processing and microstructural characterization of porous biocompatible protein polymer thin films. *Polymer, 40*(26), 7397-7407.

Buet-Gautier, K., & Boisse, P. (2001). Experimental analysis and modeling of biaxial mechanical behavior of woven composite reinforcements. *Experimental mechanics, 41*(3), 260-269.

Buhmann, M. D. (2003). *Radial basis functions: theory and implementations* (Vol. 12): Cambridge university press.

Burger, C., Hsiao, B. S., & Chu, B. (2006). Nanofibrous materials and their applications. *Annu. Rev. Mater. Res., 36*, 333-368.

Buzea, C., Pacheco, I. I., & Robbie, K. (2007). Nanomaterials and nanoparticles: sources and toxicity. *Biointerphases, 2*(4), MR17-MR71.

Campello, R. J., Moulavi, D., Zimek, A., & Sander, J. (2015). Hierarchical density estimates for data clustering, visualization, and outlier detection. *ACM Transactions on Knowledge Discovery from Data (TKDD), 10*(1), 5.

Carley, K. M., Kamneva, N. Y., & Reminga, J. (2004). *Response surface methodology* (No. CMU-ISRI-04-136). Carnegie-mellon Univ Pittsburgh Pa School of Computer Science.

Casper, C. L., Stephens, J. S., Tassi, N. G., Chase, D. B., & Rabolt, J. F. (2004). Controlling surface morphology of electrospun polystyrene fibers: effect of humidity and molecular weight in the electrospinning process. *Macromolecules, 37*(2), 573-578.

Cesa-Bianchi, N., & Lugosi, G. (2006). *Prediction, learning, and games*: Cambridge university press.

Chakraborty, U. K. (2008). *Advances in differential evolution* (Vol. 143): Springer.

Chang, H.-C., Demekhin, E. A., & Kalaidin, E. (1999). Iterated stretching of viscoelastic jets. *Physics of fluids, 11*(7), 1717-1737.

Chapelle, O., Scholkopf, B., & Zien, A. (2009). Semi-supervised learning (chapelle, o. et al., eds.; 2006)[book reviews]. *IEEE Transactions on Neural Networks, 20*(3), 542-542.

Chen, V. J., & Ma, P. X. (2004). Nano-fibrous poly (L-lactic acid) scaffolds with interconnected spherical macropores. *Biomaterials, 25*(11), 2065-2073.

Cho, I.-H., & Zoh, K.-D. (2007). Photocatalytic degradation of azo dye (Reactive Red 120) in TiO2/UV system: Optimization and modeling using a response surface methodology (RSM) based on the central composite design. *Dyes and Pigments, 75*(3), 533-543.

Coleman, J. N., Khan, U., & Gun'ko, Y. K. (2006). Mechanical reinforcement of polymers using carbon nanotubes. *Advanced materials, 18*(6), 689-706.

Colvin, V. L. (2003). The potential environmental impact of engineered nanomaterials. *Nature biotechnology, 21*(10), 1166.

Cooley, J. F. (1902). Apparatus for electrically dispersing fluids: Google Patents.

Cui, Z., Zheng, Z., Lin, L., Si, J., Wang, Q., Peng, X., & Chen, W. (2018). Electrospinning and crosslinking of polyvinyl alcohol/chitosan composite nanofiber for transdermal drug delivery. *Advances in Polymer Technology, 37*(6), 1917-1928.

Cunha, C., Panseri, S., & Antonini, S. (2011). Emerging nanotechnology approaches in tissue engineering for peripheral nerve regeneration. *Nanomedicine: Nanotechnology, Biology and Medicine, 7*(1), 50-59.

Dahman, Y. (2017). *Nanotechnology and Functional Materials for Engineers.* Elsevier.

Dantzig, G. B., & Thapa, M. N. (2006). *Linear programming 2: theory and extensions*. Springer Science & Business Media.

Darkrim, F. L., Malbrunot, P., & Tartaglia, G. (2002). Review of hydrogen storage by adsorption in carbon nanotubes. *International Journal of Hydrogen Energy, 27*(2), 193-202.

Das, S., & Suganthan, P. N. (2011). Differential evolution: A survey of the state-of-the-art. *IEEE transactions on evolutionary computation, 15*(1), 4-31.

Davoudpour, Y., Hossain, S., Khalil, H. A., Haafiz, M. M., Ishak, Z. M., Hassan, A., & Sarker, Z. I. (2015). Optimization of high pressure homogenization parameters for the isolation of cellulosic nanofibers using response surface methodology. *Industrial Crops and Products, 74*, 381-387.

Dayan, C. B., Afghah, F., Okan, B. S., Yıldız, M., Menceloglu, Y., Culha, M., & Koc, B. (2018). Modeling 3D melt electrospinning writing by response surface methodology. *Materials & Design, 148*, 87-95.

De Schoenmaker, B., Van der Schueren, L., Ceylan, Ö., & De Clerck, K. (2012). Electrospun polyamide 4.6 nanofibrous nonwovens: parameter study and characterization. *Journal of nanomaterials, 2012*, 14.

Demir, M. M., Yilgor, I., Yilgor, E., & Erman, B. (2002). Electrospinning of polyurethane fibers. *Polymer, 43*(11), 3303-3309.

Deravi, L. F., Sinatra, N. R., Chantre, C. O., Nesmith, A. P., Yuan, H., Deravi, S. K., Goss, J. A., MacQueen, L. A., Badrossamy, M. R., Gonzalez, G. M. & Phillips, M. D. (2017). Design and fabrication of fibrous nanomaterials using pull spinning. *Macromolecular Materials and Engineering, 302*(3), 1600404.

Desai, K., Kit, K., Li, J., & Zivanovic, S. (2008). Morphological and surface properties of electrospun chitosan nanofibers. *Biomacromolecules, 9*(3), 1000-1006.

Dil, E. A., Ghaedi, M., Asfaram, A., Mehrabi, F., Bazrafshan, A. A., & Ghaedi, A. M. (2016). Trace determination of safranin O dye using ultrasound assisted dispersive solid-phase micro extraction: artificial neural network-genetic algorithm and response surface methodology. *Ultrasonics sonochemistry, 33*, 129-140.

Doshi, J., & Reneker, D. H. (1995). Electrospinning process and applications of electrospun fibers. *Journal of electrostatics, 35*(2-3), 151-160.

Ester, M., Kriegel, H.-P., Sander, J., & Xu, X. (1996). *A density-based algorithm for discovering clusters in large spatial databases with noise.* Paper presented at the Kdd.

Estivill-Castro, V. (2002). Why so many clustering algorithms: a position paper. *SIGKDD explorations, 4*(1), 65-75.

Falkner, R., & Jaspers, N. (2012). Regulating nanotechnologies: risk, uncertainty and the global governance gap. *Global environmental politics, 12*(1), 30-55.

Fändrich, M., Fletcher, M. A., & Dobson, C. M. (2001). Amyloid fibrils from muscle myoglobin. *Nature, 410*(6825), 165.

Fang, J., Niu, H., Lin, T., & Wang, X. (2008). Applications of electrospun nanofibers. *Chinese science bulletin, 53*(15), 2265.

Faridi‐Majidi, R., Ziyadi, H., Naderi, N., & Amani, A. (2012). Use of artificial neural networks to determine parameters controlling the nanofibers diameter in electrospinning of nylon‐6, 6. *Journal of applied polymer science, 124*(2), 1589-1597.

Farré, M., Gajda-Schrantz, K., Kantiani, L., & Barceló, D. (2009). Ecotoxicity and analysis of nanomaterials in the aquatic environment. *Analytical and bioanalytical chemistry, 393*(1), 81-95.

Feng, L., Li, S., Li, Y., Li, H., Zhang, L., Zhai, J., Song Y., Liu B., Jiang L. & Zhu, D. (2002). Super‐hydrophobic surfaces: from natural to artificial. *Advanced materials, 14*(24), 1857-1860.

Feng, L., Xie, N., & Zhong, J. (2014). Carbon nanofibers and their composites: a review of synthesizing, properties and applications. *Materials, 7*(5), 3919-3945.

Fong, H., Chun, I., & Reneker, D. (1999). Beaded nanofibers formed during electrospinning. *Polymer, 40*(16), 4585-4592.

Forsgren, A., Gill, P. E., & Wright, M. H. (2002). Interior methods for non-linear optimization. *SIAM review, 44*(4), 525-597.

Fouda, M. M., El-Aassar, M., & Al-Deyab, S. S. (2013). Antimicrobial activity of carboxymethyl chitosan/polyethylene oxide nanofibers embedded silver nanoparticles. *Carbohydrate Polymers, 92*(2), 1012-1017.

Friess, W. (1998). Collagen–biomaterial for drug delivery. *European journal of pharmaceutics and biopharmaceutics, 45*(2), 113-136.

Gaharwar, A. K., Nikkhah, M., Sant, S., & Khademhosseini, A. (2014). Anisotropic poly (glycerol sebacate)-poly (ϵ-caprolactone) electrospun fibers promote endothelial cell guidance. *Biofabrication, 7*(1), 015001.

Geng, X., Kwon, O.-H., & Jang, J. (2005). Electrospinning of chitosan dissolved in concentrated acetic acid solution. *Biomaterials, 26*(27), 5427-5432.

Gilmour, S. G. (2006). Response surface designs for experiments in bioprocessing. *Biometrics, 62*(2), 323-331.

Gleiter, H. (2000). Nanostructured materials: basic concepts and microstructure. *Acta materialia, 48*(1), 1-29.

Gojny, F., Wichmann, M., Köpke, U., Fiedler, B., & Schulte, K. (2004). Carbon nanotube-reinforced epoxy-composites: enhanced stiffness and fracture toughness at low nanotube content. *Composites science and technology, 64*(15), 2363-2371.

Goyal, A., Reddy, A. L., & Ajayan, P. M. (2011). Flexible Carbon Nanotube ‐ Cu2O Hybrid Electrodes for Li ‐ Ion Batteries. *Small, 7*(12), 1709-1713.

Granville, V., Krivánek, M., & Rasson, J.-P. (1994). Simulated annealing: A proof of convergence. *IEEE transactions on pattern analysis and machine intelligence, 16*(6), 652-656.

Gu, S., Ren, J., & Vancso, G. (2005). Process optimization and empirical modeling for electrospun polyacrylonitrile (PAN) nanofiber precursor of carbon nanofibers. *European polymer journal, 41*(11), 2559-2568.

Guo, L., Bai, J., Li, C., Meng, Q., Liang, H., Sun, W., Li H. & Liu, H. (2013). A novel catalyst containing palladium nanoparticles supported on PVP composite nanofiber films:

Synthesis, characterization and efficient catalysis. *Applied Surface Science, 283*, 107-114.

Gupta, P., Elkins, C., Long, T. E., & Wilkes, G. L. (2005). Electrospinning of linear homopolymers of poly (methyl methacrylate): exploring relationships between fiber formation, viscosity, molecular weight and concentration in a good solvent. *Polymer, 46*(13), 4799-4810.

Gupta, V., & Kothari, V. (2012). *Manufactured fibre technology*: Springer Science & Business Media.

Ha, S.-W., Tonelli, A. E., & Hudson, S. M. (2005). Structural studies of bombyx mori silk fibroin during regeneration from solutions and wet fiber spinning. *Biomacromolecules, 6*(3), 1722-1731.

Haggenmueller, R., Gommans, H., Rinzler, A., Fischer, J. E., & Winey, K. (2000). Aligned single-wall carbon nanotubes in composites by melt processing methods. *Chemical Physics Letters, 330*(3-4), 219-225.

Hammami, M. A., Krifa, M., & Harzallah, O. (2014). Centrifugal force spinning of PA6 nanofibers–processability and morphology of solution-spun fibers. *the Journal of the Textile Institute, 105*(6), 637-647.

Hammel, E., Tang, X., Trampert, M., Schmitt, T., Mauthner, K., Eder, A., & Pötschke, P. (2004). Carbon nanofibers for composite applications. *Carbon, 42*(5-6), 1153-1158.

Hartgerink, J. D., Beniash, E., & Stupp, S. I. (2001). Self-assembly and mineralization of peptide-amphiphile nanofibers. *Science, 294*(5547), 1684-1688.

Hastie, T., Tibshirani, R., & Friedman, J. (2009). The elements of statistical learning: data mining, inference, and prediction, Springer Series in Statistics: Springer New York.

Hayati, I., Bailey, A., & Tadros, T. F. (1987). Investigations into the mechanisms of electrohydrodynamic spraying of liquids: I. Effect of electric field and the environment on pendant drops and factors affecting the formation of stable jets and atomization. *Journal of Colloid and Interface Science, 117*(1), 205-221.

Hohman, M. M., Shin, M., Rutledge, G., & Brenner, M. P. (2001). Electrospinning and electrically forced jets. II. Applications. *Physics of fluids, 13*(8), 2221-2236.

Hong, X., Edirisinghe, M., & Mahalingam, S. (2016). Beads, beaded-fibres and fibres: Tailoring the morphology of poly (caprolactone) using pressurised gyration. *Materials Science and Engineering: C, 69*, 1373-1382.

Hong, X., Harker, A., & Edirisinghe, M. (2019). Empirical modelling and optimization of pressure-coupled infusion gyration parameters for the nanofibre fabrication. *Proceedings of the Royal Society A, 475*(2225), 20190008.

Hong, X., Mahalingam, S., & Edirisinghe, M. (2017). Simultaneous Application of Pressure‐Infusion‐Gyration to Generate Polymeric Nanofibers. *Macromolecular Materials and Engineering, 302*(6), 1600564.

Hsin, Y. L., Hwang, K. C., & Yeh, C.-T. (2007). Poly (vinylpyrrolidone)-modified graphite carbon nanofibers as promising supports for PtRu catalysts in direct methanol fuel cells. *Journal of the American Chemical Society, 129*(32), 9999-10010.

Huang, C., Ouyang, Y., Niu, H., He, N., Ke, Q., Jin, X., Li, D., Fang, J., Liu, W., Fan, C. & Lin T. (2015). Nerve guidance conduits from aligned nanofibers: improvement of nerve regeneration through longitudinal nanogrooves on a fiber surface. *ACS applied materials & interfaces, 7*(13), 7189-7196.

Huang, Z.-M., Zhang, Y.-Z., Kotaki, M., & Ramakrishna, S. (2003). A review on polymer nanofibers by electrospinning and their applications in nanocomposites. *Composites science and technology, 63*(15), 2223-2253.

Hughes, T., & Chambers, C. (1889). US Patent 405, 480. *Manufacture of carbon filaments*.

Humphrey, D., Duggan, C., Saha, D., Smith, D., & Käs, J. (2002). Active fluidization of polymer networks through molecular motors. *Nature, 416*(6879), 413.

Ilonen, J., Kamarainen, J.-K., & Lampinen, J. (2003). Differential evolution training algorithm for feed-forward neural networks. *Neural Processing Letters, 17*(1), 93-105.

Iranmanesh, S., Mehrali, M., Sadeghinezhad, E., Ang, B. C., Ong, H. C., & Esmaeilzadeh, A. (2016). Evaluation of viscosity and thermal conductivity of graphene nanoplatelets nanofluids through a combined experimental–statistical approach using respond surface methodology method. *International Communications in Heat and Mass Transfer, 79*, 74-80.

Jeong, I., Lee, J., Joseph, K. V., Lee, H. I., Kim, J. K., Yoon, S., & Lee, J. (2014). Low-cost electrospun WC/C composite nanofiber as a powerful platinum-free counter electrode for dye sensitized solar cell. *Nano Energy, 9*, 392-400.

Jiang, H., Fang, D., Hsiao, B., Chu, B., & Chen, W. (2004a). Preparation and characterization of ibuprofen-loaded poly (lactide-co-glycolide)/poly (ethylene glycol)-g-chitosan electrospun membranes. *Journal of Biomaterials Science, Polymer Edition, 15*(3), 279-296.

Jiang, H., Fang, D., Hsiao, B. S., Chu, B., & Chen, W. (2004b). Optimization and characterization of dextran membranes prepared by electrospinning. *Biomacromolecules, 5*(2), 326-333.

Kabiri, S., Tran, D. N., Altalhi, T., & Losic, D. (2014). Outstanding adsorption performance of graphene–carbon nanotube aerogels for continuous oil removal. *Carbon, 80*, 523-533.

Katti, D. S., Robinson, K. W., Ko, F. K., & Laurencin, C. T. (2004). Bioresorbable nanofiber‐based systems for wound healing and drug delivery: Optimization of fabrication parameters. *Journal of Biomedical Materials Research Part B: Applied Biomaterials: An Official Journal of The Society for Biomaterials, The Japanese Society for Biomaterials, and The Australian Society for Biomaterials and the Korean Society for Biomaterials, 70*(2), 286-296.

Kenawy, E.-R., Bowlin, G. L., Mansfield, K., Layman, J., Simpson, D. G., Sanders, E. H., & Wnek, G. E. (2002). Release of tetracycline hydrochloride from electrospun poly (ethylene-co-vinylacetate), poly (lactic acid), and a blend. *Journal of controlled release, 81*(1-2), 57-64.

Ketabchi, N., Naghibzadeh, M., Adabi, M., Esnaashari, S. S., & Faridi-Majidi, R. (2017). Preparation and optimization of chitosan/polyethylene oxide nanofiber diameter using artificial neural networks. *Neural computing and applications, 28*(11), 3131-3143.

Khani, N., Nadernezhad, A., Bartolo, P., & Koc, B. (2017). Hierarchical and spatial modeling and bio-additive manufacturing of multi-material constructs. *CIRP Annals, 66*(1), 229-232.

Khanlou, H. M., Ang, B. C., Talebian, S., Barzani, M. M., Silakhori, M., & Fauzi, H. (2015). Multi-response analysis in the processing of poly (methyl methacrylate) nano-fibres membrane by electrospinning based on response surface methodology: Fibre diameter and bead formation. *Measurement, 65*, 193-206.

Khuri, A. I., & Cornell, J. A. (2018). *Response surfaces: designs and analyses*: Routledge.

Khuri, A. I., & Mukhopadhyay, S. (2010). Response surface methodology. *Wiley Interdisciplinary Reviews: Computational Statistics, 2*(2), 128-149.

Kim, B., Park, H., Lee, S.-H., & Sigmund, W. M. (2005). Poly (acrylic acid) nanofibers by electrospinning. *Materials letters, 59*(7), 829-832.

Kim, K., Luu, Y. K., Chang, C., Fang, D., Hsiao, B. S., Chu, B., & Hadjiargyrou, M. (2004). Incorporation and controlled release of a hydrophilic antibiotic using poly (lactide-co-glycolide)-based electrospun nanofibrous scaffolds. *Journal of controlled release, 98*(1), 47-56.

Kirkpatrick, S., Gelatt, C. D., & Vecchi, M. P. (1983). Optimization by simulated annealing. *Science, 220*(4598), 671-680.

Kleijnen, J. P. (1998). Experimental design for sensitivity analysis, optimization, and validation of simulation models. *Handbook of simulation: Principles, methodology, advances, applications, and practice*, 173-223.

Kolda, T. G., Lewis, R. M., & Torczon, V. (2003). Optimization by direct search: New perspectives on some classical and modern methods. *SIAM review, 45*(3), 385-482.

Koombhongse, S., Liu, W., & Reneker, D. H. (2001). Flat polymer ribbons and other shapes by electrospinning. *Journal of Polymer Science Part B: Polymer Physics, 39*(21), 2598-2606.

Koski, A., Yim, K., & Shivkumar, S. (2004). Effect of molecular weight on fibrous PVA produced by electrospinning. *Materials letters, 58*(3-4), 493-497.

Kost, J., & Langer, R. (2012). Responsive polymeric delivery systems. *Advanced drug delivery reviews, 64*, 327-341.

Kriegel, H. P., Kröger, P., Sander, J., & Zimek, A. (2011). Density‐based clustering. *Wiley Interdisciplinary Reviews: Data Mining and Knowledge Discovery, 1*(3), 231-240.

Kumbar, S., James, R., Nukavarapu, S., & Laurencin, C. (2008). Electrospun nanofiber scaffolds: engineering soft tissues. *Biomedical materials, 3*(3), 034002.

Lai, C., Guo, Q., Wu, X.-F., Reneker, D. H., & Hou, H. (2008). Growth of carbon nanostructures on carbonized electrospun nanofibers with palladium nanoparticles. *Nanotechnology, 19*(19), 195303.

Larrondo, L., & St. John Manley, R. (1981). Electrostatic fiber spinning from polymer melts. I. Experimental observations on fiber formation and properties. *Journal of Polymer Science: Polymer Physics Edition, 19*(6), 909-920.

Lee, C., Jo, S. M., Choi, J., Baek, K.-Y., Truong, Y. B., Kyratzis, I. L., & Shul, Y.-G. (2013). SiO 2/sulfonated poly ether ether ketone (SPEEK) composite nanofiber mat supported proton exchange membranes for fuel cells. *Journal of materials science, 48*(10), 3665-3671.

Lee, K. Y., Jeong, L., Kang, Y. O., Lee, S. J., & Park, W. H. (2009). Electrospinning of polysaccharides for regenerative medicine. *Advanced drug delivery reviews, 61*(12), 1020-1032.

Li, C., Vepari, C., Jin, H.-J., Kim, H. J., & Kaplan, D. L. (2006). Electrospun silk-BMP-2 scaffolds for bone tissue engineering. *Biomaterials, 27*(16), 3115-3124.

Li, D., & Xia, Y. (2004). Electrospinning of nanofibers: reinventing the wheel? *Advanced materials, 16*(14), 1151-1170.

Li, W., Li, M., Adair, K. R., Sun, X., & Yu, Y. (2017). Carbon nanofiber-based nanostructures for lithium-ion and sodium-ion batteries. *Journal of Materials Chemistry A, 5*(27), 13882-13906.

Li, W., Liang, C., Zhou, W., Qiu, J., Zhou, Z., Sun, G., & Xin, Q. (2003). Preparation and characterization of multiwalled carbon nanotube-supported platinum for cathode catalysts of direct methanol fuel cells. *The Journal of Physical Chemistry B, 107*(26), 6292-6299.

Li, W., Xiao, M., Peng, X., Garg, A., & Gao, L. (2019). A surrogate thermal modeling and parametric optimization of battery pack with air cooling for EVs. *Applied Thermal Engineering, 147*, 90-100.

Li, W. J., Laurencin, C. T., Caterson, E. J., Tuan, R. S., & Ko, F. K. (2002). Electrospun nanofibrous structure: a novel scaffold for tissue engineering. *Journal of Biomedical Materials Research: An Official Journal of The Society for Biomaterials, The Japanese Society for Biomaterials, and The Australian Society for Biomaterials and the Korean Society for Biomaterials, 60*(4), 613-621.

Li, Y., Gong, J., He, G., & Deng, Y. (2011). Fabrication of polyaniline/titanium dioxide composite nanofibers for gas sensing application. *Materials Chemistry and Physics, 129*(1-2), 477-482.

Li, Z., & Wang, C. (2013). *One-dimensional nanostructures: electrospinning technique and unique nanofibers*: Springer.

Lin, T., Wang, X., Wang, X., & Niu, H. (2010). *Electrostatic spinning assembly.* Deakin University.

Ling, Z., Cao, J., Zhang, W., Zhang, Z., Fang, X., & Gao, X. (2018). Compact liquid cooling strategy with phase change materials for Li-ion batteries optimized using response surface methodology. *Applied Energy, 228*, 777-788.

Liu, C., Fan, Y., Liu, M., Cong, H., Cheng, H., & Dresselhaus, M. S. (1999). Hydrogen storage in single-walled carbon nanotubes at room temperature. *Science, 286*(5442), 1127-1129.

Liu, H.-Y., Chen, Y., Liu, G.-S., Pei, S.-G., Liu, J.-Q., Ji, H., & Wang, R.-D. (2013). Preparation of high-quality zirconia fibers by super-high rotational centrifugal spinning of inorganic sol. *Materials and Manufacturing Processes, 28*(2), 133-138.

Liu, J.-M., & Yang, S. C. (1991). Novel colloidal polyaniline fibrils made by template guided chemical polymerization. *Journal of the Chemical Society, Chemical Communications*(21), 1529-1531.

Liu, W., Thomopoulos, S., & Xia, Y. (2012). Electrospun nanofibers for regenerative medicine. *Advanced healthcare materials, 1*(1), 10-25.

Lobo, L. S. (2017). Nucleation and growth of carbon nanotubes and nanofibers: mechanism and catalytic geometry control. *Carbon, 114*, 411-417.

Lord, R. (1878). On the instability of jets. *Proceedings of the London Mathematical Society, 10*(1), 4-13.

Lundstedt, T., Seifert, E., Abramo, L., Thelin, B., Nyström, Å., Pettersen, J., & Bergman, R. (1998). Experimental design and optimization. *Chemometrics and intelligent laboratory systems, 42*(1-2), 3-40.

Luo, C., Stride, E., & Edirisinghe, M. (2012). Mapping the influence of solubility and dielectric constant on electrospinning polycaprolactone solutions. *Macromolecules, 45*(11), 4669-4680.

Luu, Y., Kim, K., Hsiao, B., Chu, B., & Hadjiargyrou, M. (2003). Development of a nanostructured DNA delivery scaffold via electrospinning of PLGA and PLA–PEG block copolymers. *Journal of controlled release, 89*(2), 341-353.

Ma, P. X., & Zhang, R. (1999). Synthetic nano‐scale fibrous extracellular matrix. *Journal of Biomedical Materials Research: An Official Journal of The Society for Biomaterials, The Japanese Society for Biomaterials, and The Australian Society for Biomaterials, 46*(1), 60-72.

Ma, Z., Kotaki, M., Inai, R., & Ramakrishna, S. (2005). Potential of nanofiber matrix as tissue-engineering scaffolds. *Tissue engineering, 11*(1-2), 101-109.

Macossay, J., Marruffo, A., Rincon, R., Eubanks, T., & Kuang, A. (2007). Effect of needle diameter on nanofiber diameter and thermal properties of electrospun poly (methyl methacrylate). *Polymers for Advanced Technologies, 18*(3), 180-183.

Mahalingam, S., & Edirisinghe, M. (2013). Forming of polymer nanofibers by a pressurised gyration process. *Macromolecular rapid communications, 34*(14), 1134-1139.

Mahalingam, S., Pierin, G., Colombo, P., & Edirisinghe, M. (2015). Facile one-pot formation of ceramic fibres from preceramic polymers by pressurised gyration. *Ceramics International, 41*(4), 6067-6073.

Martin, C. R. (1996). Membrane-based synthesis of nanomaterials. *Chemistry of Materials, 8*(8), 1739-1746.

McCulloch, W. S., & Pitts, W. (1943). A logical calculus of the ideas immanent in nervous activity. *The bulletin of mathematical biophysics, 5*(4), 115-133.

Mellado, P., McIlwee, H. A., Badrossamay, M. R., Goss, J. A., Mahadevan, L., & Kit Parker, K. (2011). A simple model for nanofiber formation by rotary jet-spinning. *Applied Physics Letters, 99*(20), 203107.

Mikos, A. G., Bao, Y., Cima, L. G., Ingber, D. E., Vacanti, J. P., & Langer, R. (1993). Preparation of poly (glycolic acid) bonded fiber structures for cell attachment and transplantation. *Journal of biomedical materials research, 27*(2), 183-189.

Mit‐uppatham, C., Nithitanakul, M., & Supaphol, P. (2004). Ultrafine electrospun polyamide‐6 fibers: effect of solution conditions on morphology and average fiber diameter. *Macromolecular Chemistry and Physics, 205*(17), 2327-2338.

Mohamad, F., Mat Zaid, M., Abdullah, J., Zawawi, R., Lim, H., Sulaiman, Y., & Abdul Rahman, N. (2017). Synthesis and characterization of polyaniline/graphene composite nanofiber and its application as an electrochemical DNA biosensor for the detection of Mycobacterium tuberculosis. *Sensors, 17*(12), 2789.

Mondal, K., & Sharma, A. (2016). Recent advances in electrospun metal-oxide nanofiber based interfaces for electrochemical biosensing. *RSC Advances, 6*(97), 94595-94616.

Montgomery, D. C. (2017). *Design and analysis of experiments*: John wiley & sons.

Moon, J., Park, J.-A., Lee, S.-J., Zyung, T., & Kim, I.-D. (2010). Pd-doped TiO2 nanofiber networks for gas sensor applications. *Sensors and Actuators B: Chemical, 149*(1), 301-305.

Morton, W. (1902). Method of dispersing fluids. US 705691A.

Mota, C., Puppi, D., Chiellini, F., & Chiellini, E. (2015). Additive manufacturing techniques for the production of tissue engineering constructs. *Journal of tissue engineering and regenerative medicine, 9*(3), 174-190.

Myers, R. H., & Montgomery, D. C. (1995). Response surface methodology: process improvement with steepest ascent, the analysis of response surfaces, experimental designs for fitting response surfaces: New York: John Wiley and Sons, Inc.

Myers, R. H., Montgomery, D. C., & Anderson-Cook, C. M. (2016). *Response surface methodology: process and product optimization using designed experiments*: John Wiley & Sons.

Nadernezhad, A., Khani, N., Skvortsov, G. A., Toprakhisar, B., Bakirci, E., Menceloglu, Y., Unal, S. & Koc, B. (2016). Multifunctional 3D printing of heterogeneous hydrogel structures. *Scientific reports, 6*, 33178.

Nain, A. S., Sitti, M., Jacobson, A., Kowalewski, T., & Amon, C. (2009). Dry spinning based spinneret based tunable engineered parameters (STEP) technique for controlled and aligned deposition of polymeric nanofibers. *Macromolecular rapid communications, 30*(16), 1406-1412.

Nakane, K., & Ogata, N. (2010). Photocatalyst Nanofibers Obtained by Calcination of Organic-Inorganic Hybrids *Nanofibers*: IntechOpen.

Nasouri, K., Shoushtari, A. M., & Khamforoush, M. (2013). Comparison between artificial neural network and response surface methodology in the prediction of the

production rate of polyacrylonitrile electrospun nanofibers. *Fibers and Polymers, 14*(11), 1849-1856.

Nelder, J. A., & Mead, R. (1965). A simplex method for function minimization. *The computer journal, 7*(4), 308-313.

Ning, F., Cong, W., Hu, Y., & Wang, H. (2017). Additive manufacturing of carbon fiber-reinforced plastic composites using fused deposition modeling: Effects of process parameters on tensile properties. *Journal of Composite Materials, 51*(4), 451-462.

Ning, F., Cong, W., Qiu, J., Wei, J., & Wang, S. (2015). Additive manufacturing of carbon fiber reinforced thermoplastic composites using fused deposition modeling. *Composites Part B: Engineering, 80*, 369-378.

Niu, H., & Lin, T. (2012). Fiber generators in needleless electrospinning. *Journal of nanomaterials, 2012*, 12.

Nivison‐Smith, L., & Weiss, A. S. (2012). Alignment of human vascular smooth muscle cells on parallel electrospun synthetic elastin fibers. *Journal of Biomedical Materials Research Part A, 100*(1), 155-161.

Nongonierma, A. B., Maux, S. L., Esteveny, C., & FitzGerald, R. J. (2017). Response surface methodology applied to the generation of casein hydrolysates with antioxidant and dipeptidyl peptidase IV inhibitory properties. *Journal of the Science of Food and Agriculture, 97*(4), 1093-1101.

Oliveira, M. S., Yeh, R., & McKinley, G. H. (2006). Iterated stretching, extensional rheology and formation of beads-on-a-string structures in polymer solutions. *Journal of non-Newtonian fluid mechanics, 137*(1-3), 137-148.

Onwubolu, G. C., & Babu, B. (2013). *New optimization techniques in engineering* (Vol. 141): Springer.

Parhizkar, M., Mahalingam, S., Homer-Vanniasinkam, S., & Edirisinghe, M. (2018). Latest developments in innovative manufacturing to combine nanotechnology with healthcare: Future Medicine, *13*(1), 5-8.

Persano, L., Dagdeviren, C., Su, Y., Zhang, Y., Girardo, S., Pisignano, D., Huang, Y. & Rogers, J. A. (2013). High performance piezoelectric devices based on aligned arrays of nanofibers of poly (vinylidenefluoride-co-trifluoroethylene). *Nature communications, 4*, 1633.

Perutz, M. F., Finch, J. T., Berriman, J., & Lesk, A. (2002). Amyloid fibers are water-filled nanotubes. *Proceedings of the National Academy of Sciences, 99*(8), 5591-5595.

Pimentel, M. F., & Neto, B. B. (1996). Calibração: uma revisão para químicos analíticos. *Química Nova, 19*(3), 268-277.

Plagianakos, V. P., & Vrahatis, M. N. (2002). Parallel evolutionary training algorithms for "hardware-friendly" neural networks. *Natural Computing, 1*(2-3), 307-322.

Pokropivny, V., & Skorokhod, V. (2007). Classification of nanostructures by dimensionality and concept of surface forms engineering in nanomaterial science. *Materials Science and Engineering: C, 27*(5-8), 990-993.

Poole, D. L., & Mackworth, A. K. (2010). *Artificial Intelligence: foundations of computational agents*: Cambridge University Press.

Pop, E., Mann, D., Wang, Q., Goodson, K., & Dai, H. (2006). Thermal conductance of an individual single-wall carbon nanotube above room temperature. *Nano letters, 6*(1), 96-100.

Powell, M. (1998). Direct search algorithms for optimization calculations. *Acta numerica, 7*, 287-336.

Price, K., & Storn, R. (2001). Differential evolution homepage. *The URL of which is:* http://www/*ICSI. Berkeley. edu/~ storn/code. html*.

Price, K., Storn, R. M., & Lampinen, J. A. (2006). *Differential evolution: a practical approach to global optimization*: Springer Science & Business Media.

Ragavendran, M., Chandrasekhar, N., Ravikumar, R., Saxena, R., Vasudevan, M., & Bhaduri, A. (2017). Optimization of hybrid laser–TIG welding of 316LN steel using response surface methodology (RSM). *Optics and Lasers in Engineering, 94*, 27-36.

Rahmani, M., Ghasemi, E., & Sasani, M. (2017). Application of response surface methodology for air assisted-dispersive liquid-liquid microextraction of deoxynivalenol in rice samples prior to HPLC-DAD analysis and comparison with solid phase extraction cleanup. *Talanta, 165*, 27-32.

Ramakrishna, S. (2005). *An introduction to electrospinning and nanofibers*: World Scientific.

Ramakrishna, S., Fujihara, K., Teo, W.-E., Yong, T., Ma, Z., & Ramaseshan, R. (2006). Electrospun nanofibers: solving global issues. *Materials Today, 9*(3), 40-50.

Rayleigh, L. (1882). XX. On the equilibrium of liquid conducting masses charged with electricity. *The London, Edinburgh, and Dublin Philosophical Magazine and Journal of Science, 14*(87), 184-186.

Reisi-Dehkordi, A., & Eslami-Farsani, R. (2015). Prediction of high performance fibers strength using back propagation neural network. *Journal of Macromolecular Science, Part A, 52*(8), 642-647.

Reneker, D. H., & Chun, I. (1996). Nanometre diameter fibres of polymer, produced by electrospinning. *Nanotechnology, 7*(3), 216.

Reneker, D. H., Yarin, A. L., Fong, H., & Koombhongse, S. (2000). Bending instability of electrically charged liquid jets of polymer solutions in electrospinning. *Journal of Applied physics, 87*(9), 4531-4547.

Reubsaet, K. J., Norli, H. R., Hemmersbach, P., & Rasmussen, K. E. (1998). Determination of benzodiazepines in human urine and plasma with solvent modified solid phase micro extraction and gas chromatography; rationalisation of method development using experimental design strategies. *Journal of pharmaceutical and biomedical analysis, 18*(4-5), 667-680.

Rijal, N. P., Adhikari, U., Khanal, S., Pai, D., Sankar, J., & Bhattarai, N. (2018). Magnesium oxide-poly (ε-caprolactone)-chitosan-based composite nanofiber for tissue engineering applications. *Materials Science and Engineering: B, 228*, 18-27.

Roco, M. C. (2003). Nanotechnology: convergence with modern biology and medicine. *Current opinion in biotechnology, 14*(3), 337-346.

Roco, M. C., Mirkin, C. A., & Hersam, M. C. (2011). Nanotechnology research directions for societal needs in 2020: summary of international study: Springer.

Rosoff, M. (2001). *Nano-surface chemistry*: CRC Press.

Rowe, R. C., Sheskey, P., & Quinn, M. (2009). *Handbook of pharmaceutical excipients*: Libros Digitales-Pharmaceutical Press.

Rumelhart, D. E., Hinton, G. E., & Williams, R. J. (1985). *Learning internal representations by error propagation* (No. ICS-8506). California Univ San Diego La Jolla Inst for Cognitive Science.

Rupprecht, A. (1966). Preparation of oriented DNA by wet spinning. *Acta Chem Scand, 20*(2), 494-504.

Russell, S. J., & Norvig, P. (2016). *Artificial intelligence: a modern approach*: Malaysia; Pearson Education Limited.

Saad, M., Tahir, H., Khan, J., Hameed, U., & Saud, A. (2017). Synthesis of polyaniline nanoparticles and their application for the removal of crystal violet dye by ultrasonicated adsorption process based on response surface methodology. *Ultrasonics sonochemistry, 34*, 600-608.

Sahay, R., Kumar, P. S., Sridhar, R., Sundaramurthy, J., Venugopal, J., Mhaisalkar, S. G., & Ramakrishna, S. (2012). Electrospun composite nanofibers and their multifaceted applications. *Journal of Materials Chemistry, 22*(26), 12953-12971.

Sarkar, K., Gomez, C., Zambrano, S., Ramirez, M., de Hoyos, E., Vasquez, H., & Lozano, K. (2010). Electrospinning to forcespinning™. *Materials Today, 13*(11), 12-14.

Schubert, E., Sander, J., Ester, M., Kriegel, H. P., & Xu, X. (2017). DBSCAN revisited, revisited: why and how you should (still) use DBSCAN. *ACM Transactions on Database Systems (TODS), 42*(3), 19.

Shang, M., Wang, W., Yin, W., Ren, J., Sun, S., & Zhang, L. (2010). General Strategy for a Large‐Scale Fabric with Branched Nanofiber–Nanorod Hierarchical Heterostructure: Controllable Synthesis and Applications. *Chemistry–A European Journal, 16*(37), 11412-11419.

Shendokar, S., Kelkar, A., Mohan, R., Bolick, R., & Chandekar, G. (2008). *Effect of sintering temperature on mechanical properties of electrospun silica nanofibers.* Paper presented at the ASME 2008 International Mechanical Engineering Congress and Exposition.

Shi, H., Yu, Y., Zhang, Y., Feng, X., Zhao, X., Tan, H., Khan, S.U., Li, Y. & Wang, E. (2018). Polyoxometalate/TiO2/Ag composite nanofibers with enhanced photocatalytic performance under visible light. *Applied Catalysis B: Environmental, 221*, 280-289.

Shi, X., Zhou, W., Ma, D., Ma, Q., Bridges, D., Ma, Y., & Hu, A. (2015). Electrospinning of nanofibers and their applications for energy devices. *Journal of nanomaterials, 16*(1), 122.

Shirvan, K. M., Mamourian, M., Mirzakhanlari, S., & Ellahi, R. (2017). Numerical investigation of heat exchanger effectiveness in a double pipe heat exchanger filled with nanofluid: a sensitivity analysis by response surface methodology. *Powder technology, 313*, 99-111.

Sill, T. J., & von Recum, H. A. (2008). Electrospinning: applications in drug delivery and tissue engineering. *Biomaterials, 29*(13), 1989-2006.

Smith, L., & Ma, P. (2004). Nano-fibrous scaffolds for tissue engineering. *Colloids and surfaces B: biointerfaces, 39*(3), 125-131.

Son, W. K., Youk, J. H., Lee, T. S., & Park, W. H. (2004). The effects of solution properties and polyelectrolyte on electrospinning of ultrafine poly (ethylene oxide) fibers. *Polymer, 45*(9), 2959-2966.

Son, W. K., Youk, J. H., & Park, W. H. (2006). Antimicrobial cellulose acetate nanofibers containing silver nanoparticles. *Carbohydrate Polymers, 65*(4), 430-434.

Song, M. Y., Kim, D. K., Ihn, K. J., Jo, S. M., & Kim, D. Y. (2004). Electrospun TiO2 electrodes for dye-sensitized solar cells. *Nanotechnology, 15*(12), 1861.

Stein, M. L. (2012). *Interpolation of spatial data: some theory for kriging*: Springer Science & Business Media.

Storn, R., & Price, K. (1997). Differential evolution–a simple and efficient heuristic for global optimization over continuous spaces. *Journal of global optimization, 11*(4), 341-359.

Subbiah, T., Bhat, G., Tock, R., Parameswaran, S., & Ramkumar, S. (2005). Electrospinning of nanofibers. *Journal of applied polymer science, 96*(2), 557-569.

Subramani, K., & Ahmed, W. (2012). Self-Assembly of Proteins and Peptides and Their Applications in Bionanotechnology and Dentistry *Emerging Nanotechnologies in Dentistry* (pp. 209-224): Elsevier.

Teo, W. E., & Ramakrishna, S. (2006). A review on electrospinning design and nanofibre assemblies. *Nanotechnology, 17*(14), R89.

Teófilo, R. F., & Ferreira, M. (2006). Quimiometria II: planilhas eletrônicas para cálculos de planejamentos experimentais, um tutorial. *Química Nova*.

Theron, S., Yarin, A., Zussman, E., & Kroll, E. (2005). Multiple jets in electrospinning: experiment and modeling. *Polymer, 46*(9), 2889-2899.

Tiwari, J. N., Tiwari, R. N., & Kim, K. S. (2012). Zero-dimensional, one-dimensional, two-dimensional and three-dimensional nanostructured materials for advanced electrochemical energy devices. *Progress in Materials Science, 57*(4), 724-803.

Torres‐Giner, S., Pérez‐Masiá, R., & Lagaron, J. M. (2016). A review on electrospun polymer nanostructures as advanced bioactive platforms. *Polymer Engineering & Science, 56*(5), 500-527.

Tsai, P. P., Schreuder-Gibson, H., & Gibson, P. (2002). Different electrostatic methods for making electret filters. *Journal of electrostatics, 54*(3-4), 333-341.

Verreck, G., Chun, I., Peeters, J., Rosenblatt, J., & Brewster, M. E. (2003). Preparation and characterization of nanofibers containing amorphous drug dispersions generated by electrostatic spinning. *Pharmaceutical research, 20*(5), 810-817.

Vetterling, W. T., Teukolsky, S. A., Press, W. H., & Flannery, B. P. (1992). *Numerical recipes: the art of scientific computing* (Vol. 2): Cambridge university press Cambridge.

Wächter, R., & Cordery, A. (1999). Response surface methodology modelling of diamond-like carbon film deposition. *Carbon, 37*(10), 1529-1537.

Wang, C., Wang, Z., Li, M., & Li, H. (2001). Well-aligned polyaniline nano-fibril array membrane and its field emission property. *Chemical Physics Letters, 341*(5-6), 431-434.

Wang, H., Zhang, X., Wang, N., Li, Y., Feng, X., Huang, Y., Zhao, C., Liu, Z., Fang, M., Ou, G. & Gao, H. (2017). Ultralight, scalable, and high-temperature–resilient ceramic nanofiber sponges. *Science advances, 3*(6), e1603170.

Wang, L., Shi, J., Liu, L., Secret, E., & Chen, Y. (2011). Fabrication of polymer fiber scaffolds by centrifugal spinning for cell culture studies. *Microelectronic Engineering, 88*(8), 1718-1721.

Wei, Q. (2012). *Functional nanofibers and their applications*: Elsevier.

Wei, Z., Zhang, Z., & Wan, M. (2002). Formation mechanism of self-assembled polyaniline micro/nanotubes. *Langmuir, 18*(3), 917-921.

Whitesides, G. M., & Grzybowski, B. (2002). Self-assembly at all scales. *Science, 295*(5564), 2418-2421.

Witek-Krowiak, A., Chojnacka, K., Podstawczyk, D., Dawiec, A., & Pokomeda, K. (2014). Application of response surface methodology and artificial neural network methods in modelling and optimization of biosorption process. *Bioresource technology, 160*, 150-160.

Wright, M. H. (1996). Direct search methods: Once scorned, now respectable. *Pitman Research Notes in Mathematics Series*, 191-208.

Wu, C.-G., & Bein, T. (1994). Conducting polyaniline filaments in a mesoporous channel host. *Science, 264*(5166), 1757-1759.

Wu, X., Mahalingam, S., Amir, A., Porwal, H., Reece, M. J., Naglieri, V., Colombo, P. & Edirisinghe, M. (2016). Novel preparation, microstructure, and properties of polyacrylonitrile-based carbon nanofiber–graphene nanoplatelet materials. *ACS Omega, 1*(2), 202-211.

Xing, Z., Pei, J., & Keogh, E. (2010). A brief survey on sequence classification. *ACM Sigkdd Explorations Newsletter, 12*(1), 40-48.

Xu, Z., Mahalingam, S., Basnett, P., Raimi‐Abraham, B., Roy, I., Craig, D., & Edirisinghe, M. (2016). Making Nonwoven Fibrous Poly (ε‐caprolactone) Constructs for Antimicrobial and Tissue Engineering Applications by Pressurised Melt Gyration. *Macromolecular Materials and Engineering, 301*(8), 922-934.

Yamamoto, K., Otsuka, H., Takahara, A., & Wada, S.-I. (2002). Preparation of a novel (polymer/inorganic nanofiber) composite through surface modification of natural aluminosilicate nanofiber. *The Journal of Adhesion, 78*(7), 591-602.

Yarin, A., & Zussman, E. (2004). Upward needleless electrospinning of multiple nanofibers. *Polymer, 45*(9), 2977-2980.

Zanin, M. H. A., Cerize, N. N., & de Oliveira, A. M. (2011). Production of nanofibers by electrospinning technology: overview and application in cosmetics *Nanocosmetics and Nanomedicines* (pp. 311-332): Springer.

Zeng, J., Haoqing, H., Schaper, A., Wendorff, J. H., & Greiner, A. (2003). Poly-L-lactide nanofibers by electrospinning–Influence of solution viscosity and electrical conductivity on fiber diameter and fiber morphology. *e-Polymers, 3*(1).

Zeng, J., Xu, X., Chen, X., Liang, Q., Bian, X., Yang, L., & Jing, X. (2003). Biodegradable electrospun fibers for drug delivery. *Journal of controlled release, 92*(3), 227-231.

Zhang, C., Yuan, X., Wu, L., Han, Y., & Sheng, J. (2005). Study on morphology of electrospun poly (vinyl alcohol) mats. *European polymer journal, 41*(3), 423-432.

Zhang, L., Menkhaus, T. J., & Fong, H. (2008). Fabrication and bioseparation studies of adsorptive membranes/felts made from electrospun cellulose acetate nanofibers. *Journal of Membrane Science, 319*(1-2), 176-184.

Zhang, R., & Ma, P. X. (2000). Synthetic nano‐fibrillar extracellular matrices with predesigned macroporous architectures. *Journal of Biomedical Materials Research: An Official Journal of The Society for Biomaterials, The Japanese Society for Biomaterials, and The Australian Society for Biomaterials and the Korean Society for Biomaterials, 52*(2), 430-438.

Zhang, S. (2003). Fabrication of novel biomaterials through molecular self-assembly. *Nature biotechnology, 21*(10), 1171.

Zhang, S., Karaca, B. T., VanOosten, S. K., Yuca, E., Mahalingam, S., Edirisinghe, M., & Tamerler, C. (2015). Coupling infusion and gyration for the nanoscale assembly of functional polymer nanofibers integrated with genetically engineered proteins. *Macromolecular rapid communications, 36*(14), 1322-1328.

Zhang, X., & Lu, Y. (2014). Centrifugal spinning: an alternative approach to fabricate nanofibers at high speed and low cost. *Polymer Reviews, 54*(4), 677-701.

Zhang, Y., Venugopal, J., Huang, Z.-M., Lim, C., & Ramakrishna, S. (2006). Crosslinking of the electrospun gelatin nanofibers. *Polymer, 47*(8), 2911-2917.

Zhao, Z., Li, J., Yuan, X., Li, X., Zhang, Y., & Sheng, J. (2005). Preparation and properties of electrospun poly (vinylidene fluoride) membranes. *Journal of applied polymer science, 97*(2), 466-474.

Zheng, G., Yang, Y., Cha, J. J., Hong, S. S., & Cui, Y. (2011). Hollow carbon nanofiber-encapsulated sulfur cathodes for high specific capacity rechargeable lithium batteries. *Nano letters, 11*(10), 4462-4467.

Zheng, J., Zhang, H., Zhao, Z., & Han, C. C. (2012). Construction of hierarchical structures by electrospinning or electrospraying. *Polymer, 53*(2), 546-554.

Zheng, Y., Liu, Y., & Wang, A. (2011). Fast removal of ammonium ion using a hydrogel optimized with response surface methodology. *Chemical engineering journal, 171*(3), 1201-1208.

Zhou, F. L., Gong, R. H., & Porat, I. (2009). Mass production of nanofibre assemblies by electrostatic spinning. *Polymer International, 58*(4), 331-342.

Zhou, S. K., Greenspan, H., & Shen, D. (2017). *Deep learning for medical image analysis*: Academic Press.

Zhu, H. Y., Riches, J. D., & Barry, J. C. (2002). γ-alumina nanofibers prepared from aluminum hydrate with poly (ethylene oxide) surfactant. *Chemistry of Materials, 14*(5), 2086-2093.

Zhu, X., & Goldberg, A. B. (2009). Introduction to semi-supervised learning. *Synthesis lectures on artificial intelligence and machine learning, 3*(1), 1-130.

Zhu, X. J. (2005). *Semi-supervised learning literature survey*. University of Wisconsin-Madison Department of Computer Sciences.

Zong, X., Fang, D., Kim, K., Ran, S., Hsiao, B., Chu, B., Brathwaite, C., Li, S. & Chen, E. (2002). *Nonwoven nanofiber membranes of poly (lactide) and poly (glycolide-co-lactide) via electrospinning and applications for anti-adhesions.* Paper presented at the ABSTRACTS OF PAPERS OF THE AMERICAN CHEMICAL SOCIETY.

Zuo, W., Zhu, M., Yang, W., Yu, H., Chen, Y., & Zhang, Y. (2005). Experimental study on relationship between jet instability and formation of beaded fibers during electrospinning. *Polymer Engineering & Science, 45*(5), 704-709.

Appendix

Categories of Machine Learning Techniques

Machine learning techniques can be categorised in many different ways. For example, according to whether each training example is assigned a category label, they can be divided into supervised, unsupervised and semi-supervised techniques. They can also be divided according to if there is a hierarchical relationship existing between classes in the data, or according to whether the feature vector/ distance matrix is needed as input, can be divided into feature based and distance based techniques.

Supervised or Unsupervised or Semi-supervised

Machine learning techniques can be mainly divided into three categories based on the existence of labels in the model building process.

Supervised learning, which guided by the labelled examples in the learning process and can use them to apply what has been trained in the past to unseen data to predict future trends. Starts from the investigation of existing training sets, the algorithm generates an inference function to predict the output values. Once fully trained, the resulting system can provide targets on the basis of new inputs. The learning algorithm is also able to compare its output value to the labelled, expected output and lookup errors to adjust the model accordingly.

Unsupervised learning, which can infer a function of describing hidden structures without the aiding of labelling information. Rather than figure out the correct output

value, the system explores the intrinsic properties of the data and derive inferences to describe the structures of the unlabelled data.

Semi-supervised learning is a class of algorithms that falls between supervised and unsupervised learning. It combines both labelled and unlabelled data in the learning process – typically a much larger amount of unlabelled data with a small amount of labelled data. In many works, this type of data conjunction can provide considerable improvement in learning accuracy over unsupervised learning. Often semi-supervised learning is selected when acquiring a fully labelled training set is infeasible (Chapelle, Scholkopf, & Zien, 2009; X. Zhu & Goldberg, 2009; X. J. Zhu, 2005).

Feature Based or Distance Based

Machine learning methods can also be divided based on their mechanisms for operating distance measurements and features. There are mainly three types of them. Firstly, feature based methods, they need to use feature representations of original data in the training process as inputs and assign labels by examining the discriminating power of the individual variables that make up each feature. The typical feature based methods like Decision Trees and Random Forest. The second type are distance based methods, in contrast to feature based methods, feature representations are not compulsory but the pairwise distance between samples. These methods take the distance matrix calculated from all samples in the data as input and combine nearby samples together. The typical examples of these methods are K-nearest neighbours and K-Means. The third type combines the above two, such as kernel methods, which require feature representations and distance measurement definitions. They take features as input and transform them into high-

dimensional spaces using kernel function, which function similarly to distance metrics(Xing, Pei, & Keogh, 2010).

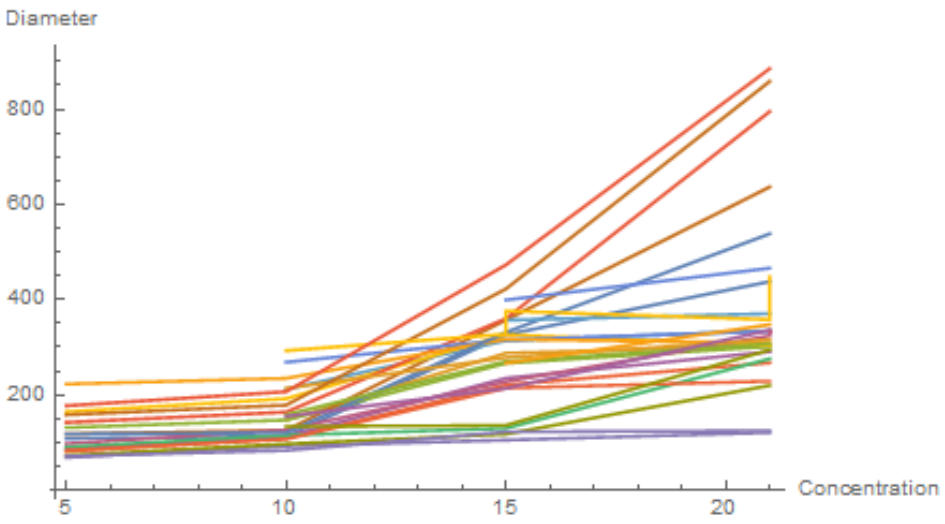

Flow rate(μL/min)	Pressure (MPa)	Rotational Speed (RPM)
500	0.1	36000
500	0.2	10000
500	0.2	24000
500	0.2	36000
500	0.3	36000
1000	0.1	36000
1000	0.2	10000
1000	0.2	24000
1000	0.2	36000
1000	0.3	36000
2000	0.1	36000
2000	0.2	10000
2000	0.2	24000
2000	0.2	36000
2000	0.3	36000
3000	0.1	36000
3000	0.2	10000
3000	0.2	24000
3000	0.2	36000
3000	0.3	36000
2000	0.1	36000
2000	0.2	10000
2000	0.2	24000
2000	0.2	36000
2000	0.3	36000
3000	0.1	36000
3000	0.2	10000
3000	0.2	24000
3000	0.2	36000
3000	0.3	36000

(a)

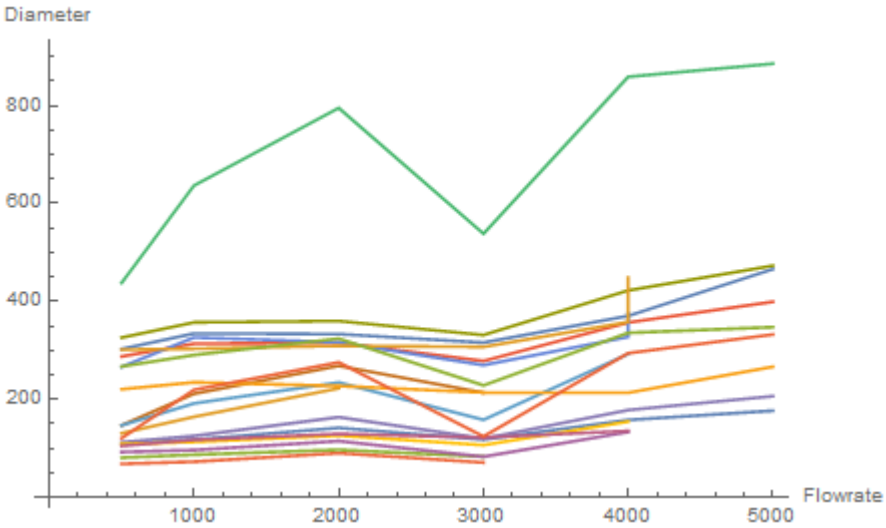

Concentration (wt%)	Pressure (MPa)	Rotational Speed (RPM)
5	0.1	36000
5	0.2	24000
5	0.2	36000
5	0.3	36000
10	0.1	36000
10	0.2	10000
10	0.2	24000
10	0.2	36000
10	0.3	36000
15	0.1	36000
15	0.2	10000
15	0.2	24000
15	0.2	36000
15	0.3	36000
21	0.1	36000
21	0.2	10000
21	0.2	24000
21	0.2	36000
21	0.3	36000

(b)

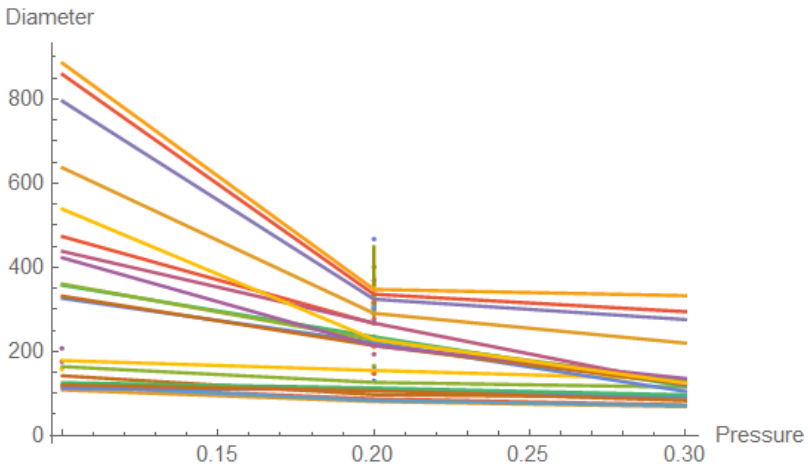

Concentration (wt%)	Flow rate (µL/min)	Rotational Speed (RPM)
5	500	24000
5	500	36000
5	1000	24000
5	1000	36000
5	2000	24000
5	2000	36000
5	3000	36000
5	4000	36000
5	5000	36000
10	500	10000
10	500	24000
10	500	36000
10	1000	10000
10	1000	24000
10	1000	36000
10	2000	10000
10	2000	24000
10	2000	36000
10	3000	10000
10	3000	24000
10	3000	36000
10	4000	24000
10	5000	36000
10	5000	36000
15	500	10000
15	500	24000
15	500	36000
15	1000	10000
15	1000	24000
15	1000	36000

—	15	2000	10000
—	15	2000	24000
—	15	2000	36000
—	15	3000	10000
—	15	3000	24000
—	15	3000	36000
—	15	4000	10000
—	15	4000	24000
—	15	4000	36000
—	15	5000	10000
—	15	5000	36000
—	21	500	10000
—	21	500	24000
—	21	500	36000
—	21	1000	10000
—	21	1000	24000
—	21	1000	36000
—	21	2000	10000
—	21	2000	24000
—	21	2000	36000

(c)

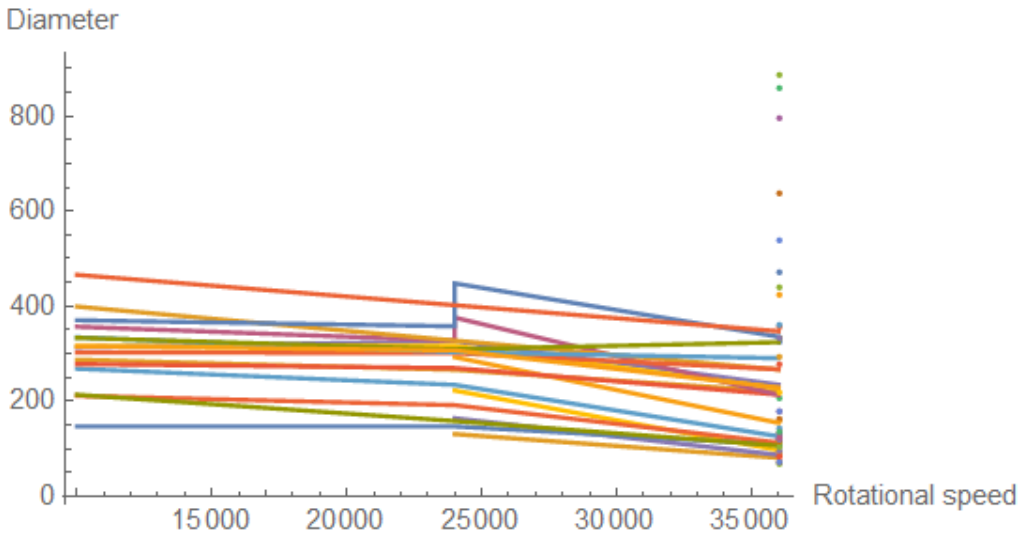

	Concentration (wt%)	Flow rate (μL/min)	Pressure (MPa)
—	5	500	0.1
—	5	500	0.2
—	5	500	0.3
—	5	1000	0.1
—	5	1000	0.2
—	5	1000	0.3
—	5	2000	0.1
—	5	2000	0.2
—	5	2000	0.3
—	5	3000	0.1

	5	3000	0.2
	5	3000	0.3
	5	4000	0.1
	5	5000	0.1
	10	500	0.1
	10	500	0.2
	10	500	0.3
	10	1000	0.1
	10	1000	0.2
	10	1000	0.3
	10	2000	0.1
	10	2000	0.2
	10	2000	0.3
	10	3000	0.1
	10	3000	0.2
	10	3000	0.3
	10	4000	0.1
	10	4000	0.2
	10	4000	0.3
	10	5000	0.1
	15	500	0.1
	15	500	0.2
	15	500	0.3
	15	1000	0.1
	15	1000	0.2
	15	1000	0.3
	15	2000	0.1
	15	2000	0.2
	15	2000	0.3
	15	3000	0.1
	15	3000	0.2
	15	3000	0.3
	15	4000	0.1
	15	4000	0.2
	15	4000	0.3
	15	5000	0.1
	15	5000	0.2
	21	500	0.1
	21	500	0.2
	21	500	0.3

—	21	1000	0.1
—	21	1000	0.2
—	21	1000	0.3
—	21	2000	0.1
—	21	2000	0.2
—	21	2000	0.3
—	21	3000	0.1
—	21	3000	0.2
—	21	3000	0.3
—	21	4000	0.1
—	21	4000	0.2
—	21	4000	0.3
—	21	5000	0.1
—	21	5000	0.2
—	21	5000	0.3

(d)

Figure 1S Fibre diameter measurements as a function of parameters: (a) varying flow rate, pressure and rotational speed with specific concentration, (b) varying concentration, pressure and rotational speed for specific flow rate, (c) varying concentration, flow rate and rotational speed for specific pressure, (d) varying concentration, flow rate and pressure for rotational speed.

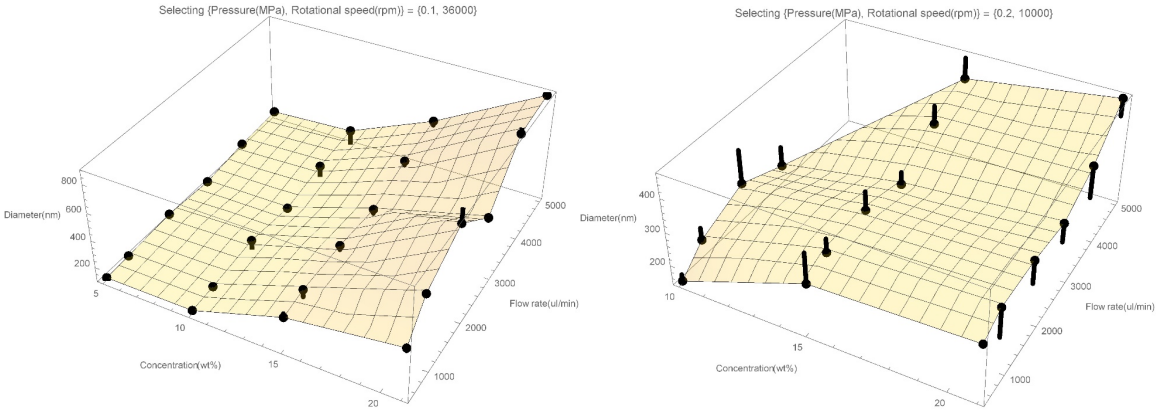

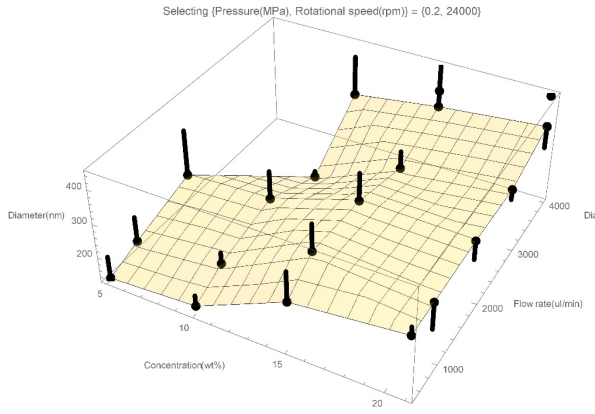
Selecting {Pressure(MPa), Rotational speed(rpm)} = {0.2, 24000}
Diameter(nm)
400
300
200
5
10
15
20
Concentration(wt%)
1000
2000
3000
4000
Flow rate(ul/min)

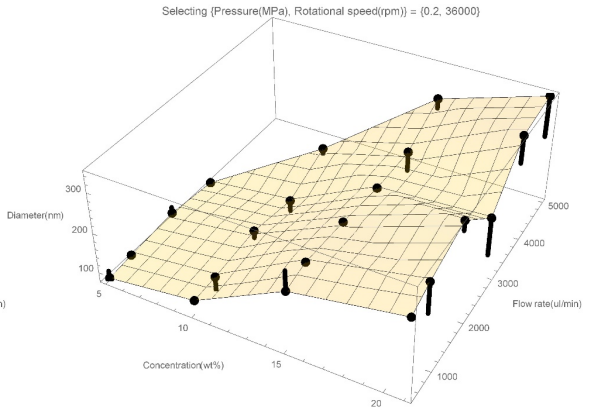
Selecting {Pressure(MPa), Rotational speed(rpm)} = {0.2, 36000}
Diameter(nm)
300
200
100
5
10
15
20
Concentration(wt%)
1000
2000
3000
4000
5000
Flow rate(ul/min)

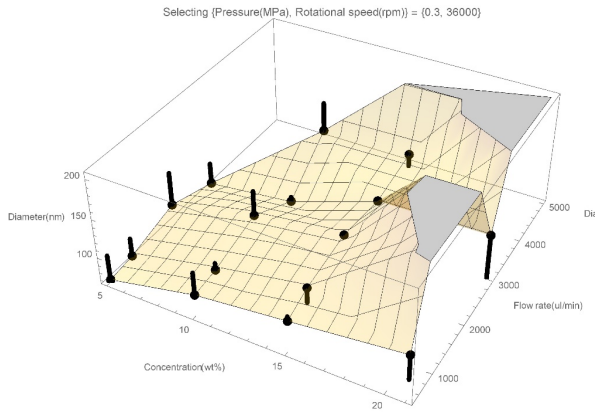
Selecting {Pressure(MPa), Rotational speed(rpm)} = {0.3, 36000}
Diameter(nm)
200
150
100
5
10
15
20
Concentration(wt%)
1000
2000
3000
4000
5000
Flow rate(ul/min)

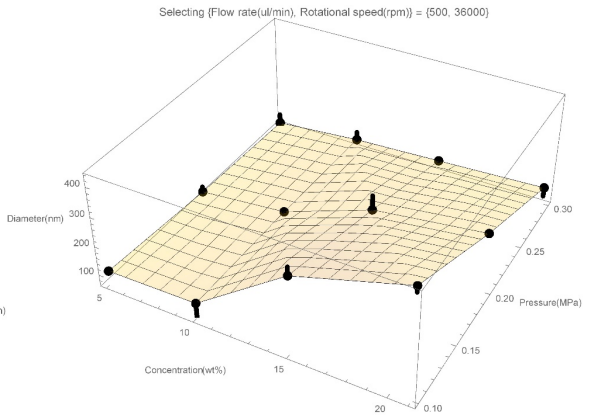
Selecting {Flow rate(ul/min), Rotational speed(rpm)} = {500, 36000}
Diameter(nm)
400
300
200
100
5
10
15
20
Concentration(wt%)
0.10
0.15
0.20
0.25
0.30
Pressure(MPa)

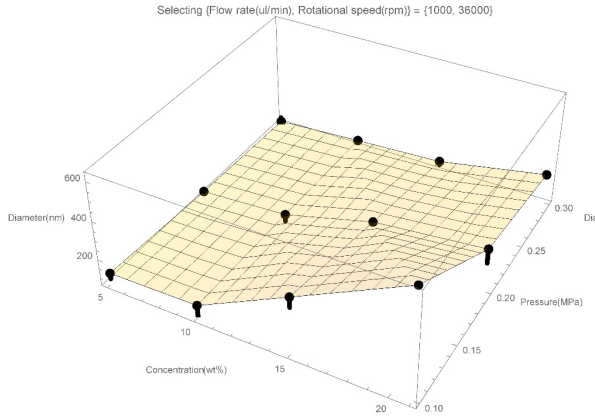
Selecting {Flow rate(ul/min), Rotational speed(rpm)} = {1000, 36000}
Diameter(nm)
600
400
200
5
10
15
20
Concentration(wt%)
0.10
0.15
0.20
0.25
0.30
Pressure(MPa)

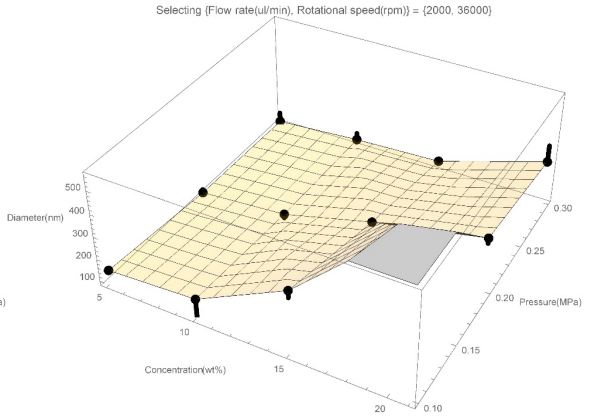
Selecting {Flow rate(ul/min), Rotational speed(rpm)} = {2000, 36000}
Diameter(nm)
500
400
300
200
100
5
10
15
20
Concentration(wt%)
0.10
0.15
0.20
0.25
0.30
Pressure(MPa)

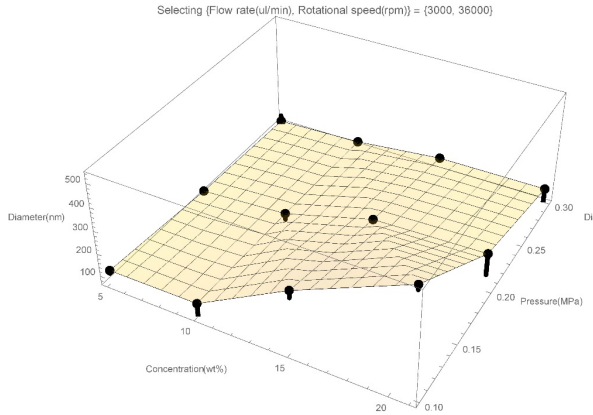
Selecting {Flow rate(ul/min), Rotational speed(rpm)} = {3000, 36000}
Diameter(nm)
500
400
300
200
100
5
10
15
20
Concentration(wt%)
0.10
0.15
0.20
0.25
0.30
Pressure(MPa)

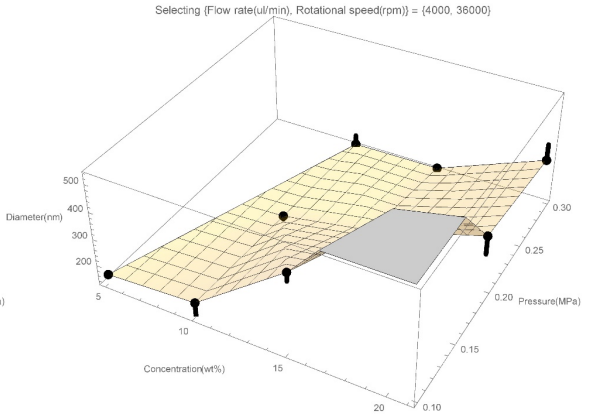
Selecting {Flow rate(ul/min), Rotational speed(rpm)} = {4000, 36000}
Diameter(nm)
500
400
300
200
5
10
15
20
Concentration(wt%)
0.10
0.15
0.20
0.25
0.30
Pressure(MPa)

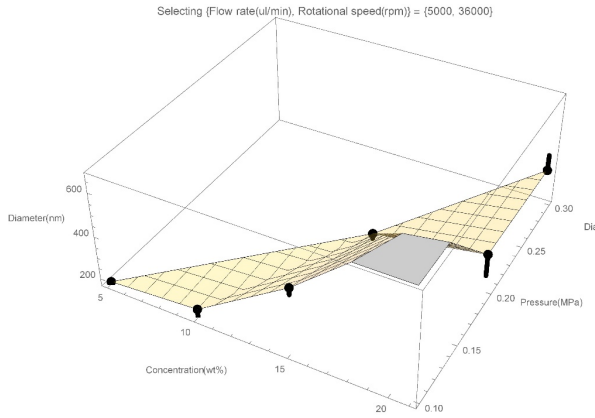
Selecting {Flow rate(ul/min), Rotational speed(rpm)} = {5000, 36000}
Diameter(nm)
600
400
200
5
10
15
20
Concentration(wt%)
0.30
0.25
0.20
0.15
0.10
Pressure(MPa)

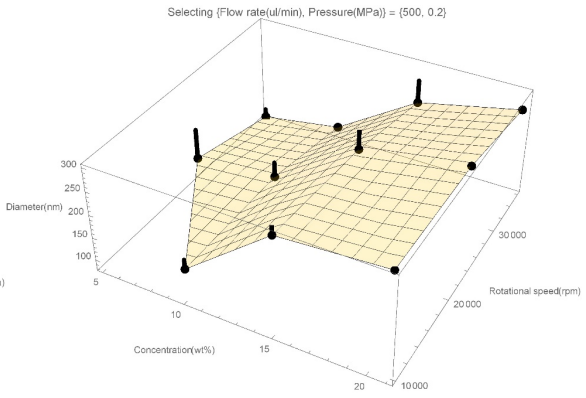
Selecting {Flow rate(ul/min), Pressure(MPa)} = {500, 0.2}
Diameter(nm)
300
250
200
150
100
5
10
15
20
Concentration(wt%)
30 000
20 000
10 000
Rotational speed(rpm)

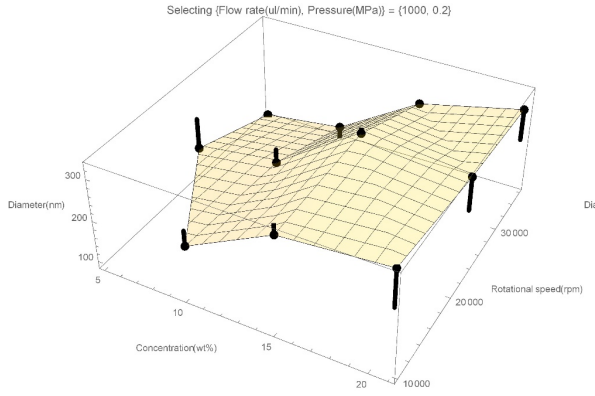
Selecting {Flow rate(ul/min), Pressure(MPa)} = {1000, 0.2}
Diameter(nm)
300
200
100
5
10
15
20
Concentration(wt%)
30 000
20 000
10 000
Rotational speed(rpm)

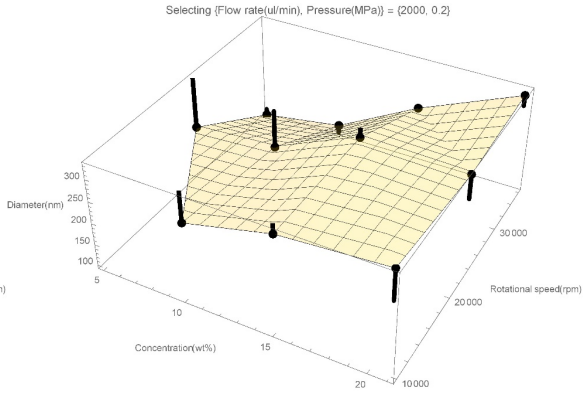
Selecting {Flow rate(ul/min), Pressure(MPa)} = {2000, 0.2}
Diameter(nm)
300
250
200
150
100
5
10
15
20
Concentration(wt%)
30 000
20 000
10 000
Rotational speed(rpm)

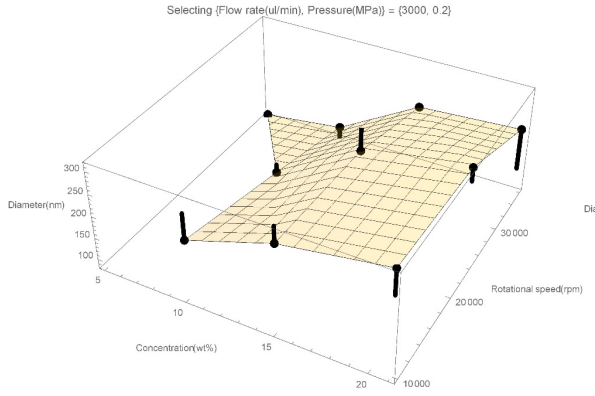
Selecting {Flow rate(ul/min), Pressure(MPa)} = {3000, 0.2}
Diameter(nm)
300
250
200
150
100
5
10
15
20
Concentration(wt%)
30 000
20 000
10 000
Rotational speed(rpm)

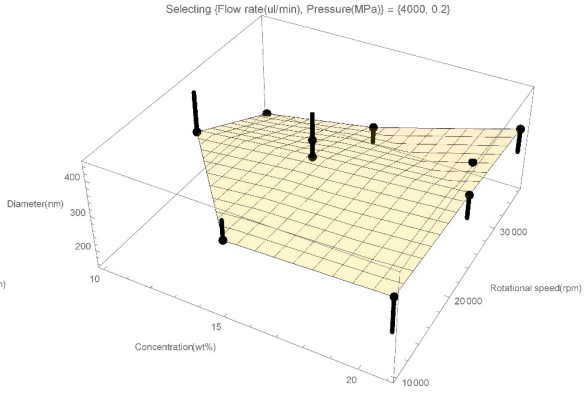
Selecting {Flow rate(ul/min), Pressure(MPa)} = {4000, 0.2}
Diameter(nm)
400
300
200
10
15
20
Concentration(wt%)
30 000
20 000
10 000
Rotational speed(rpm)

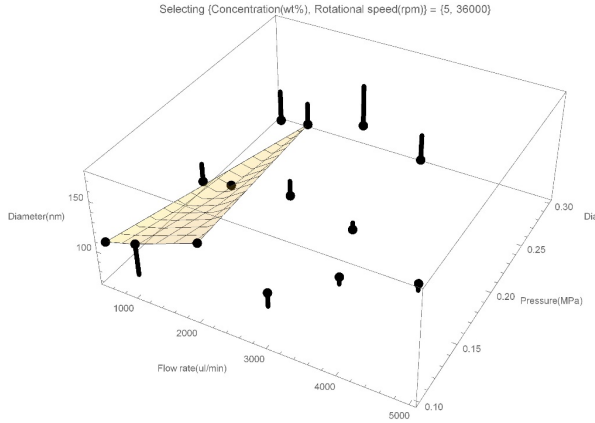
Selecting {Concentration(wt%), Rotational speed(rpm)} = {5, 36000}
Diameter(nm)
150
100
1000
2000
3000
4000
5000
Flow rate(ul/min)
0.30
0.25
0.20
0.15
0.10
Pressure(MPa)

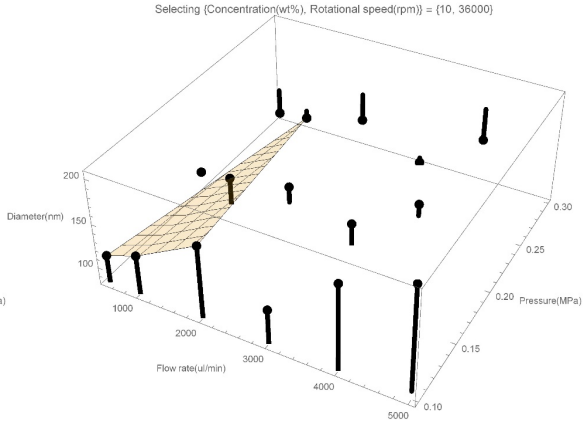
Selecting {Concentration(wt%), Rotational speed(rpm)} = {10, 36000}
Diameter(nm)
200
150
100
1000
2000
3000
4000
5000
Flow rate(ul/min)
0.30
0.25
0.20
0.15
0.10
Pressure(MPa)

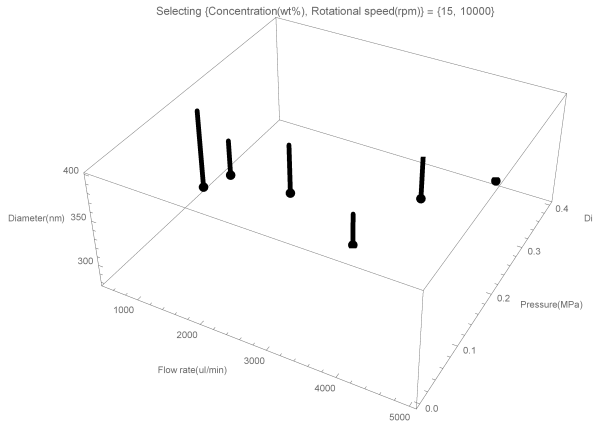
Selecting {Concentration(wt%), Rotational speed(rpm)} = {15, 10000}
Diameter(nm)
400
350
300
1000
2000
3000
4000
5000
Flow rate(ul/min)
0.0
0.1
0.2
0.3
0.4
Pressure(MPa)

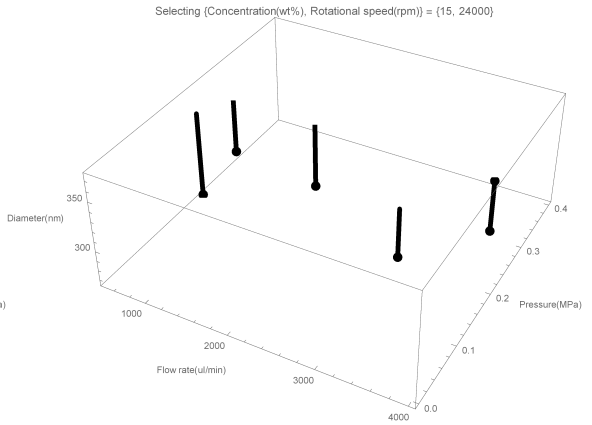
Selecting {Concentration(wt%), Rotational speed(rpm)} = {15, 24000}
Diameter(nm)
350
300
1000
2000
3000
4000
Flow rate(ul/min)
0.0
0.1
0.2
0.3
0.4
Pressure(MPa)

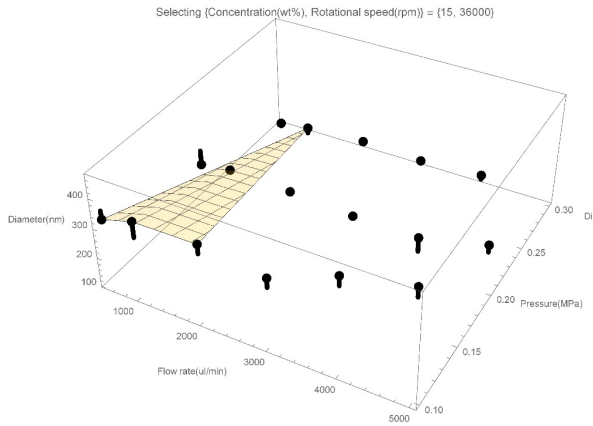
Selecting {Concentration(wt%), Rotational speed(rpm)} = {15, 36000}
Diameter(nm)
400
300
200
100
1000
2000
3000
4000
5000
Flow rate(ul/min)
0.10
0.15
0.20
0.25
0.30
Pressure(MPa)

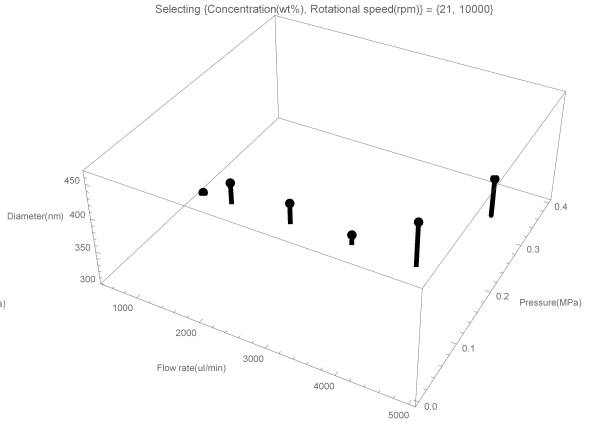
Selecting {Concentration(wt%), Rotational speed(rpm)} = {21, 10000}
Diameter(nm)
450
400
350
300
1000
2000
3000
4000
5000
Flow rate(ul/min)
0.0
0.1
0.2
0.3
0.4
Pressure(MPa)

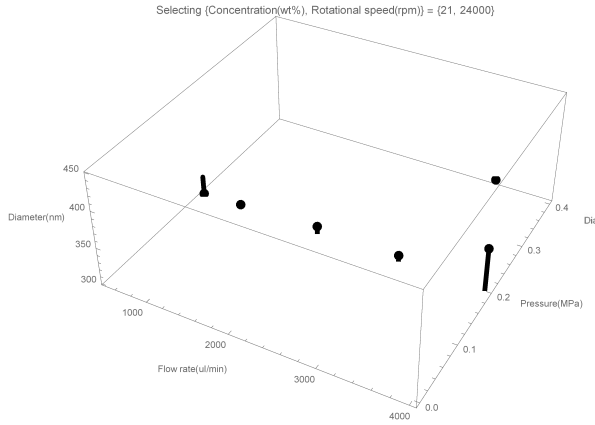
Selecting {Concentration(wt%), Rotational speed(rpm)} = {21, 24000}
Diameter(nm)
450
400
350
300
1000
2000
3000
4000
Flow rate(ul/min)
0.0
0.1
0.2
0.3
0.4
Pressure(MPa)

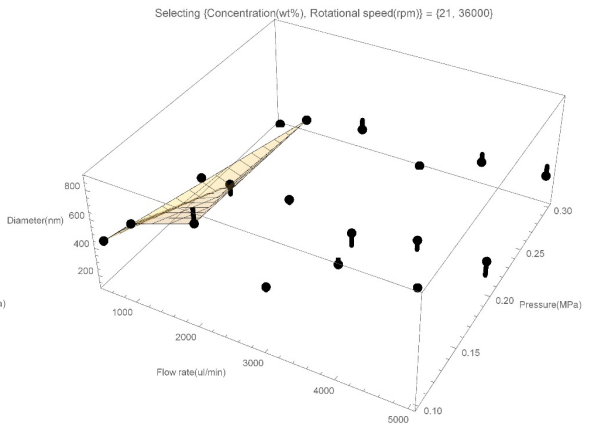
Selecting {Concentration(wt%), Rotational speed(rpm)} = {21, 36000}
Diameter(nm)
800
600
400
200
1000
2000
3000
4000
5000
Flow rate(ul/min)
0.10
0.15
0.20
0.25
0.30
Pressure(MPa)

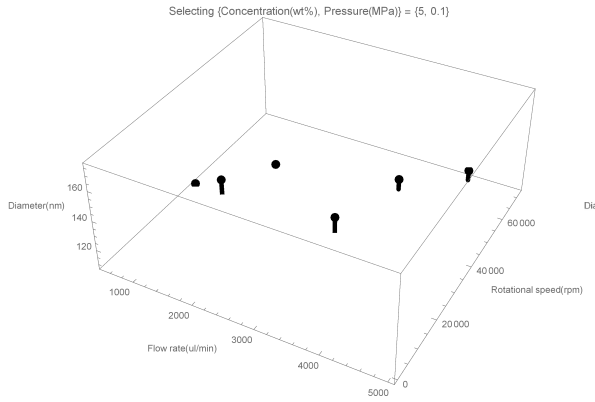
Selecting {Concentration(wt%), Pressure(MPa)} = {5, 0.1}
Diameter(nm)
160
140
120
1000
2000
3000
4000
5000
Flow rate(ul/min)
0
20000
40000
60000
Rotational speed(rpm)

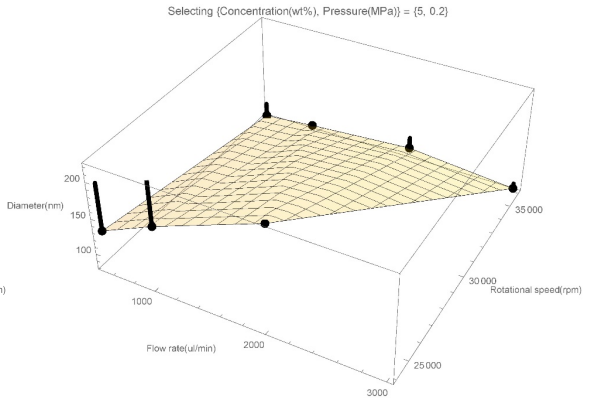
Selecting {Concentration(wt%), Pressure(MPa)} = {5, 0.2}
Diameter(nm)
200
150
100
1000
2000
3000
Flow rate(ul/min)
25000
30000
35000
Rotational speed(rpm)

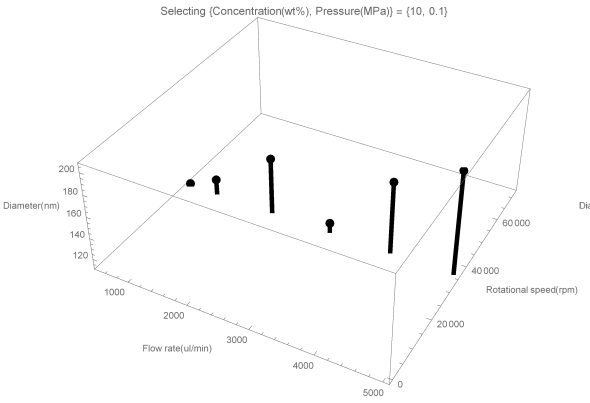
Selecting {Concentration(wt%), Pressure(MPa)} = {10, 0.1}
Diameter(nm)
200
180
160
140
120
1000
2000
3000
4000
5000
Flow rate(ul/min)
0
20 000
40 000
60 000
Rotational speed(rpm)

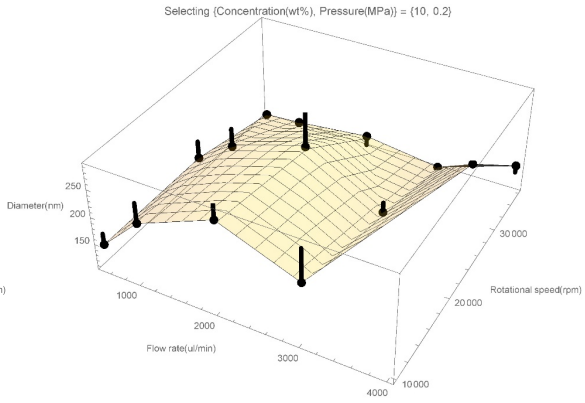
Selecting {Concentration(wt%), Pressure(MPa)} = {10, 0.2}
Diameter(nm)
250
200
150
1000
2000
3000
4000
Flow rate(ul/min)
10 000
20 000
30 000
Rotational speed(rpm)

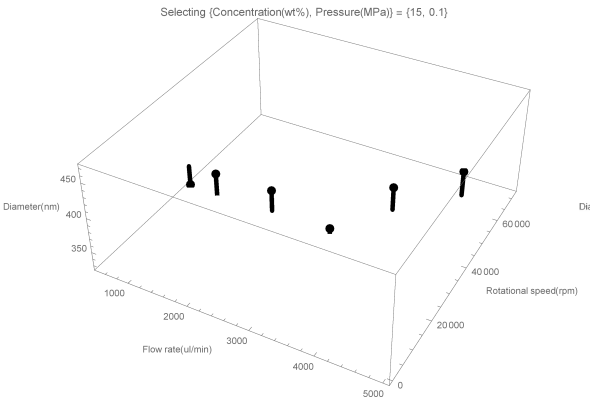
Selecting {Concentration(wt%), Pressure(MPa)} = {15, 0.1}
Diameter(nm)
450
400
350
1000
2000
3000
4000
5000
Flow rate(ul/min)
0
20 000
40 000
60 000
Rotational speed(rpm)

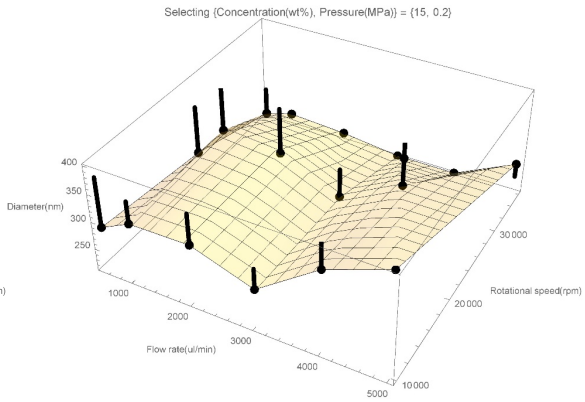
Selecting {Concentration(wt%), Pressure(MPa)} = {15, 0.2}
Diameter(nm)
400
350
300
250
1000
2000
3000
4000
5000
Flow rate(ul/min)
10 000
20 000
30 000
Rotational speed(rpm)

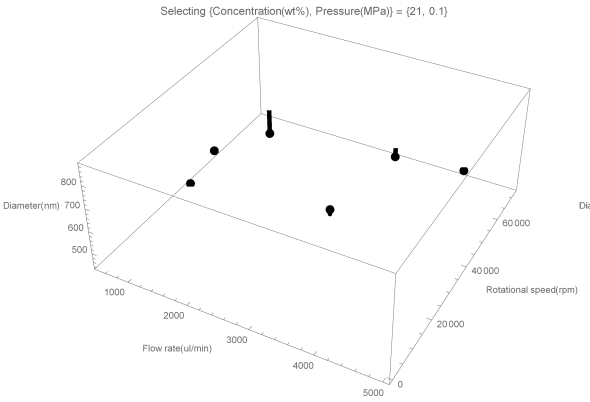
Selecting {Concentration(wt%), Pressure(MPa)} = {21, 0.1}
Diameter(nm)
800
700
600
500
1000
2000
3000
4000
5000
Flow rate(ul/min)
0
20 000
40 000
60 000
Rotational speed(rpm)

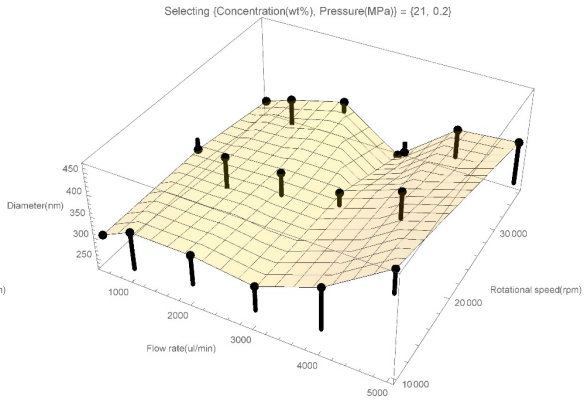
Selecting {Concentration(wt%), Pressure(MPa)} = {21, 0.2}
Diameter(nm)
450
400
350
300
250
1000
2000
3000
4000
5000
Flow rate(ul/min)
10 000
20 000
30 000
Rotational speed(rpm)

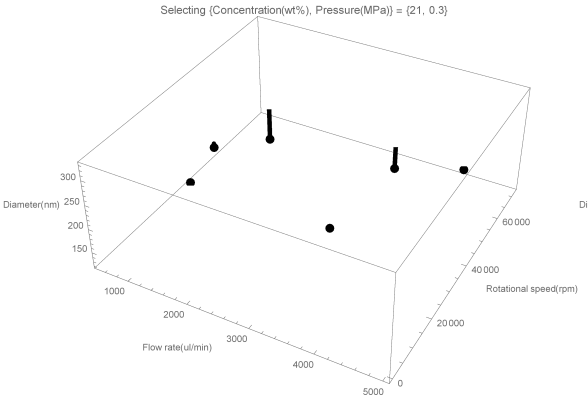
Selecting {Concentration(wt%), Pressure(MPa)} = {21, 0.3}
Diameter(nm)
300
250
200
150
1000
2000
3000
4000
5000
Flow rate(ul/min)
0
20 000
40 000
60 000
Rotational speed(rpm)

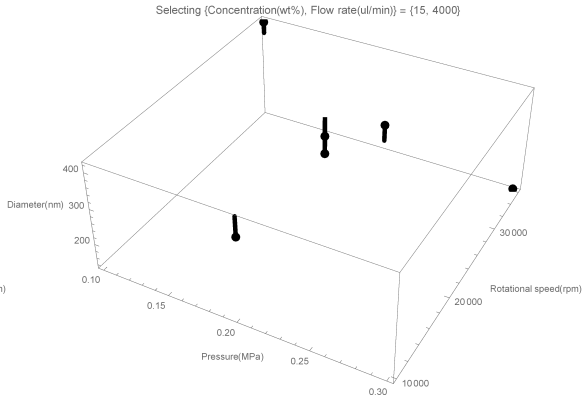
Selecting {Concentration(wt%), Flow rate(ul/min)} = {15, 4000}
Diameter(nm)
400
300
200
0.10
0.15
0.20
0.25
0.30
Pressure(MPa)
10 000
20 000
30 000
Rotational speed(rpm)

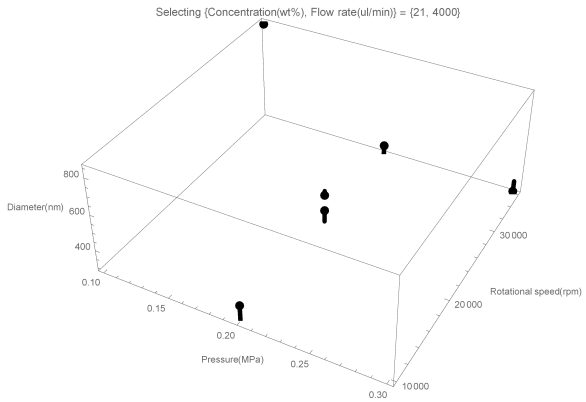

Fitting function: $-((1.89133*10^{-11}\ (1-4.10914*10^{10}\ f+2.7385*10^{7}\ f^2-7003.52\ f^3+0.594504\ f^4)\ (1+0.0918848\ c)^{2.07988}\ (1-0.0000257774\ p)^{213588.})/g^{0.111926})$

Figure 2S Residual plot of the non-linear model derived from Mellado et al.'s work: Eq. 5.3. Each of the graph shows the fibre diameter points when two parameters were fixed and with other two changing, e.g. the "Selecting{pressure (MPa), rotational speed (rpm)} = {0.1, 36000}" indicates fixing pressure and rotational speed at 0.1 MPa and 36000 rpm. The black bars indicate the residual of the data points. Due to there were no fibre formations under some experimental conditions (combinations of parameters), so some of the subplots without enough data points to form a surface.

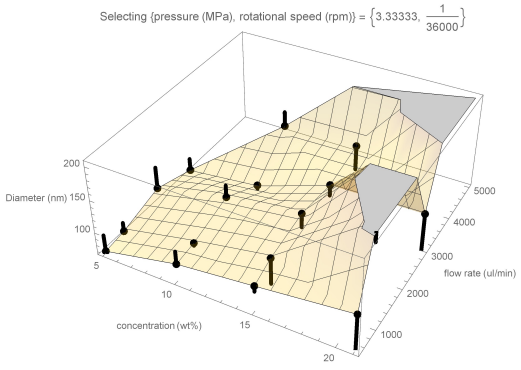

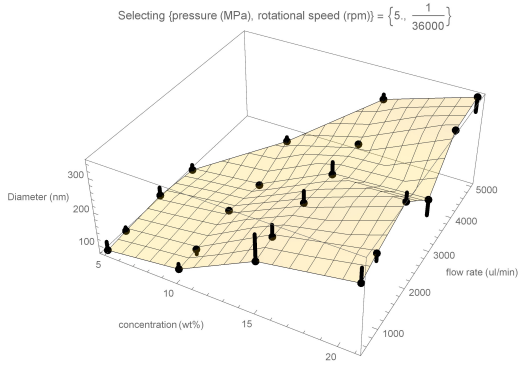

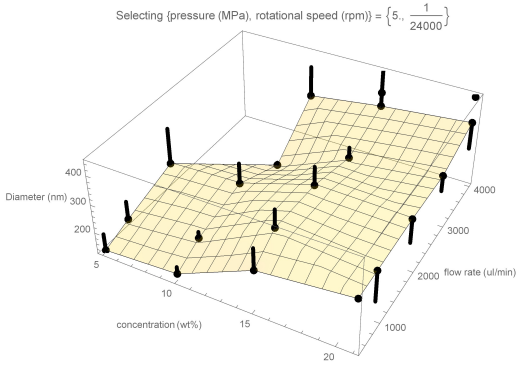
Selecting {pressure (MPa), rotational speed (rpm)} = {5., 1/24000}
Diameter (nm)
400
300
200
5
10
15
20
concentration (wt%)
1000
2000
3000
4000
flow rate (ul/min)

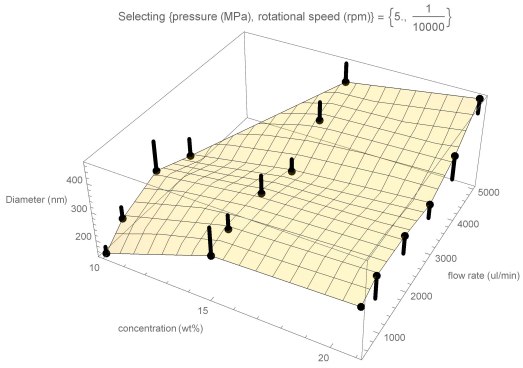
Selecting {pressure (MPa), rotational speed (rpm)} = {5., 1/10000}
Diameter (nm)
400
300
200
10
15
20
concentration (wt%)
1000
2000
3000
4000
5000
flow rate (ul/min)

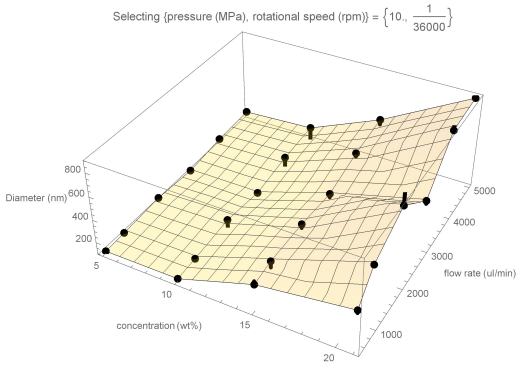
Selecting {pressure (MPa), rotational speed (rpm)} = {10., 1/36000}
Diameter (nm)
800
600
400
200
5
10
15
20
concentration (wt%)
1000
2000
3000
4000
5000
flow rate (ul/min)

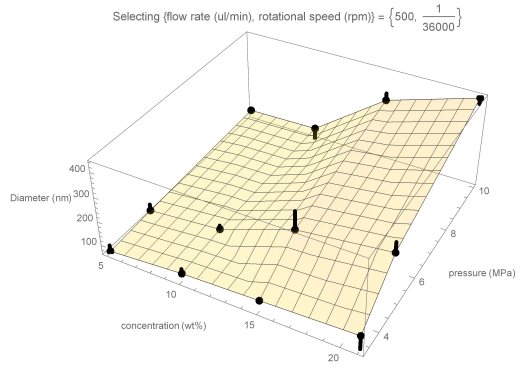
Selecting {flow rate (ul/min), rotational speed (rpm)} = {500, 1/36000}
Diameter (nm)
400
300
200
100
5
10
15
20
concentration (wt%)
4
6
8
10
pressure (MPa)

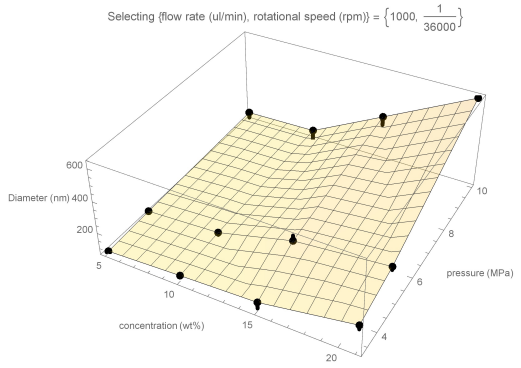
Selecting {flow rate (ul/min), rotational speed (rpm)} = {1000, 1/36000}
Diameter (nm)
600
400
200
5
10
15
20
concentration (wt%)
4
6
8
10
pressure (MPa)

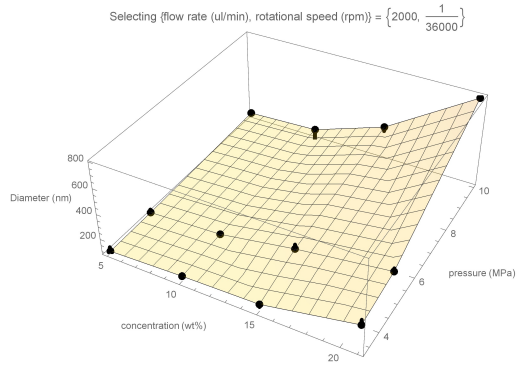
Selecting {flow rate (ul/min), rotational speed (rpm)} = {2000, 1/36000}
Diameter (nm)
800
600
400
200
5
10
15
20
concentration (wt%)
4
6
8
10
pressure (MPa)

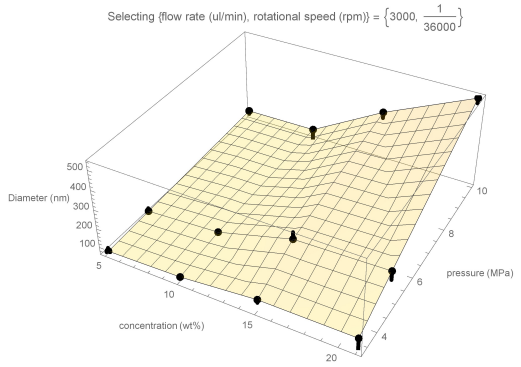
Selecting {flow rate (ul/min), rotational speed (rpm)} = {3000, 1/36000}
Diameter (nm)
500
400
300
200
100
5
10
15
20
concentration (wt%)
4
6
8
10
pressure (MPa)

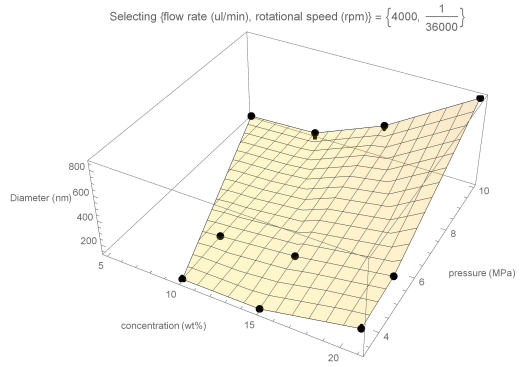
Selecting {flow rate (ul/min), rotational speed (rpm)} = {4000, 1/36000}
Diameter (nm)
800
600
400
200
5
10
15
20
concentration (wt%)
4
6
8
10
pressure (MPa)

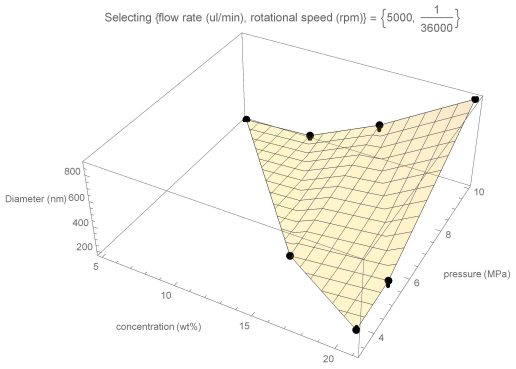
Selecting {flow rate (ul/min), rotational speed (rpm)} = {5000, 1/36000}
Diameter (nm)
800
600
400
200
5
10
15
20
concentration (wt%)
10
8
6
4
pressure (MPa)

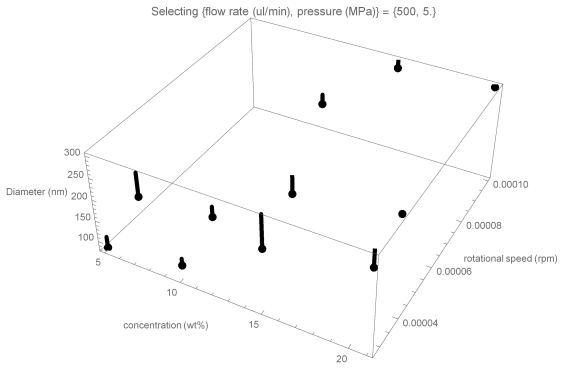
Selecting {flow rate (ul/min), pressure (MPa)} = {500, 5.}
Diameter (nm)
300
250
200
150
100
5
10
15
20
concentration (wt%)
0.00010
0.00008
0.00006
0.00004
rotational speed (rpm)

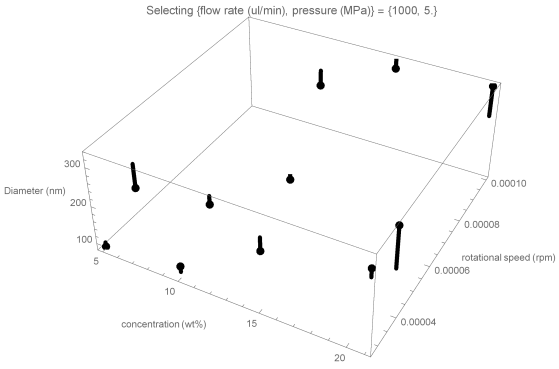
Selecting {flow rate (ul/min), pressure (MPa)} = {1000, 5.}
Diameter (nm)
300
200
100
5
10
15
20
concentration (wt%)
0.00010
0.00008
0.00006
0.00004
rotational speed (rpm)

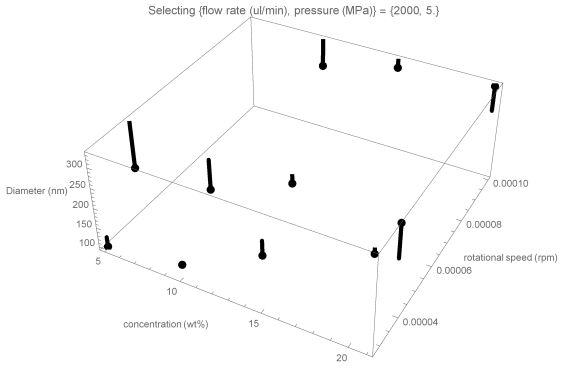
Selecting {flow rate (ul/min), pressure (MPa)} = {2000, 5.}
Diameter (nm)
300
250
200
150
100
5
10
15
20
concentration (wt%)
0.00010
0.00008
0.00006
0.00004
rotational speed (rpm)

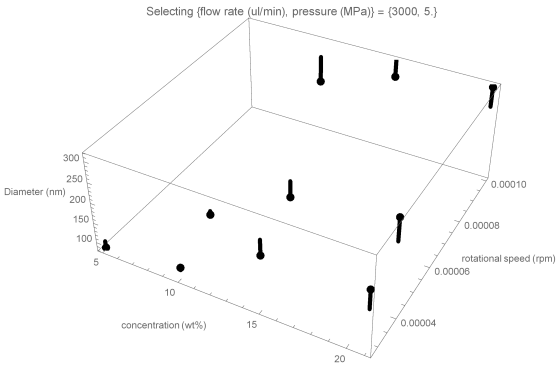
Selecting {flow rate (ul/min), pressure (MPa)} = {3000, 5.}
Diameter (nm)
300
250
200
150
100
5
10
15
20
concentration (wt%)
0.00010
0.00008
0.00006
0.00004
rotational speed (rpm)

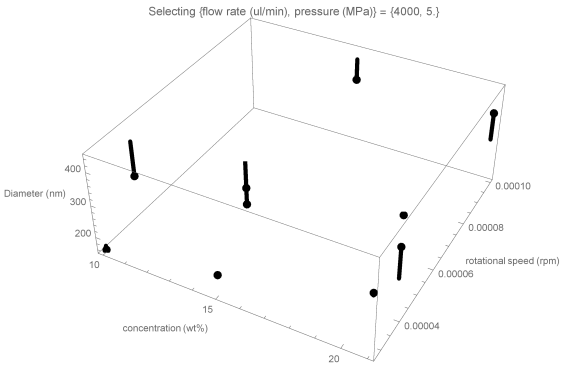
Selecting {flow rate (ul/min), pressure (MPa)} = {4000, 5.}
Diameter (nm)
400
300
200
10
15
20
concentration (wt%)
0.00010
0.00008
0.00006
0.00004
rotational speed (rpm)

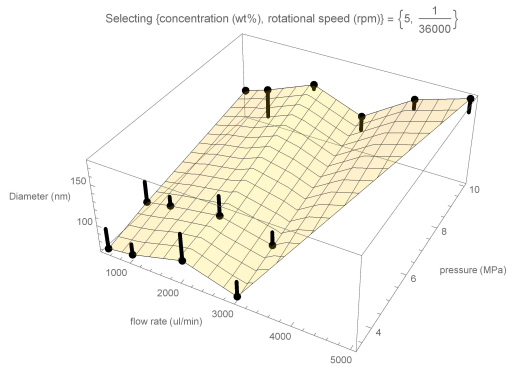
Selecting {concentration (wt%), rotational speed (rpm)} = {5, 1/36000}
Diameter (nm)
150
100
1000
2000
3000
4000
5000
flow rate (ul/min)
10
8
6
4
pressure (MPa)

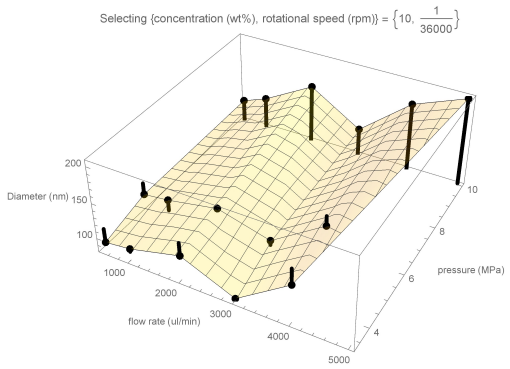
Selecting {concentration (wt%), rotational speed (rpm)} = {10, 1/36000}
Diameter (nm)
200
150
100
1000
2000
3000
4000
5000
flow rate (ul/min)
10
8
6
4
pressure (MPa)

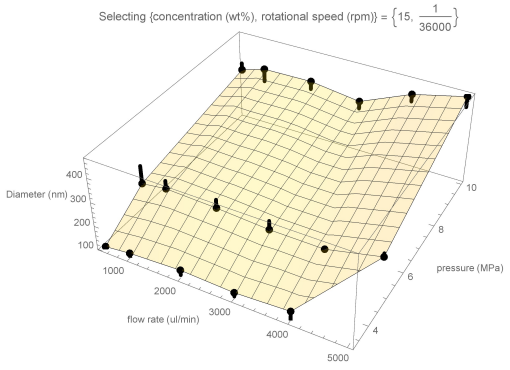
Selecting {concentration (wt%), rotational speed (rpm)} = {15, 1/36000}
Diameter (nm)
400
300
200
100
1000
2000
3000
4000
5000
flow rate (ul/min)
4
6
8
10
pressure (MPa)

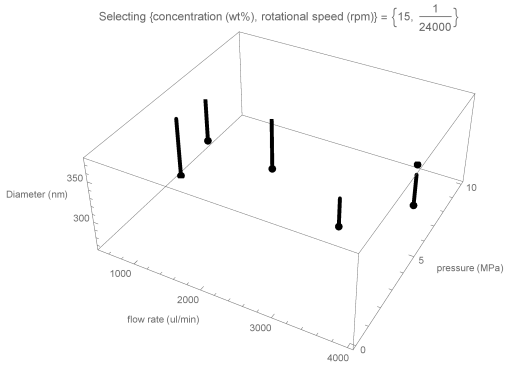
Selecting {concentration (wt%), rotational speed (rpm)} = {15, 1/24000}
Diameter (nm)
350
300
1000
2000
3000
4000
flow rate (ul/min)
0
5
10
pressure (MPa)

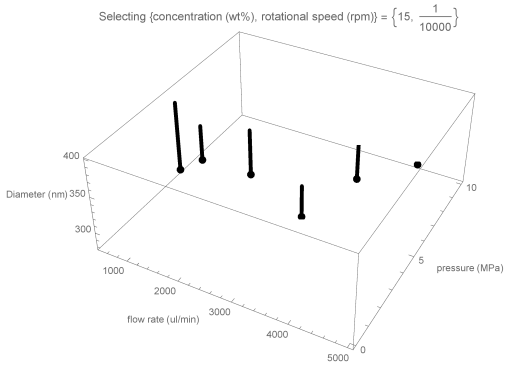
Selecting {concentration (wt%), rotational speed (rpm)} = {15, 1/10000}
Diameter (nm)
400
350
300
1000
2000
3000
4000
5000
flow rate (ul/min)
0
5
10
pressure (MPa)

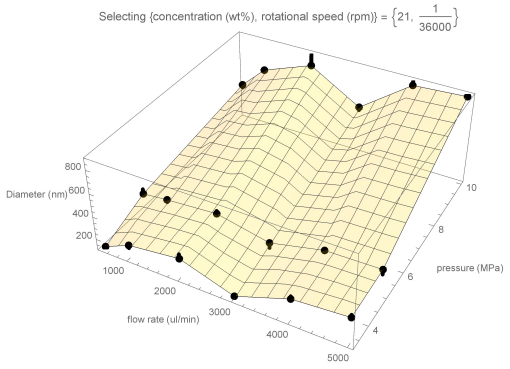
Selecting {concentration (wt%), rotational speed (rpm)} = {21, 1/36000}
Diameter (nm)
800
600
400
200
1000
2000
3000
4000
5000
flow rate (ul/min)
4
6
8
10
pressure (MPa)

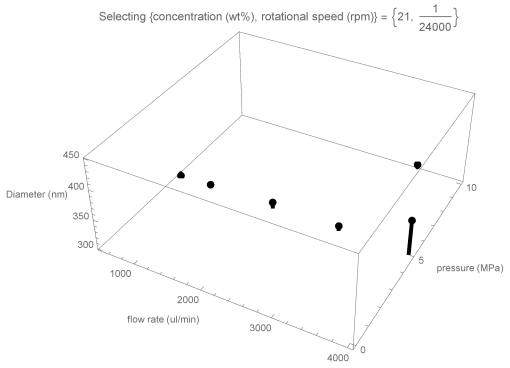
Selecting {concentration (wt%), rotational speed (rpm)} = {21, 1/24000}
Diameter (nm)
450
400
350
300
1000
2000
3000
4000
flow rate (ul/min)
0
5
10
pressure (MPa)

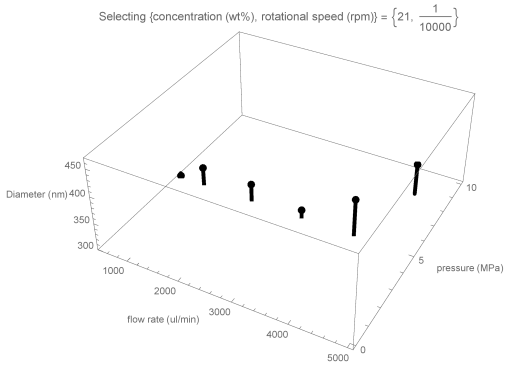
Selecting {concentration (wt%), rotational speed (rpm)} = {21, 1/10000}
Diameter (nm)
450
400
350
300
1000
2000
3000
4000
5000
flow rate (ul/min)
0
5
10
pressure (MPa)

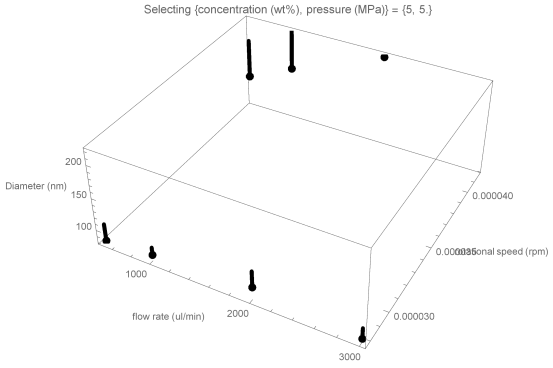
Selecting {concentration (wt%), pressure (MPa)} = {5, 5.}
Diameter (nm)
200
150
100
1000
2000
3000
flow rate (ul/min)
0.000030
0.000040
rotational speed (rpm)

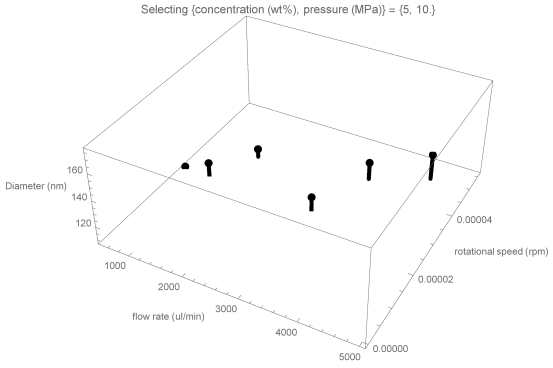
Selecting {concentration (wt%), pressure (MPa)} = {5, 10.}
Diameter (nm)
160
140
120
1000
2000
3000
4000
5000
flow rate (ul/min)
0.00000
0.00002
0.00004
rotational speed (rpm)

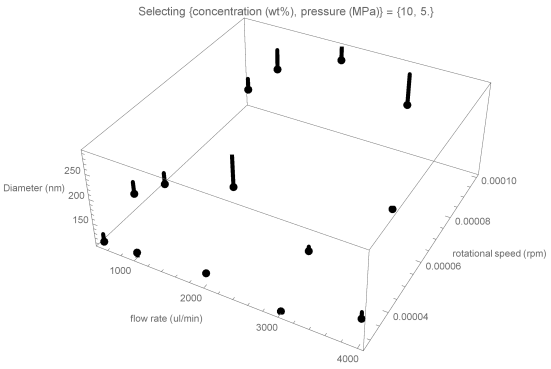
Selecting {concentration (wt%), pressure (MPa)} = {10, 5.}
Diameter (nm)
250
200
150
1000
2000
3000
4000
flow rate (ul/min)
0.00010
0.00008
0.00006
0.00004
rotational speed (rpm)

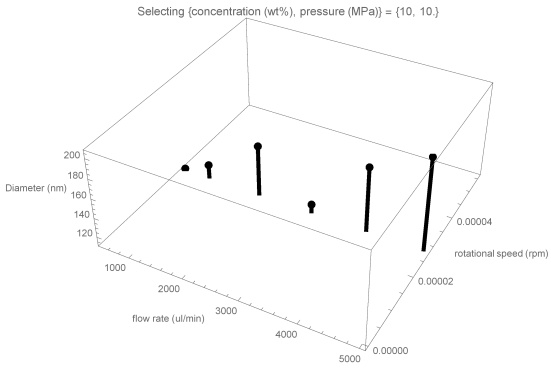
Selecting {concentration (wt%), pressure (MPa)} = {10, 10.}
Diameter (nm)
200
180
160
140
120
1000
2000
3000
4000
5000
flow rate (ul/min)
0.00004
0.00002
0.00000
rotational speed (rpm)

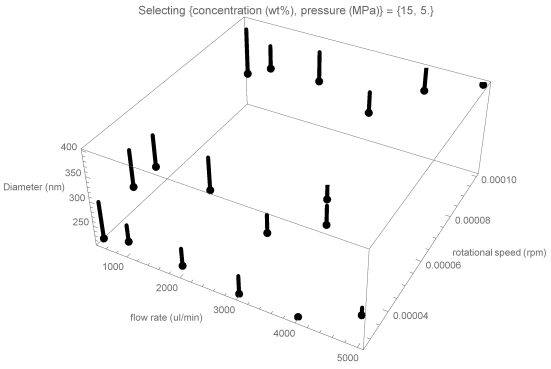
Selecting {concentration (wt%), pressure (MPa)} = {15, 5.}
Diameter (nm)
400
350
300
250
1000
2000
3000
4000
5000
flow rate (ul/min)
0.00010
0.00008
0.00006
0.00004
rotational speed (rpm)

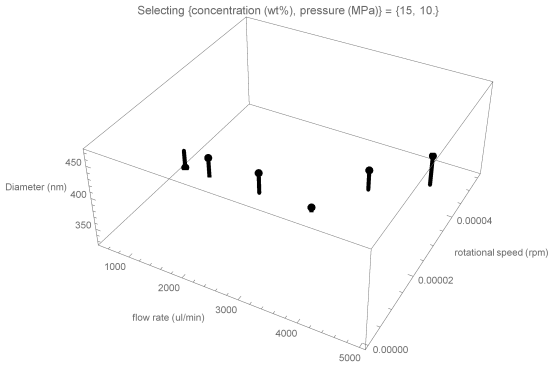
Selecting {concentration (wt%), pressure (MPa)} = {15, 10.}
Diameter (nm)
450
400
350
1000
2000
3000
4000
5000
flow rate (ul/min)
0.00004
0.00002
0.00000
rotational speed (rpm)

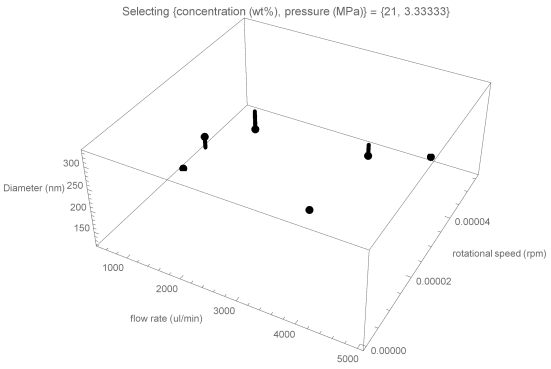
Selecting {concentration (wt%), pressure (MPa)} = {21, 3.33333}
Diameter (nm)
300
250
200
150
1000
2000
3000
4000
5000
flow rate (ul/min)
0.00004
0.00002
0.00000
rotational speed (rpm)

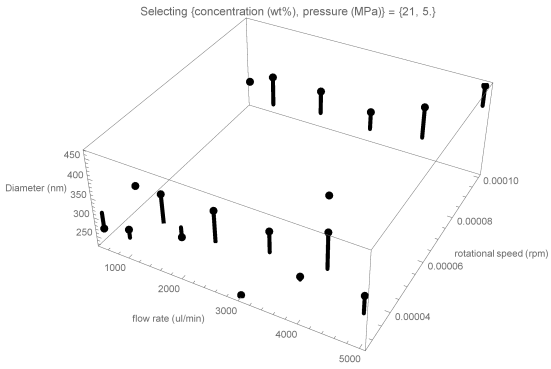
Selecting {concentration (wt%), pressure (MPa)} = {21, 5.}
Diameter (nm)
450
400
350
300
250
1000
2000
3000
4000
5000
flow rate (ul/min)
0.00010
0.00008
0.00006
0.00004
rotational speed (rpm)

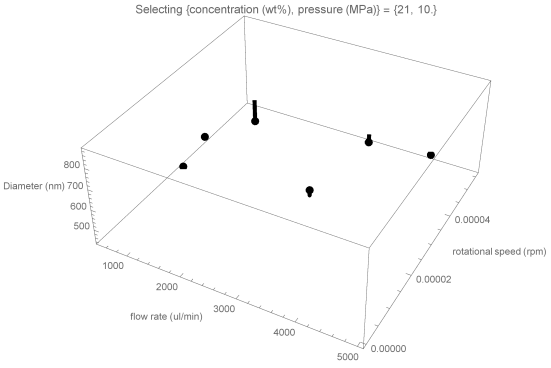
Selecting {concentration (wt%), pressure (MPa)} = {21, 10.}
Diameter (nm)
800
700
600
500
1000
2000
3000
4000
5000
flow rate (ul/min)
0.00004
0.00002
0.00000
rotational speed (rpm)

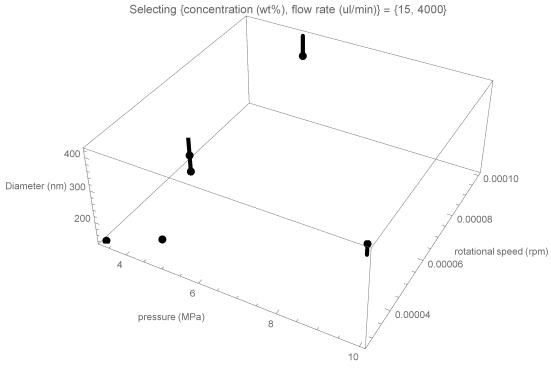
Selecting {concentration (wt%), flow rate (ul/min)} = {15, 4000}
Diameter (nm)
400
300
200
4
6
8
10
pressure (MPa)
0.00010
0.00008
0.00006
0.00004
rotational speed (rpm)

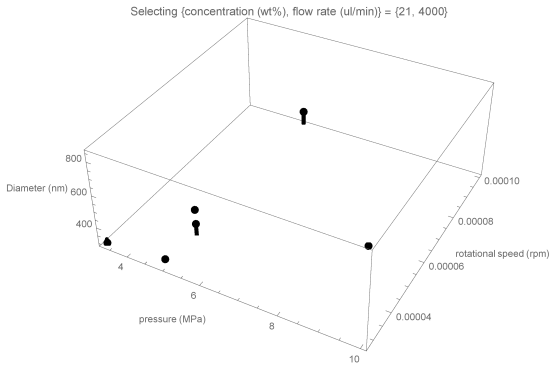

Fitting function: (1818.47 f-1.20169 f^2+0.000304486 f^3-2.55811*10^{-8} f^4) (1+0.119436 c+0.00926329 c^2) $E^{0.144034\ p}$ (g-7046.28 g^2)

Figure 3S Residual plot of non-linear model: Eq. 5.9, each of the graph shows the fibre diameter points when two parameters were fixed and with other two changing, e.g. the "Selecting{pressure (MPa), rotational speed (rpm)} = {$3.33333, \frac{1}{36000}$}" indicates fixing pressure and rotational speed at $\frac{1}{0.3}$ MPa and $\frac{1}{36000}$ rpm. The black bars indicate the residuals of the data points. Due to there were no fibre formations under some experimental conditions (combinations of parameters), so some of the subplots without enough data points to form a surface.

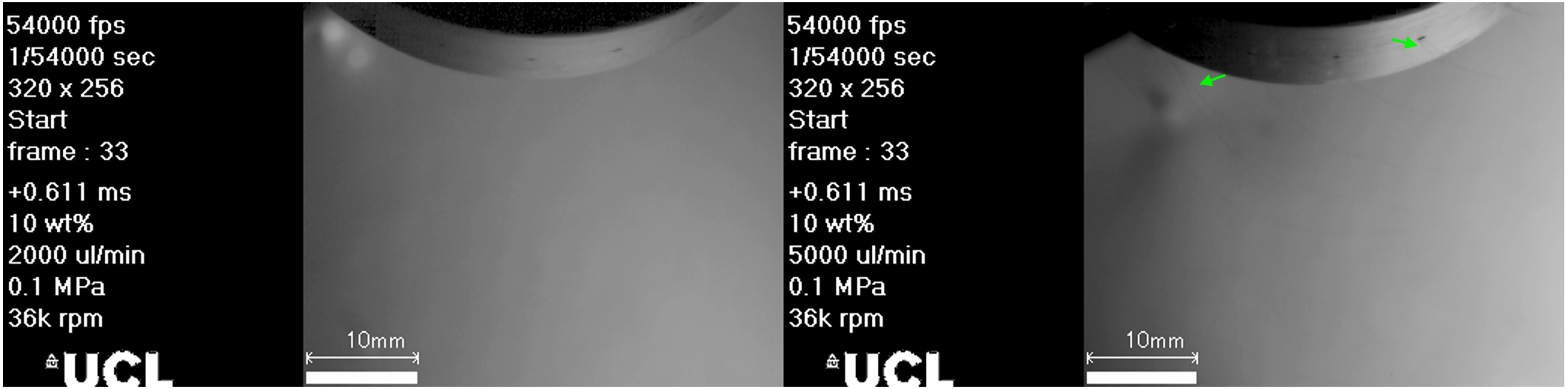

Figure 4S Screenshots of high-speed camera video for the experiments taken under different infusion flow rate, and other experimental conditions as listed at the left side of screenshots.

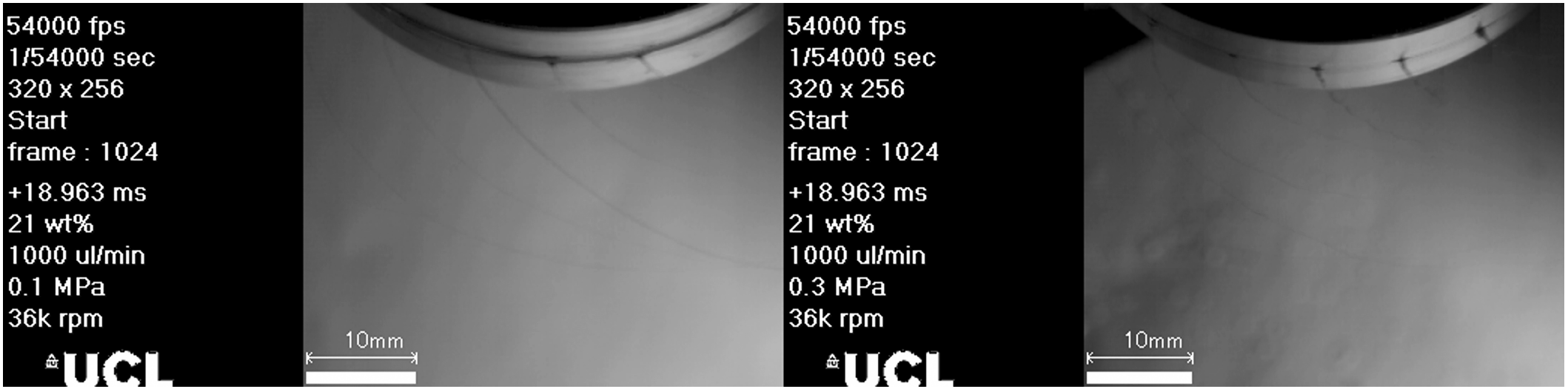

Figure 5S Screenshots of high-speed camera video for the experiments taken under different gas pressure. All the high-speed camera videos are available at: https://onlinelibrary.wiley.com/doi/full/10.1002/mame.201600564.

Table 1S ANOVA table of the most complicated quardratic linear model with inversed pressure and rotational speed parameters: Eq. 5.5.

	DF	SS	MS	F-Statistic	P-Value
c	1	1.04036×10^{6}	1.04036×10^{6}	301.699	7.32274×10^{-30}
c^2	1	8020.6	8020.6	2.32592	0.130904
f	1	121 359.	121 359.	35.1932	6.08795×10^{-8}
c f	1	21 634.2	21 634.2	6.27379	0.0141398
f^2	1	13 850.9	13 850.9	4.01667	0.0481993
g	1	13 146.4	13 146.4	3.81236	0.0541284
c g	1	45 276.5	45 276.5	13.1299	0.000491089
f g	1	33.4053	33.4053	0.00968732	0.921825
g^2	1	9251.93	9251.93	2.683	0.105078
p	1	517 546.	517 546.	150.085	1.48079×10^{-20}
c p	1	361 317.	361 317.	104.779	1.51414×10^{-16}
f p	1	10 791.9	10 791.9	3.12959	0.0804282
g p	1	0.	0.	0.	1.
p^2	1	0.794415	0.794415	0.000230375	0.987925
Error	86	296 558.	3448.35		
Total	100	2.45915×10^{6}			

Table 2S Fitting residual of the non-linear model derived from Mellado et al.'s work: Eq. 5.3.

Concentration (wt%)	Flow Rate (ul/min)	Pressure (MPa)	Rotational Speed (rpm)	Residuals (nm)
10	500	0.1	36000	-77.2691
10	1000	0.1	36000	-68.8837
10	2000	0.1	36000	-45.5835
10	3000	0.1	36000	-111.966
10	4000	0.1	36000	-84.2124
10	5000	0.1	36000	-94.1369
15	500	0.1	36000	-9.47051
15	1000	0.1	36000	13.1177
15	2000	0.1	36000	-6.72247
15	3000	0.1	36000	-65.7164
15	4000	0.1	36000	-12.7235
15	5000	0.1	36000	-8.10936
21	500	0.1	36000	-116.578
21	1000	0.1	36000	69.201
21	2000	0.1	36000	195.897
21	3000	0.1	36000	-100.501
21	4000	0.1	36000	172.658
21	5000	0.1	36000	144.474
5	500	0.1	36000	31.6045
5	1000	0.1	36000	40.3299
5	2000	0.1	36000	57.2179

5	3000	0.1	36000	18.1989
5	4000	0.1	36000	35.4302
5	5000	0.1	36000	23.7424
10	500	0.2	36000	17.0635
10	500	0.3	36000	-10.6241
10	1000	0.2	36000	21
10	1000	0.3	36000	-2.15657
10	2000	0.2	36000	28.1731
10	2000	0.3	36000	19.0964
10	3000	0.2	36000	-5.18032
10	3000	0.3	36000	-17.7046
10	4000	0.2	36000	21.3063
10	4000	0.3	36000	20.0868
15	500	0.2	36000	52.2218
15	500	0.3	36000	-5.49125
15	1000	0.2	36000	62.4236
15	1000	0.3	36000	7.57039
15	2000	0.2	36000	41.299
15	2000	0.3	36000	14.9677
15	3000	0.2	36000	6.42922
15	3000	0.3	36000	-4.97041
15	4000	0.2	36000	-23.1529
15	4000	0.3	36000	-11.6671
15	5000	0.2	36000	-7.06055
21	500	0.2	36000	-36.6033
21	500	0.3	36000	-41.7704
21	1000	0.2	36000	-21.8394
21	1000	0.3	36000	53.0871
21	2000	0.2	36000	-11.1265
21	2000	0.3	36000	95.2781
21	3000	0.2	36000	-137.351
21	3000	0.3	36000	-77.7498
21	4000	0.2	36000	-68.3636
21	4000	0.3	36000	62.9035
21	5000	0.2	36000	-102.854
21	5000	0.3	36000	63.7733
5	500	0.2	36000	32.7401
5	500	0.3	36000	-60.4548
5	1000	0.2	36000	42.6456
5	1000	0.3	36000	-47.8735
5	2000	0.2	36000	54.2182
5	2000	0.3	36000	-19.9125
5	3000	0.2	36000	34.0111
5	3000	0.3	36000	-36.3884
10	500	0.2	10000	-93.0116
10	500	0.2	24000	-41.3899

10	1000	0.2	10000	-30.8543
10	1000	0.2	24000	2.16344
10	2000	0.2	10000	15.2536
10	2000	0.2	24000	36.7316
10	3000	0.2	10000	-58.1264
10	3000	0.2	24000	-55.4846
10	4000	0.2	24000	55.2933
15	500	0.2	10000	44.1251
15	500	0.2	24000	34.9538
15	1000	0.2	10000	63.92
15	1000	0.2	24000	90.0637
15	2000	0.2	10000	47.4761
15	2000	0.2	24000	64.5228
15	3000	0.2	10000	-15.9959
15	3000	0.2	24000	-5.89478
15	4000	0.2	10000	28.7207
15	4000	0.2	24000	20.3527
15	5000	0.2	10000	29.5737
15	4000	0.2	24000	68.9517
21	500	0.2	10000	11.7177
21	500	0.2	24000	-24.8315
21	1000	0.2	10000	32.5163
21	1000	0.2	24000	-32.3721
21	2000	0.2	10000	3.88641
21	2000	0.2	24000	-51.4172
21	3000	0.2	10000	-48.9619
21	3000	0.2	24000	-86.4615
21	4000	0.2	10000	-37.573
21	4000	0.2	24000	-76.2482
21	5000	0.2	10000	7.33354
21	4000	0.2	24000	13.9336
5	500	0.2	24000	-47.4474
5	1000	0.2	24000	-11.499
5	2000	0.2	24000	46.0796

Table 3S Fitting residual of the non-linear model: Eq. 5.9.

Concentration (wt%)	Flow Rate (ul/min)	1/ Pressure (1/MPa)	1/ Rotational Speed (1/rpm)	Residual (nm)
10	500	10	1/36000	-77.6684
10	1000	10	1/36000	-137.606
10	2000	10	1/36000	-86.8119
10	3000	10	1/36000	-112.048

10	4000	10	1/36000	-112.52
10	5000	10	1/36000	-116.54
15	500	10	1/36000	29.2214
15	1000	10	1/36000	-53.7275
15	2000	10	1/36000	-31.3979
15	3000	10	1/36000	-31.2368
15	4000	10	1/36000	-31.8521
15	5000	10	1/36000	-31.8608
21	500	10	1/36000	-20.3824
21	1000	10	1/36000	2.5852
21	2000	10	1/36000	191.226
21	3000	10	1/36000	-21.2192
21	4000	10	1/36000	157.719
21	5000	10	1/36000	106.694
5	500	10	1/36000	0.590244
5	1000	10	1/36000	-31.1777
5	2000	10	1/36000	0.136965
5	3000	10	1/36000	-13.372
5	4000	10	1/36000	-6.53676
5	5000	10	1/36000	-5.94807
10	500	5	1/36000	-0.714619
10	500	3.33333	1/36000	29.2311
10	1000	5	1/36000	-38.6911
10	1000	3.33333	1/36000	9.12466
10	2000	5	1/36000	-18.2431
10	2000	3.33333	1/36000	31.675
10	3000	5	1/36000	-27.1753
10	3000	3.33333	1/36000	5.87228
10	4000	5	1/36000	-12.995
10	4000	3.33333	1/36000	36.7581

15	500	5	1/36000	49.4031
15	500	3.33333	1/36000	6.0202
15	1000	5	1/36000	-2.1492
15	1000	3.33333	1/36000	-19.3155
15	2000	5	1/36000	1.69826
15	2000	3.33333	1/36000	-0.641444
15	3000	5	1/36000	4.8682
15	3000	3.33333	1/36000	1.50607
15	4000	5	1/36000	-48.4216
15	4000	3.33333	1/36000	-15.4359
15	5000	5	1/36000	-24.5174
21	500	5	1/36000	3.04578
21	500	3.33333	1/36000	-31.727
21	1000	5	1/36000	-75.0288
21	1000	3.33333	1/36000	8.75018
21	2000	5	1/36000	-24.0598
21	2000	3.33333	1/36000	74.9126
21	3000	5	1/36000	-94.0642
21	3000	3.33333	1/36000	-61.6651
21	4000	5	1/36000	-68.3207
21	4000	3.33333	1/36000	61.3597
21	5000	5	1/36000	-101.623
21	5000	3.33333	1/36000	73.4952
5	500	5	1/36000	18.8354
5	500	3.33333	1/36000	32.5487
5	1000	5	1/36000	1.25748
5	1000	3.33333	1/36000	23.2591
5	2000	5	1/36000	15.3357
5	2000	3.33333	1/36000	43.073
5	3000	5	1/36000	7.2988

5	3000	3.33333	1/36000	27.2967
10	500	5	1/10000	20.4166
10	500	5	1/24000	32.2885
10	1000	5	1/10000	36.5314
10	1000	5	1/24000	33.0624
10	2000	5	1/10000	101.729
10	2000	5	1/24000	83.4111
10	3000	5	1/10000	59.1123
10	3000	5	1/24000	18.2805
10	4000	5	1/24000	117.352
15	500	5	1/10000	89.8901
15	500	5	1/24000	86.9827
15	1000	5	1/10000	40.1537
15	1000	5	1/24000	78.3735
15	2000	5	1/10000	55.1226
15	2000	5	1/24000	80.4987
15	3000	5	1/10000	36.9536
15	3000	5	1/24000	51.0627
15	4000	5	1/10000	54.515
15	4000	5	1/24000	53.3185
15	5000	5	1/10000	63.3993
15	4000	5	1/24000	101.918
21	500	5	1/10000	-2.11992
21	500	5	1/24000	24.8541
21	1000	5	1/10000	-87.4355
21	1000	5	1/24000	-79.1461
21	2000	5	1/10000	-68.4256
21	2000	5	1/24000	-54.957
21	3000	5	1/10000	-56.4013
21	3000	5	1/24000	-30.421

21	4000	5	1/10000	-96.1287
21	4000	5	1/24000	-65.0681
21	5000	5	1/10000	-52.2486
21	4000	5	1/24000	25.1137
5	500	5	1/24000	66.0585
5	1000	5	1/24000	74.5043
5	2000	5	1/24000	136.949